Modelling of Crystallisation Processes: Batch to Continuous

Thesis Submitted to
AcSIR
For the Award of the
Degree of DOCTOR OF PHILOSOPHY in Engineering Sciences

By
AJINKYA VIKRAM PANDIT
Registration Number: 20EE13J26044

Under the guidance of
Dr. Vivek V. Ranade

CSIR-National Chemical Laboratory (CSIR-NCL)
Pune - 411 008, India

July 2018

Certificate

This is to certify that the work incorporated in this Ph.D. thesis entitled "Modelling of Crystallisation Processes: Batch to Continuous" submitted by **Mr. Ajinkya Vikram Pandit** to Academy of Scientific and Innovative Research (AcSIR) in fulfilment of the requirements for the award of the Degree of **Doctor of Philosophy in Engineering Sciences**, embodies original research work under our supervision. We further certify that this work has not been submitted to any other University or Institution in part or full for the award of any degree or diploma. Research material obtained from other sources has been duly acknowledged in the thesis. Any text, illustration, table etc., used in the thesis from other sources, have been duly cited and acknowledged.

Mr. Ajinkya Vikram Pandit
Student
Chemical Engineering &
Process Development,
CSIR-NCL, India

Dr. Vivek V. Ranade
Supervisor
School of Chemistry &
Chemical Engineering,
Queen's University, UK

Declaration

I, hereby declare that the work incorporated in this thesis entitled **"Modelling of Crystallisation Processes: Batch to Continuous"** submitted to Academy of Scientific and Innovative Research (AcSIR) in fulfilment of the requirements for the award of the degree of **Doctor of Philosophy in Engineering Sciences** has been carried out by me and under the supervision of Dr. Vivek V. Ranade, presently posted at School of Chemistry and Chemical Engineering, Queen's University, Belfast, UK. This work has not been submitted to any other University or Institution in part or full for the award of any degree or diploma. Research material obtained from other sources has been duly acknowledged in the thesis.

Mr. Ajinkya Vikram Pandit
CSIR-National Chemical Laboratory
Pune-411008, India

Dedicated To My Loving Parents

Abstract

Crystallization is a critical unit operation for the separation and/or purification of solid products in the pharmaceutical, specialty and bulk chemical industries. Recent investigations have demonstrated that continuous crystallization potentially offers several advantages over batch crystallization (improved product consistency, reduced operating costs, faster processing, better control etc.). However, widespread implementation of continuous crystallization processes is still lacking due to the complex process dynamics involved. Mathematical modeling can go a long way towards reducing the uncertainties involved in the scale up and design of crystallization processes. The present thesis hopes to build a generalized framework to model continuous crystallization processes. The first chapter reviews recent advances in the fields of:

1. Process Analytical Technologies typically used to characterize crystallization processes
2. Batch Crystallization: Modeling and Control Strategies
3. Continuous Crystallization

Key gaps were identified which formed the basis for further investigation. Chapter 2 presented a simple model for interpreting the Chord Length Distribution (CLD) data measured by the Focused Beam Reflectance Measurement (FBRM) probe to obtain the Particle Size Distribution (PSD). The model was demonstrated to provide useful information for the PSD of various particle systems from FBRM probe measured CLD data. The model in conjunction with the FBRM probe can potentially enable the rapid, online and in-situ measurement of the PSD. Chapter 3 presented a generalized methodology to model batch crystallization processes using the Population Balance Equation (PBE). An approach to estimate key crystallization kinetic parameters was also described and implemented for an industrially relevant paracetamol-ethanol system. The model was successful in capturing key trends observed in batch crystallization experiments. Chapter 4 focused on developing a generalized framework to model variable density batch and continuous crystallization processes. Continuous crystallization experiments were performed in a novel crystallizer using an industrially relevant sodium nitrite-water system. The procedure described in Chapter 3 was used to estimate key crystallization kinetic parameters in conjunction with batch crystallization experiments. Using the model, it was identified that increasing the plug flow behavior of the continuous crystallizers favored higher yields, narrower PSDs and faster response times.

Acknowledgement

First and foremost, I would like to thank my advisor Dr. Vivek V. Ranade, without whom this work would not have been possible. Discussions with Sir helped me gain better insights into chemical engineering fundaments and also how to conceptualize *appropriate* solution strategies. I find myself still struggling with these aspects but getting better (I hope) under his continued guidance. I would also like to thank him for his constant patience in dealing with me, for always encouraging me to explore new (sometimes off topic) ideas and to collaborate with other researchers. It has been a tremendous learning experience – one for which I am very grateful for. Finally, I would like to add that his work ethic is very inspiring to everyone around him (academic and non-academics alike) and that it's been an honour to pursue a PhD under his guidance.

I would like to thank all of my lab mates – Ankit, Akshay, Dhananjay and Deepankar. Discussions with them have helped me gain a broader knowledge of Chemical Engineering and on several occasions get clarity on my own research problem. When stuck, it was always helpful to discuss difficulties with my lab mates. Implementing certain ideas together was especially rewarding. The work environment in our lab was always very pleasant and stimulating. I believe that this coupled with seeing my lab mates showing initiative and pursuing their individual problems gave me a lot of motivation to see my efforts through. I would like to thank the seniors of our lab group – Dev Gupta, Madhavi Sardeshpande, Amarveer Chilkha and Ranjeet Utikar for sharing with us their personal PhD experiences and some words of guidance.

I would like to thank Dr. Rahul Bhambure. His experience as an experimentalist was immensely helpful in designing and performing better experiments. I would like to thank him for taking the time and the effort to explore ideas with me which were not directly related to his work. The work done with him helped me gain a better understanding of the practical challenges facing crystallisation processes and was crucial in shaping the further direction of my work. With regards to experimentation, I would like to thank Dr. Sunil Joshi and his lab group for always being helpful. Not being much of an experimental group ourselves, Dr. Joshi and his lab group helped me with everything right from lab gloves to nitrogen cylinders. I sincerely hope I was not too much of an annoyance.

I would like to thank all my course co-ordinators for teaching me the required skills to undertake the PhD research. I would like to thank the workshop staff for being supportive and always being available (even sometimes at crazy short notices) to fabricate complex jobs. I would like to thank the administrative staff at NCL for putting up with my sluggishness in dealing with paper work and always being very helpful.

I would like to thank all of my friends and especially Akash and Priyanka for being very supportive throughout the four to five years of my PhD. Finally, I would like to thank my family, and especially my parents for their continued support throughout all these years and encouraging me to pursue my vision however outlandish it might seem.

Table of Contents

List of Figures

List of Tables

Chapter 1. Introduction

The manufacturing of specialty chemicals, bulk chemicals and pharmaceutical or agrochemical active ingredients often involve products or intermediates in a solid form. Crystallisation plays an important role as the separation and purification unit operation to obtain these solid products. The crystal size distribution and the crystal shape are the important parameters to judge the product quality. The width of the distribution and the mean size are important product specifications. These attributes influence desirable product properties depending on the area of application and in downstream solid's handling.

The first step in optimizing any crystallisation operation is to develop tools to assess the product quality. In this regard, recently there has been a lot of progress in terms of measuring the product characteristics. Advanced process analytical technologies are now capable of delivering those characteristics accurately and inline. Further, technologies have also developed to reliably measure the variables that directly affect the product quality such as the degree of super-saturation. Having sophisticated measurement techniques in turn allows for the effective control and rapid advancement of the crystallisation processes.

Typically, crystallisation is carried out in a batch mode of operation. The batch mode of operation is easy to implement in terms of process understanding as also in terms of engineering. However, it is observed that during the batch mode of operation, there is a batch to batch variability in the product quality. This variability causes problems in the downstream processing and as such is not desirable. The variability in the product quality is caused due to fluctuations in industrial operating conditions, presence of external seeds etc. Recently, a lot of efforts have been directed in developing control strategies to mitigate this fluctuation.

Due to limitations imposed by the batch mode of operation, recently there has been a surge of interest in the continuous mode of operation for crystallisation. The continuous process is more challenging to understand in terms of the process physics and more cumbersome to implement. However, it has been shown by many researches to potentially offer numerous advantages over the batch mode of operation. Different configurations of crystallizers have been investigated which opened up new avenues for process optimization and enable utilizing

process conditions which were unattainable in the batch operation. This in turn offers the possibility for more control over the particle size and shape of the product.

The present chapter aims to set the background for presenting the results of this work by briefly reviewing key contributions in crystallisation technology with regards to process analytical technology, batch crystallisation and continuous crystallisation. The next three subsections briefly review the previous work done along three key aspects: characterizing crystallisation processes, batch crystallisation processes and continuous crystallisation processes. This is followed by a brief summary of previous work. Finally the scope and the organization of the present thesis is discussed.

1.1. Characterizing Crystallisation Processes

Process Analytical Technologies (PAT's) are critical in optimization of crystallisation processes as they identify the key measures of product quality (such as crystal morphology, size etc.) as also critical process variables that affect them (super-saturation, solid's loading etc.). The data collected by the PAT's can be used to develop improved process understanding, evolve better operating protocols, achieve continuous improvement in technology and develop better control strategies. Especially in the pharmaceutical industry and in general for crystallisation, PAT's are indispensable especially due to the high amounts of uncertainties and the lack of understanding in such systems. Excellent reviews for the state of the art in PAT's were provided by Lawrence et. al. (2004) and Simon et. al. (2015).

The criteria for the product quality used in crystallisation are typically the crystal size distribution and the crystal shape. The product specifications are important as they affect the downstream processing unit operations as also are specific depending upon the area of applications. For example, different polymorphic forms have different solubility, different sizes/shapes of crystals have different flowability and filterability. PAT's are thus indispensable for the monitoring of such product characteristics to ensure the products meet their specifications. The PAT's may be characterized as being:

1. Online: Measurements done as the experiment is progressing. A sample may be diverted to the measurement unit which may or may not be returned.

2. At-line: Measurements done on the site of the experiments
3. Offline: Measurements done at a separate site
4. In-line: Measurements done real time at the location where the process is occurring. However, these may affect the flow profile
5. Non-invasive: Same as in-line with the difference that the sensor is never in contact with the process fluid and thus does not affect the process

Typically for crystallisation processes, at-line or offline methods are not the first choice because of the time delays in collecting the sample and analyzing the sample. Especially in a highly transient process such as crystallisation, such a time delay, and perturbations caused in the sample state due to exposure to the environment introduce errors into the analysis. Thus in-line or non-invasive methods are generally the preferred methods for crystallisation processes.

The key thermodynamic variable that affects the crystallisation process is the degree of super saturation. Both the nucleation rates and growth rates are known to be functions of the degree of super-saturation. The super-saturation may be represented as:

$$S = \frac{C - C^*}{C^*} \tag{1.1}$$

Thus, PAT's in crystallisation processes are primarily devoted towards monitoring the super-saturation profile and key product qualities such as the crystal size distribution, morphology and in some cases, the solid's loading. The different technologies for monitoring each of these variables are briefly discussed below.

1.1.1. Super-saturation

For the measurement of the super-saturation, the Attenuated total reflectance-Fourier transform infrared (ATR-FTIR) spectroscopy has been widely utilized (Lawrence et. al., 2004). The main purpose of this probe is to analyze the contents of the solution phase. It is even possible to track the concentrations of multi-component solutions as is often seen in pharmaceutical applications (Figure 1.1.1).

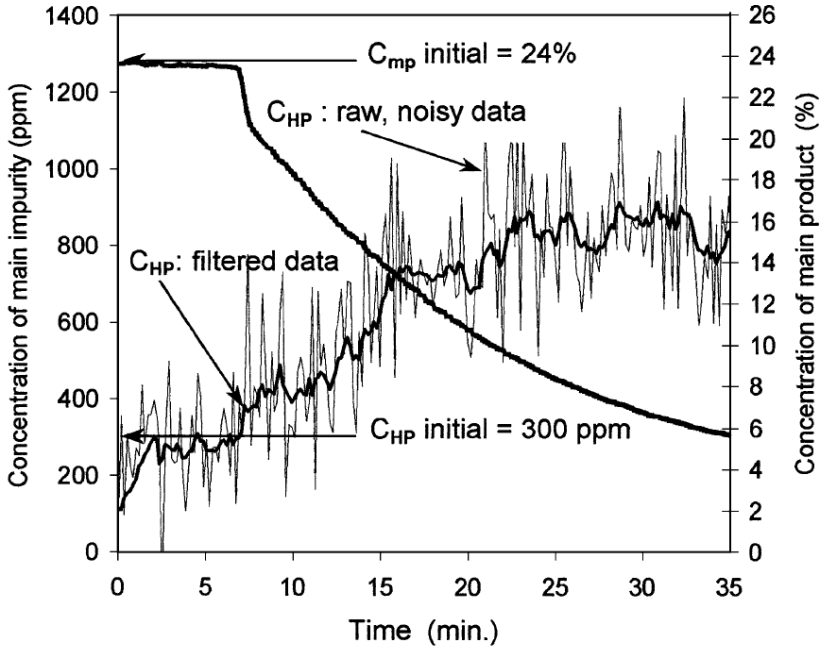

Figure 1.1. Concentration of the solute and the impurity simultaneously measured in-line using an ATR-FTIR probe during crystallisation (Lawrence et. al., 2004)

In some cases, it is also possible to use conductivity measurements for tracking the solute concentration. However, such an effort requires considerable calibration before it can be used as the conductivity values change with respect to concentration and temperature rather than just concentration.

1.1.2. Particle Size

There are several techniques available to directly measure the particle size distribution (PSD). The most popular ones are the Laser Diffraction and the Microscopy methods. These enable a complete characterization of the PSD curve, however, are offline methods. Hence, it is difficult to obtain PSD results using these methods for transient processes such as crystallisation as we are limited to only investigating the 'equilibrated' samples. As described earlier, offline methods of size analysis inevitably introduce errors into the characterization of the sample for crystallisation processes.

Particle Vision and Measurement (PVM) is another widely used measurement device which extends the microscopy technique and enables the measurement of PSD in-situ and online. Two dimensional images of the particles as viewed from the probe window are recorded which are later processed to obtain the PSD. The Focused Beam Reflectance Measurement (FBRM) probe is also widely used to study crystallisation. The FBRM probe works on the

principle of laser back-scattering. Both these methods are important because of the fact that they enable in-line measurements as described above. Although these methods do affect the internal flow, careful placement of the probe helps to give reliable measurements.

1.1.3. Particle Shape

Essentially the only way to monitor particle shape is to in some sense 'directly' view the crystals. In such cases, offline microscopy based methods are useful as they enable this view. Apart from this, the inline method of PVM as described above also enables the direct detection of the particle shape. In some case, the data recorded by the FBRM can also be interpreted in some way to infer the particle shape although this requires previous validation.

1.1.4. Solid's Loading

A nephelometer (or turbidity probe) is often used to study crystallisation systems. The nephelometer is a light scattering based technique that records the concentration of solid's in the solution. It allows for the in-line measurements for solid's loading, however, the results provided by this method do not give any information regarding the PSD. The main advantage of this method is that it is relatively cheap and easy to implement. Moscosa-Santillan et. al. (2000) demonstrated the use of a turbidity probe to reliably control the dynamics of the crystallisation processes.

1.1.5. FBRM for PSD measurement

From all the PAT's, in the present work, we will focus on the use of the Focused Beam Reflectance Measurement (FBRM) probe for characterizing particle size. The FBRM is a useful tool to monitor the PSD because it is inline. In a FBRM, a laser is emitted from a laser source inside the probe. The source is rotated around the probe axis such that the laser revolves remaining parallel to the probe axis. The laser traces a cylindrical surface around the probe axis inside the probe. A very high speed of rotation is used (in the present study the tangential speed of the source was set to 2 m/s). At the probe tip is a sapphire window which is in contact with the solution wherein the particle measurements are to be made. A schematic of the inner mechanism of the FBRM is shown in the Figure 1.1.2. Whenever the revolving laser encounters a particle along its circular path it gets reflected back into the probe. Each instance of this reflection is treated as one count of particle detection and the duration of time for

which the beam is reflected multiplied by the tangential speed of the laser becomes the length of the chord which the laser 'traces' on the particle surface (Figure 1.1.3). Thus, in course of time and in dense solutions, multiple particles are recorded by the FBRM probe and hence we obtain the number of counts and the particle chord length distribution (CLD) data. The CLD measured by the FBRM probe, although related to the PSD, bears no obvious resemblance to the PSD as is evident from the system description. The CLD data needs to be interpreted in some way to obtain information regarding the PSD.

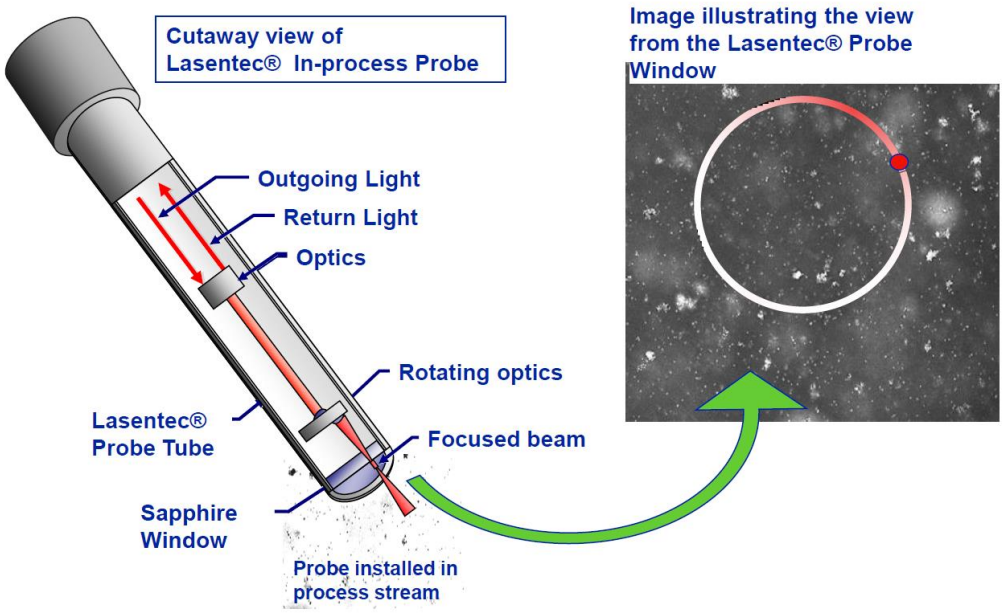

Figure 1.2. Inner mechanisms of an FBRM probe (Mettler Toledo training manual)

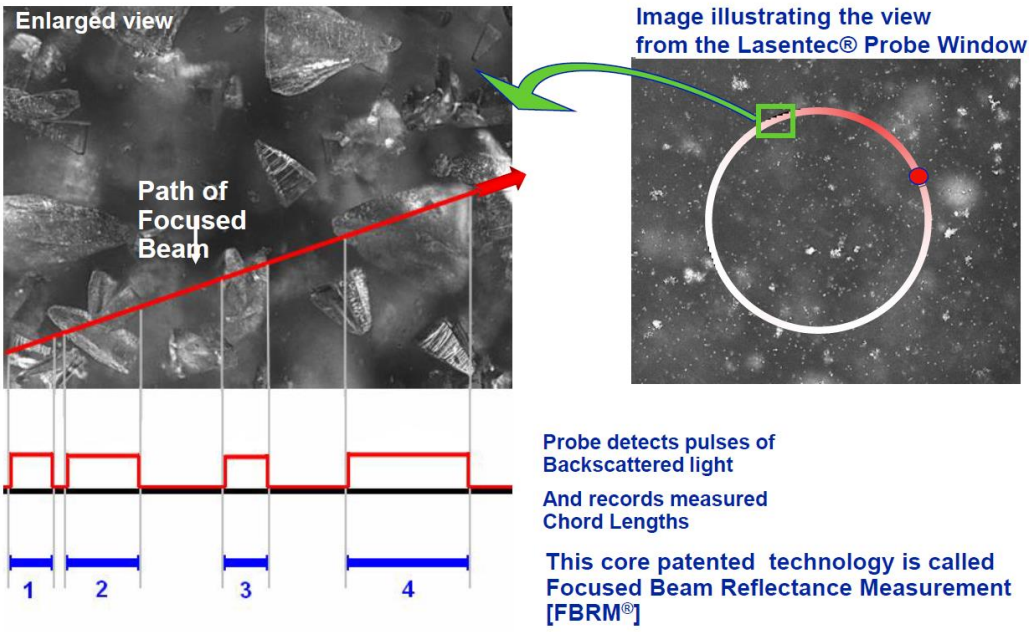

Figure 1.3. Signal detection in an FBRM probe (Mettler Toledo training manual)

1.1.6. Interpreting FBRM data

Much work has been done recently to address the problem of translating the CLD as recorded by the FBRM to the PSD. Li et. al. (2013) developed an empirical method for the determination of the PSD from the CLD. Multiple fingerprint CLD's for known particle sizes were first meticulously determined over the size range of interest. The actual PSD was estimated as the one which yielded the same CLD as the measured CLD by a linear combination of the fingerprint CLD's. However, this method requires a lot of standardized data (fingerprint CLD's) in order to calibrate the model for a specific system before it starts to make predictions. Gathering this standardized data is not always possible and is definitely time consuming and cumbersome. Besides, the aforementioned publication, other efforts directed towards solving the CLD to PSD problem all follow a definite methodology. First the CLD of a single isolated particle (or equivalently a mono-disperse system) is derived theoretically. Then, the CLD is derived theoretically for a system with a known PSD. Finally, the inverse problem of determining the PSD for a known CLD is addressed. Having established the first part, the second part is relatively straightforward. Several efforts have been directed to specifically address the first part of the problem. Li et. al. (2005) presented a two part study to determine the PSD from the CLD measurements for non-spherical particles. First, a model to determine the CLD for a spherical particle. The model was extended to allow for various particle shapes using a 2D super ellipsoidal function. However, the model only considered a fixed 2D particle projection to determine the CLD and did not account for the different particle orientations and the subsequent effect on the 2D projections. In the model presented by Ruf et. al. (2000) all possible 2D projections of the 3D shape (with different orientations) were considered for determining the CLD. The approach to calculate the CLD from the 2D particle projection is fundamentally similar to the 2D model proposed previously.

The inverse problem of determining the PSD from a known CLD is more troublesome. Typically, the PSD is estimated iteratively by starting from a guess PSD and comparing the predicted CLD and the measured CLD to evaluate the direction of the iteration. However, due to the non-linear nature of the CLD expressions obtained from the single particle models, the inverse problem becomes an ill posed mathematical problem. The most popular methods include the Least Squares (LS) and the Constrained Least Squares (CLS) algorithms (Li et. al., 2005). However, when CLD measurements are noisy, as are typically observed for the case of

crystallisation systems, oscillations or negative values are obtained for the PSD's using these methods. To overcome this pitfall, Li et. al. (2005) proposed an iterative Non-Negative Least Squares algorithm for the inversion problem. Worlitschek et. al. (2003) extended the model proposed by Ruf et. al. (2000) by considering the method of projection onto convex sets (POCS) to solve the inversion problem. Agimelen et. al. (2015) reported an algorithm to estimate the PSD from CLD measurements for needle shaped crystals. Appropriate single particle CLD models reported in literature were used and the algorithm required no additional information such as approximate particle size range or particle aspect ratio to constrain the iterative procedure as for previous efforts. Along similar lines as in previous works, in Chapter 2 a model was proposed for the CLD to PSD problem. Appropriate modeling assumptions led to a simpler expression for the single particle CLD than obtained in previous studies. This coupled with the assumption of standard size distribution shapes to represent particle populations, enabled the implementation of the model using simple spread sheeting tools.

These efforts and some continuing advances are enabling the use of FBRM technology for the reliable monitoring of PSD. This is evidenced by the rise in the use of the FBRM technology specifically with regards to crystallisation.

1.2. Batch Crystallisation Processes

1.2.1. Introduction

Batch processes are the most commonly used crystallisation unit operations. Hence, it is obvious that a large body of research in crystallisation is devoted towards specifically understanding the dynamics of batch crystallisation and specifically in evolving reliable control strategies. Batch processes are preferred as they are easy to implement from a process understanding point of view as well as from an engineering point of view. However, the convenience of batch processes comes at the potential costs of time, money and product quality. It is said potential because continuous processes have yet to be established completely as being the preferred choice for crystallisation.

One of the major limitations of the batch processes is the batch to batch variability in the product quality. The variability occurs due to fluctuating industrial operating conditions. As

such the nucleation kinetics are very sensitive to changes in operating conditions and the effect of fluctuations are immediately translated into variable product quality. One of the way to get around it is to develop robust control strategies. Recently a lot of work has been focused on developing sophisticated control strategies for batch crystallisation processes. These have in some sense to some extent mitigated the effect of fluctuations on the product quality.

Chapter 3 presents a general protocol to estimate key parameter values for the crystallisation kinetic model. A novel experimentation scheme coupled with appropriate modeling studies was proposed as a robust method to estimate key parameter values. The review presented in the following section helped identify important tools to implement the said protocol. First, the general modeling framework for batch crystallisation processes is discussed. Then numerical methods used to obtain the solution for the model equations are discussed. The next section highlights how crystallisation kinetics is dealt with in batch processes. Finally, a discussion is presented dealing with different control strategies investigated for batch crystallisation.

1.2.2. Mathematical Model

Population balance equations are used to develop models for batch crystallisation process. The population balance equations track the change in the number density distribution function of the crystals in the crystallizer with time. Since the process is operated in a batch mode, a transient population balance equation needs to be solved. The transient PBE may be written as (Ramakrishna, 2000):

$$\frac{\partial n(L,t)}{\partial t} + \frac{\partial G(L,t)n(L,t)}{\partial L} = B_0(t)\delta(L - L_{nuc}) \tag{1.2}$$

Here B_0 stands for the rate of nucleation of particles. L is the particle size co-ordinate, G is the crystal growth rate, δ is the Kronecker delta function, L_{nuc} is the size of the nucleating particles and $n(L,t)$ is the number density distribution function. Other phenomena such as breakage and agglomeration may also be represented by adding suitable source terms on the right hand side however, this is beyond the scope of the present text. For a detailed description of these

phenomena kindly refer to Ramakrishna (2000). It is also necessary to solve the dissolved solute's concentration equation along with the PBE as the growth rates and nucleation rates are typically represented using a super-saturation driving force rate expression. The expression for the rate of change of dissolved solid's concentration may be obtained by differentiating the expression for the total solute mass with time and by suitably re-arranging the expression to suit the numerical method used. The total mass of solute will not change and hence the differential will equate to zero. The expression for the total solute mass may be written as (Pandit et. al., 2015):

$$M_S = V_R C M_w + V_R \rho_p \frac{\pi}{6} \int_0^\infty L^3 \, n(L,t) dL \tag{1.3}$$

Suitable energy balance equations may also be evolved if the heat of crystallisation/dissolution is high enough and an adiabatic process is considered. However, typically, batch crystallizers are operated such that the temperature profile is controlled externally and precisely. So, any changes due to the liberation of heat of crystallisation/dissolution are typically compensated for by the control system.

1.2.3. Numerical Methods

Analytical solutions for the steady state population balance were provided by Randolph and Larson[11]. However, owing to the transient nature of the problem at hand and the increasingly complex expressions for nucleation rates and growth rates, an analytical solution to the problem is not always possible. It is imperative then to use numerical methods to solve the population balance equation. Several methods are available to solve the PBE. Population balance equations (PBEs) have been widely used to model crystallisation and dissolution processes. A detailed review of a subset of the methods to solve population balance equations is given by Ramkrishna (2000). Analytical solutions, moment based methods (standard method of moments and quadrature method of moments), discretization based methods (fixed pivot and moving pivot), and the method of weighted residuals were reviewed. It is possible to obtain analytical solutions to the PBE, however, this is limited to a few cases depending upon the type of mathematical expressions used to represent growth/nucleation kinetics as well as for other phenomena considered (aggregation/breakage). Analytical

solutions for the population balance equation for simple cases such as size independent crystal growth rate and a power law type nucleation rate are provided in the work of Ramakrishna (2000).

Another class of methods for the solution of the PBE are those which track moments of the particle size distribution rather than tracking complete distribution also known as moment based methods. Simple systems (not involving breakage or aggregation), may be addressed suitably by using the standard method of moments (Randolph et. al., 1988). For more complex systems, involving aggregation and breakage, several new methods such as the quadrature method of moments (Marchisio et. al., 2003) and the direct quadrature method of moments have been proposed (Marchisio et. al., 2005). The solutions obtained from such methods are computationally efficient, however, are less descriptive as it is difficult to extract the complete particle size distribution information from only the known moments. This inverse problem is not a mathematically well-posed problem, that is, there may exist multiple solutions to the problem. There are methods of extracting the particle size distribution from known moments however; those are not besides their own limitations.

Table 2.1: Overview of methods available for the solution of the population balance equation (Pandit et. al., 2015)

Method Name	**Brief Description**	**Strengths**	**Weaknesses**
Discretization Based Methods	Solution by discretization of the particle size co-ordinate and transforming PBE into a set of ODE's	Enable the complete determination of the PSD	Computationally expensive
(a) Fixed Pivot	The change in number of particles in each discretization element tracked	Relatively easy to implement	Prone to numerically induced errors
(b) Moving Pivot	The change in the location of the boundaries of each discretization element tracked	Computationally more efficient than fixed pivot; Not prone to numerically induced errors	Relatively more complex to implement
Moment Based Methods	Solution by transforming PBE into set of ODE's representing rate of change of a chosen set of moments	Computationally efficient; Easy to implement	Does not enable the complete determination of the PSD
Method of Characteristics	Set of characteristics of the PBE is obtained enables the reduction of the PBE into a set of ODE's	Highly efficient for simple physics	Approach difficult to implement for complex physics
High Resolution Finite Volume	Extends the mathematical treatment of solution of equations of flow by finite volume methods to solve PBE	Allows coarser gird; Prevents numerical errors	Computationally expensive; relatively new and hence invalidated

Discretization based methods for the solution of the PBE enable the complete description of the particle size distribution. In these methods, typically, the domain of the particle size is broken into discrete bins and the number of particles in these bins is tracked with time. However, one should be careful in implementing these methods as they are prone to numerically induced errors. Recently, high resolution finite volume (HRFV) methods have been gaining importance for the solution of PBEs (Gunawan et. al., 2004). These methods are derived from a general finite volume class of methods which are typically used to solve flow and wave propagation problems (Leveque, 2002). The method has the advantages of tapping the sophisticated numerical methods which have been developed to solve the more popular flow and wave propagation problems and as such is very robust. Apart from this, the fixed and moving pivot methods are also two popular discretization based methods for the solution of the population balance equations (Ramakrishna, 2000) . A comparison between the pros and cons of using each method are shown in Table 2.1.

1.2.4. Crystallisation Kinetics

One of the most difficult things in modeling crystallisation processes is determining the crystallisation kinetics. The crystallisation kinetics includes both the kinetics of crystal growth and kinetics of nucleation. Even in nucleation there are two types: primary and secondary. One of the primary confusions in this section is that the phenomena themselves are not well understood. This leads to a wide array of rate expressions which have been reported to represent both nucleation and growth rates. Owing to the wide range of expressions, there is no consensus in terms of characterizing the kinetics of a system.

1.2.4.1. Crystal Growth

Crystal growth is typically modeled as a two-step process. In the first step, the solute molecules are moved to near the crystal surface by convection and diffusion. In the second step, the molecules near the crystal surface attach to the crystal lattice and cause the ‘growth’ of the crystal. The first step is thus the mass transfer step and the second step is the surface integration step (Karpinski, 1985). Typically, it can be assumed that the crystal growth is limited by the surface integration step and the mass transfer step is sufficiently faster in comparison (Pandit et. al., 2015; Worlitschek et. al., 2004). The surface integration step can

be related to the degree of super-saturation in the form of a reaction rate type of expression to obtain the growth of the crystal surface as:

$$G = k_{r0}\exp\left(-\frac{E_A}{RT}\right)(C - C^*(T))^g \tag{1.4}$$

The value of the activation energy for the growth rate expression is known to lie in range of 4 x 10^7 to 8 x 10^7 J/kmol-K. The value of the growth rate exponent, g, is reported to be approximately equal to 2. Nothing was reported with regards to the pre-exponential constant, k_{r0}.

1.2.4.2. Nucleation

For an unseeded crystallisation, the onset of crystallisation is caused by homogeneous primary nucleation. Primary nucleation is the nucleation where the solute molecules in a supersaturated solution within themselves aggregate to form nuclei. By unseeded it is implied that no external seeds or crystals were added to induce nucleation. Now as the crystals in the solution grow in number and size, secondary nucleation starts to gain importance. Secondary nucleation is the generation of nuclei which may be attributed to the breakage by some mechanism of already existing crystals (Davey et. al., 2001; Myerson, 2002; Mersmann, 1995). Typically, after this regime sets in, that is the number of crystals in the solution becomes sizeable, secondary nucleation is the dominant mechanism for nucleation. The primary nucleation rate can be represented by a simple power law relation as (Davey et. al., 2001; Myerson, 2002):

$$B_{0,pri} = k_1(\Delta C)^{n_1} \tag{1.5}$$

There are several relations to model secondary nucleation. The different rate laws used to model the secondary nucleation rate are listed in Table 2.2. The first law listed in this table was found to be extremely sensitive and not reliable. The second relation is too simplistic as it is known that the rate of secondary nucleation is dependent loosely speaking on the number of crystals present in the solution owing to the mechanism proposed for the secondary nucleation. Pandit et. al. (2015) hypothesized that secondary nucleation occurs due to some small parts chipping off from the surface of bigger crystals. The smaller particles which get chipped off then become the new ‘seed’ crystals. The rate of nucleation thus seems to be

directly proportional to the total surface area of the crystals in the solution as opposed to the total number of crystals. The secondary nucleation rate considered as such may be written as:

$$B_{0,sec} = k_2 M_2 (\Delta C)^{n_2} \tag{1.6}$$

Here, M_2 is the second moment of the number density distribution function. The total nucleation rate is thus a sum of the contributions due to primary and secondary nucleation and can be represented as:

$$B_0 = B_{0,pri} + B_{0,sec} \tag{1.7}$$

Table 2.2. Laws to represent secondary nucleation reported previously (Pandit et. al., 2015)

No	Rate Expression	Parameters	Reference
1	$B_{0,sec} = E\frac{k_a M_2 D}{d_m^4}\exp\left(-\pi\left(\frac{\gamma_{sl} d_m^2}{kT}\right)\frac{1}{ln\Delta C}\right)$	k_a: Shape factor d_m: Molecular diameter γ_{sl}: Interfacial surface tension D: Diffusivity k: Boltzman constant ΔC: Supersaturation E: Probability of nucleation	Worlitschek et. al. (2004)
2	$B_{0,sec} = k_N \Delta C^n$	ΔC: Supersaturation k_N: Rate Constant	Myerson (2002)
3	$B_{0,sec} = k_N' W^i M_T^j \Delta C^n$	k_N': Rate Constant W: Agitation Rate M_T: Suspension Density ΔC: Supersaturation	Myerson (2002)
4	$B_{0,sec} = k_N'' M_T^j \Delta C^n$	k_N': Rate Constant M_T: Suspension Density ΔC: Supersaturation	Myerson (2002)

1.2.4.3. Dissolution

The dissolution rate of the particles is a strictly mass transfer problem. The solution is under-saturated and the rate of shrinkage of the particles can be determined according to the rate of mass transfer from the solid phase into the solution phase. Paramount in accurately

calculating the rate of dissolution is to have reliable estimates for the coefficient of mass transfer. Once the mass transfer is known the rate of shrinkage of the particles can be written as:

$$D = k_d \frac{M_w}{\rho_p} (C^*(T) - C) \tag{1.8}$$

The procedure to calculate the mass transfer coefficient is reported by Worlitschek et. al (2004) and also by Mersmann (2000). The value of the mass transfer coefficient depends upon the physical properties of the system as well as the critical system operating parameters such as the power dissipation rate.

1.2.4.4. Estimating Kinetic Parameters

With the advent of more reliable process analytical technologies, more reliable kinetic parameters may be estimated. However, the kinetic parameters that are developed are inherently system-specific. This is the case especially for the case of secondary nucleation. As the nucleation progresses and the number of particles in the system increase, the secondary mode of nucleation starts dominating the crystallisation process. Thus, the secondary mode of nucleation has a major impact on the evolution of the crystallisation processes. However, the inherent nature of secondary nucleation is in fact system specific. Hence, on changing operating parameters such as impeller speed or on changing crystallizer configuration, it is expected that the kinetic parameters for secondary nucleation are not transferred and need to be reworked.

There are several studies that work on determining the kinetic parameters for crystallisation processes. These studies develop a mathematical model to represent the particular crystallisation processes. The model discussed earlier is the most common framework for modeling batch crystallisation processes. The model predictions are then made to match the experimental measurements for particle size distribution, super-saturation profile or the evolution of one of the moments by changing appropriate kinetic model parameter values. This then translates into an optimization problem wherein starting from an initial guess of kinetic parameters, the final parameters are obtained iteratively. Such a procedure was adopted by Worlitschek et. al. (2004) as well as by Pandit et. al. (2015) to estimate the kinetic

parameters for a system of paracetamol-ethanol. The protocol mentioned in the above section was developed in Chapter 3. A novel experimentation scheme was coupled with modeling studies to estimate key parameter values. It was argued that as opposed to previous studies, the presented scheme validated the model parameter values over a larger range of operating conditions and hence were more reliable.

1.2.5. Control of Batch Processes

The control of batch processes is a topic of immense interest in crystallisation. This is because one of the chief issues in using batch crystallisation is the batch to batch variability in the product quality. This variability arises typically due to fluctuations in industrial operating conditions. It is essential to develop a robust control system so that the effect of such fluctuations can be mitigated. Also, another topic of interest is to identify optimum operating protocols and operating strategies which make it possible to achieve a finer control over the product quality and in some cases make accessible product characteristics which previously were not unattainable. In this section, some of the recent efforts directed towards evolving control strategies for batch processes are discussed.

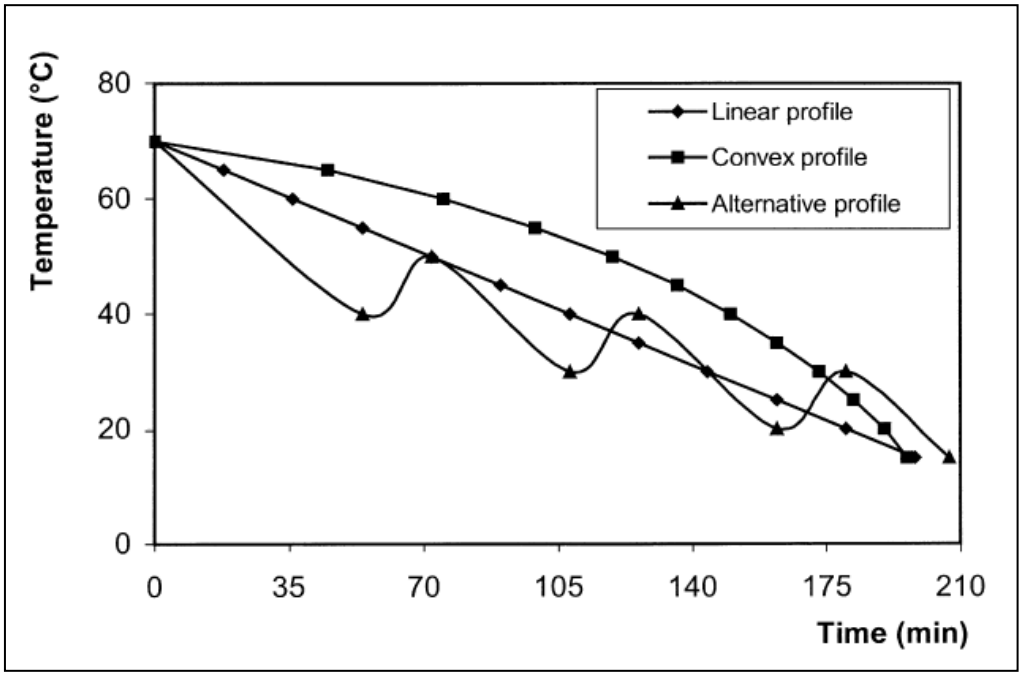

Figure 1.4. Temperature time trajectories employed for batch cooling crystallisation of glycine in water (Moscosa-Santillan et. al., 2000)

Moscosa-Santillan et. al. (2000) investigated the potential of online turbidity measurements to identify optimum operating protocols for seeded batch cooling crystallisation processes.

Seeded batch-cooling crystallisation was carried out in 3 temperature-time trajectories (Figure 1.4). It was found that the alternating trajectory yielded much narrower CSD than the other two. Also, turbidity measurements were found to be effective in identifying operating conditions favoring secondary nucleation and thus helped in identifying alternate protocols to avoid that phenomenon.

Choong et. al. (2004) developed an optimization framework for batch cooling crystallisation processes based on the method of simulated annealing. The optimization algorithm needs only a single variable referred to as the performance index from the phenomenological model to carry out the optimization rather than the unreliable and messy calculation of gradients. It was shown that the developed optimization framework could successfully identify the temperature profiles which yielded bigger sized particles with lesser coefficient of variation than would have been attained using standard linear and convex temperature profiles. Using the optimization framework, it was found that several operating variables such as cooling profile, seed size, seed mass, batch time, initial and final temperatures etc. may be optimized.

Nagy (2009) presented a novel two-level control approach for batch crystallisation processes. On the higher level, a phenomenological model-based control strategy was used to determine the trajectory of the super-saturation curve based on the target CSD and the changing operating conditions. The trajectory is then fed to a lower level super-saturation controller which drives the system according to the desired concentration versus time trajectory by changing the crystallizer temperature. The control strategy was seen to be effective in identifying the optimal super-saturation trajectory in order to obtain a desired CSD.

Lewiner et. al. (2002) proposed a novel method to monitor the crystallisation process online using the ATR-FTIR spectroscopy to measure the super-saturation. The cooling crystallisation of two agrochemical compounds was investigated. Using the ATR-FTIR method to measure super-saturation, a fines dissolution loop was implemented. First, the solution crystallizes and is allowed to reach equilibrium concentration while maintaining the solution temperature. The fines dissolution loop was then implemented. It was found that the fines dissolution loop was effective in providing more reproducible results as also bigger sized particles (Figure 1.5).

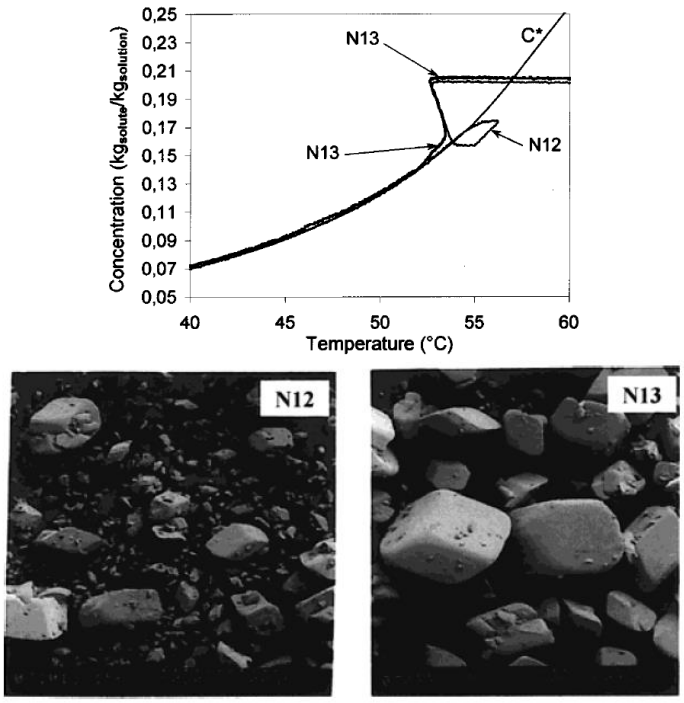

Figure 1.5. The super-saturation profile in the fines dissolution loop and the corresponding micrographs of the crystals as reported by Lewiner et. al. (2002)

Chung et. al. (1999) investigated optimal seeding strategies for the batch cooling crystallisation of potassium nitrate in water. Three batch control objective functions were investigated: the minimization of the weight mean size, the coefficient of variation and the ratio of the nucleated mass of the crystals to the seed mass. It was found that the optimizing the seed distribution can have a larger impact on the final crystal properties than optimizing the super-saturation profile.

Ward et. al. (2011) developed a dimensionless population balance modeling framework to model seeded batch cooling crystallisation process. The use of non-dimensional numbers effectively allows making more generalized conclusions which are not limited to any specific system. The authors investigated different optimal super saturation profiles for their effectiveness in minimizing secondary nucleation and maximizing growth or in minimizing the mass of nucleated crystals. It was found that the optimal profile suggested by Mullin-Nyvlt was the best as it provided good results even with no information about the kinetics available a-priori. It was also concluded that the distribution of the seed crystals play a more influential role in determining final product properties than the super saturation profile. Primarily optimization efforts should be directed towards evolving optimum seed profiles.

1.3. Continuous Crystallisation Processes

1.3.1. Introduction

Continuous crystallisation processes have been gaining importance in the recent years as an alternative to batch processes for the production of pharmaceutical, specialty and bulk chemicals involving crystallisation. Conventionally, industrial crystallisation processes are operated in batch mode. However, a continuous mode of operation potentially offers several advantages over the batch mode of operation. Due to fluctuations in the upstream process conditions and operating conditions as well as due to variability in batch handling there is inevitably variability in the batch to batch product quality. Continuous processes are known to offer more robust control on the process dynamics and hence can reduce the variability in the product quality.

The continuous mode of operation also allows the utilization of operating space which was previously inaccessible in the batch mode of operation. This fact can be harnessed to effectively improve the process efficiency. Apart from the improved process efficiency, a utilization of a larger operating space provides access over a wider range of particle sizes (both bigger and smaller sized), particle shapes and crystal properties which can be produced. It is not always possible to produce these product characteristics in a batch mode of operation due to the inherent limitations imposed on the degree of super-saturation allowable. A continuous mode of operation effectively reduces the labor and operational costs which are required in batch processes and sometimes also saves on utilization of space.

Accurate mathematical models are usually necessary to realize the advantages of the continuous crystallisation processes. In Chapter 4 a generalized modeling framework was developed for modeling both batch and continuous crystallisation processes. A tanks-in-series framework typically used for capturing mixing effects in chemical reactors was integrated with the population balance equation models popularly used for modeling crystallisation processes. The key aspects of mathematical modelling of continuous crystallisation are briefly discussed in the following.

1.3.2. Modeling Methodology

Population balance equations are used to model both batch and continuous crystallisation processes. Models for continuous processes have additional inflow and outflow terms in all relevant equations (mass balance, population balance, energy balance) as opposed to the batch processes. Further, batch processes are variable volume processes. Continuous processes may be fixed volume or fixed flow rate. Models need to be suitably developed to account for the relevant cases. The continuous processes typically investigated can be categorized as being some variation of a cascade of MSMPR crystallizers. Steady state population balance equations (PBE's) are formulated for each of the MSMPR crystallizers and suitable connections are added to represent recycle streams and connections between the crystallizers. The PBE for the i^{th} MSMPR is of the form:

$$G_i \tau_i \frac{dn_i}{dL} + n_i = 0 \tag{1.9}$$

The equations for the concentration in each of the MSMPR units can be written as:

$$C_{i-1} = C_i + M_{T,i} \tag{1.10}$$

The equation for temperature is not written because the units are typically operated under isothermal conditions. The steady state population balance equations are solved analytically to obtain the expressions for the number density function in each of the crystallizer units. The above PBE is a boundary value problem with the boundary at *L=0* represented by n_0 or the nucleation rate. Simple power law relations are used to model the growth rates and nucleation rates by relating them to the super-saturation driving force. The kinetic parameters for the nucleation and growth rates are found out by fitting the model predicted CSD against a CSD obtained experimentally. The model is then used to simulate different scenarios or to study the effect of different operating parameters on the product yield and purity parameters.

Although this modeling platform is fairly robust, the kinetic parameters are highly sensitive to the operating parameters and crystallizer geometry considered. The effect of operating parameters such as impeller speed on the nucleation rate constants was not investigated in

the studies considered here. It is known, that the secondary nucleation rate is largely affected by the impeller speed and the flow dynamics. As such, due to the difficulty in dealing with the secondary nucleation rates, the models developed here are not easily transferrable to different configurations and need to be calibrated independently.

The model for the plug flow crystallizer is based on the standard plug flow or axial dispersion models. The steady state population balance for a plug flow crystallizer can be written as:

$$u_x \frac{\partial n}{\partial x} + G \frac{\partial n}{\partial L} = 0 \tag{1.11}$$

The equation for the concentration can be written as:

$$u_x \frac{dC}{dx} = -3\rho_S k_V \int L^2 \, n(L) dL \tag{1.12}$$

The constitutive laws for nucleation and growth are the same as considered in the case of the MSMPR crystallizers. Again the kinetic parameters need to be determined specifically for the case of the system investigated. The kinetic parameters are determined by fitting model predicted CSD's to the experimental CSD's. Such a model has been used to investigate cooling as well as anti-solvent crystallisation previously. Suitable equations may be added as may be relevant to the system to model different configurations (e.g. Multiple addition points, heat transfer etc.). The population balance equations to account for dispersion along the axial direction (Axial Dispersion Model) as also accounting for the fluctuations in growth rate (Growth Dispersion Model) have been shown to provide better accuracy to model such crystallizers.

Typically, models are formulated without considering the effect of change in volume due to crystallisation. However, for highly soluble systems (eg. Paracetamol in ethanol), volume changes significantly affect the crystallisation dynamics. Recently, Su et. al. (2015) proposed a generic framework to model crystallisation processes – batch and continuous, which included the effect of changing volume. However, the model was formulated for a cascade of MSMPR's and as such only accounted for fixed volumetric flow rate processes. In plug flow crystallisers and other similar types of 'closed' crystallisers, the volume of the crystalliser is

fixed and the outlet flow rate changes instead of the volume on account of crystallisation. Vetter et. al. (2014) performed an extensive simulation study specifically for the cascade of MSMPR crystallisers. The effect of number of stages, temperature, anti-solvent fraction and residence time in each crystalliser on the particle size distribution was studied.

As the model parameters are not transferrable, it is important that the experimental data be available for the specific system so that system specific kinetic parameters may be determined. Thus, it is important to characterize the process with experimental data such as dissolved solids' concentration, particle size distribution or turbidity among other things. Process analytical technologies (PAT's) are used to determine these characteristics either online or offline. A detailed description of the PAT's typically used for crystallisation is provided in earlier sections.

1.3.3. Experimental studies

Due to difficulty in the a-priori prediction of the system behavior for different configurations, it is important to investigate the configurations experimentally. The model may then be calibrated based on experimental data and further used to explore the operating variable space for determining the optimum operating protocols. Various different continuous crystallisation configurations have been investigated in the recent years. Alvarez et. al. (2011) investigated the continuous crystallisation of cyclosporine using a multistage mixed suspension mixed product removal cascade with recycle (Figure 1.6). It was found that the temperature of the third crystallizer and the recycle ratio were effective parameters to control the product purity and yield. However, it was found that the product yield and purity had an inverse relationship with each other regardless of the operating conditions.

Quon et. al. (2012) investigated the continuous reactive crystallisation of aliskiren hemifumarate using two MSMPR crystallizers in series (Figure 1.7). A model was developed, validated and was used to study the effect of the temperatures and the residence times in the first and the second crystallizers on the product purity and product yield. It was found that the product purity and the yield had an inverse monotonic relationship.

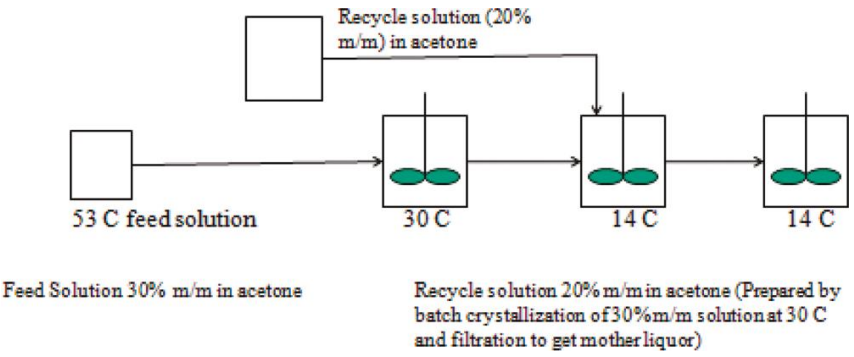

Figure 1.6. A multistage mixed suspension mixed product removal crystallizer considered by Alvarez et. al. (2011)

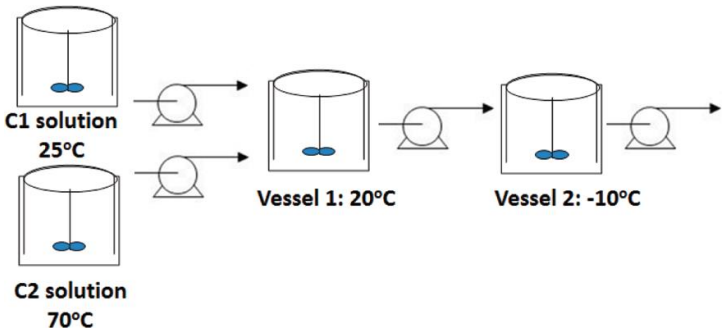

Figure 1.7. Configuration for the continuous reactive crystallisation of Aliskiren Hemifumarate considered by Quon et. al. (2012)

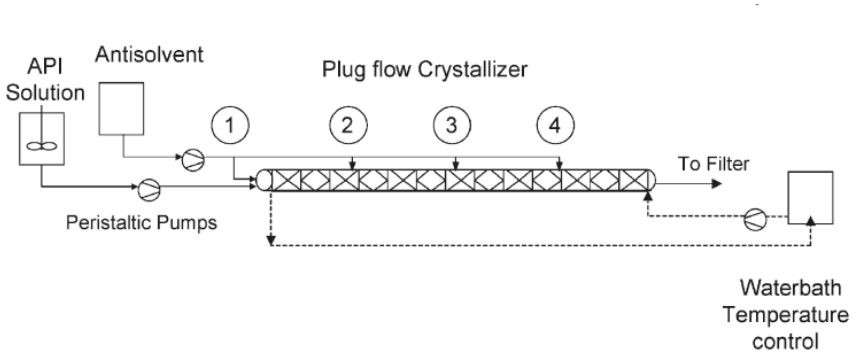

Figure 1.8. Configuration for the continuous anti-solvent crystallisation in a plug flow crystallizer with multiple anti-solvent addition points as considered by Alvarez et. al. (2009)

Alvarez et. al. (2010) investigated the continuous anti-solvent crystallisation of ketoconazole, flufenamic acid and L-glutamic acid in nonconventional plug flow crystallizers (Figure 1.8). The strategy to control particle size using multiple addition points for the anti-solvent was investigated. Kenics type static mixers were used to promote mixing inside the crystallizer. A growth rate dispersion model was seen to provide good results as opposed to the standard axial dispersion or plug flow models.

Wong et. al. (2012) investigated the cooling crystallisation of cyclosporine and the anti-solvent crystallisation of deferasirox using a single stage continuous mixed suspension mixed

product removal crystallizer with a continuous recycle (Figure 1.9). The system proposed offers a lower operational demand, in terms of number of unit operations and space constraints in comparison to equivalent cascade configurations. It was found that the recycle ratio was an effective operating parameter to control the product purity and yield. The product properties could be controlled effectively by using operating conditions of a single crystallizer. It was also found that the system investigated provided better results in comparison to the multistage MSMPR crystallizers (with and without recycle).

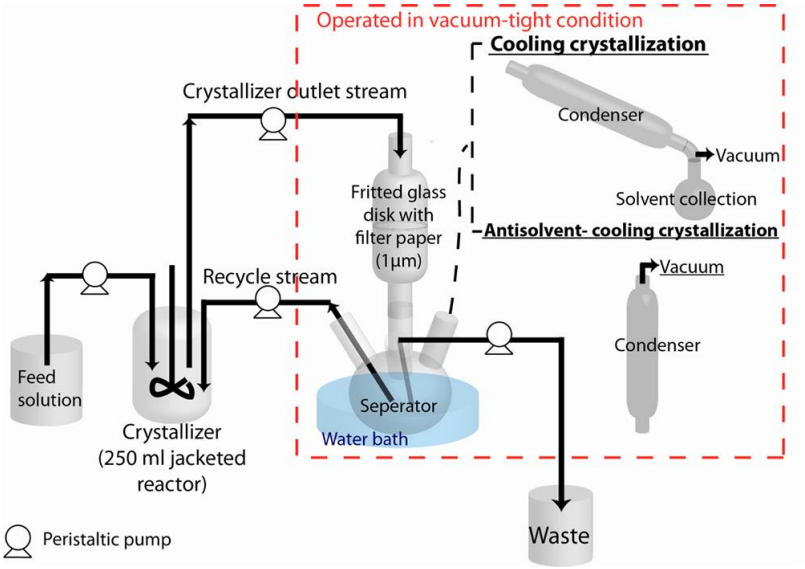

Figure 1.9. Configuration for the continuous crystallisation in a single stage MSMPR with recycle system as considered by Wong et. al. (2012)

Zhang et. al. (2012) investigated the continuous combined anti solvent and cooling crystallisation of a model API using a cascade MSMPR (Figure 1.10). The effect of changing the crystallizer temperatures, antisolvent addition points and the residence times on the crystal properties (crystallinity and morphology) purity and yield were investigated. It was found that addition of anti-solvent in the second crystallizer resulted in crystals of favorable crystallinity and morphology for downstream processing.

Lawton et. al. (2009) investigated a novel continuously oscillating baffled crystallizer (COBC) for the continuous crystallisation of a model API (Figure 1.11). The COBC delivered the isolation of the model API in just 12 minutes as opposed to 9hr and 40 mins in a similar batch operated process. The advantage of the COBC assembly is that it can be scaled up very easily as the tube diameters do not change much while scaling up and thus maintaining the flow physics consequently the crystallizer behavior.

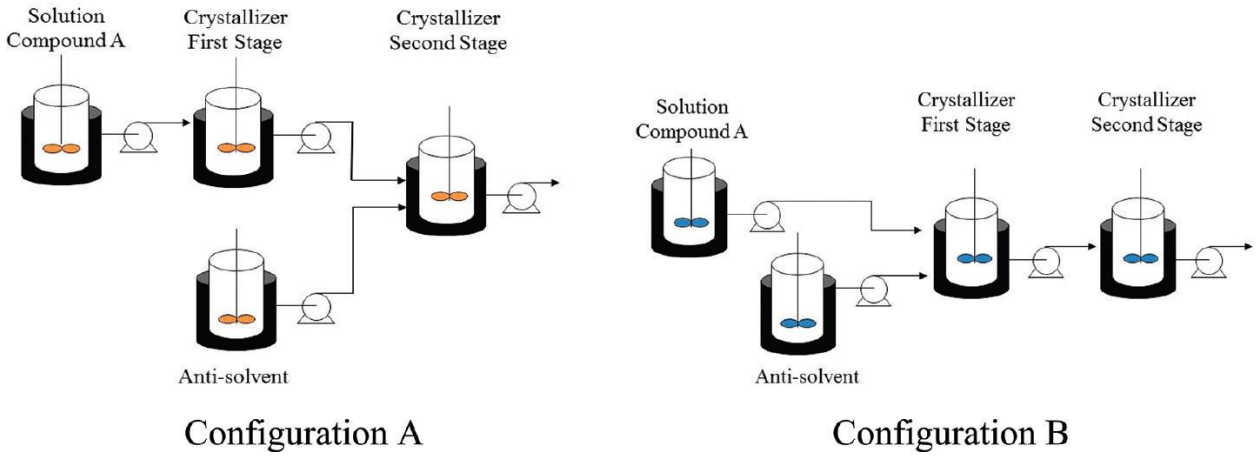

Figure 1.10. Cascaded MSMPR system for the continuous cooling/anti-solvent crystallisation of used by Zhang et. al. (2012)

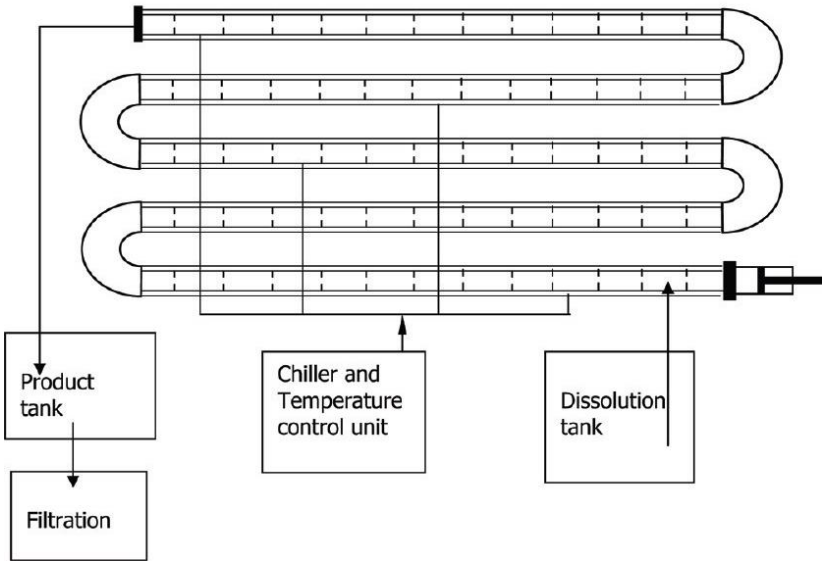

Figure 1.11. Continuously oscillating baffle crystallizer assembly used by Lawton et. al. (2009)

Zhang et. al. (2014) investigated the integration of the continuous crystallisation of aliskiren hemifumarate within a pilot plant. Different configurations of the control systems (feedback, feedforward, feedback and feedforward) were investigated to control the concentrations, solid loading and the liquid-level in the continuous crystallizers. Process analytical technologies (PAT's) were used to monitor the concentration and the solid loading online to provide feedback to the control systems. The flow rate of the solvent to the crystallizer was manipulated to achieve the required control. The feedback system was effective in mitigating the slow changes in concentration from upstream units. The feedback system was effective in mitigating the fast disturbances in flow rate. The authors proposed a combination of

feedback and feedforward systems to control the crystallisation process operations. The product produced satisfied product requirements and more importantly had consistent properties.

Weidmeyer et. al. (2017) investigated the use of helically coiled flow tubes (HCT) for the continuous seeded shape selective crystallisation of potash alum (Figure 1.12). It was observed that crystallisation did not lead to blockages in HCT's as opposed to conventional flow tubes. Smaller crystals also had a higher RTD which provided more time for growth. Because of this HCT's were seen to have the potential to give narrower size distributions.

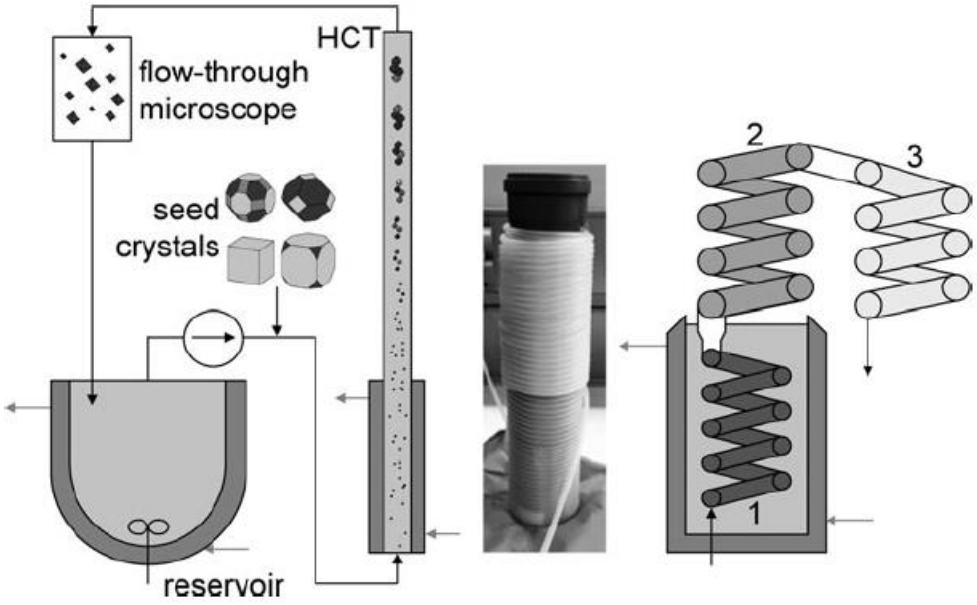

Figure 1.12. Schematic of the experimental setup used by Weidmeyer et. al. (2017) with reservoir, pump, helically coiled flow tube crystallizer (HCT), and flowthrough microscope, and geometrical details of the HCT. Tube section 1 is dark-gray colored, tube section 2 is gray colored, and tube section 3 is light-gray colored

The above mentioned studies demonstrate the potential advantages of a continuous mode of operation over a batch mode of operation. However, the effectiveness of the continuous crystallisation route were only proven on a lab scale. Issues regarding scaling up were not addressed in most cases. Mathematical modeling can go a long way towards reducing the uncertainties associated with crystalliser design and scale up. Modeling studies coupled with experimental studies are thus essential for good crystalliser design. In Chapter 4, a novel

continuous crystalliser assembly was investigated experimentally on similar lines as the studies presented here. Then, a generalized framework to model batch and continuous crystallisation processes was formulated and implemented for the specific continuous crystalliser assembly considered.

1.4. Summary of previous work

Significant progress has been made in Process Analytical Technologies (PAT's) which are used to monitor key process and product characteristics. Product characteristics such as size, shape are important from the point of view of product efficacy and downstream processing (flowability, filterability). Key process characteristics such as solute concentration (extent of supersaturation) are important as they govern key crystallisation processes (nucleation, growth). The progress in PAT's has served to foster the progress of the crystallisation technology due to improved process understanding. The Focused Beam Reflectance Measurement (FBRM) probe is one of the popular tools to monitor crystallisation processes as it allows for the online and in-situ monitoring of the Chord Length Distribution (CLD). Various inversion models have been developed to extract the Particle Size Distribution (PSD) data from the measured raw CLD data.

Majority of the crystallisation processes in the industry are carried out in a batch mode of operation. However, there is often a problem of batch-to-batch variability associated with using batch processes. The problem of variability is mitigated by identifying better operating protocols and better process control strategies. To accomplish both these objectives, it is essential to develop sophisticated process models to capture the complex dynamics of crystallisation processes. Crystallisation process models are based on solving the Population Balance Equation (PBE). Various methods for the solution of the PBE's are available keeping in mind different objectives (full resolution of the PSD, ease of implementation, simulation speed, robustness etc.). These models require the specification of kinetic parameter values which depend upon both, the specific crystallisation systems and the process equipment considered. By and large these parameter values are not available in literature and need to be estimated on a case by case basis. The PSD is an important product quality attribute because of the impact on the product efficacy and the downstream processing. Temperature

cycling has been shown to be effective operating strategy in controlling the PSD in batch processes.

Continuous mode of operation offers many potential benefits over the batch mode of operation of crystallizers. However, there is a gap in the understanding of continuous processes which hinders the migration of crystallisation technology from batch to continuous processes. Due to system specific nature of fundamental crystallisation phenomena such as secondary nucleation, breakage and agglomeration, the dynamics of crystallisation processes is very system specific. Hence, much of the work in developing continuous crystalliser technology has gone into the lab scale experimental investigation of different configurations of continuous crystallisers. Developed mathematical models are highly system specific and have limited predictive capabilities. Issues with regards to scaling up are largely unaddressed. The COBC shows promise in this regard as scaling up for that technology is inherently easy.

1.5. Scope & organization of the Thesis

The focus of the present thesis is the modeling of batch and continuous cooling crystallisation processes. Modeling studies can potentially aid to improve process understanding, identify optimal operating protocols, assess novel experimental assemblies and reduce uncertainties associated with scale up. However, it should be noted that, modeling studies must always be coupled with experimental studies to evolve useful models.

The chapter-wise specific objectives of the thesis were:

(a) Chapter 2: To develop a simple model to enable the online and in-situ measurement of the Particle Size Distribution using the Focused Beam Reflectance Measurement probe
(b) Chapter 3: To develop a generic framework to model batch crystallisation processes and estimate key crystallisation kinetic parameters
(c) Chapter 4: To develop a generic framework to model variable volume batch and continuous crystallisation processes
(d) Chapter 5: To summarize key results of the thesis

A brief description the work carried out in each of the above-mentioned Chapters is given below.

The Particle Size Distribution (PSD) can be extracted from the raw CLD data using suitable inversion models. However, these models are cumbersome to implement and often need the specification of an additional parameter which needs to be determined experimentally. In certain cases, non-linearities imposed of the inversion problem make it impossible to obtain a stable solution. In Chapter 2, a simple model was proposed for the CLD to PSD inversion problem and was implemented using simple spread sheeting tools. The model was validated for different systems of regularly shaped particles (no variation in shape), irregularly shaped particles (variation in shape) as also for systems of practical relevance. The proposed tool coupled with the raw data measured by the FBRM probe can provide valuable insights into the evolution of the PSD in crystallisation process.

Modeling of crystallisation processes is important from a process design point of view, specifically for evolving better operating protocols and control strategies. Accurate estimates for key crystallisation kinetic parameters are a pre-requisite for any crystallisation process models. These parameter values are specific to the solute-solvent pair considered and are typically unavailable in literature. Previous studies focus on seeded crystallisation and validate the model over a very limited range of operation. Chapter 3 focuses on proposing and validating a rigorous procedure for estimating key crystallisation kinetic parameter values using unseeded batch cooling crystallisation. Crystallisation kinetic parameter values were estimated for a Paracetamol-Ethanol system. Novel experiments based on the observed hysteresis in particle counts were performed. A mathematical model based on the population balance framework was formulated and solved using appropriate numerical methods. First, a procedure to estimate key crystallisation kinetic parameters was proposed and implemented. Then, a rigorous validation was performed using estimated key crystallisation kinetic parameters to simulate the hysteresis experiments.

Implementation of continuous crystallisation processes can be daunting due to the complex process dynamics involved. Recent work done focused primarily on the lab scale experimental investigation of continuous crystallisation processes. Chapter 4 focuses on developing a generalized tool for modeling both batch and continuous crystallisation processes. Unseeded

batch and continuous cooling crystallisation of Sodium Nitrite in Water were considered. A novel lab scale continuous cooling crystallisation assembly was investigated experimentally.

A generalized mathematical tool was developed for the simulation of fixed volume continuous crystallisers which allowed for varying the mixing characteristics to match those specific to the crystalliser considered. Crystallisation kinetic parameter values were estimated using the batch process data by a procedure described in Chapter 3. Continuous crystallisation simulations were performed. Influence of key operating/design parameters (jacket temperature, residence time, mixing behaviour) on important design parameters of mean, time for steady state and yield were investigated using the model.

Symbols & Notations

Symbol	Description	Unit
S	Supersaturation	kmol/m^3
C	Concentration of solute in liquid phase	kmol/m^3
C^*	Saturation concentration of solute in liquid phase	kmol/m^3
$n(L,t)$	Number density distribution function	#/m^3
L	Particle size co-ordinate	m
t	Time	s
G	Growth rate	m/s
B_0	Nucleation rate	#/(m^3-s)
δ	Kronecker delta function	-
L_{nuc}	Size of nucleus	m
M_S	Mass of solute	kg
V_R	Volume of reactor	m^3
M_w	Molecular weight of solute	kg/kmol
ρ_p	Density of particle	kg/m^3
k_{r0}	Growth rate pre-exponential constant	m/s
E_A	Activation energy	kJ/kmol
R	Universal gas constant	kJ/(kmol-K)
T	Temperature of solution	K
g	Growth rate exponent	-
k_1	Primary nucleation rate constant	#/(m^3-s)
n_1	Primary nucleation rate exponent	-
D	Dissolution rate	kg/s
k_d	Mass transfer coefficient for dissolution	m/s
τ	Mean residence time	s
u_x	Superficial velocity along x-direction	m/s
x	Co-ordinate along crystallizer length	m

References

Agimelen O., Hamilton P., Haley I., Nordon A., Vasile M., Sefcik J., Mulholland A., 2015. Estimation of particle size distribution and aspect ratio of non-spherical particles from chord length distribution. Chemical Engineering Science, 123 pp.629-640.

Alvarez, A.J. and Myerson, A.S., 2010. Continuous plug flow crystallisation of pharmaceutical compounds. Crystal Growth & Design, 10(5), pp.2219-2228.

Alvarez, A.J., Singh, A. and Myerson, A.S., 2011. Crystallisation of cyclosporine in a multistage continuous MSMPR crystallizer. Crystal Growth & Design, 11(10), pp.4392-4400.

Choong, K.L. and Smith, R., 2004. Optimization of batch cooling crystallisation. Chemical Engineering Science, 59(2), pp.313-327.

Chung, S.H., Ma, D.L. and Braatz, R.D., 1999. Optimal seeding in batch crystallisation. The Canadian Journal of Chemical Engineering, 77(3), pp.590-596.

Davey, R.; Garside, J., 2001. From Molecules to Crystallizers; Oxford University Press: New York, 1st edition.

Gunawan, R., Fusman, I., Braatz, R. D., 2004. High Resolution Algorithms for Multidimensional Population Balance Equations. Particle Technology and Fluidization. AIChE Journal. 50 (11), pp.2737-2749.

Karpinski, P. H., 1985. Importance of the Two-Step Crystal Growth Model. Chemical Engineering Science, 40(4), pp.641-646.

Kumar S.; Ramkrishna D., 1996. On the Solution of Population Balance Equations by Discretization – II: A Moving Pivot Technique. Chemical Engineering Science, 51(8), pp.1333-1342.

Lawrence, X.Y., Lionberger, R.A., Raw, A.S., D'Costa, R., Wu, H. and Hussain, A.S., 2004. Applications of process analytical technology to crystallisation processes. Advanced Drug Delivery Reviews, 56(3), pp.349-369.

Lawton, S., Steele, G., Shering, P., Zhao, L., Laird, I. and Ni, X.W., 2009. Continuous crystallisation of pharmaceuticals using a continuous oscillatory baffled crystallizer. Organic Process Research & Development, 13(6), pp.1357-1363.

LeVeque, R. J., 2002. Finite Volume Methods for Hyperbolic Problems. Cambridge Univ. Press: New York.

Lewiner, F., Fevotte, G., Klein, J.P. 0061nd Puel, F., 2002. An online strategy to increase the average crystal size during organic batch cooling crystallisation. Industrial & Engineering Chemistry Research, 41(5), pp.1321-1328.

Li H., Grover M., Kawajiri Y., Rousseau R., 2013. Development of an empirical method relating crystal size distributions and FBRM measurements. Chemical Engineering Science, 89, pp.142-151.

Li M., Wilkinson D., 2005. Determination of non-spherical particle size distribution from chord length measurements Part 2: Experimental validation. Chemical Engineering Science, 60, pp.4992-5003.

Li M., Wilkinson D., 2005. Determination of non-spherical particle size distribution from chord length measurements. Part 1: Theoretical analysis. Chemical Engineering Science, 60, pp.3151-3265.

Marchisio, D. L.; Fox, R. O., 2005. Solution of population balance equations using the direct quadrature method of moments. Journal of Aerosol Science, 36, pp.43-73.

Marchisio, D. L.; Pikturna, J. T.; Fox, R. O.; Vigil R. D.; Barresi A. A, 2003, Quadrature Method of Moments for Population-Balance Equations. AIChE Journal, 49(5), pp.126-1276.

McGlone T., Briggs N., Clark C., Brown C., Sefcik J. and Florence A., 2015. Oscillatory Flow Reactors (OFRs) for Continuous Manufacturing and Crystallisation. Organic Process Research & Development, 19(9), pp.1186-1202.

Mersmann, A., 1995. Crystallisation Technology Handbook. Marcel Dekker: New York.

Mettler Toledo, Mechanism of FBRM probe. Mettler Toledo training manual.

Moscosa-Santillan, M., Bals, O., Fauduet, H., Porte, C. and Delacroix, A., 2000. Study of batch crystallisation and determination of an alternative temperature-time profile by on-line turbidity analysis—application to glycine crystallisation. Chemical Engineering Science, 55(18), pp.3759-3770.

Moscosa-Santillan, M., Bals, O., Fauduet, H., Porte, C. and Delacroix, A., 2000. Study of batch crystallisation and determination of an alternative temperature-time profile by on-line turbidity analysis—application to glycine crystallisation. Chemical Engineering Science, 55(18), pp.3759-3770.

Myerson A. S., 2002. Handbook of Industrial Crystallisation; Butterworth-Heinemann: Massachusetts.

Nagy, Z.K., 2009. Model based robust control approach for batch crystallisation product design. Computers & Chemical Engineering, 33(10), pp.1685-1691.

Pandit, A.V. and Ranade, V.V., 2015. Modeling Hysteresis during Crystallisation and Dissolution: Application to a Paracetamol–Ethanol System. Industrial & Engineering Chemistry Research, 54(42), pp.10364-10382.

Quon, J.L., Zhang, H., Alvarez, A., Evans, J., Myerson, A.S. and Trout, B.L., 2012. Continuous crystallisation of aliskiren hemifumarate. Crystal Growth & Design, 12(6), pp.3036-3044.

Ramkrishna, D., 2000. Population Balances: Theory and Applications to Particulate Systems in Engineering; Academic Press: San Diego, 1st edition.

Randolph, A. D. and Larson, M. A., 1988. Theory of Particulate Processes: Analysis and Techniques of Continuous Crystallisation. San Diego, CA: Academic Press, Inc.

Ruf A., Worlitschek J., Mazotti M., 2000. Modeling and Experimental analysis of PSD measurements through FBRM. Particle & Particle Systems Characterization, 2000, 17, pp.167-179.

Simon, L.L., Pataki, H., Marosi, G., Meemken, F., Hungerbühler, K., Baiker, A., Tummala, S., Glennon, B., Kuentz, M., Steele, G. and Kramer, H.J., 2015. Assessment of recent process analytical technology (PAT) trends: a multiauthor review. Organic Process Research & Development, 19(1), pp.3-62.

Su Q., Nagy Z. K., Rielly C., 2015. Pharmaceutical crystallisation processes from batch to continuous operation using MSMPR stages: Modelling, design, and control. Chemical Engineering and Processing: Process Intensification, 89, pp.41-53.

Vetter T., Burcham C., Doherty M., 2014. Regions of attainable particle sizes in continuous and batch crystallisation processes. Chemical Engineering Science, 106, pp.167-180.

Ward, J.D., Yu, C.C. and Doherty, M.F., 2011. A new framework and a simpler method for the development of batch crystallisation recipes. AIChE Journal, 57(3), pp.606-617.

Wiedmeyer V., Anker F., Bartsch C., Voigt A., John V. and Sundmacher K., 2017. Continuous Crystallization in a Helically Coiled Flow Tube: Analysis of Flow Field, Residence Time Behavior, and Crystal Growth. Industrial & Engineering Chemistry Research, 56(13), pp.3699-3712.

Wong, S.Y., Tatusko, A.P., Trout, B.L. and Myerson, A.S., 2012. Development of continuous crystallisation processes using a single-stage mixed-suspension, mixed-product removal crystallizer with recycle. Crystal Growth & Design, 12(11), pp.5701-5707.

Worlitschek J., Hocker T., Mazzotti M. 2005. Restoration of PSD from Chord Length Distribution Data using the Method of Projection onto Convex Sets. Particle & Particle Systems Characterization, 22, pp.81-98.

Worlitschek, J.; Mazzotti, M., 2004. Model-Based Optimization of Particle Size Distribution in Batch-Cooling Crystallisation of Paracetamol. Crystal Growth & Design. 4(5), pp.891-903.

Zhang, H., Lakerveld, R., Heider, P.L., Tao, M., Su, M., Testa, C.J., D'Antonio, A.N., Barton, P.I., Braatz, R.D., Trout, B.L. and Myerson, A.S., 2014. Application of continuous crystallisation in an integrated continuous pharmaceutical pilot plant. Crystal Growth & Design, 14(5), pp.2148-2157.

Zhang, H., Quon, J., Alvarez, A.J., Evans, J., Myerson, A.S. and Trout, B., 2012. Development of continuous anti-solvent/cooling crystallisation process using cascaded mixed suspension, mixed product removal crystallizers. Organic Process Research & Development, 16(5), pp.915-924.

Chapter 2. Measurement of Particle Size Distribution

This chapter has been reproduced from the following manuscript:

Pandit A., Ranade V., 2016. Chord length distribution to particle size distribution. *AIChE Journal*, 62, pp.4215–4228. doi:10.1002/aic.15338

2.1. Introduction

The Particle Size Distribution (PSD) is an important product quality parameter in the crystallization industry as it affects downstream processing (filterability, flowability etc.) as also product efficacy (stability, rate of dissolution etc.). Measurement of the PSD is thus an important problem for assessing product quality as well as for modelling the kinetics of the nucleation and crystal growth for improved crystalliser design. There are several techniques available to measure the PSD. The most popular ones are the Laser Diffraction and the Microscopy methods. These enable a complete characterization of the PSD curve however, are offline methods. Hence it is difficult to obtain PSD results using these methods for transient processes such as crystallization as we are limited to only investigating the 'equilibrated' samples. A nephelometer (or turbidity probe) is often used to study crystallization systems. However, even though it allows for the in-situ and online measurements, the results provided by this method do not give any information regarding the PSD.

The Mettler Toledo Particle Vision and Measurement (PVM) is another popular measurement device which extends the microscopy technique and enables the measurement of PSD in-situ and online. Two dimensional images of the particles as viewed from the probe window are recorded which are later processed to obtain the PSD. The Mettler Toledo Focused Beam Reflectance Measurement (FBRM) probe is also widely used to study crystallization. The FBRM probe works on the principle of laser back-scattering. A laser is emitted from a laser source inside the probe. The source is rotated around the probe axis such that the laser revolves remaining parallel to the probe axis. The laser traces a cylindrical surface around the probe axis inside the probe. A very high speed of rotation is used (in the present study the

tangential speed of the source was set to 2 m/s). At the probe tip is a sapphire window which is in contact with the solution wherein the particle measurements are to be made. Whenever the revolving laser encounters a particle along its circular path it gets reflected back into the probe. Each instance of this reflection is treated as one count of particle detection and the duration of time for which the beam is reflected multiplied by the tangential speed of the laser becomes the length of the chord which the laser 'traces' on the particle surface. Thus, in course of time and in dense solutions, multiple particles are recorded by the FBRM probe and hence we obtain the number of counts and the particle chord length distribution data (CLD).

The CLD measured by the FBRM probe, although related to the PSD, bears no obvious resemblance to the PSD. The CLD data needs to be interpreted in some way to obtain information regarding the PSD. Much work has been done recently to address this problem. Li et. al. (2013, Part 1 & 2) developed an empirical method for the determination of the PSD from the CLD. Multiple fingerprint CLD's for known particle sizes were first meticulously determined over the size range of interest. The actual PSD was estimated as the one which yielded the same CLD as the measured CLD by a linear combination of the fingerprint CLD's. However, this method requires a lot of standardized data (fingerprint CLD's) in order to calibrate the model for a specific system before it starts to make predictions. Gathering this standardized data is not always possible and is definitely time consuming and cumbersome. Besides, the aforementioned publication, other efforts directed towards solving the CLD to PSD problem all follow a definite methodology. First the CLD of a single isolated particle (or equivalently a monodisperse system) is derived theoretically. Then, the CLD is derived theoretically for a system with a known PSD. Finally, the inverse problem of determining the PSD for a known CLD is addressed. Having established the first part, the second part is relatively straightforward. Several efforts have been directed to specifically address the first part of the problem. Li et. al. (2005, Part 1 & 2) presented a model to determine the CLD for a spherical particle. The model was extended to allow for various particle shapes using a 2D super ellipsoidal function. However, the model only considered a fixed 2D particle projection to determine the CLD and did not account for the different particle orientations and the subsequent effect on the 2D projections. In the model presented by Ruf et. al. (2000) all possible 2D projections of the 3D shape (with different orientations) were considered for

determining the CLD. The approach to calculate the CLD from the 2D particle projection is fundamentally similar to the 2D model proposed previously.

The inverse problem of determining the PSD from a known CLD is more troublesome. Typically, the PSD is estimated iteratively by starting from a guess PSD and comparing the predicted CLD and the measured CLD to evaluate the direction of the iteration. However, due to the non-linear nature of the CLD expressions obtained from the single particle models, the inverse problem becomes an ill posed mathematical problem. The most popular methods include the Least Squares (LS) and the Constrained Least Squares (CLS) algorithms (Li et. al., 2005, Part 1 & 2). However, when CLD measurements are noisy, as are typically observed for the case of crystallization systems, oscillations or negative values are obtained for the PSD's using these methods. To overcome this pitfall, Li et. al. (2005, Part 1 & 2) proposed an iterative Non-Negative Least Squares algorithm for the inversion problem. Worlitschek et. al. (2003) extended the model proposed by Ruf et. al. (2000) by considering the method of projection onto convex sets (POCS) to solve the inversion problem. Agimelen et. al. (2015) reported an algorithm to estimate the PSD from CLD measurements for needle shaped crystals. Appropriate single particle CLD models reported in literature were used and the algorithm required no additional information such as approximate particle size range or particle aspect ratio to constrain the iterative procedure as for previous efforts.

The methodology used in the present study also follows the definite approach used by previous authors wherein, first a single particle CLD model is proposed and later the inversion problem (deriving PSD from CLD) is addressed. However, it differs from previous approaches on two important fronts. First, the model for the single particle CLD is fundamentally different from the models reported in literature. This leads to a mathematically very simple expression for the CLD of a single particle. Second, instead of solving for all the number of particles in each bin of the discretized PSD, the PSD is assumed to be modelled by a suitable distribution function (Normal, Lognormal). This reduces the number of parameters to be iterated to only two: the mean and the variance of the distribution. As a result of both of these distinctions, the inversion problem becomes straightforward and can be solved using simple spread sheeting tools. The model was then validated for two systems consisting of spherically shaped ceramic beads. The model was then evaluated for three systems of irregularly shaped particle systems consisting of: (a) sand particles; (b) plasma alumina particles and (c) zinc dust

particles. By irregularly shaped, it is implied that particle shape within the system is not uniform. The model was then successfully applied to two particle systems of practical relevance: (a) paracetamol crystals and (b) p-aminophenol crystals. The performance of the model was compared with the popular models reported by Li et. al. (2005, Part 1 & 2) and Worlitschek et. al. (2003). The model coupled with the FBRM measured CLD is a powerful tool to monitor the PSD even in transient processes such as crystallization.

2.2. Mathematical Model

2.2.1. Single Particle Model

As mentioned previously, the first problem that needs to be addressed is:

For a single particle of diamater D, what is the probability that a 'randomly cut' chord measures as having its length between X_1 and X_2 (where X_1 and $X_2 < D$)?

This problem statement is similar to the one proposed by Bertrand, in the Bertrand's Paradox (a classic paradox in probability theory). It is important to note that the important variable in the problem is the length of the randomly cut chord rather than identifying a specific random chord itself. The key issue in this problem is the interpretation of the 'randomly cut' chord. The length of a random chord may be determined in three ways (as stated in the paradox):

(a) Method 1: One point may be arbitrarily fixed on the circle and the other may be chosen at random along the circumference of the circle. The chord joining the two points is then the random chord and the length depends upon the position of the second point in relation to the first point.

(b) Method 2: The distance of the chord from the centre of the circle is enough to specify its length. This distance may then vary from 0 to the (known) radius of the circle. The length may then be calculated once a random value is assigned for the distance of the chord from the center of the circle.

(c) Method 3: For every point within the circle, there is a chord such that the considered point is the midpoint of the chord. So, the problem of randomly chosing a chord may then be equated to randomly chosing a point within the circle. The length may then be determined once the poistion of the point is known.

In the paradox, it is demonstrated that the different interpretations of the randomness of the chord lead to different results. The classical solution of the paradox is that there is no 'right' solution. An appropriate definition of randomness must be chosen depending upon the physcial scenario considered to obtain an appropriate answer. More information regarding the Bertrand Paradox is provided in Appendix A1. The FBRM views a 2D projection of the particle. Methods 1 and 2 provide a 1D solution (random variable along the radius or the circumference of the circle) to the problem and it may be inferred that information is lost regarding the orientation of the chord with respect to a fixed frame of reference (for instance the FBRM probe). Method 3 is the only method that addresses the 2D nature (area of the circle) inherent in the physcial system considered. Previous researchers have used a methodology parallel to Method 2. However, in the present text, it is argued that Method 3 is a more accurate interpretation to determine the length of a randomly cut chord for the case of a FBRM than Methods 1 or 2.

The laser views a 2-D projection of the particle. Considering the case of a spherical particle (of diameter 'D'), the 2D projection is a circle with the same diameter *D*. Now, it should be noted that for every point inside the circle, there is associated with it, a unique chord for which the considered point is the midpoint of the chord.Thus, chosing a random chord of a circle is equivalent to choosing a random point inside the circle.The locus of the midpoints of the chord of the same length is a circle with dimensions as shown in Figure 2.1(a). Any point on the circle (dotted line) corresponds to a chord with length *x* and every chord with length *x* will have its midpoint on the circle (dotted line). For a chord whose length is between *x* and *y*, it is necessary that its midpoint should lie in the shaded area given in Figure 2.1(b).

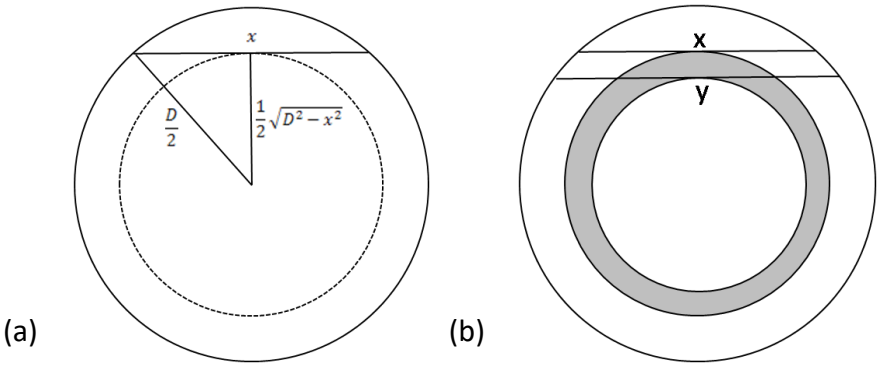

Figure 2.1. (a) Circle defined by a chord of length x (b) Area considered to measure chord length between x and y

The probability of measuring a chord with size between *x* and *y* (*x*<*y*), or *P(x,y,D)*becomes the ratio of the area of the shaded region to the total area of the circle:

$$P(x, y, D) = \frac{y^2 - x^2}{D^2} \quad (2.1)$$

Since the probability, that a measured chord has a size less than or equal to the particle size, is unity and also it is clear from direct substitution into Equation (1) that:

$$P(0, D, D) = 1 \quad (2.2)$$

It is worth noting that for the probability function defined here, the following property holds (*y*<*z*):

$$P(x, y, D) + P(y, z, D) = P(x, z, D) \quad (2.3)$$

Also, since no chord length greater than the diameter can be measured, the following definition must be made for all *z*>*D*:

$$P(D, z, D) = 0 \quad (2.4)$$

2.2.2. Particle Size Distribution to Chord Length Distribution

Particle size distributions and chord length distributions are typically represented in the form of histograms. The entire relevant span of the particle size co-ordinate is divided into discrete 'bins'. The bin sizes, typically, are either uniform or increase logarithmically starting from the first bin, depending upon how the measurements were made or what convention was adopted. The histogram plots the frequency, or number of particles, as is applicable in the present study, that are recorded in each of these bins.

2.2.2.1. CLD for a monodisperse collection of particles

The histogram for the PSD of a collection of monodisperse particles is represented by a single peak. The location of the peak corresponds to the bin representing the size of the monodisperse particles. In a normalized form, the value of the peak will be unity. A normalized PSD for a collection of monodisperse particles of size 95μm is shown in Figure 2.2. The bins are considered to be uniformly sized having width equal to 10μm and the domain considered extending from 0 to 150μm. It is useful to define a representative size, wherein,

each particle contained in the bin can be assumed to be of the corresponding representative size. The histogram shown in Figure 2.2 is plotted versus the representative bin size.

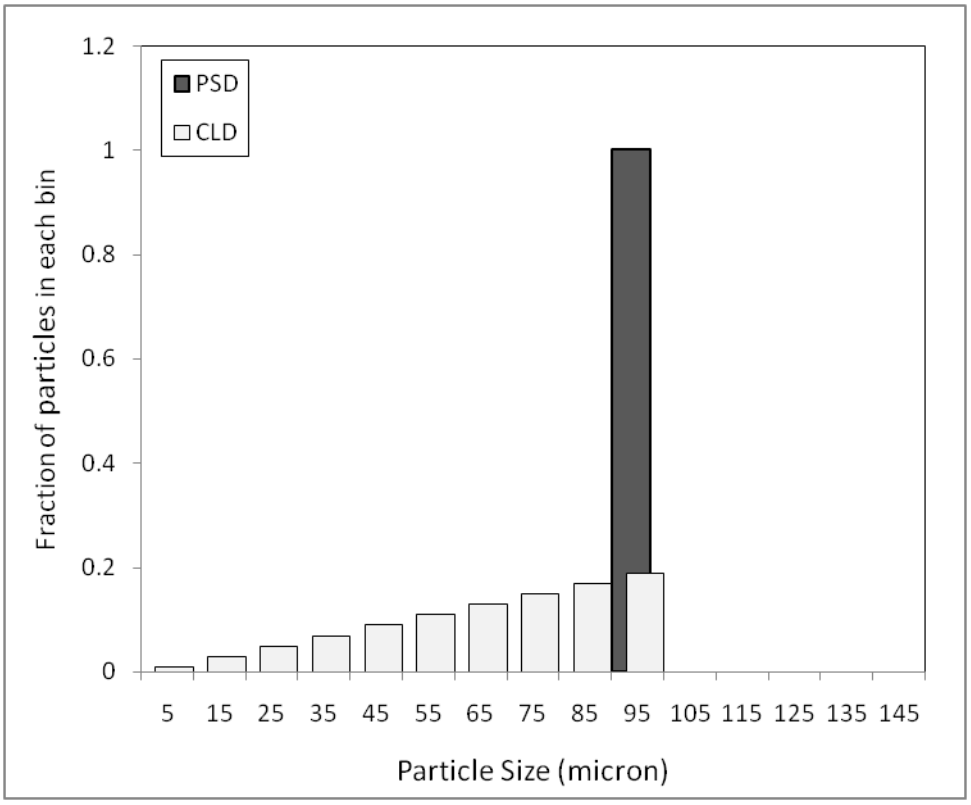

Figure 2.2. Particle Size Distribution and Chord Length Distribution for a collection of monodisperse particles of 95μm size

In the previous section the problem of determining the probability of measuring a chord within a particular size range, say for instance between x and y, for a single particle was addressed. Now, provided that the number of particles is large enough, the aforementioned probability can be equated to the fraction of the total number of particles (for a monodisperse system) which would be measured as having chords between sizes x and y. This important assumption allows the determination of the CLD from a single particle model and has been reported by other researchers as well (Li et. al., 2005; Ruf et. al., 2000). The assumption is a statistical assumption in the sense that it gains validity as the sample size of the number of particles recorded increases and can be assumed to be true when the number of particles is sufficiently high. It is expected that the number of particles recorded by the FBRM are sufficiently high enough that the aforementioned assumption is valid.

Suppose the particle size co-ordinate is distributed into k bins. Let L_{i-1} and L_i denote the lower and upper boundaries of the i^{th} bin. L_0 will typically be set to zero. Let the number of particles

in the i^{th} bin be denoted as N_i and the representative size of the i^{th} bin (defined as the midpoint of the boundary points of the i^{th} bin), by X_i. For the present case, let us assume that all the monodisperse particles are contained in the m^{th} bin. Let the total number of particles in the system be denoted by N_T. Let the number of particles measured in the i^{th} bin for a general PSD be N_i and for a CLD be M_i. Let the fraction of the total particles (contained in the m^{th} bin) measured as having chords in the i^{th} bin, be denoted by $A_{i,m}$. As defined in the previous section, the probability of measuring a chord in the i^{th} bin for a particle belonging to the m^{th} bin can be written as $P(L_{i-1}, L_i, L_m)$. It should be noted, that the particle size here was taken as the upper boundary (L_m) rather than the representative bin boundary (X_m). This is done so as to make the calculations more lucid and as will be demonstrated later by extensive validation, does not affect the model applicability.

From the assumption that the fraction of total particles (contained in the m^{th} bin) measured as having chords in the i^{th} bin is equal to the probability of measuring the chord in the i^{th} bin for a single particle belonging to the m^{th} bin, we may write the following equality:

$$A_{i,m} = \frac{M_i}{N_m} = P(L_{i-1}, L_i, L_m) \quad (2.5)$$

Here, $i \leq m$. As discussed in the previous section, if $i>m$, then $A_{i,m}$ is equal to zero. It should be noted that for a monodisperse system of particles contained in the m^{th} bin, the total number of particles is the number of particles contained in the m^{th} bin and hence:

$$N_m = N_T \qquad (2.6)$$

From Equation (5), the number of particles in the i^{th} bin in the CLD may be written as:

$$M_i = P(L_{i-1}, L_i, L_m) N_m$$

The number of particles represented by M_i is the required CLD. For a system of monodisperse particles (belonging to a single bin: m^{th} bin), the normalized CLD can be obtained by dividing M_i with the total number of particles. For a sample case of a collection of particles contained between the 90 to 100μm size range, the normalized chord length distribution obtained using the above described methodology is shown in Figure 2.2. A uniform bin size of 10μm and a domain ranging from 0 to 150μm are considered. The total number of particles may also be obtained by summing the number of particles in each bin in the CLD. Thus we have:

$$\sum_{i=1 to\ m} A_{i,m} = 1 \qquad (2.7)$$

Hence, all the particles considered are accounted for. In the next section, a procedure to obtain the CLD from a given PSD is discussed.

2.2.2.2. CLD for a known PSD

A PSD is a histogram which plots the number of particles measured versus the size ranges or the bins in which they are measured in. It is similar to the CLD with the difference that the size ranges correspond to the actual sizes (as defined appropriate) of the particles rather than chord sizes. The monodisperse system discussed in the previous section is a special case where the sizes of the particles are limited to just one bin. A more general PSD will contain particles in many of the bins considered in the domain similar to the CLD obtained in the previous section. Now, the only difference between the monodisperse case and the present case is that instead of the CLD being computed only from one bin (like the m^{th} bin considered in the previous study), all the bins considered in the general PSD will contribute to the bins of the CLD. So, the problem of converting a PSD into a CLD is reduced to counting the contributions of each of the bin of the PSD towards each of the bin of the CLD and adding them up. With this in mind, we define a new variable $M_{i,j}$ to be the number of particles whose actual size corresponds to the j^{th} bin, being counted as having a chord size which corresponds to the i^{th} bin. With this definition, in the previous section the value of M_i calculated actually corresponds to $M_{i,m}$ in the new notation. The notation M_i retains its definition, of being the total number of particles in the i^{th} bin in the CLD, although now it has a deeper meaning as being the sum of the contributions from all the different bins, rather than just from an arbitrary m^{th} bin.

Now, the contribution of, say the j^{th} bin of the PSD, towards the i^{th} bin of the CLD, in terms of the number of particles, may be calculated using the analysis presented in the previous section. Thus, keeping in mind the new variable definitions, we may write the following equality:

$$M_{i,j} = P(L_{i-1}, L_i, L_j)N_j \qquad (2.8)$$

The total number of particles in each bin can be calculated by simply summing all the contributions of the different bins.

$$M_i = \sum_{j=i\ to\ k} M_{i,j} \quad (2.9)$$

Where, k is the total number of bins. The bins are summed starting from the present bin index. This is because the contribution of the bins from the PSD with a size smaller than the present bin towards chords being measured in the present bin will be zero. The values M_i are the required CLD.

Also, since we are counting all of the particles, it is interesting to note and it may also be rigorously derived that the total number of particles is in fact conserved. Hence,

$$N_T = \sum_{i=1\ to\ k} M_i \quad (2.10)$$

The normalized CLD may be obtained by dividing the CLD with the total number of particles. Let A_i denote the fraction of the total particles being measured as a chord in the i^{th} bin. Then we may write the following relation:

$$A_i = M_i / N_T \quad (2.11)$$

2.2.3. The Inverse Problem

Several methods are proposed to solve the inverse problem of calculating the PSD from the CLD[2,5,6]. In the present study, a simple iterative method starting from a guess PSD is used. A guess PSD represented in the form of a 2 parameter normal or lognormal distribution function is considered and the corresponding CLD is determined using the PSD to CLD model described in the previous section.

A two parameter normal distribution function is represented by the following function:

$$f(x) = \frac{1}{\sigma\sqrt{2\pi}} e^{\frac{-(x-\mu)^2}{\sigma^2}} \quad (2.12)$$

The two parameter lognormal distribution is represented by the following expression:

$$f(x;\mu,\sigma) = \frac{1}{2x\sigma\sqrt{2\pi}} e^{-\frac{(lnx-\mu)^2}{\sigma^2}} \quad (2.13)$$

In the above equation, the two parameters μ and σ^2 stand for the mean and the variance of the distribution functions. It is known that this function arises in various types of naturally occurring distributions and hence, it should also be sufficient to describe the distribution considered in the present study. To obtain the corresponding PSD, first, the bin boundaries

and the representative sizes of each bin need to be finalized. The number of particles in each bin N_i is then the value of the respective distribution function evaluated at X_i. For any sort of distribution function to be valid the following equality must hold:

$$\int_0^\infty f(x)dx = 1 \qquad (2.14)$$

However, because of discretizing the domain, the area of the discrete PSD will not be unity. Hence, we need to correct for this to avoid any errors. This is done by reassigning the number in each bin as follows:

$$N_{i,corrected} = \frac{N_i}{\sum_i N_i(L_i - L_{i-1})} \qquad (2.15)$$

These new corrected values were now referred to as N_i.

The values for the 2 parameters (mean and variance) required for the full specification of either the normal or the lognormal distribution can be determined by optimizing the R^2 error (R^2 should be closest to 1) between the measured and the model predicted CLD. A simple multi parameter optimization routine available with most spread sheeting tools is sufficient for these purposes. The algorithm for this process is given in Figure 2.3.

To quantify the error between the derived CLD and the measured CLD, the coefficient of determination or R^2 was used. The R^2 value can be calculated as follows:

$$\bar{M} = \frac{1}{k}\sum_{i=1\ to\ k}(M_{i,experiment} - M_{i,model}) \qquad (2.16)$$

$$SS_{tot} = \sum_{i=1\ to\ k}(M_{i,exp} - \bar{M})^2 \qquad (2.17)$$

$$SS_{res} = \sum_{i=1\ to\ k}(M_{i,model} - M_{i,exp})^2 \qquad (2.18)$$

$$R^2 = 1 - \frac{SS_{res}}{SS_{tot}} \qquad (2.19)$$

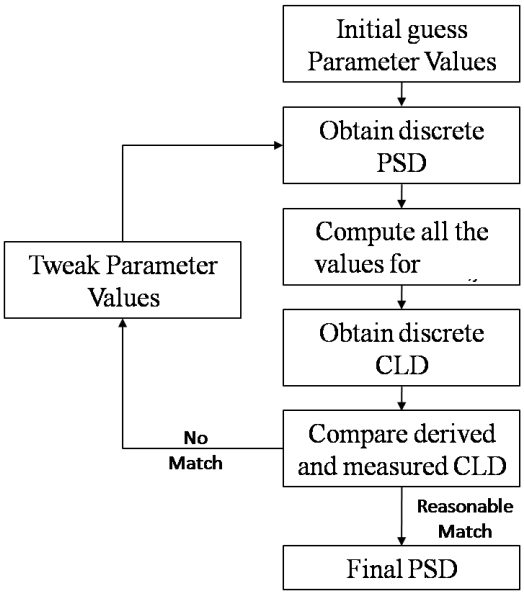

Figure 2.3. Algorithm to determine PSD from CLD

2.2.4. PSD measurement through Image Analysis

Before presenting model results, it is worthwhile to spend some time on how the PSD may be obtained through image analysis. The image analysis procedure for determining the particle sizes is outlined in Figure 2.4. A series of 2D images were taken for the given system of particles under a microscope. The images were then converted into binary images (having just 2 colours: black and white). The binary images further treated to fill the holes inside the particles, remove any overlapping particles, separate touching particles, remove particles on the image boundary which were incomplete and remove the background noise to obtain reliable data. These binary images were then used to identify particles. The image pixel size in terms of pixel/μm is known from image calibration. From the last stage of image analysis, and the known pixel/μm ratio from calibration, the visible area of the particles within one image can be calculated in μm^2. In the present study, after this area is obtained, the spherically equivalent diameter was obtained for each particle which is defined as the diameter of a sphere having the same visible cross sectional area as the visible area obtained for a particle using image analysis. This spherically equivalent diameter was obtained for a series of particles. The PSD may be obtained by specifying the bin spacing to be used and counting the number of particles that fall within each size range from the data obtained in the previous step.

The processing of images was done using the *ImageJ* software.

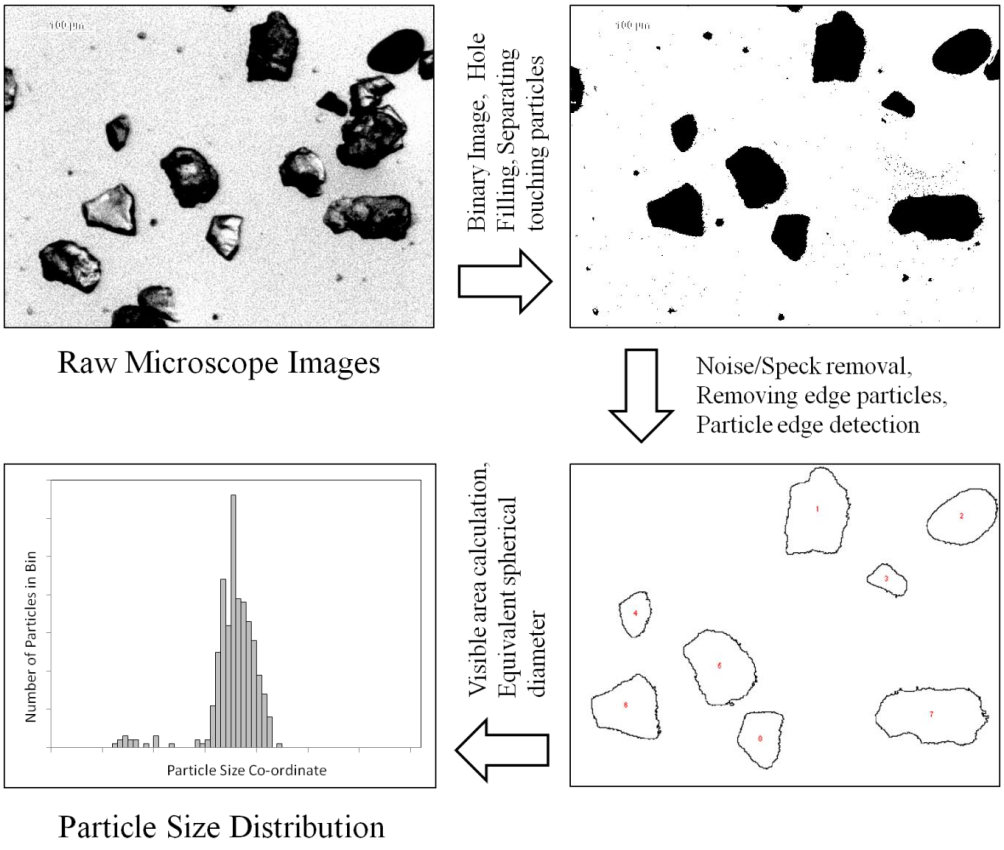

Figure 2.4. Procedure used to determine the PSD through image analysis

2.3. Results & Discussions

2.3.1. Model Validation for Regularly shaped particles

The above presented model was first validated for a system of regularly shaped particles. By regularly shaped, it is implied that the particles considered in the present section were nearly spherical. The PSD was available for a calibration sample used for the FBRM probe. The FBRM probe calibration sample consisted of nearly perfect spherical ceramic particles. Shown in Figure 2.5(a), is an image of the particles taken using a PVM. It can be assumed that the particles are spherical in shape. Based on the images captured by the PVM, a PSD was prepared for the lengths and widths measured for different particles obtained from image analysis. The PSD is shown in the Figure 2.5(b).

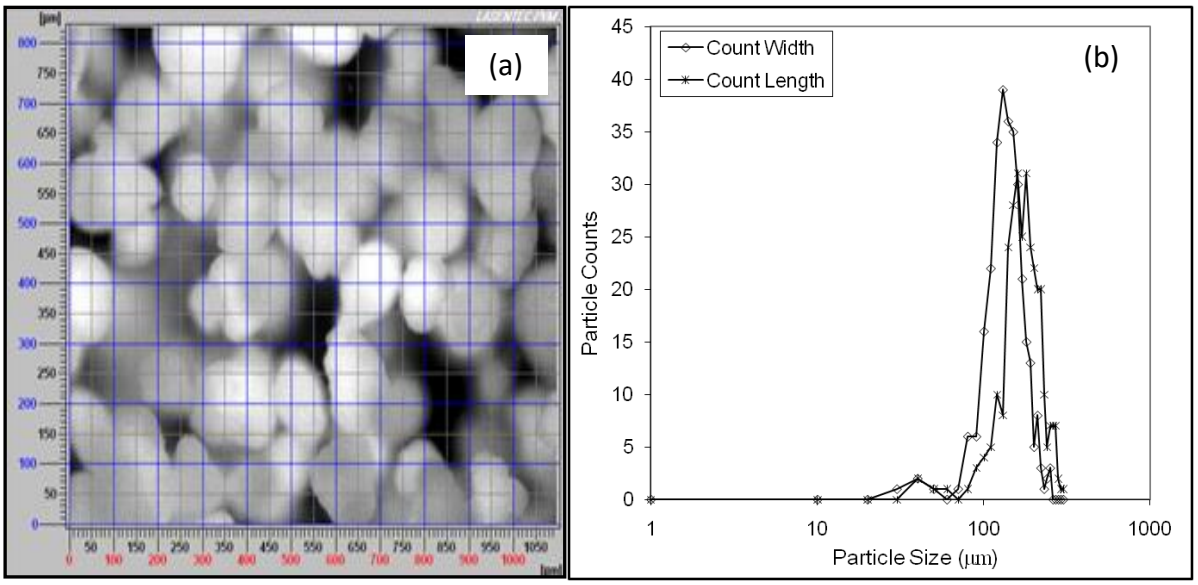

Figure 2.5. (a) Images obtained from calibration sample for theFBRM probe consisting of ceramic beads using a PVM probe (b) Comparison between the PSD measured using the particle widths and particle lengths obtained using PVM

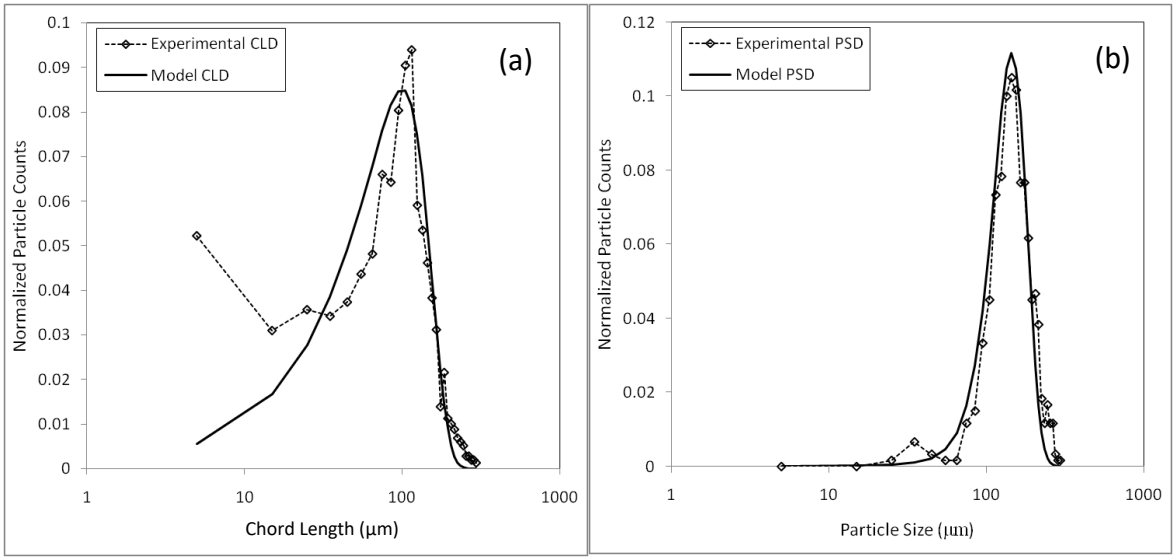

Figure 2.6. (a) Comparison between normalized CLD measured using FBRM for a system consisting of ceramic beads and the normalized fitted CLD used for the model (b) Comparison between the normalized experimental PSD obtained for a system of ceramic beads obtained using PVM and the normalized model predicted PSD

A cumulative PSD, obtained by summing the individual length and width distributions, was considered as the PSD of the sample. The cumulative PSD was then normalized by division with the total number of particles to enable comparison with the calculated PSD. The normalized PSD obtained is shown in Figure 2.6(b). The PSD was obtained through the image analysis done on a random sample size of 600 particles. The corresponding CLD of the calibration sample was also known. The CLD was also normalized by dividing the CLD with the

total number of chords measured. The presented model was applied to extract the PSD from the measured CLD. A two parameter normal distribution function was used to represent the PSD. A uniform bin size of 10μm with a domain spanning a range of 0 to 300μm was used corresponding to the type of data available from PSD/CLDmeasurements. All the distributions considered were normalized by dividing with the respective total number of particles/chords, as was relevant, to enable comparison. The 2 parameter values (mean and variance) for representing the PSD were obtained by fitting the normalized CLD obtained from the present model with the normalized CLD measured using FBRM. A comparative plot between the two is shown in Figure 2.6(a). The R^2 value of for the fit was 0.92. The R^2 value obtained is quite low. As can be seen from the Figure, there is a significant mismatch between the model-predicted CLD and the experimental CLD especially in a size range less than 10μm.The comparison between the normalized PSD measured experimentally and the normalized PSD predicted using the model is shown in Figure 2.6(b).

As can be seen in figure, the model accurately predicts the PSD using just the CLD information.

The model was then validated against another data set for regularly shaped particles. The data reported by Li et. al. (2005, Part 2) was used for the model validation. An image of the ceramic bead particles used by Li et. al. (2005, Part 2) is provided in the cited work. It was seen from the image, that the particles were nearly spherical and could be classified as regularly shaped particles. A two parameter normal distribution function was used to model the PSD. The PSD for the sample of ceramic particles was extracted from the CLD measured using the FBRM probe as reported by Li et. al. (2005, Part 2). The 2 parameter values for representing the PSD were determined by fitting the normalized model CLD to the normalized experimentally measured CLD using an optimization routine to tweak the mean and the variance parameters such that the R^2 value is closest to unity: a condition for complete match. For the present data set, an optimized R^2 value of 0.9794 was obtained corresponding to the fit between the normalized experimental and normalized model CLD's shown in Figure 2.6(a). A comparison between the normalized PSD measured using Image Analysis as reported by Li et. al. (2005, Part 2), the normalized PSD obtained using the model presented by Li et. al. (2005, Part 2) and the normalized PSD obtained using the present model is shown in Figure 2.7(b). As can be seen from Figure 2.7(b), the normalized PSD's obtained using the present

model is in excellent agreement with the PSD obtained through image analysis. The PSD obtained using the Li et. al. (2005, Part 2) model also predicts the PSD accurately.

The model proposed by Li et. al. (2005, Part 2) does provide a better fit in comparison to the present model, although marginally so. The present model assumes a shape for the particle size distribution as log-normal and normal distribution function. This assumption was shown to be sufficient to describe various systems as demonstrated in the chapter. The assumption reduces the number of unknowns to only 2 parameters – the mean and the variance of the considered distribution and hence makes the optimization problem very simple. In contrast, the model proposed by Li et. al. (2005, Part 2) optimizes for the number of particles in every bin, greatly increasing the number of unknowns and consequently the complexity of the optimization problem. Due to this difference, the present model is expected to lose out on some accuracy as opposed to the one proposed by Li et. al. (2005, Part 2) as a cost for simplifying the optimization problem. However, the present model is good enough for practical purposes to provide for accurate PSD information for regularly (spherical) shaped particles. In the next section we discuss the model validity for the case of irregularly shaped particles.

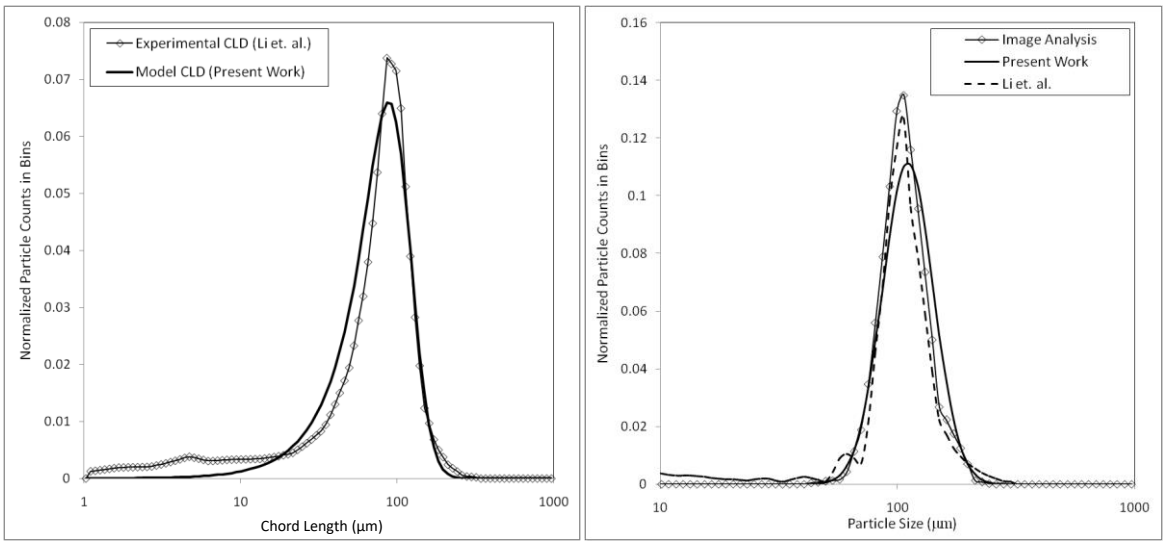

Figure 2.7. (a) Comparison between the normalized CLD obtained using present model and the normalized experimentally measured CLD (using FBRM, Li et. al. (2005)[3]) for a system of ceramic bead particles (b) Comparison between the normalized PSD obtained using Image analysis (reported by Li et. al. (2005)[3]), and the model predicted PSD's using the present model and the model presented by Li et. al. (2005)[3] for a system of ceramic bead particles

2.3.2. Evaluation of Model for Irregularly Shaped Particles

In this section, the model validity for different systems of irregularly shaped particles is considered. By irregularly shaped, it is implied that no specific shape or similarity of shape can be established within the system of particles considered.

2.3.2.1. Sand Particles

Normal sand procured at a local dealer was first passed through a sieving tower. The sand trapped within the sieve ranges of $50\mu m$ to $103\mu m$ was considered for the experiment. Around 8g of sand was taken and it was washed with sulphuric acid to remove any organic impurities. After this, it was repeatedly washed using distilled water over a $50\mu m$ sieve to remove any particles or impurities smaller than $50\mu m$. The sand was charged into a 250ml reactor along with 200ml of distilled water. The temperature of the mixture was maintained at 25^0C. The FBRM probe was inserted into the reactor to record the chord length distribution. The solution was stirred using a pitched blade down flow impeller with a stirring speed (800 RPM) which was sufficiently high enough to ensure that the mixture was well-mixed and well suspended. The sufficiency of the stirring speed to ensure well-mixed conditions was verified by increasing the stirrer speed gradually until a point where the number of counts recorded by the FBRM probe did not increase with increasing impeller speed. The CLD of the sample was recorded for a period of 10min using the FBRM probe under these conditions.

The sand particles were then separated from the solution and the PSD was determined by observing the particles under a microscope (Image Analysis). A sample image taken under a microscope for the present case is shown in Figure 2.8(a). A binary image was obtained through image processing of the sample image as shown in Figure 2.8(b). The PSD was determined by processing the sizes of 380 particles. The normalized PSD obtained from Image Analysis is shown in Figure 2.9(b).

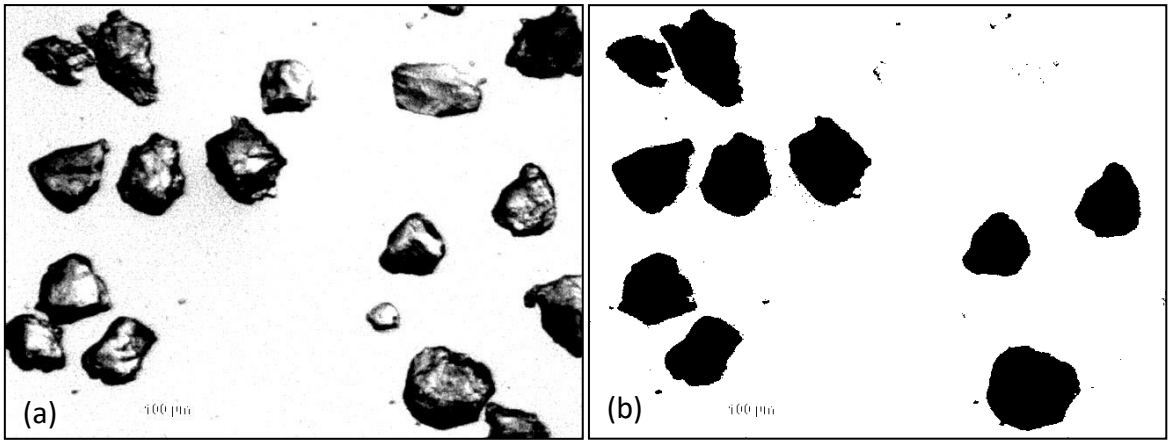

Figure 2.8. (a) Images taken under a micro scope for a sample of sand particles (b) Binary image obtained after image processing of image shown in (a)

From image analysis, it was observed, that although the particles were separated using a sieving tower, there were debris particles which had sizes less than 10μm. Now, even though they were visible under a microscope, characterizing their size was not possible. The minimum particle size from the measured sample recorded through image analysis was 16μm. The presence of debris particles is also indicated by the CLD measured by the FBRM as shown in Figure 2.9(a). In the normalized CLD shown in Figure 2.9(a), two peaks can be seen, one corresponding to a size less than 10μm and another around the 60 to 70μm mark. This suggests that the PSD of the present sample is actually a bimodal distribution. Now, in the present study, the PSD is modelled as a unimodal distribution. Hence, the resulting CLD is also unimodal. The approach may be extended easily for the case of bimodal distributions. For a bimodal distribution, the function would be modelled as a sum of two independent lognormal or gaussian distribution functions. The bimodal distribution will then be characterized using 4 parameters: the mean and the variance parameters of both distributions. The CLD may be obtained from the PSD by the procedure discussed in the manuscript. For the inverse problem, starting from a guess PSD, the 'true' PSD may be obtained by an iterative procedure similar to the case of the inverse problem of a unimodal distribution. However, in case of two parameters (as in the unimodal case), there will be 4 parameters which need to be iterated.

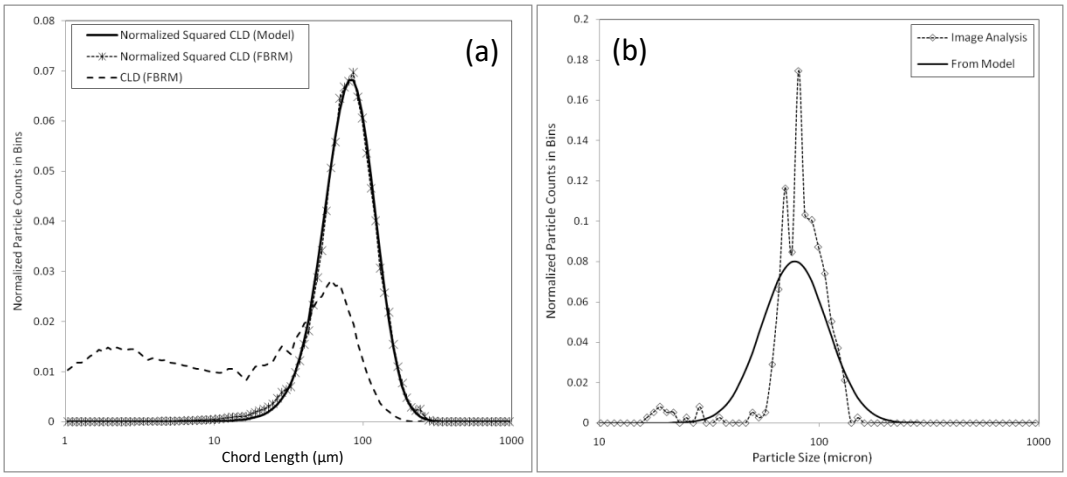

Figure 2.9. (a) Comparison between the normalized square weighted CLD obtained using the present model, the normalized square weighted CLD measured using FBRM (averaged over 1 min) and the normalized CLD measured using FBRM (averaged over 1 min) for a sample of irregularly shaped sand particles (b) Comparison between the PSD obtained using the present model and the PSD obtained using Image Analysis for a sample of irregularly shaped sand particles

In the present case, the PSD for particles lower than 10μm could not be obtained reliably through image analysis. Hence, instead of considering a bimodal distribution, the model was selectively evaluated for bigger sized particles (more than 10μm) using a two parameter (mean and variance) unimodal log normal distribution. To do this, the square weighted CLD is considered instead of the normal CLD. The square weighted CLD is used to specifically analyze the distribution of bigger sized particles in collection particles which span different size ranges. The square weighted CLD may be obtained by multiplying the number of particles in each bin by the square of the respective representative bin size. The square weighted CLD can be normalized by dividing each of the resulting terms in the bins by the sum of resulting terms in each bin spanning the entire domain. A comparison between the normalized square weighted CLD and the normalized CLD for the system of sand particles considered is shown in Figure 2.9(a). As can be seen, the normalized square weighted CLD tracks the distribution among the bigger sized particles and the lower sized particles are essentially ignored.

To determine the PSD, the R^2 value for the fit between the normalized square weighted CLD's obtained using the FBRM probe and through model was optimized to be close to unity. For the present case, an R^2value of 0.998 was obtained. The respective comparison between the normalized square weighted CLD's obtained experimentally and the one used in the model is shown in Figure 2.9 (a). The comparison between the normalized PSD obtained through image

analysis and from the model is shown in Figure 2.9(b). Logarithmic bin spacing was used to calculate the PSD such that there are 100 bins which span a domain starting from 1 to 1000μm and a bin size of 0.0715 for the first bin. As can be seen from Figure 2.9(b), the model is able to predict the mean of the PSD very well; however, the variance or the spread parameter of the PSD was not predicted well. The actual distribution is seen to be narrower than the one obtained using the model. However, we may conclude that the agreement is reasonable. A discussion on the possible reasons for the discrepancy is presented later is this section after considering other similar cases for systems of irregularly shaped particles.

2.3.2.2. Plasma Alumina

The validity of the presented model was tested for a system of plasma alumina particles. An image of the plasma alumina particles used by Li et. al. (2005, Part 2) is provided in the cited work. As was seen from the image, similar to the case of sand particles, there was no similarity in shape that can be inferred. A two parameter (mean and variance) lognormal distribution was considered to model the PSD. The PSD for the present case was derived by fitting the normalized model CLD with the normalized CLD measured using the FBRM probe as reported by Li et. al. (2005, Part 2) such that the R^2 value of the deviation is closest to unity. The R^2value for the present case was found to be 0.9947 and the corresponding comparison between the normalized model CLD and the normalized FBRM measured CLD as reported by Li et. al. (2005, Part 2) is shown in Figure 2.10(a). A comparison between the normalized PSD obtained from Image Analysis as reported by Li et. al. (2005, Part 2), and the normalized PSD's obtained using the present model and the best prediction using the model presented by Li et. al. (2005, Part 2) is shown in Figure 2.10(b). As can be seen from Figure 2.10(b), similar to the case of sand particles, the present model accurately predicted the mean of the PSD but could not capture the spread of the PSD. The PSD predicted using the model presented by Li et. al. (2005, Part 2) shows a good agreement for larger size particles apart from reasonably predicting the mean. This is because the model presented by Li et. al. (2005, Part 2) allows for the description of an additional 'particle shape factor'. The value of the 'shape factor' can be determined by either fitting model predictions to both the CLD and the PSD or through information known beforehand about the particular system.

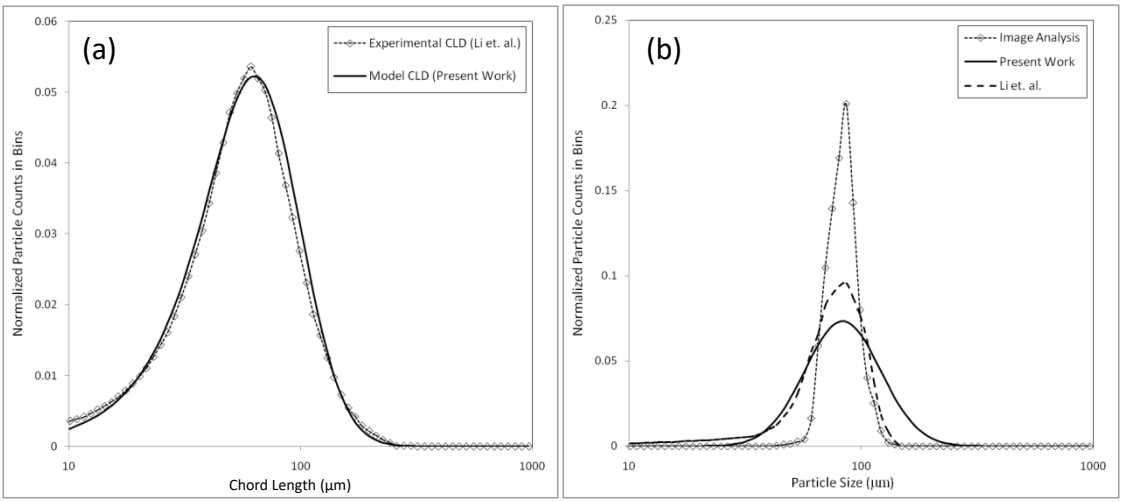

Figure 2.10. (a) Comparison between the normalized CLD obtained using present model and the normalized experimentally measured CLD (using FBRM, Li et. al. (2005)[3]) for a system of plasma alumina particles (b) Comparison between the normalized PSD obtained using Image analysis (reported by Li et. al. (2005)[3]), and the model predicted PSD's using the present model and the model presented by Li et. al. (2005)[3] for a system of plasma alumina particles

2.3.2.3. Zinc Dust

The validity of the present model is tested against another system of irregularly shaped particles: zinc particles. An image of the zinc dust particles used by Li et. al. (2005, Part 2) is provided in the cited work. As was seen in the image, no pattern could be inferred regarding the shape of the particles. A two parameter (mean and variance) lognormal distribution was considered to model the PSD. The parameter values for mean and variance were obtained by fitting the normalized model derived CLD with the normalized CLD measured using the FBRM as reported by Li et. al. (2005, Part 2). A R^2 value of 0.976 was obtained for the fit. A comparison between the measured normalized CLD's obtained by, fitting and measurement using the FBRM, is shown in Figure 2.11(a). The PSD for the sample was reported by Li. et. al (2005, Part 2) which was measured using Image Analysis. A comparison between the normalized PSD reported by Li et. al. (2005, Part 2) and the normalized PSD's obtained using the present model and the model presented by Li et. al. (2005, Part 2) is shown in Figure 2. 11(b). As can be seen from Figure 2.11(b), the model predictions from the present analysis, predicts the mean of the PSD reasonably well, however, as in previous cases of irregularly shaped particles, the variance is not predicted accurately.

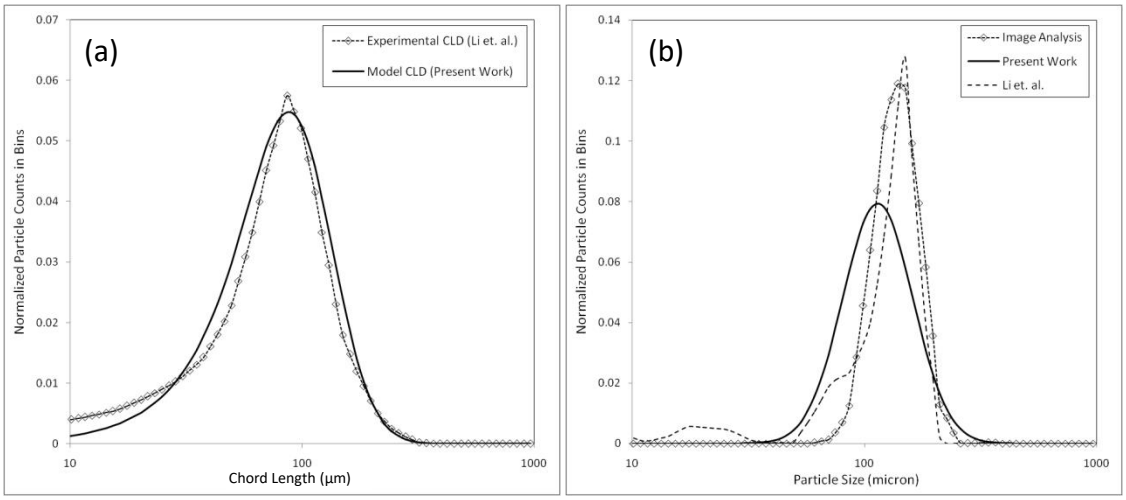

Figure 2.11. (a) Comparison between the normalized CLD obtained using present model and the normalized experimentally measured CLD (using FBRM, Li et. al. (2005)3) for a system of zinc dust particles (b) Comparison between the normalized PSD obtained using Image analysis (reported by Li et. al. (2005)3), and the model predicted PSD's using the present model and the model presented by Li et. al. (2005)3 for a system of zinc dust particles

The PSD predicted by the model presented by Li et. al. (2005, Part 2) agreed well with experimental data apart from additional particles predicted in a size range below 50μm. As for the previous case, the better agreement can be attributed to the use of an additional 'shape factor'. For irregularly shaped particle systems, it was consistently observed that the mean of the PSD predicted by the model was in reasonable agreement with the experimentally measured mean, while the variance was not. This mismatch was also observed for the model presented by Li et. al. (2005, Part 2). For irregularly shaped particles, there arise 2 ambiguities. Firstly, how to define the particle size for an irregularly shaped particle and thereafter find the particle size distribution experimentally. Secondly, from the point of view of the model, the question of determining the CLD for an irregularly shaped particle system becomes important. The particle size in the present study was defined as the equivalent diameter of a circle which represents the same area as the projected area of the particle visible through the microscope. Due to such a definition, the orientation of the particle with regards to the microscope has an important role in determining particle size and the particle size distribution. Although how this impacts the particle size distribution and what is the range of uncertainty introduced by it is not entirely clear. However, from the findings reported in the manuscript, what we can say about such systems is that the mean can be accounted for accurately using the model.

2.3.3. Application of Model for Real Systems

In the previous sections, we evaluated the model validity for a system of particles which are regularly and irregularly shaped. It was concluded that the model could accurately predict the PSD for the case of regularly shaped particles and could predict the PSD for irregularly shaped particles reasonably well. In the present section, the focus is on applying the model for two sets of particles which are practically relevant.

2.3.3.1. Paracetamol Crystals

In the present section, the model was applied for a system of Paracetamol crystals. This system is a popular subject for crystallization studies besides its practical relevance. For the purposes of model validation, the previous work done by Worlitschek et. al. (2005) was considered. In the work presented, the authors have used a method of Projection onto Convex Sets (POCS) for the problem of restoration of a PSD from a measured CLD. For the validation of the POCS method, they have considered a system of 1% vol. acetaminophen (Paracetamol) in a toluene solution. The CLD data was interpreted using the POCS method to obtain a restored PSD. The restored PSD was then compared with the other offline methods to obtain a sample PSD: laser diffraction and TSI Aerosizer. The method was seen to adequately predict the particle size distribution.

In the present study, the validity of the present model for a system of paracetamol crystals is evaluated by deriving the PSD from the experimental CLD data and comparing the model predicted PSD against experimental PSD measurements. The experimental measurements of the CLD and the PSD for this section, used in the present study, were previously reported by Worlitschek et. al. (2005).

An image of the Paracetamol crystals used by Worlitschek et. al. (2005) is given in the cited work. The CLD measurements were noisy. The CLD measurements are noisy when the sample being measured has a low particle concentration (< 2% holdup). In such cases, the CLD needs to be smoothened before applying the present model. For high particle concentrations (> 5% holdup), the CLD measurements have negligible noise and do not need smoothening. Typically, the presented model works well for high particle concentrations as the model predicted CLD may be compared directly against the measured CLD. For low particle concentrations, the noisy CLD can be smoothened by averaging out the CLDs measured over

a brief time interval. However, the CLD reported by Worlitschek et. at. (2005) was an instantaneous CLD. The noise in the CLD is representative of the finite sample measured by the FBRM. Smoothening in effect cancels out this dependency on 'local' samples and is representative of the entire particle system and does not affect the CLD to PSD conversion. In the present study, the restored CLD data provided by Worlitschek et. al. (2005), which is essentially a smoothened representation of the raw CLD data was considered. A comparison between the raw CLD data and the restored CLD reported by Worlitschek et. al. (2005) is given in the cited work.

A two parameter lognormal distribution was considered to model the PSD of the present system. The parameter values for the PSD were obtained by fitting the CLD obtained using the present model to the CLD measurements reported by Worlitschek et. la. (2005). A comparison between the normalized CLD obtained using the present model and the measured CLD (restored) reported by Worlitschek et. al. (2005) is shown in the Figure 2.12(a). The data was obtained in terms of 360 logarithmically spaced bins ranging from sizes of 1 to 1000 microns. The R^2 value of the fit was0.996. The values for the mean and variance were obtained to be 3.65 and 0.65 respectively.

To enable comparison of the presented derived PSD data with the measured PSD data reported by Worlitschek et. al. (2005), two types of distributions derived from the PSD need to be defined. Firstly the discretized length weighted logarithmic distribution $n_{1,ln}$ and secondly the discretized volume weighted logarithmic distribution $n_{3,ln}$. For an arbitrary j^{th} bin, the following can be shown to be true:

$$n_{1,ln}(X_j) = \frac{X_j N_j}{\mathrm{B_1 w_s}} \qquad (2.20)$$

$$n_{3,ln}(X_j) = \frac{X_j^3 N_j}{\mathrm{B_3 w_s}} \qquad (2.21)$$

Where w_s is the logarithm of the ratio of expansion of the bins and for the present case has the value 0.0192. The other symbols $B_1$and B_3stand for the first and the third moments of the discretized PSD.

The general i^{th} moment of a discretized PSD may be determined by using the following relation:

$$B_i = \sum_j X_j^i N_j \quad (2.22)$$

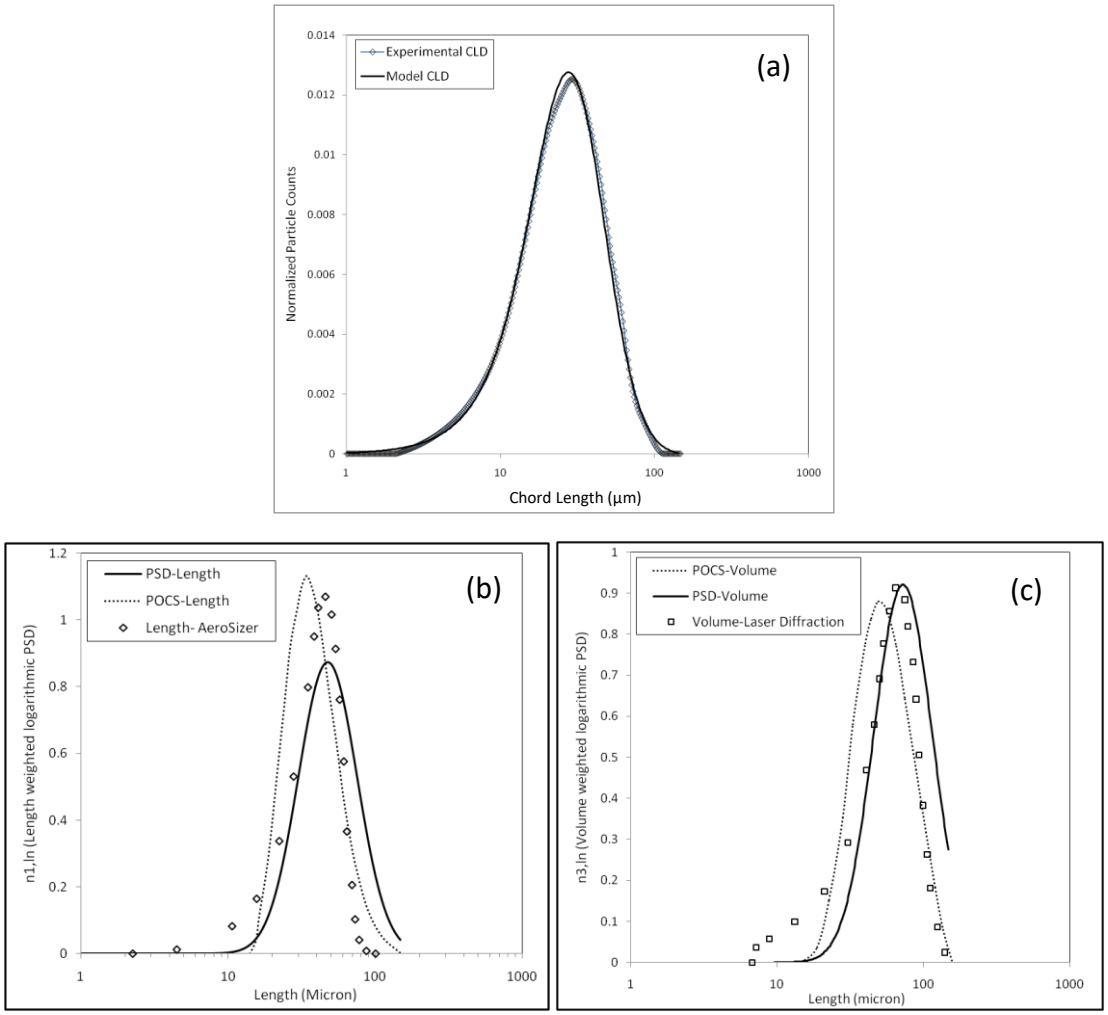

Figure 2.12. (a) Comparison between the restored CLD (Dotted line)(Worlitschek, Hocker and Mazotti (2005)[5]) and the derived CLD using the present model (b) A comparison between the discretized length-weighted logarithmic distributions obtained using the POCS method (POCS-Length) (Worlitschek, Hocker and Mazotti (2005)[5]), the derived PSD in the present model (PSD-Length) and the TSI Aerosizer (Worlitschek, Hocker and Mazotti (2005)[5]) (c) A comparison between the discretized volume-weighted logarithmic distributions obtained using the POCS method (POCS-Volume) (Worlitschek, Hocker and Mazotti (2005)[5]), the derived PSD in the present model (PSD-Volume) and laser diffraction (Worlitschek, Hocker and Mazotti (2005)[5])

A comparison of the discretized length weighted logarithmic distribution between the PSD calculated from the present study, the data obtained using the POCS method and from the TSI Aerosizer is shown in Figure 2.12(b). A comparison of the discretized volume weighted logarithmic distribution between the PSD calculated from the present study, the data obtained using the POCS method and from the TSI Aerosizer is shown in Figure 2.12(c). As can be seen from both the figures, the present model yields reasonable comparison with methods

for offline determination of PSD. In the volume weighted distribution for the PSD, there is an abruptness at the end because no bin sizes larger than 150 micron were considered for calculation.

Thus, we can conclude that even with the assumption of spherically shaped particles, the present model is seen to predict useful results. The present model is thus valid for predicting the PSD from the FBRM measured CLD for a system of paracetamol crystals.

2.3.3.2. Para-Aminophenol Crystals

Para-Aminophenol is a commercially important chemical (used in the manufacturing of paracetamol) which is obtained through crystallization. In the present study, the validity of the present model is tested for a system of p-Aminophenol crystals in water. Water was chosen as a solvent as p-Aminophenol is sparingly soluble in water. An industrial sample of p-Aminophenol was considered for analysis. An image of the p-Aminophenol crystals in water is shown in Figure 2.13(a). As can be seen from the Figure, there is a lot of debris (smaller crystals) apart from the bigger crystals. This suggests that this considered sample PSD might actually be bimodal. This is confirmed by the CLD measurements shown in Figure 2.13(b). The average chord size in the lower size range of the bimodal distribution shown in Figure 2.13(b), appears to be below 10μm. The PSD of the Para-Aminophenol crystals was determined in the present study through Image Analysis of images obtained using a microscope. The minimum size recorded using Image Analysis for the present system was 29μm. Sizes below this size range could not be resolved using image analysis. This is similar to the problem of validation for sand particles covered in one of the previous sections. As done for the case of sand, since, out of the bimodal distribution, we have the PSD data only for the larger size class, the model validity was tested only within the larger size range.

A unimodal template PSD represented using a two parameter log normal distribution, as done in the previous sections, was considered. In the model discussed in the present work, the values for the two parameters (mean and variance) of the PSD are obtained by fitting the model predicted CLD to the experimental CLD. A square weighted CLD, which may be derived from the CLD by a procedure mentioned in the section dealing with sand particles, gives preference to larger size particles. The smaller size particles are apparently *artificially filtered* from the data. The values of the two parameters of the PSD were instead obtained by fitting

the model predicted normalized squared CLD to the experimentally measured (using FBRM) normalized squared CLD. A comparison between the fitted model predicted normalized squared CLD and the experimentally measured normalized squared CLD is shown in Figure 2.13(b). The R^2 value for the fit was found to be 0.997. The PSD was measured using the Image Analysis procedure discussed earlier. A sample of 380 particles was measured. A comparison between the model-predicted normalized PSD and the normalized PSD obtained through Image Analysis is shown in Figure 2.13(c).

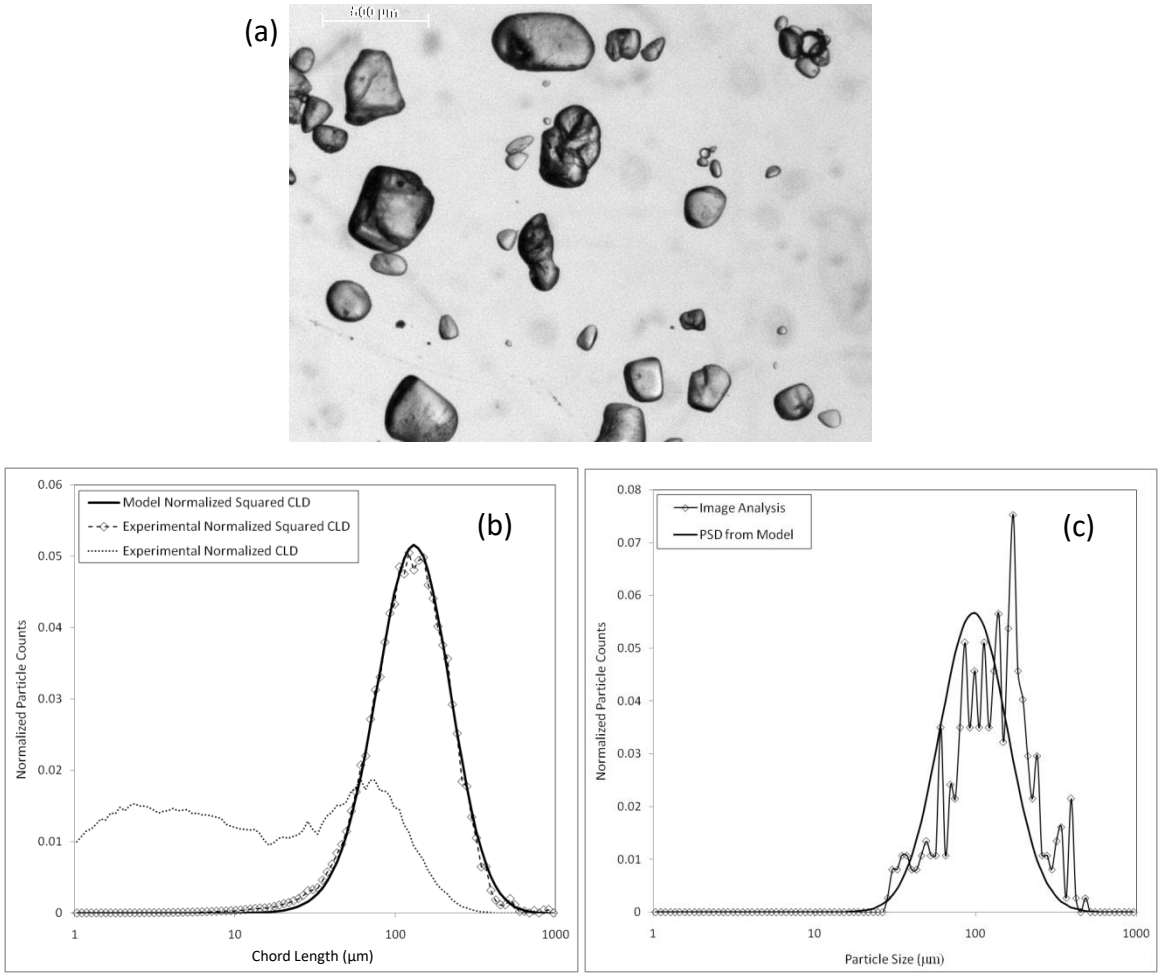

Figure 2.13. (a) Raw micrograph of p-Aminophenol crystals (b) Comparison between the normalized squared CLD obtained using present model and the normalized experimentally measured (using FBRM) squared and non-squared CLD for a system of p-Aminophenol crystals (c) Comparison between the normalized PSD obtained using Image analysis and the model predicted PSD for a system of p-Aminophenol crystals

The model is seen to slightly under-predict the mean particle size however, accurately accounts for the variance. It may be concluded that the presented model accurately predicted the PSD for the case of Para-Aminophenol crystals.

2.3.4. A Word on Model Applicability

A comparison between the expected values of the diameter (mean diameter) and the standard deviations for each of the distributions reported in the present study for different systems is given in Table 1. The model was seen to predict good results for the case of spherical or regularly shaped particles. This was encouraging but expected as the model was fundamentally based on the assumption that the particles are spherical in shape. The model, when applied to a system of irregularly shaped particles, was seen to predict the mean accurately but over predict the standard deviation. This observation was consistent across all the three systems considered in this category. The discrepancy in the predictions points to the fact that the information about the shape is important. However, the shape itself varies within such systems. So, any model, built using a uniform shape assumption will face such limitations while predicting the PSD for an irregularly shaped particle system. For instance, even the model presented by Li et. al. (2005, Part 1 & 2), which allows the particle shape to be ellipsoidal and provides an adjustable parameter to tune the particle shape specific to a system, failed to capture the standard deviation accurately for the system of plasma alumina particles. Then, two systems of particles which are the potential application areas for the presented model were considered. The present model was seen to reasonably predict the PSD for a system of paracetamol particles as also for the case of p-aminophenol particles. Thus, even though, the model assumes a spherical particle shape, it still accurately predicts the PSD. The reason for this could be that the particles within a system of crystals are uniformly shaped as opposed to the shape variation which is typically seen in irregularly shaped systems.

A word of caution is necessary while using the present model. This does not have to do with the model itself but more with regards to the limitations in determining the CLD for particular systems using the FBRM. Sometimes, like in the case of glass particles, air bubbles, liquid-liquid emulsions and such, the optical properties of the particle/bubble/drop become important. The CLD then depends upon, whether and to what extent, the laser gets reflected back from the particle surface. The present model does not account for the optical properties of the particles and is not fit for use for systems with transparent particles/bubbles/drops. For applications related to such systems kindly refer to Kail et. al. (2009). Another difficulty arises where in due to inadequate suspension, larger particles tend to stay at the bottom of

the vessel. In such cases, the CLD is measured for only the suspended, smaller sized particles. This results in an under prediction of the PSD. Adequate care should be taken that the particles are always uniformly suspended. In any case, it is good practise to validate the model once, against results from image analysis or other offline sizing techniques, while considering a particle system other than the one reported in the present study.

2.4. Conclusions

In the present study a simple model was presented to derive the Particle Size Distribution (PSD) from a Chord Length Distribution (CLD) measured by the FBRM probe. The model does not require the specification of any parameter and enables the direct calculation of the PSD from known CLD measurements using simple spread sheeting tools. The model was first validated for two systems of regularly shaped (spherical) particles both consisting of ceramic beads. The model was seen to accurately predict the PSD. The model was then evaluated for various systems for a system of irregularly shaped particles: sand, plasma alumina and zinc dust. By irregularly shaped, it was implied that the shape of the particles within the system is not constant. The model was seen to reasonably predict the PSD, wherein the mean of the PSD was accurately predicted and the variance was over predicted. The model validity was then tested for a couple of systems of particles which are expected to be potential application areas of the presented model: paracetamol crystals and p-aminophenol crystals. The model was seen to accurately predict the PSD for these cases. The performance of the present model for these system was seen to be at par with the popular models presented by Li et. al. (2005, Part 1) and Worlischek et. al. (2005). These models are quite complex to implement for reasons discussed earlier as also require the specification of an additional parameter(s) for particle shape. In comparison the present model is rather simple (can be implemented using only simple spread sheeting tools) and does not require the specification of additional parameters.

Acknowledgments

The authors of the present work wish to thank Mettler Toledo for providing us with the measured Particle Size Distribution data obtained through image analysis using the Mettler Toledo PVM probe for a system of spherical, fully opaque, ceramic spheres. Authors are grateful to financial support for this work by CSIR through Mastflo [OLP3026] and Indus MAGIC [CSC123] projects.

Symbols & Notation

Symbol	Description	Unit
$P(x, y, D)$	Probability of measuring a chord between x and y for a circle of diameter 'D'	-
D	Diameter of sphere/circle	m
L_i, L_{i-1}	Upper and lower boundary locations respectively of the i^{th} bin	m
N_i	Number of particles in the i^{th} bin in the PSD	#
M_i	Number of particles in the i^{th} bin in the CLD	#
$A_{i,m}$	Fraction of the particles contained in the m^{th} bin in the PSD measured as having chords of size belonging to the i^{th} bin of the CLD	-
A_i	Fraction of the total particles measured as having chords of size belonging to the i^{th} bin of the CLD	-
N_T	Total number of particles	#
μ	Model parameter referencing mean particle size	m
σ^2	Model parameter referencing variance/spread of particle sizes	m^2
B_i	i^{th} moment of the distribution considered	$\#\text{-}m^i$
X_j	The representative pivot location of the j^{th} bin	m
$n_{1,ln}$	Discretized length weighted logarithmic distribution	-
$n_{3,ln}$	Discretized volume weighted logarithmic distribution	-
w_s	Logarithm of the ratio of the bin expansion; $w_s = \ln\left(\frac{L_i}{L_{i-1}}\right)$	-

References

Agimelen O., Hamilton P., Haley I., Nordon S., Vasile M., Sefcik J., Mulholland A., 2015. Estimation of particle size distribution and aspect ratio of non-spherical particles from chord length distribution. *Chemical Engineering Science*, 123, pp.629-640.

Kail N., Marquardt W., Briesen H., 2009. Estimation of particle size distributions from focused beam reflectance measurements based on an optical model. *Chemical Engineering Science*, 64(5), pp.984-1000.

Li H., Grover M., Kawajiri Y., Rousseau R., 2013. Development of an empirical method relating crystal size distributions and FBRM measurements. *Chemical Engineering Science*, 89, pp.142-151.

Li M., Wilkinson D., 2005. Determination of non-spherical particle size distribution from chord length measurements. Part 1: Theoretical analysis. *Chemical Engineering Science,* 60, pp.3151-3265.

Li M., Wilkinson D., 2005. Determination of non-spherical particle size distribution from chord length measurements. Part 2: Experimental validation. *Chemical Engineering Science,* 60, pp.4992-5003

Ruf A., Worlitschek J., Mazotti M., 2000. Modelling and Experimental analysis of PSD measurements through FBRM. *Particle & Particle Systems Characterisation*, 17, pp.167-179.

Worlitschek J., Hocker T., Mazzotti M., 2005. Restoration of PSD from Chord Length Distribution Data using the Method of Projection onto Convex Sets *Particle & Particle Systems Characterisation*, 22, pp.81-98.

Chapter 3. Population Balance Modelling for Batch Crystallisation Processes

This chapter has been reproduced from the following manuscript:

Pandit, A.V. and Ranade, V.V., 2015. Modeling Hysteresis during Crystallisation and Dissolution: Application to a Paracetamol–Ethanol System. Industrial & Engineering Chemistry Research, 54(42), pp.10364-10382.

3.1. Introduction

Crystallization is a topic which has great commercial interest. This process is most often encountered when one wishes to produce high-value speciality chemicals. The quality of the chemicals produced, is assessed primarily with regards to the product purity, the crystal morphology (shape of crystal) and the particle size distribution. The particle size distribution as a quality assessment parameter becomes important because of certain size requirements imposed by the applicability or the further processing of the chemicals. It is desirable to be able to quantitatively capture the effect that the operating parameters have on these parameters in order to optimize the process to make it more economical. Also, a thorough understanding of the influence of these operating parameters helps in troubleshooting the process and formulating guidelines which make required product goals (particle size distribution, product purity, crystal shape) achievable.

In this work, a modelling framework is presented which is capable of describing crystallization and dissolution processes in a batch crystallizer. The focus was on understanding cooling crystallization and dissolution of a well-known system of paracetamol - ethanol. The framework may be extended with few obvious modifications to describe evaporative crystallization, anti-solvent crystallization or for operation in a continuous crystallizer, although, this is beyond the scope of the present work. The quantitative description of crystallization processes often requires determining unknown parameter values required for the growth and nucleation rate expressions for a given system. Using the presented framework, a methodology to reliably estimate unknown nucleation parameter values from

known growth parameter values for a sample system of paracetamol – ethanol was demonstrated.

In this work, experiments were performed to understand cooling crystallization. A Focused Beam Reflectance Measurement (FBRM) probe was used to monitor the changes in the particle size distribution occurring during crystallization and dissolution processes. The FBRM probe allows the online and in situ characterization of the particle size distribution (PSD) that emerges especially in dense solutions (Ruf et. al., 2000). Although instead of giving the 'true' particle size distribution, the FBRM measures the Chord Length Distribution (CLD), which is representative of the PSD (Ruf et. al., 2000). Such on-line measurements are essential since crystallization and dissolution processes are inherently transient, with number and size of particles dynamically changing with time, as the solution tries to attain equilibrium. It is not always feasible to obtain reliable information from offline measurements, as; first, the PSD will keep dynamically changing during the interval when the sample was removed and was studied; and second, the sample, being small in volume, will try to equilibrate with the surroundings (temperature) very fast which also influences the PSD significantly. The FBRM probe has been used previously to determine the solubility curve which is most fundamental for any crystallization study (Barrett et. al., 2002; Kim et. al., 2005; Kim et. al., 2007). Barrett et. al. (2002) used the FBRM probe to determine the Meta-stable zone width in cooling crystallization. Hermanto et. al. (2010) used the FBRM probe to monitor the crystal size in a study to ensure batch to batch size consistency in anti-solvent crystallization. Worlitschek et. al. (2004) used the FBRM in a study to determine the crystallization kinetics during cooling crystallization. Although not relevant to the present study, it is worthwhile to note that the FBRM has also been used to understand the dynamics of crystal shape change during crystallization, for example, O'Sullivan et. al. (2005) used the FBRM to study the polymorphic transformation of d-Mannitol.

Previously, much work has been done in trying to modify the crystal size distribution and the crystal shape using cycles of crystallization and dissolution (Lovette et. al., 2002; Jiang et. al., 2014). In these studies, a saturated solution containing initial seed crystals, was cooled at a specified cooling rate to a specified temperature to induce crystal growth and nucleation. The solution is then immediately reheated, at a specified heating rate, to its initial state. It was observed that the crystal population properties, such as the mean size as well as the crystal

shape, were seen to change towards the desired objective (for instance mean size increased) after undergoing such cycles. However, in the present study, instead of trying to modify the crystal size, the aim was to extract the crystallization kinetics model from the crystallization and dissolution cycles. Hence, instead of starting with a saturated solution with some initial seed crystals, as in the previous experiments, an undersaturated solution was considered as a starting point. The solution was cooled until a specified temperature was reached, where in crystallization had already occurred, and then reheated back to the initial undersaturated state causing dissolution of the crystals generated during crystallization. The heating rate and the cooling rate employed for one cycle were kept equal in magnitude. The number of particle counts and the particle chord length distribution were recorded online by a Focused Beam Reflectance Measurement (FBRM) probe. The solution temperature was also recorded online using a temperature sensor. Transient measurements using FBRM revealed a hysteresis in particle counts with respect to temperature when paracetamol - ethanol system was caused to undergo crystallization followed by complete dissolution. Further, it was observed that the shape of the hysteresis curve as influenced by the operating parameter of cooling/heating rate. The observed hysteresis in particle counts is expected due to the Meta Stable Zone Width (MSZW) and the consequent late onset on nucleation. However, the exact shape of the hysteresis curve, after the onset of nucleation, is governed by the crystallization kinetics; more specifically, the kinetics of nucleation (primary and secondary) and the kinetics of crystal growth. The parameter values required to implement the aforementioned kinetic models are not always known from previous text. The hysteresis curve and the influence that the heating/cooling rate has on it, provides an excellent way to characterize the crystallization kinetics of the system and serves as a rigorous validation case for crystallization – dissolution models.

Some comments on previous work on modelling crystallization – dissolution are warranted here before the present contributions are described. Population Balance Equations (PBE) have been widely used to model crystallization and dissolution processes. A detailed review of a subset of the methods to solve population balance equations is given by Ramkrishna (2000). Ramkrishna (2000) reviews analytical solutions, moment-based methods: standard method of moments and quadrature method of moments, discretization based methods: fixed pivot and moving pivot as well as the method of weighted residuals. It is possible to

obtain analytical solutions to the PBE, however, this is limited to a few cases depending upon the type of mathematical expressions used to represent growth/nucleation kinetics as well as for other phenomena considered (aggregation/breakage). Analytical solutions for the population balance equation for simple cases such as size independent crystal growth rate and a power law type nucleation rate are provided in Ramakrishna (2000). Another class of methods for the solution of the PBE are those which track moments of the particle size distribution rather than tracking complete distribution also known as moment based methods. Simple systems (not involving breakage or aggregation), like in the present study, may be addressed suitably by using the standard method of moments (Randolph et. al., 1988). For more complex systems, involving aggregation and breakage, several new methods such as the quadrature method of moments (Marchisio et. al., 2003) and the direct quadrature method of moments (Marchisio et. al., 2005) have been proposed. The solutions obtained from such methods are computationally efficient, however, are less descriptive as it is difficult to extract the complete particle size distribution information from only the known moments. This inverse problem is not a mathematically well-posed problem, that is, there may exist multiple solutions to the problem. There are methods of extracting the particle size distribution from known moments however; those are not besides their own limitations. Discretization based methods for the solution of the PBE enable the complete description of the particle size distribution. In these methods, typically, the domain of the particle size is broken into discrete bins and the number of particles in these bins is tracked with time. However, one should be careful in implementing these methods as they are prone to numerically induced errors. Recently, the High Resolution Finite Volume (HRFV) methods have been gaining importance for the solution of Population Balance Equations (Gunawan et. al., 2004). These methods are derived from a general Finite Volume class of methods which are typically used to solve flow and wave propagation problems (LeVeque, 2002). The method has the advantages of tapping the sophisticated numerical methods which have been developed to solve the more popular flow and wave propagation problems and as such is very robust. Apart from this, the fixed and moving pivot methods are also two popular discretization based methods for the solution of the population balance equations (Ramakrishna, 2000; Kumar et. al., 1996).

In this work, a mathematical framework is presented to model crystallization and dissolution processes by solving the population balance equation for nucleation, growth and dissolution. The population balance equation tracks the changes in the particle size distribution with time. The framework includes the solution of the population balance equation (PBE) on two levels:

(a) The solution of just the crystallization stage of the experiment using a computationally efficient, but, less informative method of moments
(b) The solution using a High Resolution Finite Volume (HRFV) scheme coupled with the Moving Pivot method for the complete description of the particle size distribution during both the crystallization and dissolution stages of the experiment.

For a system of paracetamol and ethanol, the kinetic model for crystal growth was available in literature however; a reliable model for nucleation was not available. In the next section, the experiments performed and the experimental results obtained, which form the basis for the present work is described.

3.2. Experimental Section

In the present study, paracetamol was used as the solute and ethanol as the solvent. Experiments were performed to understand the dissolution and re-crystallization of paracetamol. The crystallization was brought about in the present study by cooling the solution to below the solubility temperature. 45 gm of paracetamol was mixed with 200 ml of ACS grade Ethanol in a 250 ml glass reactor. The glass reactor was then inserted into a Mettler Toledo OptiMAX reactor assembly. A down flow pitched blade four-blade stirrer (diameter 38mm; blades at an angle of 45^0) was used to agitate the solution. A constant agitator speed of 400 RPM was maintained for all experiments. A Mettler Toledo focused beam reflectance measurement (FRBM) probe was inserted into the reactor for the in-situ and online monitoring of particle counts and particle chord length distribution. It should be noted that the tip speed of the impeller is approximately around 0.63 m/s which is lesser than, but not significantly so, the 2 m/s tangential speed of the FBRM laser. This suggests that particle motion might affect the FBRM probe measurements. However, the deviation in the number of particle counts measured as well as the particle chord lengths measurements due to particle motion is not significant. This was verified multiple times by comparing the respective chord length distributions and particle counts for different samples at different

impeller speeds (above the critical suspension speed). The OptiMAX reactor assembly allows for controlled heating and cooling of the solution as well as to control the stirring speed. The entire set up is connected to a computer for the continuous acquisition of data. A schematic of the experimental setup is shown in Figure 3.1.

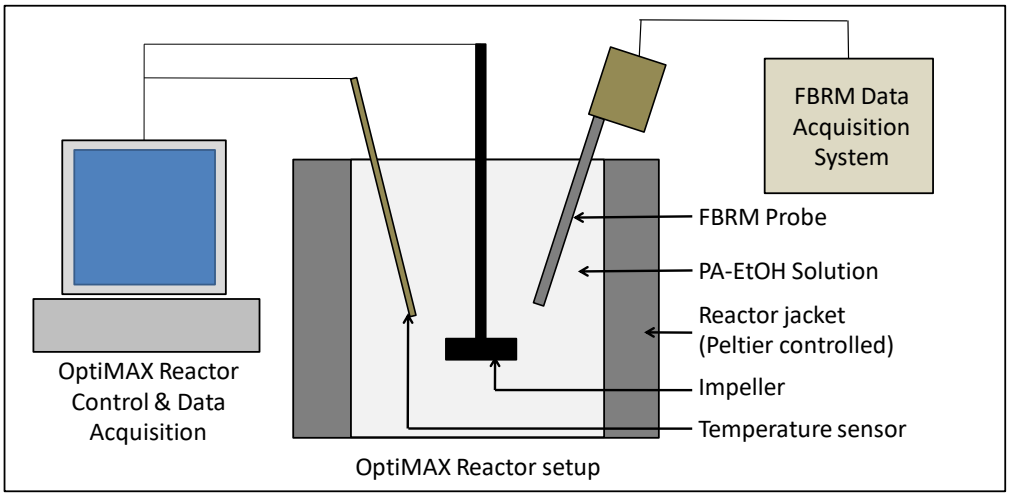

Figure 3.1. Schematic of Experimental Setup

The OptiMAX reactor setup allows for precise control over the heating and cooling rates via Peltier elements. A temperature probe is inserted into the reactor vessel to continuously monitor the temperature. The heating/cooling rate is controlled precisely by a control system using the online temperature data and correspondingly manipulating the jacket temperature to obtain the desired heating/cooling rates. The FBRM probe works on the principle of laser back-scattering. A laser is emitted from a laser source inside the probe. The source is then moved in a circular fashion such that the laser emitted is parallel to the probe axis and the laser traces a cylindrical surface around the probe axis inside the probe. A very high speed of rotation is used (in the present study the tangential speed of the source was set to 2 m/s). At the probe tip is a sapphire window which is in contact with the solution in which the particle measurements are to be made. As the laser is moving, in the solution just near the probe tip, if it were to pass over a particle, the laser gets reflected back inside the probe. Each instance of this reflection is treated as one count of particle detection and the duration of time for which the beam is reflected is then used to work out the length of the chord which the laser 'cuts' on the particle surface. Thus, in course of time and in dense solutions, multiple particles are recorded by the FBRM probe and hence we obtain the number of counts and the particle chord length distribution data. It is clear that when the solute is completely dissolved in the

solution, the probe will record a base line number of counts which correspond to the noise (stray reflections etc.). As the crystallization begins and new crystals start to appear, the number of particles measured by the FBRM steadily starts to increase. Further, the growth of the crystals is reflected in the evolution of the measured chord length distribution. More and more chords in a larger size range are measured with time as crystallization progresses.

In the present study, 45 gm of Paracetamol is mixed with 200 ml of Ethanol and inserted into a 250 ml glass reactor. The reported solubility temperature reported by Granberg et. al. (1999) for this concentration of solute is around 318 K. The solution temperature was first taken to 323 K, and then held constant and provided with adequate time to ensure complete dissolution of the solute. The solution was then cooled at a particular constant cooling rate (0.3, 0.5 and 0.7 K/min) until the solution reaches 263 K. Between the point when the cooling is started and when the solution reaches 263 K, the solution crystallizes. As soon as the solution reaches 263 K, the solution is heated at a heating rate equal in magnitude to the cooling rate previously employed. As the temperature increases, the particles slowly start to dissolve. The solution temperature is allowed to increases until a set point of 323 K is reached. The heat of dissolution and crystallization are not accounted for as the OptiMAX temperature system is sufficient to maintain the required linear heating/cooling profiles for the rates considered in the present study as may be verified from Figure 3.2. It is seen that the particles have completely dissolved even before this point is reached. This cycle is repeated for different heating/cooling rates. The temperature profile employed corresponding to various heating/cooling rates (1, 0.7, 0.5 and 0.3 K/min respectively) and the corresponding particle counts measured by the FBRM probe is plotted in Figure 3.2 as a function of time. The cooling is initiated from 323 K. As the solution temperature crosses (drops below) the solubility temperature (318 K), the solution starts becoming supersaturated, more so as the temperature decreases further. However, it does not crystallize and a clear solution, which is as observed visually, is recorded by the FBRM (Figure 3.2). During cooling, suddenly, at a particular temperature, crystals start to appear in the solution and the solution is no longer clear. This is referred to the crystallization temperature. As we cool further, the crystallization progresses and more and more crystals are produced. This increase in the crystal population and hence the crystal number density, can be confirmed by visual inspection as also by the fact that the number of counts recorded by the FBRM increases sharply. This increase in

number of counts continues until a point when the solution is no longer in a supersaturated state and it has precipitated out all the excess dissolved solids. At this point, the solubility is equal to the dissolved solids concentration. In the present text, we will refer to this point as the equilibration point. For the case of 0.7 K/min cooling rate, it was observed that there was crystallization even while heating the solution. This was because the equilibration point was not reached during the cooling stage.

On further heating the solution after the equilibration point, the counts start to decrease gradually due to sustained dissolution until all the particles disappear and we again have a clear solution. Due to the late onset of nucleation brought about by the solution being in an unstable supersaturated state, if we were to plot the particle count versus the reactor temperature for each of the cooling/heating rates, we will observe a hysteresis in particle counts where the curve forms a closed loop. Further, we observe that the shape of the hysteresis loop is influenced by the heating/cooling rate employed. Such hysteresis loop (particle counts versus temperature plot) is plotted for different heating/cooling rates of 0.3, 0.5 and 0.7 K/min and shown in Figure 3.3. In Figure 3, the arrows indicate the direction of the experiment, starting from 323 K in accordance with the procedure mentioned earlier. It was observed that as we decrease the heating/cooling rates; there is a peculiar 'twisting' of the hysteresis loop. The twisting effect is most pronounced in the 0.3 K/min experiment hysteresis loop. As can be seen in Figure 3.3, the solution reaches equilibration at around 285 K, which is much before 263 K. From the equilibration point till 263 K, the number of counts recorded is relatively constant. The dissolution begins as soon as we start heating the solution from 263 K causing a decrease in the number of counts. Thus, this leads to 2 different hysteresis loops instead of 1 hysteresis loop as observed for the 0.7 K/min experiment. This is referred to as 'twisting' of the hysteresis loop in the present work.

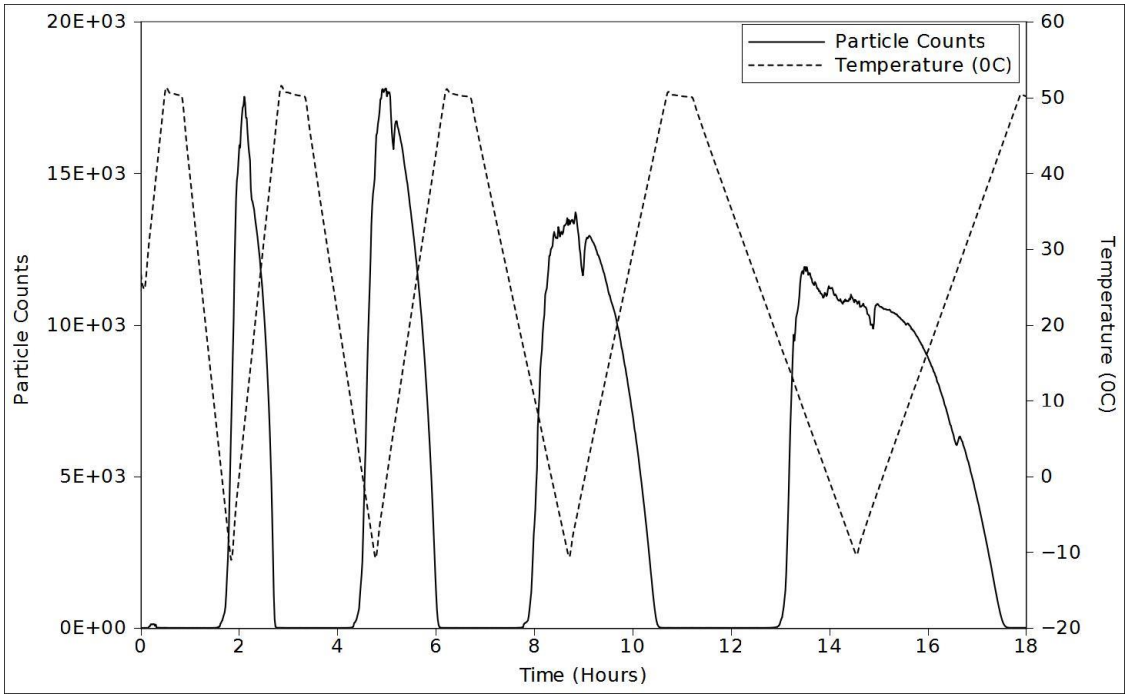

Figure 3.2. Experimental Temperature profile employed, and the corresponding particle counts recorded by the FBRM probe as a function of time

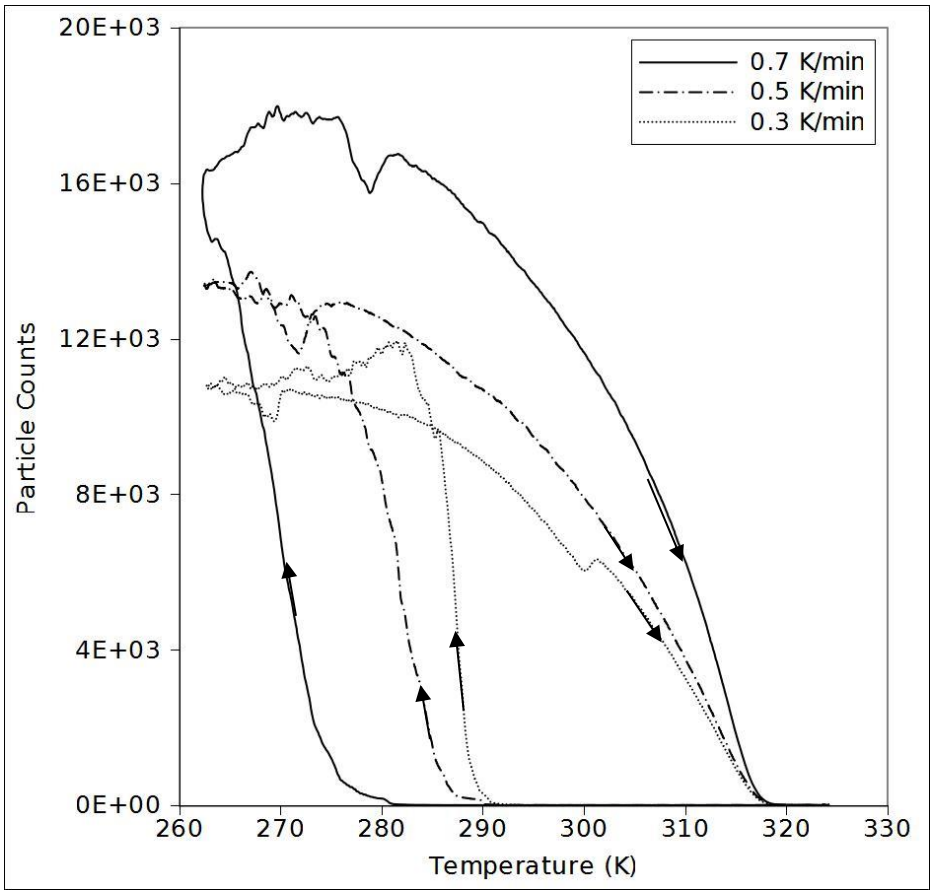

Figure 3.3: Hysteresis loop plots for various heating/cooling rates

In the present study we have attempted to explain this trend by developing a model which is capable of quantitatively capturing this trend. It is clear that the 'twisting' of the loop arises as a result of a combination of the interaction of the phenomenon of nucleation, crystal growth, and dissolution. In the present study, mathematical model is proposed which captures the contributions of each of these phenomena and their influence on the overall particle size distribution. The hysteresis experiments serve as a rigorous validation case of this mathematical model.

3.3. Model Equations

3.3.1. Population Balance Equation

Population Balance Models are usually employed for monitoring changes in the size distribution of large populations for example in cell growth, bubbles in reactors or as in the case considered in the present study, a population of crystals.

Typically, the number density function *f(X)* is used to represent the size distribution of a population of particles. The size distribution is relative to a particular size co-ordinate (length, volume) of the crystal which is relevant for the particular system in question. In the present study, the length will be considered as the size co-ordinate. Suppose the number density is represented as a function of the particle length co-ordinate *X* as *f(X)*. Then, *f(X)dX* is defined as the number of particles having a length between *X* and *X+dX*.

Suppose that *G* represents the growth rate or the shrink rate (in the case of dissolution) of the particle as a function of the particle length co-ordinate. This growth/shrinkage rate may be dependent or independent of the particle size apart from several other variables such as the solution temperature, the concentration etc. In general, *G(X)* thus stands for the rate of change in particle length per unit time. A detailed description of the growth rate used in this work will be presented later. The population balance equation which tracks the change/evolution of the particle number density function can be written as:

$$\frac{\partial f}{\partial t} + \frac{\partial Gf}{\partial X} = B_0\,\delta(X - X_{nuc}) \qquad 3.1$$

Where B_0 is nucleation rate (number/unit time) and X_{nuc} is initial size of nucleated particles.

In the present study, it should be noted that the only mechanism for the change in the number distribution functions are the growth/shrinkage of particles and the introduction of new particles through nucleation. Other mechanisms of change typically encountered are the breakage or the aggregation of particles which will be ignored in the present study for the purpose of retaining simplicity of the model. The model may be easily extended to include these if need arises. The introduction of new particles during crystallization occurs due to nucleation. Nucleation is assumed to introduce new particles at the particular nucleating size X_{nuc}. $\delta(X - X_{nuc})$ represents the Dirac delta function where:

$$\delta(X - X_{nuc}) = 0; \;\; X \neq X_{nuc} \qquad 3.2$$

$$\delta(X - X_{nuc}) = +\infty; \;\; X = X_{nuc} \qquad 3.3$$

Thus particles are introduced at a rate given by B_0 and at a location specified by X_{nuc}. The nucleation rate B_0 depends on several variables such as the system considered, the degree of supersaturation etc. A detailed description of the nucleation rate function employed in the present study will be given later. Another assumption made in the present study is that the size of the nucleating particle is the same which is assumed to be the minimum size considered in the present study. This may not necessarily be true considering the various mechanisms for the secondary nucleation.

Typically due to complicated mathematical expressions employed for representing growth and nucleation rates, it is not always possible to solve the equation analytically. Several numerical approaches are available to obtain the solution of the equation. A brief description of these methods, their strengths and their weaknesses are listed in Table 1.1. As can be seen from Table 1.1, each of the methods has their own pros and cons.

The aim of the present model was to extract the crystallization kinetics model (for crystal growth, nucleation and dissolution) from the hysteresis experiments. The hysteresis experiments consist of three stages:

1. Crystallization Stage 1 (crystallization while cooling the solution from an initial temperature of 323 K to 263 K)
2. Crystallization Stage 2: Only for the case of 0.7 K/min experiment (crystallization while heating the solution from 263 K to the equilibration point, around 275 K)

3. Dissolution Stage

Sometimes, like in the experiment with the 0.7 K/min cooling rate, the solution is still supersaturated (that is the dissolved solids' concentration is more than the solubility) even at 263 K. So, while heating the solution again, crystallization is still taking place as the solution is still supersaturated. As, we are heating the solution, the solubility increases with temperature. Moreover, the dissolved solids concentration decreases with increasing nucleation and growth. There comes a point, or temperature, where the dissolved solids concentration equals the solubility and the solution is no longer supersaturated. This is referred to here as the equilibration point. The crystallization is arrested at this point and further heating of the solution causes the dissolution process to initiate.

In the present study, the crystallization kinetics (growth and nucleation parameters) were determined by fitting the simulation results obtained by using the method of moments approach to the experimental results of Crystallization Stage 1 for different cooling/heating rates. The hysteresis results serve as the validation of the kinetics, as the dissolution of particles depends entirely on the particle size distribution that has arisen after the crystallization stages. Thus, having sufficient agreement with the hysteresis loop and successfully capturing the effect of the cooling/heating rate on the hysteresis loop serves as a thorough validation for the kinetics of crystallization. However, hysteresis results cannot be simulated using the method of moments approach due to obvious difficulty in describing the death rate of particles due to dissolution. It becomes important to resolve the complete particle size distribution. For the hysteresis results, the first and second crystallization stages were simulated using the HRFV method and the parameter values obtained by using the Method of Moments. The dissolution stage was then simulated using the moving pivot method. The hysteresis results were compared with experiments to obtain a validated crystallization kinetics model. This methodology can be extended in general to determine the crystallization kinetics for different systems. Given below is a detailed description of the various methods used for the solution of the population balance equation in the present study.

3.3.2. Method of Moments

3.3.2.1. Moment Equations

Instead of resolving the complete particle size distribution with time, the method of moments tracks the moments of the particle size distribution with time. The equation for a general k^{th} moment of a particle size distribution is presented as Equation 3.4.

$$M_k = \int_0^\infty X^k f(X) dX \qquad 3.4$$

It is possible to condense the population balance equation as a set of ordinary differential equations of the moments of the particle size distribution. The general form of the ordinary differential equations which track the change in an arbitrary k^{th} moment with time can be written as shown in Equation 3.5. For a detailed derivation of the moment equations kindly refer to Randolph et. al. (1988).

$$\frac{dM_k}{dt} = (0)^k B_0(t) + \int_0^\infty kX^{k-1} 2G(X) f(X) dX \qquad 3.5$$

An additional factor of 2 appears in the present equation as the growth rate considered in the present study is the growth rate of a surface. The growth rate of the particle dimension, like diameter, for spherical particles, will be twice the growth rate of the surface to account for growth at both sides. To model the present system we will consider only size independent growth. The rationale for this is presented in the later section which addresses the crystal growth constitutive law. It can be seen that the equation includes twice the growth rate. This is done as the growth rate here is considered as the rate of growth of a surface. The rate of growth in the particle diameter will thus be twice (on both sides) of this growth rate. Keeping these points in mind the equation for the rate of change of moments is presented as:

$$\frac{dM_k}{dt} = (0)^k B_0(t) + 2kG(t) M_{k-1} \qquad 3.6$$

Thus, theoretically, for the moment equations derived for the present case (growth and nucleation), it is possible to derive any number of moment equations. In the present study, we have restricted the model to calculation of the first 5 moments (k = 0 to 4) as these are the moments that will be required later. The rest may also be solved, but are not needed as the solution of higher order moment equations does not affect the lower order moment

equations. The governing equations for the first five moments are presented as Equations 3.7 to 3.11:

$$\frac{dM_0}{dt} = B_0(t) \quad 3.7$$

$$\frac{dM_1}{dt} = 2G(t)M_0 \quad 3.8$$

$$\frac{dM_2}{dt} = 4G(t)M_1 \quad 3.9$$

$$\frac{dM_3}{dt} = 6G(t)M_2 \quad 3.10$$

$$\frac{dM_4}{dt} = 8G(t)M_3 \quad 3.11$$

For the case of crystallization from a clear solution, the initial conditions of all moments will be zero. In general, if one wishes to simulate crystallization starting from a solution already containing a particle population, such as in the case of seeding, the initial conditions for the moments can be found by calculating the moments from the known particle size distribution of the population.

3.3.2.2. Equation for Concentration

The total mass of the solute in the system can be written as:

$$M_T = V_R C M_w + V_R \rho_p \frac{\pi}{6} \int_0^\infty X^3 f(X) dX \quad 3.12$$

The equation can be written in terms of the third moment of the population balance equation as:

$$M_T = V_R C M_w + V_R \rho_p \frac{\pi}{6} M_3 \quad 3.13$$

Now the total mass of the solute in the system will not change with time as we are not adding any mass into the system. Hence the rate of change of the total mass of the solute will be equal to zero. Hence differentiating the above equation with time, we obtain the equation for the rate of change of dissolved solute concentration with time as:

$$\frac{dC}{dt} = -\left(\frac{\rho_p}{M_w}\right)\left(\frac{\pi}{6}\right)\frac{dM_3}{dt} \quad 3.14$$

The concentration equation along with the moment equations derived earlier need to be solved simultaneously.

3.3.2.3. Equation for Temperature

While cooling the solution from 323 K to 263 K at a time, a fixed cooling rate (0.3, 0.5 and 0.7 K/min) is employed. The rate of temperature change of the solution is thus controlled. The equation for the rate of change of temperature with respect to time is thus trivial and can be written as:

$$\frac{dT}{dt} = \frac{R}{60} \qquad 3.15$$

Where *R* is heating rate in K/min. It is important to track the temperature accurately as temperature of the solution is the most important factor which influences the crystallization phenomenon. In the present case, the equation is trivial as the solution temperature is reliably controlled using the OptiMAX reactor setup and effects due to the heat of dissolution and crystallization may be ignored. However, in cases where this is not necessarily true, the heat balance must be appropriately handled to obtain the equation for the rate of change in temperature.

The solubility data reported by Granberg et. al. (1999) for the system of paracetamol and ethanol and within the range of temperatures considered in the present study, can be represented in the form of an exponential type expression as:

$$C^*(T) = 0.524\, e^{(0.0193T)} \qquad 3.16$$

The moment equations (Equations 3.7 to 3.11) are solved simultaneously along with the equation for concentration (Equation 14) and the equation for temperature (Equation 3.15) to find the solution of the population balance equation. A detailed account of the solution implementation is presented in the solution methodology section.

3.3.3. High Resolution Finite Volume

3.3.3.1. Equations for Discrete Particle Size Distribution

In some cases, it is desirable to obtain the information of the complete particle size distribution as a function of time. In such cases, it is not sufficient to solve the moment

equations. For instance, in few cases, such as for dissolution relevant for the present study, the shrinkage rate is dependent on the particle size, as discussed later. For obvious reasons, such a problem cannot be tackled by the method of moments. This particle size dependency significantly impacts the model predictions. Thus, to simulate for the entire hysteresis loop, we need to use a more descriptive model which resolves the entire particle size distribution. In the present case, we will solve the population balance equation for the case of crystallization using a high resolution finite volume (HRFV) scheme first proposed by Leveque (2002) and then implemented for the case of crystallization processes by Gunawan et. al. (2005). The HRFV scheme enables us to obtain the complete resolution of the particle size distribution.

In the High Resolution Finite Volume (HRFV) method, the particle size co-ordinate domain is broken into several discrete bins. Now the growth of the crystals causes the particles from a bin to grow into another bin. The nucleation of particles causes the addition of particles into the bin size corresponding to the nucleation size. Thus, in summary with this method, the changes in the number of particles which are present in each of these bins with time due to growth and nucleation during crystallization were tracked. This method leads to a discrete particle size distribution as opposed to a continuous particle size distribution, which is obtained when a solution to a population balance equation can be worked out analytically. The discrete particle size distribution can be written as a function of the continuous particle size distribution. The number of particles in each bin is defined in the HRFV scheme can be written as:

$$f_i = \int_{X_i-h/2}^{X_i+h/2} f dX \qquad 3.17$$

In the present study, we have considered that growth is size independent. The details of the mechanism of crystal growth and the constitutive law applied to quantify the growth rate are presented in the subsequent section. Using an explicit time stepping method and a high resolution finite volume algorithm that is second order almost everywhere, the equation for the number of particles in the i^{th} bin in the next time instant can be written as:

$$f_n^{m+1} = f_n^m - \frac{2kG}{h}(f_n^m - f_{n-1}^m) - \frac{kG}{h}\left(1 - \frac{2kG}{h}\right)[(f_{n+1}^m - f_n^m)\varphi_n - (f_n^m - f_{n-1}^m)\varphi_{n-1}] \qquad 3.18$$

Here, it should be noted that the growth rate is actually twice the growth rate of the surface and hence the factor of 2 is multiplied to every growth rate to obtain equations in the form of the crystal surface growth rate. The flux limiter function, ϕ_n, depends upon the local degree of smoothness of the distribution. This is quantified as a ratio of two consecutive gradients as:

$$\theta_n = \frac{f_n^m - f_{n-1}^m}{f_{n+1}^m - f_n^m} \qquad 3.19$$

It can be seen that θ_n will have a value close to one when the distribution is locally smooth. There have been several forms proposed for the choice of the flux limiter. The role of the flux limiter is to limit the error induced in the simulation results due to numerical dispersion. For a detailed discussion of the flux limiters please refer to the review on finite volume methods presented by Leveque (2002). In the present method, we use the Van Leer flux limiter which is known to provide a full second order accuracy and is total variation diminishing, which implies that the algorithm will not introduce numerical dispersion. The Van Leer flux limiter is written as:

$$\varphi_n = \frac{\theta_n + |\theta_n|}{1 + |\theta_n|} \qquad 3.20$$

While implementing this method, we should be careful in dealing with the boundary conditions. As stated earlier, the domain along the size co-ordinate is discretized into a finite number of bins. It can be inferred from the above equation, that there arises a problem when we try to formulate the equations for the number of particles in the next time instant in the boundary bins (first and last) as they require the specification of information outside the domain considered. Equations for these bins need to be separately specified. For the first bin, wherever information for a bin outside the domain is required, it is set to zero. Also, it is assumed that the nucleation of particles adds particles into the first bin. Thus, the equation for number of particles in the first bin for the next time instance may be written as:

$$f_1^{m+1} = f_1^m - \frac{2kG}{h} f_1^m - \frac{kG}{h}\left(1 - \frac{2kG}{h}\right)(f_2^m - f_1^m)\varphi_1 + kB_0 \qquad 3.21$$

$$\theta_1 = \frac{f_1^m}{f_2^m - f_1^m} \qquad 3.22$$

For the first bin, the flux limiter is defined just as everywhere else. For the last bin, a boundary condition known as the absorbing boundary condition is used where in the number of particles in the last bin will not change with time. In the present text, the upper bin boundary is taken to be much higher than the size range of interest. In such a case, the boundary condition at the upper boundary does not affect the solution. However, if the bin boundary is to be chosen near the size range of interest, more attention needs to be paid in formulating the required boundary condition. Typically for such cases, boundary conditions from a general class of boundary conditions, known as absorbing boundary conditions need to be implemented. These boundary conditions are typically used to study the reflection, transmission and dissipation nature of waves in various medium. Absorbing boundary conditions are in general mathematically extremely complex and as such beyond the scope of the present text. The equation for the last bin can be written as:

$$f_N^{m+1} = f_N^m \qquad 3.23$$

This completes the formulation of the equations for the number of particles in each bin. Now, for simulations of cases where the solution is initially completely clear, we run into a numerical difficulty in evaluating the ratio of the consecutive gradients as both have a value of zero. Hence, for this case, the ratio is set as one. This is keeping in line the physical meaning of ϑ_n which is relevant. This changes the scheme to a first order upwind scheme at these points. However, this does not affect the solution as much as this is only for cases where there are no particles in the bins and is only done to ensure numerical stability of the model. Thus, we may still claim the second order accuracy that is provided by the Van Leer flux limiter.

3.3.3.2. Equation for Concentration

The total mass of the solute in the system can be written as in Equation 3.12. The contribution of the population of crystals (total volume of crystals) was calculated by using the third moment of the number distribution function. Now, as we are considering discrete bins, the third moment can also be written as:

$$M_3 = \int_0^\infty x^3 f(x) dx = \sum_{i=1}^N X_i^3 f_i \qquad 3.24$$

This transforms the more general integral moment into the discrete form of the equation. Here, particles which are lesser than the minimum size of the domain (say 1 micron) will not

be considered. This is the size range where we are adding the nucleating particles. From simulations, it was observed, and even through some simple calculations, it may be verified, that the contribution of the nucleating particles towards the mass is smaller than the permissible error in the mass balance. Thus, the contribution of the nucleating particles towards mass will not be considered. As we are not adding any solute into the system, the total mass of the solute phase must be constant. Hence the rate of change of the solute mass must be zero. By substituting the third moment expression in the total solute mass equation, differentiating the total solute mass with time and rearranging the equation we obtain a rate change equation for the dissolved solute concentration as:

$$\frac{dC}{dt} = -\left(\frac{\rho_p}{M_w}\right)\left(\frac{\pi}{6}\right)\sum_{i=1}^{N} X_i^3 \frac{df_i}{dt} \qquad 3.25$$

It should be noted that since we are using a fixed grid method, the size of each grid will not change with time. This equation can be solved numerically by using an explicit scheme which we have also used to solve the population balance equation. More details of the discrete form of HRFV method are provided in Annexure A2.

The equation for the rate of change of the solution temperature is the same as the one employed for the method of moments (Equation 3.15). We however, will need a discrete form of Equation 3.15 in order to be able to solve this equation simultaneously with the other equations. The equation itself is fairly straightforward and the temperature can be represented by the analytical solution but, the present work focuses on laying a framework to model crystallization processes. The equation for change in temperature may in general be linked to the rate of crystallization process for which a simultaneous solution will become important. For these reasons, the equation for temperature will be solved within the framework presented simultaneously with the other equations required for the implementation of the HRFV scheme.

3.3.4. Moving Pivot Method

3.3.4.1. Equations for Moving Pivot Method

The dissolution stage is very important as it is directly influenced by the crystallization stage or rather the particle size distribution and the concentration that has emerged after the

crystallization stage has been completed. Hence, for the purposes of validation of the crystallization kinetics, it is best to also analyse and validate the dissolution curve. Now, we are faced with an obstacle when we try to simulate the dissolution of a particle population using the methods described above. During dissolution, the total number of particles in the system is reducing owing to some particles completely disappearing. To enable the use of the method of moments to simulate this case, an explicit definition of a death rate of particles or the rate of disappearance of particles is required. An explicit specification of this rate of disappearance is not possible. The dissolution rate depends upon the particle size, dissolved solids' concentration and the heating rate. As the dissolution rate is size dependent, this presents a limitation in using the method of moments. Also, if we were to use the high resolution finite volume scheme, again, we would need to explicitly specify the rate of disappearance and hence this method suffers the same limitations as the method of moments. For the high resolution scheme there have been various types of boundary condition which one may impose on the lower boundary of the domain which might simulate dissolution. This class of boundary conditions is referred to as the absorbing type of boundary conditions and are widely used to analyze wave mechanics. The implementation of these is not feasible owing to the mathematical complexity that is inherent in the formulation of the boundary condition equations and also lack of literature specific to dissolution.

Hence, in the present work, to simulate dissolution, we have used the moving pivot method. The moving pivot method is a class of discretization-based methods for the solution of the population balance equation presented by Kumar et. al. (1996). In this method, like in all discretization based methods, the domain of interest along the size co-ordinate is divided into various discrete bins. The difference between this method and the previous method is that, in this method, we will track the bin boundary and representative size locations along the size co-ordinate axis with time rather than tracking the change in the number of particles in each bin. Now, this approach is fundamentally different than the HRFV approach and by design removes any errors on account of numerical diffusion. For a detailed derivation of the model equations please refer to Kumar et. al. (1996). The equations for the bin boundaries may be written as:

$$\frac{dV_i}{dt} = -2S \text{ for } i = 1{:}\,N+1 \qquad 3.26$$

In the above equation, the rate of shrinkage of the bin boundary is twice the rate of shrinkage of the surface as the contribution from both sides due to the shrinkage of a sphere needs to be considered, similar to growth. Here V_i refers to the lower boundary of the i^{th} bin. As there are *N* bins, there will be *N+1* bin boundary locations. It is also important to track the representative bin size locations for the *N* bins. The equations for the representative size of the i^{th} bin may be written as:

$$\frac{dX_i}{dt} = -2S \text{ for } i = 1{:}N \qquad 3.27$$

As, the particles which are present in a bin will stay within that bin as the bin boundary locations will change with time, the rate of change of the number of particles in each bin can be equated to zero. The above equations were recast into an explicit form consistent with the form presented in the HRFV section. The discrete forms of Equations 3.26 and 3.27 are presented in the Annexure A2 as Equations A2.3 and A2.4. This completes the formulation of the moving pivot equations.

3.3.4.2. Equation for Concentration

The total mass of the solute in the system can be written as given in Equation 3.12. The discrete form for the third moment may be written as shown in Equation 3.24. This transforms the more general integral moment into the discrete form of the equation. Here, particles which are lesser than the minimum size of the domain (say 1 micron) will not be considered. The rate of change of dissolved solids concentration equation may be obtained from the mass balance equation for solute mass and by making similar assumptions as for the case of Equation 3.25. By substituting the expression for the third moment in the equation for total mass, differentiating the equation with respect to time and rearranging the equation, the equation for the rate of change of dissolved concentration was obtained as:

$$\frac{dC}{dt} = -\left(\frac{\rho_p}{M_w}\right)\left(\frac{\pi}{6}\right)\sum_{i=1}^{N} 3X_i^2 f_i \frac{dX_i}{dt} \qquad 3.28$$

It should be noted that since for dissolution, the moving pivot method was used. The number of particles in each bin will not change and only the change in the representative size of respective bins was tracked. Hence, differentiating a moment will only differentiate the size part of the expression. The equation is solved numerically using an explicit fixed time step

method. A discrete equation for the dissolved solute concentration was formulated consistent with the HRFV scheme framework and is presented in the Annexure A2 as Equation A2.5. The concentration is evaluated at each time step evaluating the above equation simultaneously along with the discretized equations for representative size.

The equation for the rate of change of the solution temperature is the same as the one employed for the method of moments and can be written as Equation 3.15.

3.3.5. Constitutive Laws

3.3.5.1. Equation for Crystal Growth

Crystal growth is typically modelled as a two-step process. In the first step, the solute molecules are moved to near the crystal surface by convection and diffusion. In the second step, the molecules near the crystal surface attach to the crystal lattice and cause the 'growth' of the crystal. The first step is thus the mass transfer step and the second step is the surface integration step (Karpinski, 1985). In the present study, it was assumed that the crystal growth is limited by the surface integration step and the mass transfer step is sufficiently faster in comparison. This assumption has also been made previously by Worlitschek et. al. (2004). The surface integration step can be related to the degree of supersaturation in the form of a reaction rate type of expression to obtain the growth of the crystal surface as:

$$G = k_{r0}\exp\left(-\frac{E_A}{RT}\right)(C - C^*(T))^g \qquad 3.29$$

The value of the activation energy for the growth rate expression is known to lie in range of 4 x 10^7 to 8 x 10^7 J/kmol-K. The value obtained by Worlitschek et. al. (2004) was found to be 4.16 x 10^7 J/kmol-K which lies within the reported range of values. The value of the growth rate exponent, g, is reported to be approximately equal to 2 (Karpinski, 1985). The value obtained by Worlitschek et. al. (2004) was found to be 1.9 which is in close agreement to the previously reported value for the growth rate exponent. Nothing was previously reported with regards to the pre-exponential constant, k_{r0}. The value of the constant obtained by Worlitschek et. al. (2004) for this parameter was 21. In the present study, the growth kinetic parameters were not determined, but rather the values determined by Worlitschek et. al. (2004) were used and the focus was on finding the nucleation kinetics parameters, the values for which are largely unknown in published literature.

3.3.5.2. Equation for Nucleation

For an unseeded crystallization, as is considered in the present study, the onset of crystallization is caused by homogeneous primary nucleation. Primary nucleation is the nucleation where the solute molecules in a supersaturated solution within themselves aggregate to form nuclei. By unseeded it is implied that no external seeds or crystals were added to induce nucleation. Now as the crystals in the solution grow in number and size, secondary nucleation starts to gain importance. Secondary nucleation is the generation of nuclei which may be attributed to the breakage by some mechanism of already existing crystals (Davey, 2001; Myerson, 2002; Mersmann, 1995). Typically, after this regime sets in, that is the number of crystals in the solution becomes sizeable, secondary nucleation is the dominant mechanism for nucleation. The primary nucleation rate can be represented by a simple power law relation as (Davey, 2001; Myerson, 2002):

$$B_{0,pri} = k_1(\Delta C)^{n_1} \qquad 3.30$$

There are several relations to model secondary nucleation. The different rate laws used to model the secondary nucleation rate are listed in Table 1.2. The first law listed in this table was found to be extremely sensitive and not reliable. The second relation is too simplistic as it is known that the rate of secondary nucleation is dependent loosely speaking on the number of crystals present in the solution owing to the mechanism proposed for the secondary nucleation. In the present study, it is hypothized that the nucleation occurs due to some small particles chipping off from the surface of bigger crystals. The smaller particles which get chipped off then become the new crystals. The rate of nucleation thus seems to be directly proportional to the total surface area of the crystals in the solution as opposed to the total number of crystals. The influence of the impeller speed and the agitation rate on the nucleation rate is beyond the scope of the present text and hence will not be considered in the nucleation rate expression. Based on these considerations, a nucleation rate expression similar to the 4th nucleation rate expression were adopted in the present study, (as listed in Table 1.2) with the change that the nucleation rate is proportional to the total surface area (proportional to the second moment of the number size distribution) rather than the suspension density. Thus, the secondary nucleation rate used in the present study is written as:

$$B_{0,sec} = k_2 M_2 (\Delta C)^{n_2} \quad 3.31$$

As in the present text, it was hypothized that the secondary nucleation rate is proportional to the total particle surface area, an increase in the total area will cause a proportional increase in the secondary nucleation rate. Hence the exponent for this term is kept as 1.

The total nucleation rate is thus a sum of the contribuions due to primary and secondary nucleation and can be represented as:

$$B_0 = B_{0,pri} + B_{0,sec} \quad 3.32$$

The nucleation rate is evaluated at each time instant and the number generated is added into the bin with the minimum size.

3.3.5.3. Equation for Dissolution

The dissolution rate of the particles is a strictly mass transfer problem. The solution is undersaturated and the rate of shrinkage of the particles can be determined according to the rate of mass transfer from the solid phase into the solution phase. Paramount in accurately calculating the rate of dissolution is to have reliable estimates for the coefficient of mass transfer. The procedure to calculate the mass transfer coefficient used in the present study, is the one presented by Worlitschek et. al (2004) and also presented by Mersmann (2000) and is presented in the Annexure A2.

Once the mass transfer is known the rate of shrinkage of the particles can be written as:

$$S = k_d \frac{M_w}{\rho_p} (C^*(T) - C) \quad 3.33$$

It is worthwhile to note that the dissolution rate comes into play only when the solution is undersaturated. In cases when the solution is supersaturated, crystal growth and nucleation will occur and the shrinkage rate should be assigned a value zero.

3.3.6. Solution Methodology

3.3.6.1. Method of Moments

The method of moment's equations presents an initial value ordinary differential equation problem. The moment equations were solved for the crystallization stage 1 that is when the

solution was cooled from the initial temperature of 323 K to 263 K. at 323 K the solution was undersaturated. Experimental observations indicate that the nucleation/crystallization does not begin immediately but after a particular time which is related to the metastable zone width for that cooling rate. In the present study, the onset of nucleation was not modelled. The model presented is for the case where crystallization has initiated. Thus, the initial temperatures used in the present model for the different cooling rates are the corresponding temperatures when the nucleation was first detected by the FBRM probe. When the solution is completely clear, a small number of particle counts are measured by the FBRM probe which keeps fluctuating in a narrow band (say 10 to 20). This is referred to as the baseline zero counts. The temperature at which the onset of nucleation occurs is defined in the present study as the temperature when the counts measured by the FBRM probe deviates out of this narrow band which corresponds to zero counts. The limits for this narrow band are calibrated over a substantial period of samples when the temperature is decreasing from 323 K to the crystallization point. The initial conditions for the moments can be evaluated if the particle size distribution in the solution is known beforehand. The moments then simply become the moments of this particle size distribution. Corresponding to the initial conditions of the experiments of a clear undersaturated solution, the initial value for all the moments was taken to be zero. The initial conditions used for the present study are shown in Table 3.1. The equation for the dependence of solubility on the temperature used in the present study is given as Equation 3.16.

Table 3.1: Initial Conditions used for simulations using the method of moment's solver (*Based on experimental observation of nucleation at different cooling rates)

Parameter	Description	Value	Unit
M_0, M_1, M_2, M_3, M_4	First 5 moments	0 (For a clear solution)	-
C	Dissolved Solids Concentration	1.5	mol/L or kmol/m^3
T_{nuc} (0.3 K/min)	Crystallization temperature for 0.3 K/min rate	295*	K
T_{nuc} (0.5 K/min)	Crystallization temperature for 0.5 K/min rate	289*	K
T_{nuc} (0.7 K/min)	Crystallization temperature for 0.7 K/min rate	286*	K

The system of ordinary differential equations was solved using ODE15s which is a standard MATLAB solver for a system of stiff equations. It is a variable order solver based on numerical differentiation formulas.

3.3.6.2. High Resolution Finite Volume Method

From experiments it was observed that while cooling the solution from 323 K to 263 K at the specified cooling rate, crystallization takes place. Now, after reaching 263 K, the solution was immediately heated up at a heating rate equal in magnitude to the cooling rate. It was observed, especially for the experiment employing a 0.7 K/min rate that crystallization takes place for some time in the heating stage too. This is because the crystallization is not fast enough for the solution to equilibrate within the time it takes it to reach 263 K. This crystallization occurring in the heating stage shall be referred as Crystallization Stage 2 in the present work and the one occurring during the cooling stage as Crystallization Stage 1. As one increases the temperature of the solution, the solubility starts increasing. In Crystallization Stage 2, as we heat the solution, the dissolved solids concentration starts decreasing (due to continual crystallization) and the solubility starts increasing as opposed to both of them decreasing in Crystallization Stage 1. The crystallization is arrested when both the aforementioned quantities become equal. The HRFV scheme was used to simulate the crystallization occurring in both crystallization stages.

For the simulation of the first stage of crystallization, the initial conditions used for the method of moment's simulations were used as the state is the same. The equation for the dependence of solubility on the temperature used in the present study is given as Equation 3.16. Experimentally it was observed that the maximum particle size was definitely less than 300 micron with an average particle diameter ranging between 30 to 40 microns. For these reasons, the maximum size for the considered domain was chosen to be 1000 micron. The minimum size which can be recorded by the FBRM is 1 micron. Thus it is useless to use a size less than this observable size. Thus the minimum size of the domain is 1 micron. A uniform grid spacing of 1 micron was used to discretize the size domain and a time step of 0.1s was used. It was shown previously that at these values the solution is independent of the grid size and the time step. The number of particles in each of the 1000 bins obtained was selected to

be uniformly zero as initially there is a clear solution. In case a particle population already exists, this initial condition should be modified suitably.

Experimentally, the crystallization stage 2 immediately follows crystallization stage 1. Hence, the discrete particle size distribution obtained after the completion of the first stage was given as input for the initial condition of the second stage. The other simulation parameters (minimum size, maximum size, grid spacing, time step etc.) are the same as for crystallization stage one except that the rate of temperature change is now positive to simulate heating. The crystallization occurring during stage 2 is arrested when the dissolved solution concentration becomes equal to the solubility at that particular temperature. The solver was terminated when such a criteria was met.

3.3.6.3. Moving Pivot Method

The moving pivot method is used for the dissolution stage of the experiment that is from the equilibration point till the solution is heated to 323 K. Complete dissolution can be inferred from the FBRM counts data when there is no further change in the counts with increasing temperature. Also, the counts, at this point, can be seen to lie within a range where a baseline zero count is typically recorded (10 to 20 counts). The counts then after this point, keep fluctuating in the narrow baseline zero count range meaning a completely clear solution.

The minimum size recorded by the FBRM is 1 micron. Below this size, the particles are practically invisible. In the present study, the contribution of particles crossing this size (having size less than 1 micron) was neglected. This assumption is reasonable as the mass contribution and the contribution towards the total particle surface area by particles below the 1 micron size is negligible. It was verified through simulations that neglecting the contribution of the particle below 1 micron does not affect simulation results. Physically, when particles go to extremely small sizes, the rate of disappearance is extremely high. At extremely small sizes, it is known that the size dependency of the solubility becomes important. Solubility increases, exponentially so, with decreasing size. So, even in a diffusion limited mass transfer regime (which is observed for small sizes), smaller particles will have faster dissolution rates owing to the increased under saturation driving force and a larger surface area to volume ratio. Moreover, the contribution of the particles in this size range towards the total mass of the system is negligible and as such can be ignored.

While simulating using the moving pivot method, a collection of particles (in a particular bin/size range), is assumed to have a size denoted by a so-called representative size. So, when the representative size of a bin goes below the 1 micron threshold size, in the present study, the entire collection of particles in that bin is assumed to have dissolved. In reality, this will be a continuous process with smaller particles disappearing first and then the larger particles. However, in the present case, all the particles represented by a particular size will disappear as soon as the size falls below the threshold size of 1 micron. As a consequence of this, if one plots the total number of particles in a system (the 0^{th} moment) with time (or temperature), one would observe that the curve is made of a series of decreasing steps. The steps correspond to locations where the bin size goes below the 1 micron size. Although this effect is not desirable, it is still a valid solution of the population balance equation for the dissolution case. This is because the contribution at that size towards the total mass, regardless of the number of particles in the bin, is negligible, that is the total mass of the system before and after the step does not exceed the permitted error margin. This was ensured by verifying that no mass balance error is introduced during the dissolution stage. Also, simulations were performed by changing various parameters: the threshold size of 1 micron to a size below 1 micron, the number of grid points as well as by allowing for contribution of particles below the threshold size. It was found that there was no impact on the simulation results by making the aforementioned changes. This implies that the contribution of the particles below the 1 micron size was negligible and the procedure adopted in the present study is reasonable. For a finer grid, these steps become less and less separated and a nearly continuous total number of particles versus time curve may be obtained.

As this stage is implemented after the second stage of crystallization, the initial conditions of this stage are equal to the final conditions obtained after the simulation of the second stage. The equation for the dependence of solubility on the temperature used in the present study is given as Equation 3.16. The only solver parameter required for this method is the time step. The time step of 0.1s is used which is the same as used in the previous methods. Simulations were carried out until the solution temperature reached 323 K. No other solver parameters need to be specified.

The results are discussed in the following section.

3.4. Results & Discussion

The aim of the present study was to determine the kinetics of crystal growth and nucleation for a system of paracetamol and ethanol. To do this, experiments were conducted by cooling a solution at different cooling rates starting from an undersaturated point (at 323 K) to until the solution temperature reaches 263 K. The concentration of paracetamol in ethanol is such that the solution becomes saturated at 45^0C. During this stage, crystallization occurs. The nucleation is initiated at a temperature below 318 K depending upon the cooling rate and the corresponding metastable zone width. The prediction of the onset of nucleation is beyond the scope of the present text. The experimentally observed values of nucleation temperature were used instead. Simulations were thus started from corresponding values of nucleation temperature depending upon the cooling/heating rate employed for experimentation. The list of unknown parameters and their expected range of values (available from literature) is given in Table 3.2.

Table 3.2: List of parameters required for model along with range for the values reported in literature

Parameter	Physical Significance	Expected Value
k_{g0}	Pre-exponential constant for growth	Not known
E_A	Activation energy for growth law	[4e7 – 8e7][20]
g	Growth law exponent	[1.6 – 2.5] [19]
k_1	Pre-exponential constant for primary nucleation	Not known
n_1	Primary nucleation rate exponent	[1 – 3][20]
k_2/k_1	Ratio between the secondary and primary nucleation rates' pre-exponential constant	Not known
n_2	Secondary nucleation rate exponent	Not known

A similar study to estimate the growth and nucleation kinetics was done by Worlitschek et. al. (2004). The authors had presented a methodology to determine the crystallization and nucleation kinetics for a system of paracetamol and ethanol. The rate expression for the crystal growth presented in that study is the same that is used in the present study. However, in that study, they had not considered unseeded crystallization and hence had not included the primary nucleation rate expression. Also, as mentioned before, the rate expression for the secondary nucleation rate uses parameter values which seem very unphysical. For instance, the value for the nucleation parameter, probability of nucleation, in the first expression given in Table 1.2, was found to be 7 x 10^{-20}. Further, it was found that the

simulation results were extremely sensitive to this parameter value. Hence, in the present study, the parameters for growth determined by Worlitschek et. al. (2004) were used and the primary and secondary nucleation rate parameters were estimated by fitting model results to experimental results. The parameter values for growth presented by them which will be used in the present study are given in Table 3.3.

Table 3.3: List of parameter values for growth kinetics presented by Worlitschek et. al. (2004)[6]

Parameter	Physical Significance	Expected Value
k_{g0}	Pre-exponential constant for growth	21
E_A	Activation energy for growth law	4.16e7
g	Growth law exponent	1.9

The values for the parameters (primary and secondary nucleation rate), were obtained by fitting the model predictions, obtained using the method of moments, to the experimentally obtained values for one cooling rate (0.7 K/min), for crystallization stage 1 (cooling from 323 K to 263 K). Then simulations for the crystallization stage 1 were performed for the other cooling rates (0.3 K/min and 0.5 K/min) using the parameter values obtained and compared to the respective experimentally obtained results. After sufficient agreement with experimental results is established, simulations for crystallization stage 1 were performed using the High Resolution Finite Volume (HRFV) scheme. The simulation results from the HRFV scheme were validated against the simulation results obtained from the method of moments. As both the methods are solving the same population balance equation, there should be an exact match between the results obtained from both of these methods. After confirming this agreement, simulations for the entire hysteresis experiment were performed for 0.3, 0.5 and 0.7 K/min heating/cooling rates. The simulation results were compared with the experimentally obtained hysteresis experiment results.

3.4.1. Estimating unknown parameter values

The first step towards fitting the model results to the experimental results is always to determine which parameters are the most sensitive in the system. The parameters for which the values are not known can be listed as:

1. Primary Nucleation Rate constant (k_{Pri})
2. Primary Nucleation Rate exponent (n_{Pri})

3. Secondary Nucleation Rate constant (k_{Sec})
4. Secondary Nucleation Rate exponent (n_{Sec})

First, particular range of base case parameter values were identified by comparing the model predictions with the experimentally obtained results for crystallization stage 1 for a cooling rate of 0.7 K/min. The base case parameters were obtained through trial and error and are only representative parameters to help carry out assessment of sensitivity of parameters. They provide a rough agreement with experimental results and also identify the approximate orders of the more realistic values. The base case parameters obtained in the present case are listed in Table 3.4.

Table 3.4: List of base case parameters used for simulations

Parameter	Values
k_{g0}	21
E_A	4.16e7
g	1.9
k_1	1.5e5
n_1	2
k_2/k_1	50
n_2	4.5

The sensitivity analysis was done by varying each of the unknown parameter values by around 100% and decreasing by around 50% and comparing the model predictions of the three (base case, 100 % increase, and 50% decrease). The normalized 0^{th} moments obtained from the simulation results using different parameter values were compared. This normalized 0^{th} moment was chosen for comparison as described later, the normalized simulation results were compared to the normalized FBRM particle counts data. The normalization was done by dividing the 0^{th} moment everywhere with the corresponding 0^{th} moment's obtained at 263 K. The results for the sensitivity analysis are shown in Figure 3.4.

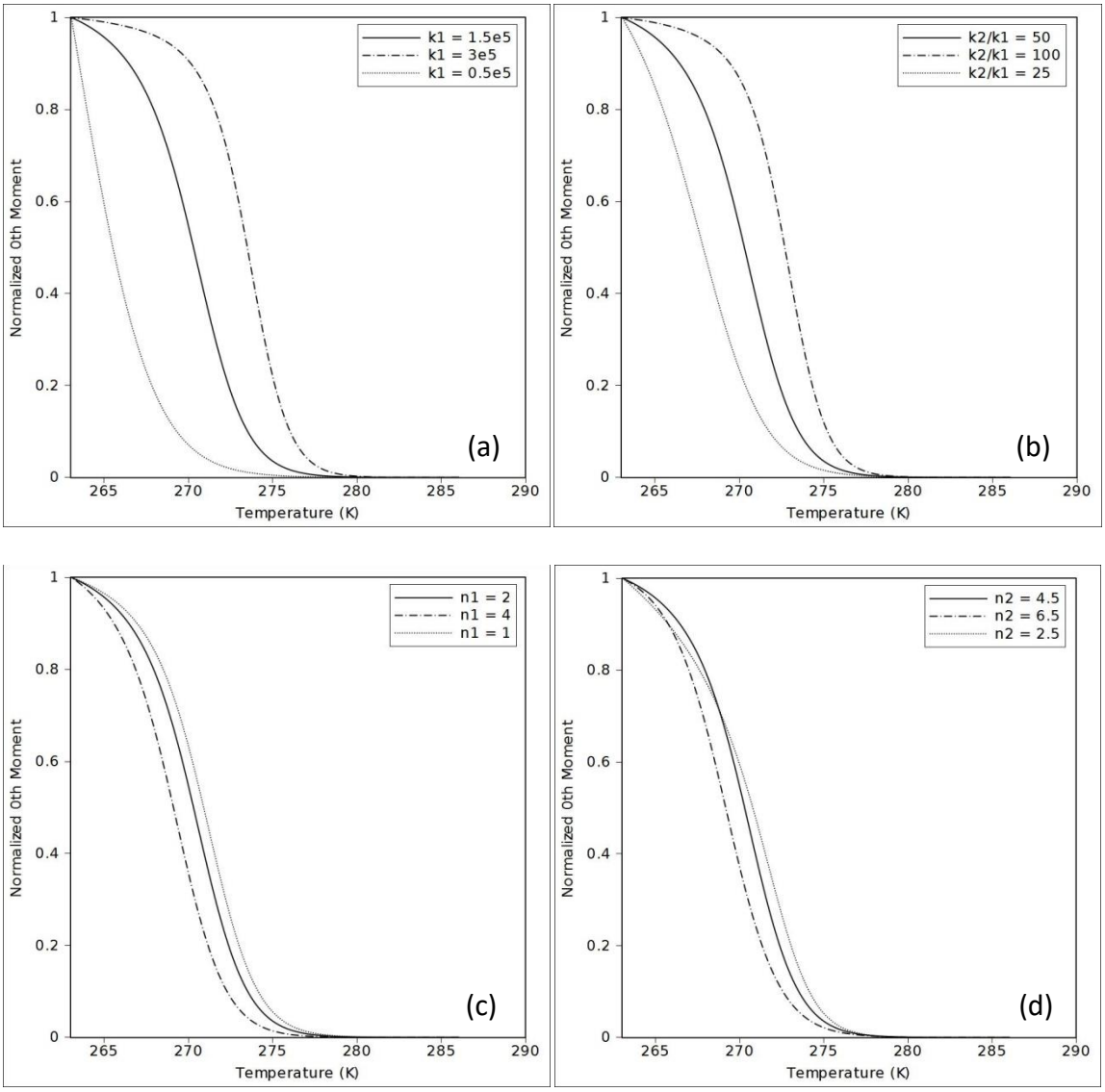

Figure 3.4: Sensitivity analysis results for (a) Pre-exponential constant of primary nucleation rate expression (b) Ratio of pre-exponential constants for secondary and primary nucleation rate expressions (c) Primary nucleation rate exponent (d) Secondary nucleation rate exponent

As can be seen from the results shown in Figure 3.4, the model predictions are most sensitive to the pre-exponential constants for primary and the ratio between the constants for secondary and primary nucleation (Figures 4a and 4b). The model predictions are not as sensitive to the exponents (Figures 4c and 4d). Hence, a representative value of 2 was chosen for the primary nucleation rate exponent corresponding to the range specified in the literature. Values for the exponent of supersaturation in the secondary nucleation rate have been reported previously, however, the nucleation rate expression adopted and the flow configuration were substantially different. For instance, the value for the exponent, for the case of a fluidized bed was reported to be 3.3 (Mersmann, 1995). Apart from this, not much

has been reported with regards to the expected range of values for this parameter. In the present study, a representative value of 4.5 was chosen for the secondary nucleation rate exponent. Although this assumption has no basis, it was shown that the model is not as sensitive to this value within the range that the sensitivity was investigated (Figure 3.4d). Also, the range of values chosen for measuring sensitivity is inclusive of the single reported value for this parameter. Now, it can be seen that as both the parameter values (the ratio and the primary nucleation rate constant) were increased, the normalized counts curve versus the temperature became steeper with the nucleation happening faster and the curve reaching a 'plateau' earlier. Correspondingly, as these parameter values were decreased, the curve became less steep with the nucleation proceeding slower as compared to the base case. Thus, it may be inferred that both the parameters have the same influence on the model predictions.

One set of parameter values (nucleation and growth parameters) is required for the complete simulation of the hysteresis loop. From the previous analysis, it can be argued that it may be possible that multiple such sets may exist, where simulations using any of the multiple parameter sets would show sufficient agreement with experimental results. Starting from the base case parameter values, these values may be obtained by increasing one parameter and decreasing the other parameter sufficiently such that there is agreement between the model predictions and experimental results. Indeed such a case is observed as shown in Figures 5. In, Figure 3.5, three pairs of parameter values, for the parameters of primary rate constant, ratio, were compared against the experimentally obtained results for the cooling/heating rate of 0.7 K/min. The comparison was made between the normalized FBRM particle counts data and the normalized 0^{th} moment data obtained through simulations. As described previously, the simulated normalized 0^{th} moment at a particular temperature was obtained by dividing the 0^{th} moment from simulations at that particular temperature by the 0^{th} moment from simulations at 263 K. Analogous to this definition, the normalized count data at a particular temperature was obtained by dividing the particle counts measured by the FBRM at that particular temperature by the particle counts recorded by the FBRM at 263K, which is also the minimum temperature considered in the experiment. The simulation results were compared with the experimental results by comparing the simulated normalized 0^{th} moment against the experimentally obtained, normalized FBRM particle counts data.

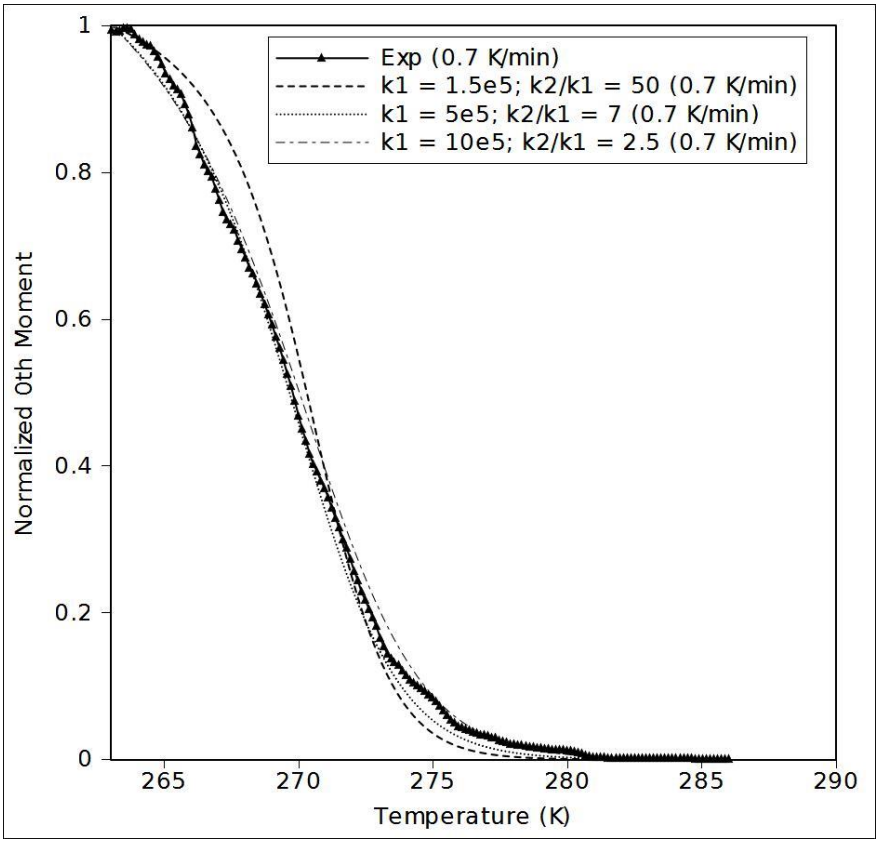

Figure 3.5: Comparison between the normalized 0th moment versus temperature curve obtained from simulation results using three sets of parameter values and experimental results for the 0.7 K/min cooling/heating rate experiment for the crystallization stage 1

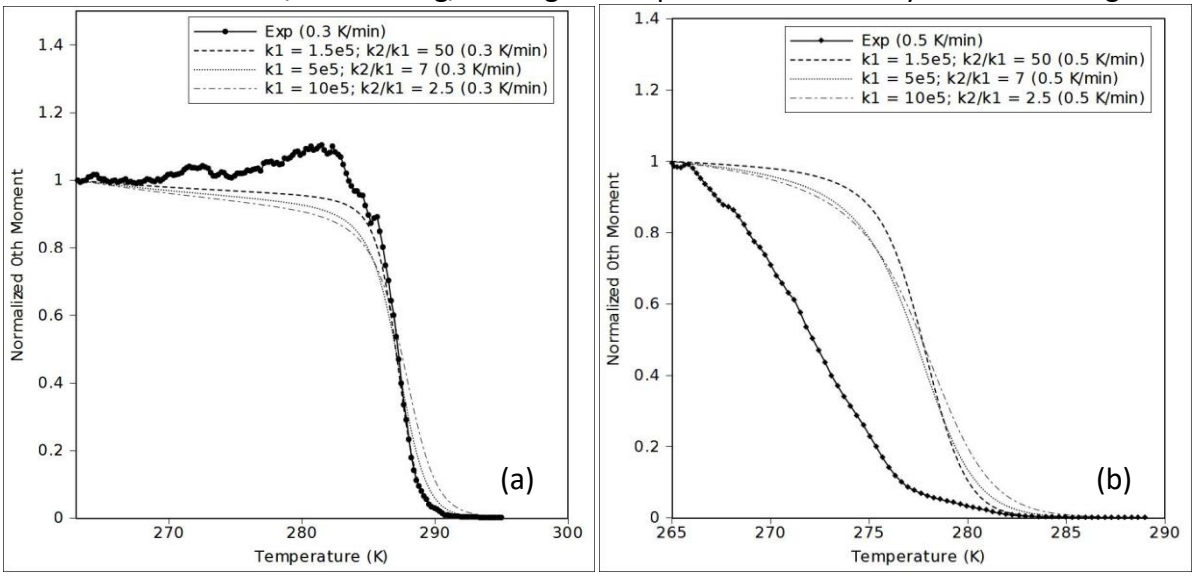

Figure 3.6: Comparison between the normalized 0th moment versus temperature curve obtained from simulation results using three sets of parameter values and experimental results for the for the crystallization stage 1using a cooling/heating rate of (a) 0.3 K/min (b) 0.5 K/min

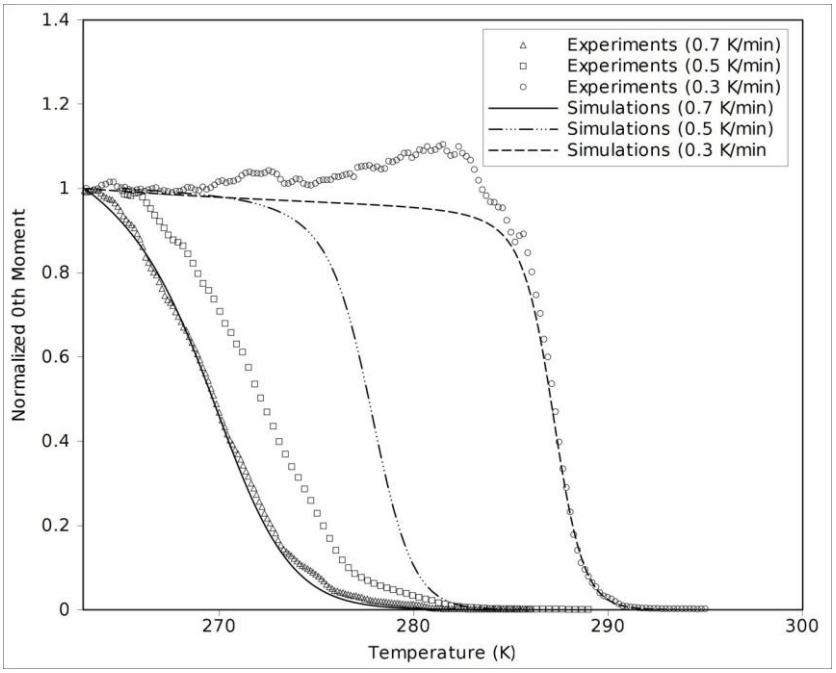

Figure 3.7: Comparison between simulation results and experimental results of the normalized 0^{th} moment for crystallization stage 1 using finalized parameter values

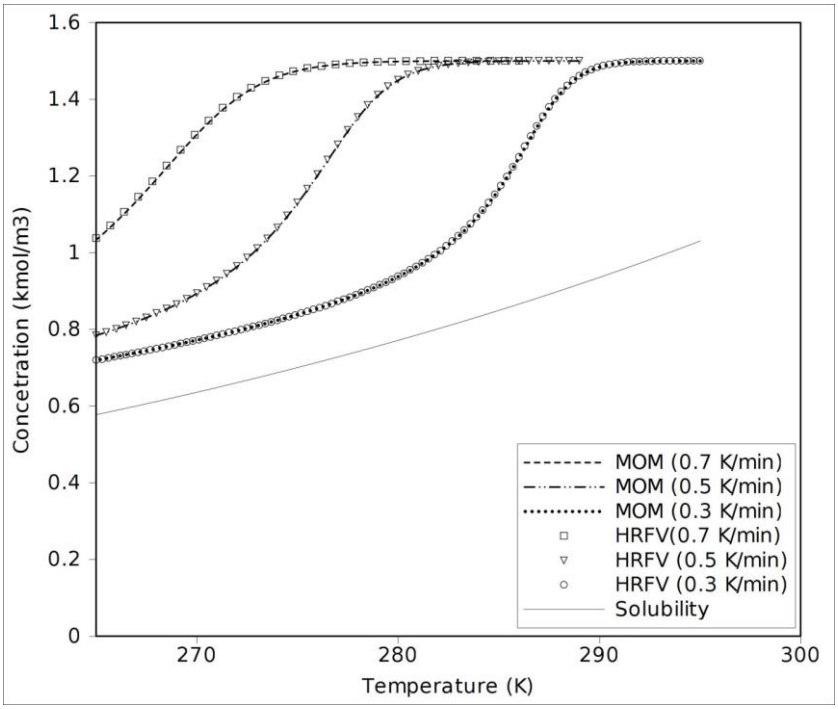

Figure 3.8: Comparison between simulation results for crystallization stage 1 dissolved solids concentration for the cooling rates of 0.3, 0.5 and 0.7 K/min done by using the method of moments (MOM) and the high resolution finite volume (HRFV) scheme

The contribution of the primary nucleation may be assessed by considering on the first part of the curve (between a temperature range of say 286 K and the crystallization temperature, 275 K) where primary nucleation is expected to be the dominant mode of nucleation. It may

be inferred from the parameter values and also the simulation results that as we increase the primary nucleation rate constant (k_1 from 1.5 x 10^5 to 1 x 10^6) and decrease the ratio (k_2/k_1 from 50 to 2.5) to compensate for that, the contribution of the primary nucleation increases and the shape of the normalized 0^{th} moment curve changes. The parameter values need to be adjusted such that the shape of the experimentally obtained normalized 0^{th} moment curve is accurately captured. The presented three sets of parameters can be seen as the limiting sets of parameter values as increasing the primary nucleation to a value more than 1 x 10^6 or decreasing it further than 1.5 x 10^5 will cause the shape of the normalized 0^{th} moment curve to go out the bounds set by the simulation results using these parameters.

The simulation results using these three sets of parameter values were compared against the corresponding experimental results for the other cooling rates of 0.3 and 0.5 K/min as shown in Figure 3.6. From Figures 5 & 6, it can be seen that all the simulation results from the three sets of parameter values show reasonably good agreement with experimental results for the heating/cooling rates of 0.3 and 0.7 K/min. However, model predictions show relatively larger difference with the experimental data for the 0.5 K/min cooling rate. Plausible reasons for this peculiar observation are not clear at this point of time and will require further investigation. Based on the results obtained for the 0.3 and 0.7 K/min experiments, it can be said that the simulation results using the three sets of parameters form the bounds for adequate agreement with experimental results as discussed earlier. For the present study, the second parameter set (k_1 = 5 x 10^5; k_2/k_1 = 7) will be used for further simulation. A comparison between the normalized 0^{th} moment versus temperature curves obtained from experiments and from simulations using the aforementioned parameter values for all three cooling rates were are shown in Figure 3.7. The plot showing the comparison between the dissolved solids concentration versus temperature curve obtained from simulations for different heating rates and the solubility curve is given in Figure 3.8. It was found that the error in the total mass accumulated with time and was below 1% at the end of the simulation for all cooling rates.

3.4.2. Hysteresis Simulations

For simulating the hysteresis results, the crystallization stages of the population balance equation need to be solved using the HRFV scheme. First, the HRFV scheme needs to be verified for numerical accuracy by comparing the simulation results against the results obtained from the method of moments. Simulations were done using the finalized parameter values using both the method of moments and the HRFV scheme for crystallization stage 1. A comparison between the dissolved solids concentration and the normalized 0^{th} moment versus temperature curves for different cooling rates using both the methods are shown in Figures 8 and 9. The initial conditions used in the solution of the population balance equation are the same as those used for the method of moments and are presented in Table 3.1.

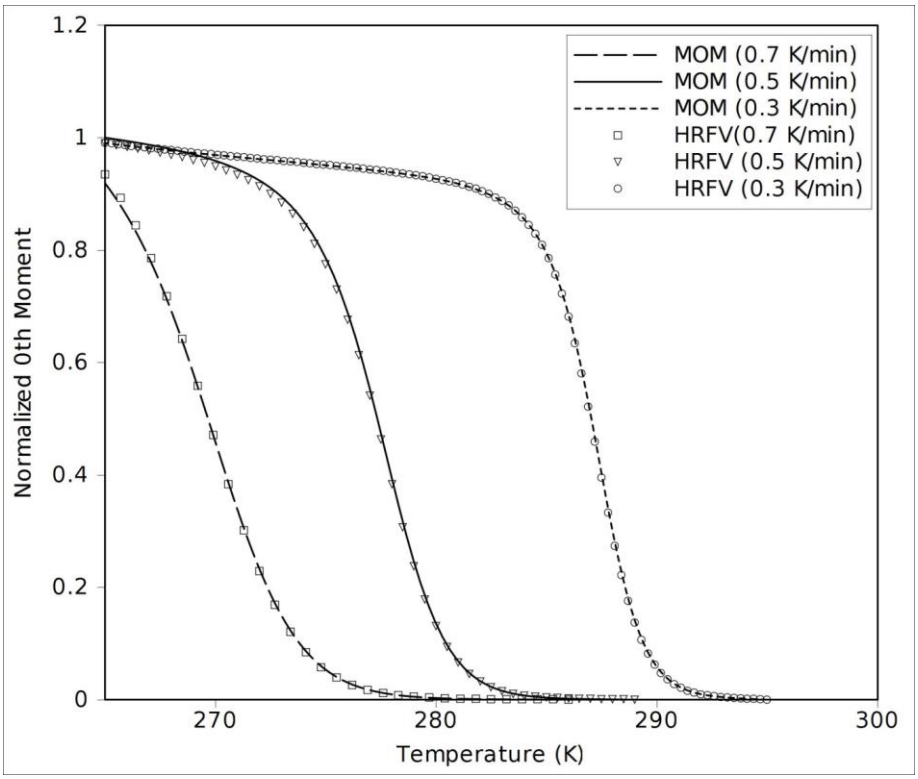

Figure 3.9: Comparison between simulation results for crystallization stage 1 of the normalized 0^{th} moment for the cooling rates of 0.3, 0.5 and 0.7 K/min done by using the method of moments (MOM) and the high resolution finite volume (HRFV) scheme

It can be seen from Figures 8 and 9 that there is an exact agreement between the simulation results obtained using the method of moments and the high resolution finite volume schemes. This is expected as both these methods are means to solve the same population balance equation using the same parameter values. This confirms that the implementation of the high resolution finite volume scheme is accurate.

As mentioned previously, the hysteresis experiment can be considered to consist of three parts:

1. Crystallization stage one (where the solution is cooled from 323 K to 263 K using a specified cooling rate)
2. Crystallization stage two (where the solution is heated from 263 K to the equilibration point where crystallization is arrested using a heating rate equal in magnitude to the cooling rate)
3. Dissolution stage (the solution is heated from the equilibration point back to 323 K)

As explained in the model development section, the first two parts, crystallization stage 1 and 2 were simulated using the HRFV scheme and the dissolution stage was simulated using the moving pivot methods. Experimentally, these stages are performed successively without any gaps. This was recreated virtually by setting the initial condition for the simulations of the next stage equal to the final condition of the simulations of the latest completed stage. The normalized 0^{th} moments obtained from such simulations of the hysteresis for different cooling/heating rates were compared with the corresponding experimentally obtained normalized 0^{th} moment (or total number) versus the temperature. The comparison between experimental and simulation results for the cooling/heating rates of 0.7, 0.5 and 0.3 K/min are given in Figures 10, 11 and 12 respectively. The care was taken to ensure that numerical errors (HRFV implementation) are insignificant and solutions are valid.

The hysteresis curve is a stringent validation case for the crystallization and growth kinetics as well as overall mathematical model. The shape of the dissolution curve is dependent on the particle size distribution that arises at the initiation of the dissolution stage. This particle size distribution is in turn dependent on the growth and nucleation kinetics. Thus, if there is sufficient comparison between the simulated and experimental results for the hysteresis curve, it is reasonable to say that the model is accurate in describing the growth and nucleation kinetics and the related kinetic parameters obtained are realistic.

For comparison, the simulated hysteresis curve was normalized by the procedure used in the method of moments' case, and the normalized curve was compared with the normalized FBRM particle counts data for the entire course of the hysteresis. The FBRM counts data was also normalized by the procedure described in the previous sections. For the case of 0.5 K/min

cooling/heating rate, it was already known that there is insufficient comparison between experimental and simulated results during the crystallization stage 1 for the choice of parameters finalized (Figure 3.7). However, it can be seen that the comparison of the hysteresis curve, as shown in Figure 3.11 is still reasonable. This suggests that even though the crystallization stage 1 was not accurately predicted, the simulation results are still very close to the realistic values. As can be seen from the above figures, there is an excellent comparison for heating/cooling rates of 0.3 and 0.7 K/min shown in Figures 12 and 10 respectively. This implies that for these two cases, the model accurately represents the realistic scenario.

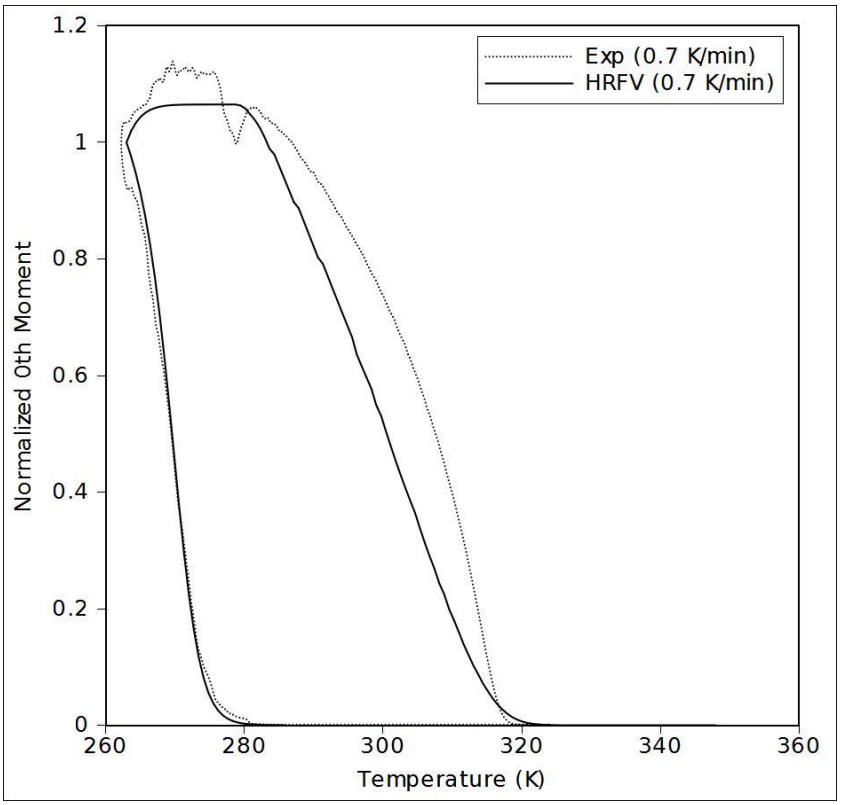

Figure 3.10: Comparison between hysteresis simulation and experimental results for a heating/cooling rate of 0.7 K/min

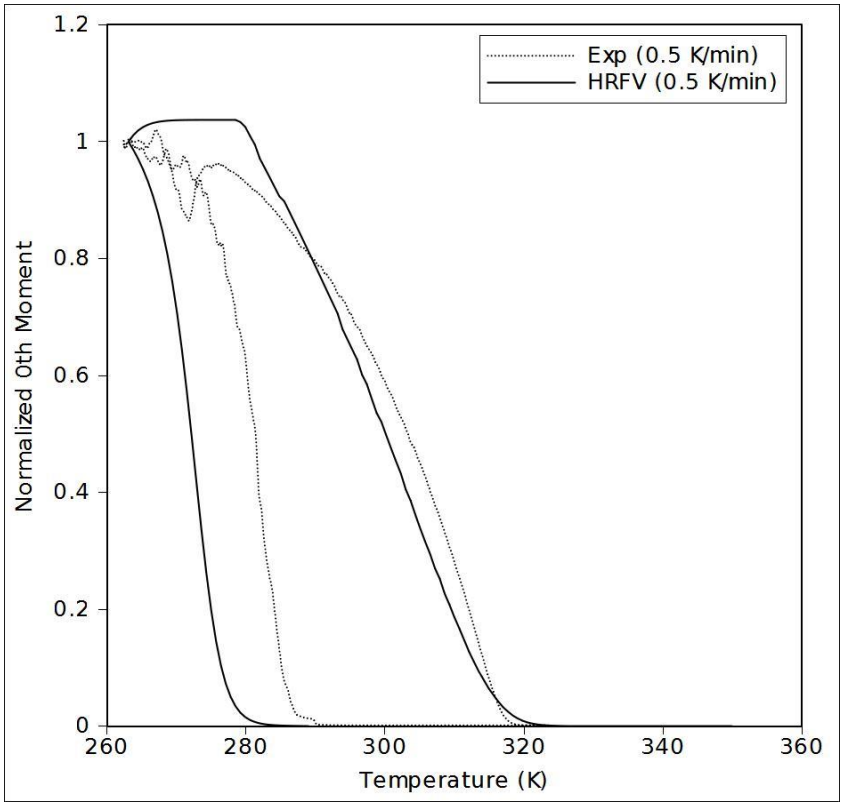

Figure 3.11: Comparison between hysteresis simulation and experimental results for a heating/cooling rate of 0.5 K/min

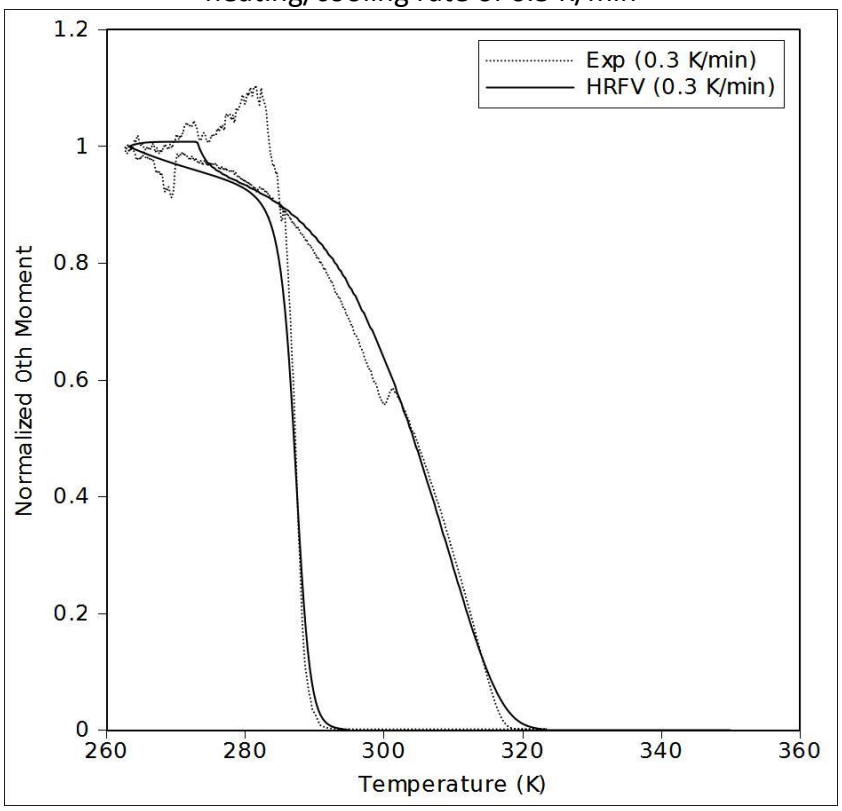

Figure 3.12: Comparison between hysteresis simulation and experimental results for a heating/cooling rate of 0.3 K/min

3.4.3. Average Particle Size during Hysteresis

The normalized average particle diameter obtained from simulations were compared with the normalized mean chord lengths for different temperatures over the entire range of the hysteresis experiment for a mean cooling/heating rate of 0.5 K/min. The average particle size may be obtained from the simulated results by taking the ratio of the 1^{st} and the 0^{th} moments. The mean chord length can be obtained by taking the ratio of the 1^{st} and 0^{th} moments of the chord length distribution measured by the FBRM.

The value for the average particle size at 263 K obtained from simulations for a cooling/heating rate of 0.5 K/min was found to be 73.72 micron. The particle size distribution at 263 K for the 0.5 K/min experiment was derived from the FBRM chord length distribution measurements by using the model presented by Pandit et. al. (2015) and the corresponding average particle size was found to be 32.48 microns (corresponding to a mean chord length of 23.56 microns). It was found that the simulations results over predicted the average particle sizes derived from experimental measurements at 263 K for the heating rates of 0.3 and 0.7 K/min. One possible reason why the simulations over predict the value for the average particle size, may be because breakage might be occurring in the system which actually leads to a kind of *normalization* of the particle size. As the impeller speed was not changed throughout the experiments, the average power input to the system was not changed. Thus, if breakage was in fact significant, it would lead to similar particle sizes across all cooling rates due to the constant power input. Hence, it seems that, as the present model does not account for the breakage of particles, the simulation results over predict the mean particle sizes. A detailed analysis of this hypothesis is however beyond the scope of this work. In order to evaluate the ability of the developed model to capture observed trends of variation of the average particle size with time, comparison of normalized average particle size was carried out.

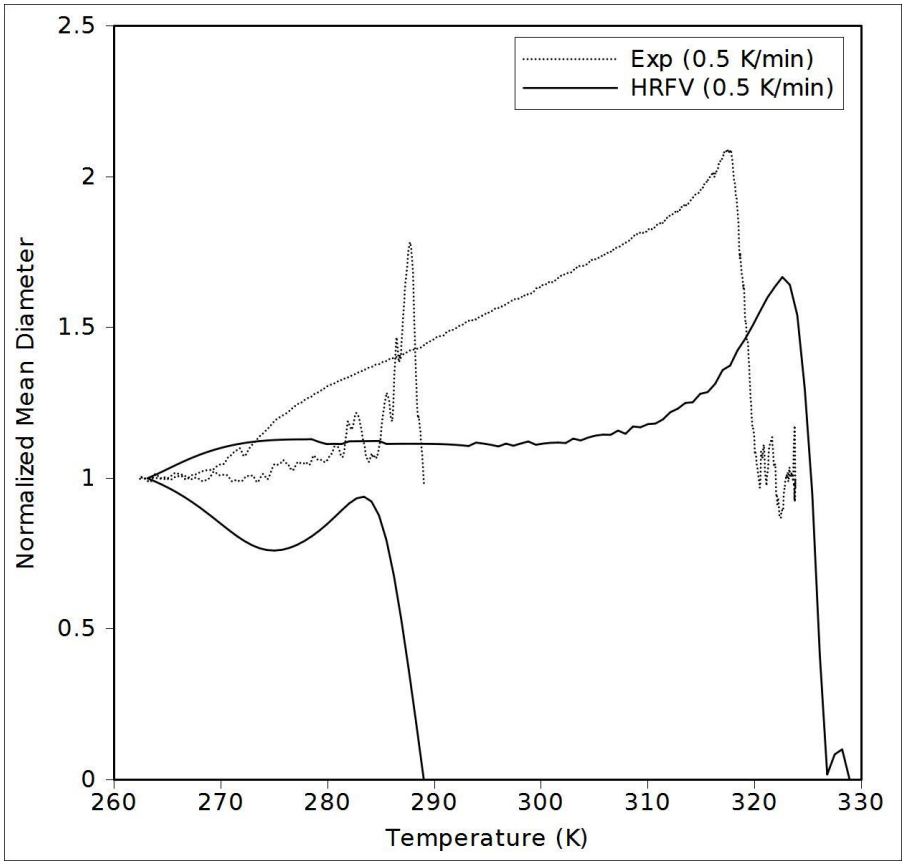

Figure 3.13: Comparison between the normalized simulated average particle diameter and the normalized mean chord length of the entire temperature range of the hysteresis experiment for a heating/cooling rate of 0.5 K/min (simulated average particle size and mean chord length at 263 K used for normalization are 73.72 microns and 23.56 microns respectively)

The simulated average particle sizes, obtained over the entire temperature range of the hysteresis experiment, were normalized by dividing them with the simulated average particle size obtained at 263 K. The mean chord lengths obtained from the FBRM results over the course of the hysteresis experiments were normalized by dividing them with the measured mean chord length at 263 K. A comparison between the normalized simulated average particle size and the normalized mean chord lengths for a sample cooling/heating rate of 0.5 K/min over the entire temperature range of the hysteresis experiment is shown in Figure 3.13. It was assumed here that the trends observed in the normalized mean chord lengths are fairly representative of trends which would be observed for the *true* average particle size. It can be seen from Figure 3.13, that the model could qualitatively predict the counter intuitive trend that the average particle size actually increases as dissolution progresses. Further, the model could also predict reasonably that the average particle size does not change significantly in the crystallization stage 1. Similar agreement was also observed for other two cooling/ heating rates and results are not shown here for the sake of brevity. The sudden increase in

mean particle size is expected immediately after the onset of nucleation as new particles are forming and they are growing. The average particle size would grow on account of crystal growth and would reduce on account of the increasing nucleation of crystals brought about when secondary nucleation becomes important. It would appear that this 'equilibrium' between nucleation of smaller sized particles and growth of particles to maintain a constant average particle size continues over the rest of the duration of the crystallization after onset. The counter-intuitive trend is observed during dissolution, where the average particle size is seen to actually increase. Due to shrinkage one might think that the average particle size would also decrease. However, it would seem that as the smaller sized particles disappear faster than the shrinkage of the bigger size particles, the average particle size increases before eventually decreasing.

The approach and framework developed here were thus shown to be a reliable and robust to model crystallization and dissolution processes. The developed approach, models and results will be useful for simulating industrially relevant crystallization – dissolution processes.

3.5. Conclusions

A framework was presented to model crystallization and dissolution processes by solving the population balance equation for nucleation, growth and dissolution. Experiments were performed where a paracetamol-ethanol system was cooled from an undersaturated state to a point until after the crystallization has occurred and then, from this point, immediately reheated to the initial undersaturated state. The rates employed for heating and cooling were equal in magnitude and were varied (0.3, 0.5 and 0.7 K/min). A hysteresis was observed in particle counts recorded online and in-situ by the FBRM probe with respect to temperature. The hysteresis curve was seen to be significantly influenced by the rate employed for heating/cooling. This curve and the effect of the different heating/cooling rates characterizes the coupled kinetics of crystallization and dissolution and serves as a thorough validation case for models for crystallization and dissolution processes.

A mathematical model was proposed based on the population balance equation for nucleation, growth and dissolution. The population balance equation was first solved for the Crystallization Stage 1 using the method of moments. The unknown parameters required for the nucleation kinetic model were obtained by fitting simulation results against experimental

results for a heating/cooling rate of 0.7 K/min. Previous values reported by Worlitschek et. al. (2004) were used for the growth kinetics model used for simulation. It was found that there may be multiple sets of values for the unknown parameters which may yield 'acceptable' solutions. The differences between these sets were discussed and one set of parameter values was finalized. Simulations using the finalized parameter values were compared with experimental results for the heating/cooling rates of 0.3 and 0.5 K/min for Crystallization Stage 1.

Using the finalized parameters, simulations were done for the complete range of experimental conditions to obtain the hysteresis curve for the three heating/cooling rates of 0.3, 0.5 and 0.7 K/min. Simulations were performed by obtaining the solution to the population balance equation using the High Resolution Finite Volume Scheme for when crystallization is occurring and the Moving Pivot Method for when dissolution occurs. The results from the HRFV scheme for the crystallization stage 1 were compared against those obtained by the method of moments' results for verification. Simulations were then performed to obtain the hysteresis curve and the normalized hysteresis curves obtained from experiments and simulations were compared. The model was seen to provide a good agreement against experimental results for the three heating/cooling rates of 0.3, 0.5 and 0.7 K/min considered in the present study. The model can thus be considered to be validated. The model was seen to over predict the average particle size obtained, however, could qualitatively capture the counter intuitive trend observed as the average diameter was plotted versus the temperature over the course of the hysteresis experiments.

The model was successful in capturing the hysteresis curve obtained in experiments. This suggests that accurate nucleation kinetics were determined for a system of paracetamol-ethanol. The presented methodology may be used to simulate the crystallization and dissolution processes or determine kinetics parameters for other systems. Further work will be directed along extending the model to include phenomena like breakage and aggregation to increase the applicability of the model for industrially relevant processes.

Acknowledgement

Authors are grateful to financial support for this work by CSIR through Mastflo [OLP3026] and Indus MAGIC [CSC123] projects.

Symbols & Notation

Symbol	Description	Unit
E_A	Activation energy for crystal growth	J/kmol-K
N_A	Avogadro number (equal to 6.023E26)	no. particles/kmol
k	Boltzmann constant (equal to 1.38E-23)	m^2-kg/(s^2-K)
k_1	Constant for the rate expression used for primary nucleation	-
k_2	Constant for the rate expression used for secondary nucleation	-
R	Cooling/Heating Rate employed for experimentation	K/min
ΔC	Degree of supersaturation (equal to $C - C^*(T)$)	kmol/m^3 or mol/lit
ρ_p	Density of solute crystals	kg/m^3
ρ_l	Density of solvent	kg/m^3
d_s	Diameter of the impeller	m
D	Diffusion coefficient	m^2/s
δ	Dirac delta function	-
C	Dissolved solute concentration	kmol/m^3 or mol/lit
C^m	Dissolved solute concentration at the m^{th} time instance	kmol/m^3 or mol/lit
n_1	Exponent for the rate expression used for primary nucleation	-
n_2	Exponent for the rate expression used for secondary nucleation	-
h	Grid size or span of each bin, employed for solution of discrete equations	m
g	Growth rate exponent	-
G	Growth rate of the crystal surface	m/s
X_{nuc}	Initial size of the nucleated particles	m
η_l	Kinematic viscosity of solvent	N-s/m^2
M_k	k^{th} Moment of the particle size distribution function	m^k
V_i, V_{i+1}	Lower and upper boundary pivot locations of the i^{th} bin	m
k_d	Mass transfer coefficient for dissolution	m/s
ϵ	Mean specific power input	m^2/s^3
d_m	Molecular diameter	M
M_w	Molecular weight of solute	kg/kmol or g/mol
B_0	Nucleation rate	(no. particles/m^3-s)
N	Number of discrete size elements or bins	-
f_n^m	Number of particles in the n^{th} bin at the m^{th} time instance	(no. particles/m^3)
f_n	Number of particles in the n^{th} bin	(no. particles/m^3)
X	Particle size co-ordinate; in this case, the diameter of particle	m

$f(X)$	Particle size distribution function as a function of particle size co-ordinate 'X'	(no. particles/m^3-m)
k_{r0}	Pre-exponential constant for the growth rate	m/s
$B_{0,pri}$	Rate of primary nucleation	(no. particles/m^3-s)
$B_{0,sec}$	Rate of secondary nucleation	(no. particles/m^3-s)
X_i	Representative pivot location of the i^{th} bin	m
Sc	Schmidt number	-
S	Shrinkage rate of the crystal surface during dissolution	m/s
$C^*(T)$	Solubility of the solution in the solvent as a function of temperature 'T'	kmol/m^3 or mol/lit
v_s	Stirrer speed	1/s
T	Temperature	K
T^m	Temperature at the m^{th} time instance	K
t	Time	s
k	Time step employed for solution of discrete equations	s
M_T	Total mass of the solute in the system	kg
R	Universal gas constant (equal to 8314)	J/kmol
V_R	Volume of the reactor	m^3

References

Barrett P., Glennon B., 2002. Characterizing the Metastable Zone Width and Solubility Curve Using Lasentec FBRM and PVM. Chemical Engineering Research & Design. 80(7), pp.799-805.

Davey R., Garside J., 2001. From Molecules to Crystallizers; Oxford University Press: New York, 1st edition.

Granberg R., Rasmuson A., 1999. Solubility of Paracetamol in Pure Solvents. Journal of Chemical & Engineering Data. 44, pp.1391-1395.

Gunawan R., Fusman I., Braatz R., 2004. High Resolution Algorithms for Multidimensional Population Balance Equations. Particle Technology and Fluidization. AIChE Journal. 50 (11), pp.2737-2749.

Hermanto M., Chow P., Tan R., 2010. Implementation of Focused Beam Reflectance Measurement (FBRM) in Antisolvent Crystallization to Achieve Consistent Product Quality. Crystal Growth & Design, 10 (8), pp.3668-3674.

Jiang M., Zhu X., Molaro M., Rasche M., Zhang H., Chadwick K., Rainmondo D., Kim K., Zhou L., Zhu Z., Wong M., O'Grady, D., Hebrault D., Tedesco J., Braatz R., 2014. Modification of crystal shape through deep temperature cycling. Industrial Engineering & Chemistry Research, 53, pp.5325-5336

Karpinski P., 1985. Importance of the Two-Step Crystal Growth Model. Chemical Engineering Science, 40(4), 641-646.

Kim D., Kim, K., 2007. Solubility of Cyclotrimethylenetrinitramine (RDX) in Binary Solvent Mixtures. Journal of Chemical Engineering Data, 52 (5), pp.1946–1949.

Kim Y., Méndez del Río J., Rousseau R., 2005. Solubility and prediction of the heat of solution of sodium naproxen in aqueous solutions. Journal of Pharmaceutical Science. 94(9), pp.1941–1948.

Kumar S., Ramkrishna D., 1996. On the Solution of Population Balance Equations by Discretization – II: A Moving Pivot Technique. Chemical Engineering Science, 51(8), pp.1333-1342.

LeVeque R., 2002. Finite Volume Methods for Hyperbolic Problems. Cambridge Univ. Press: New York.

Lovette M., Muratore M., Doherty M., 2012. Crystal Shape Modification through Cycles of Dissolution and Growth: Attainable Regions and Experimental Validation. AIChE Journal, 58 (5), pp.1465−1474.

Marchisio D., Fox R. O., 2005. Solution of population balance equations using the direct quadrature method of moments. Journal of Aerosol Science, 36, pp.43-73.

Marchisio D., Pikturna J., Fox R., Vigil R., Barresi A., 2003. Quadrature Method of Moments for Population-Balance Equations. AIChE Journal. 49(5), 1266-1276.

Mersmann A., 1995. Crystallization Technology Handbook. Marcel Dekker: New York.

Myerson A., 2002. Handbook of Industrial Crystallization; Butterworth-Heinemann: Massachusetts.

O'Sullivan B., Glennon B., 2005. Application of in Situ FBRM and ATR-FTIR to the Monitoring of the Polymorphic Transformation of d-Mannitol. Organic Process Research & Development. 9(6), pp.884–889.

Pandit A., Ranade V., 2016. Chord length distribution to particle size distribution. AIChE Journal, 62, pp.4215–4228.

Ramkrishna D., 2000. Population Balances: Theory and Applications to Particulate Systems in Engineering. Academic Press: San Diego, 1st edition.

Randolph A., Larson M., 1988. Theory of Particulate Processes: Analysis and Techniques of Continuous Crystallization. San Diego, CA: Academic Press, Inc.

Ruf A., Worlitschek J, Mazzotti M., 2000. Modeling and Experimental Analysis of PSD Measurements through FBRM. Particle & Particle Systems Characterization, 17, pp.167-179.

Wan J., Wang X., Ma C., 2009. Particle Shape Manipulation and Optimization in Cooling Crystallization Involving Multiple Crystal Morphological Forms. AIChE Journal, 55 (8), pp.2049−2061.

Worlitschek J., Mazzotti M., 2004. Model-Based Optimization of Particle Size Distribution in Batch-Cooling Crystallization of Paracetamol. Crystal Growth & Design, 4(5), pp.891-903.

Chapter 4. Continuous Crystallization Processes

4.1. Introduction

Continuous crystallization processes have been gaining importance in the recent years as alternatives to batch processes for the production of pharmaceutical, specialty and bulk chemicals involving crystallisation (Nagy et. al., 2013). Even though, industrial crystallisation processes rely heavily on batch processing, these processes have known issues of increased operating costs and variations in batch-to-batch product quality (Su et. al., 2015). Continuous processes are also known to offer more robust control on the process dynamics (Su et. a., 2015) and allow the utilization of operating parameter spaces previously inaccessible through batch processes (Pena et. al., 2015). Utilization of a larger operating parameter space provides access over a wider range of particle sizes (both bigger and smaller sized), particle shapes and crystal properties which cannot be produced using batch processes. Finally, a continuous mode of operation effectively reduces the labour and operational costs typically required in batch processes and have better utilization of physical space.

Even with all these advantages, the industrial application of continuous processes for crystallisation is limited. The dynamics of operation of continuous crystallisers are complex. Owing to that and a general lack of process understanding, figuring out operating protocols is in itself a task. Optimizing the protocols to suit the desired product specifications or implementing process control on continuous crystallisers are even more challenging. Modelling studies can go a long way towards alleviating these inconveniences. Modelling studies can help identify better operating protocols (Vetter et. al., 2014) as well as aid in improved process control (Jolliffe et. al, 2016). Scaling up of chemical engineering processes is known to be a difficult task in itself. Through modelling, known scale up protocols (mixing, heat transfer behaviour) may be suitably tailored to obtain useful estimates for scaled up crystalliser behaviour. Good modelling studies can hence substantially reduce uncertainties associated with the design, operation, control and scale up of continuous crystallisation processes.

As summarised in Chapter 1, most investigations into continuous crystallisation deal with experimentation on laboratory scales. Thus, the state of the art for modelling of continuous crystallisation processes is still lacking. Population balance models have widely been used to model crystallisation processes (Ramakrishna, 2000; Su et. al., 2015). Steady state modelling studies have been performed for both MSMPR and plug flow types of continuous crystallisers. Brown et. al. (2015) developed a steady state plug flow PBE based model for the anti-solvent crystallisation in a continuously oscillating baffled crystalliser (COBC). Su et. al. (2015) developed a generalized transient framework to model both batch and continuous crystallisation processes using MSMPR stages. The model accounted for the volume changes which occur during crystallisation especially in highly soluble systems. The model was also used to assess the robustness of the C-control strategy which is popular in batch systems.

There are a couple of shortcomings in the model presented by Su et. al. (2015) in terms of being a 'generalised' modeling framework. First, due to changes in volume after crystallisation in highly soluble systems, considering 'fixed volume crystallisers', the outlet flowrate will change which was not accounted for. Second, the model did not consider the thermal behaviour of crystallisers. For highly exothermic systems (especially relevant for cooling crystallisation), the cooling of the process fluid is complicated by the extreme heat release due to crystallisation. This heat release has a direct impact on the subsequent temperature profile which in turn affects the crystalliser behaviour. Further, scaling up substantially changes the thermal behaviour of any process equipment. Hence, operating protocols need to be suitably modified to account for the scale up. Inclusion of the thermal behaviour of crystallisers in the model would allow for using the standard scale up protocols of general process equipment to reliably predict scaled up crystallisation processes.

In the present Chapter, a generalized framework to model batch and continuous crystallisation processes was proposed and implemented. The framework included the changes in outlet flow rate that occur in 'fixed volume crystallisers' for highly soluble systems. Additionally the thermal behaviour of crystallisers was modelled by considering a heat balance equation. A typical system of sodium nitrite in water was considered for the study. First the experimental methods for both the batch and continuous crystallisers were discussed. Then, a mathematical model based on a popular tanks-in-series framework was formulated for both batch and continuous processes. Values for key crystallisation kinetic

parameters for systems are typically not known (Pandit et. al., 2015). A suitable methodology to estimate the values discussed in Chapter 3 was used to estimate the values for key crystallisation kinetic parameters. The parameter values were estimated through batch modelling studies. Suitable protocols were also developed to estimate heat transfer parameters.

It is proposed that the crystallisation kinetic parameter values obtained through batch studies can be used for continuous crystallisation studies. For continuous crystallisation, first, the mixing behaviour of the novel crystalliser assembly was characterised through modelling and experimental studies. Then, heat transfer studies were performed to estimate the key heat transfer parameter values. Finally, the continuous crystallisation of sodium nitrite in water was investigated both experimentally and using the model. The model was then used to understand the effect of operating parameters/design parameters on key processes performance parameters such as the yield, time to reach steady state, mean and variance of the outlet PSD.

4.2. Experimental Section

4.2.1. Materials

The crystallisation of sodium nitrite (NaNO2) in water was investigated. Sodium nitrite (97% Extra pure) from LOBA Chemie was used. DI water of MILI-Q standard taken from a Siemens filteration assembly was used. For the mixing experiments, table salt was used to prepare saturated salt solution.

4.2.2. Batch process

Batch experiments were carried out in a setup similar to the one described in Chapter 3 as shown in Figure 1. A 250ml OptiMAX reactor setup was used. The jacket temperature in OptiMAX setup is controlled electronically using Peltier elements. That coupled with a sophisticated control system allows for precise control over the crystalliser temperatures. The particle counts and chord length distributions were measured using an FBRM probe. The working principle of the probe was discussed in Chapter 2. A constant stirrer speed of 800 RPM was used for all the experiments. Hysteresis style experiments (as described in Chapter 3) were carried out. Temperature cycling was done between 55^0C and 25^0C i.e. the solution

was cooled from 55^{0}C to 25^{0}C and then immediately heated back to 55^{0}C. Equal magnitudes were employed for both the heating and cooling rates for each cycle. The effect of the heating/cooling rate on the crystallisation of sodium nitrite for values of 0.3, 0.5 and 0.7 K/min was investigated.

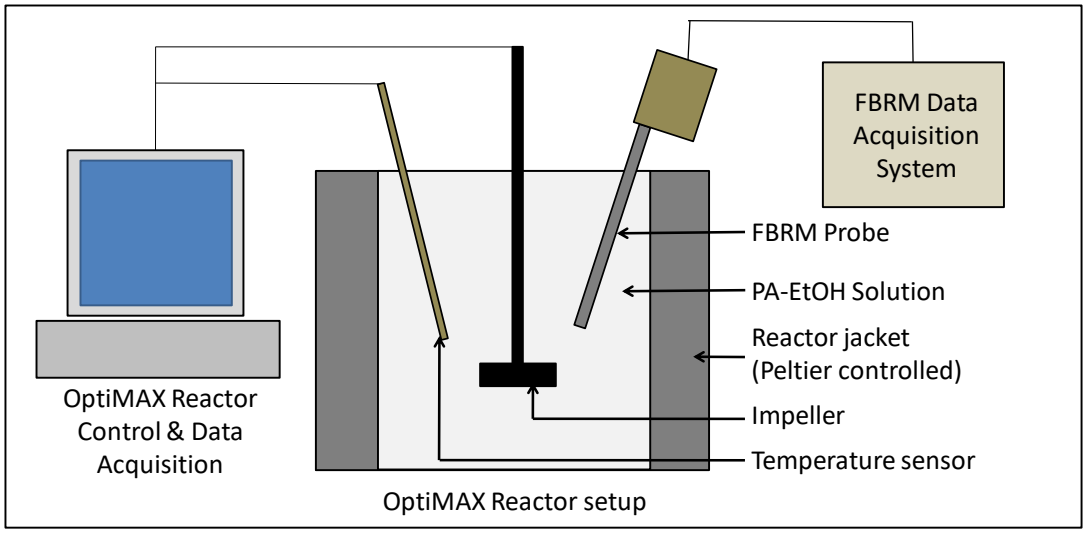

Figure 4.1. Schematic of Experimental Setup

4.2.3. Continuous process

A novel continuous crystalliser - provided by Technoforce - used for continuous crystallisation processes. The crystalliser was a jacketed plug flow crystalliser with a novel impeller design. The crystalliser assembly and the novel impeller design are shown in Figure 4.2. The overall schematic of the experimental setup is shown in Figure 4.3. The impeller shaft was connected to a motor via a reduction box. The reduction box reduced the impeller speed from 1300 RPM of the motor to a maximum of 62 RPM in crystalliser. The impeller speed was controlled using a variable frequency drive (VFD) which was connected to a three phase power supply. The impeller speed was kept at 62 RPM under all conditions. The total crystalliser liquid volume was 1.3L. The jacket connected to a Julabo chiller assembly (FP50 - HL) which pumps cooling fluid through the jacket at a high flowrate of 24 LPM. The solution was pumped into the crystalliser using a peristaltic pump in the flow rate range of (20 to 80 ml/min).

Classical residence time distribution (RTD) experiments were done to characterise the mixing behaviour of the novel crystallisers. A saturated salt solution was used as the tracer. The tracer was injected into the inlet stream using a syringe to resemble a pulse input. The outlet concentration of the salt solution was monitored using a conductivity probe. RTD experiments were carried out at different flowrates and different crystalliser configurations. Heat transfer

experiments were carried out by varying the jacket set-point temperatures (1^0C and 8^0C). The transient temperature response at the crystalliser outlet was measured. For crystallisation experiments, a solution of Sodium Nitrite and DI Water saturated at room temperature (~24^0C) was used as the feed solution. Temperature measurements were performed as in the case of heat transfer experiments.

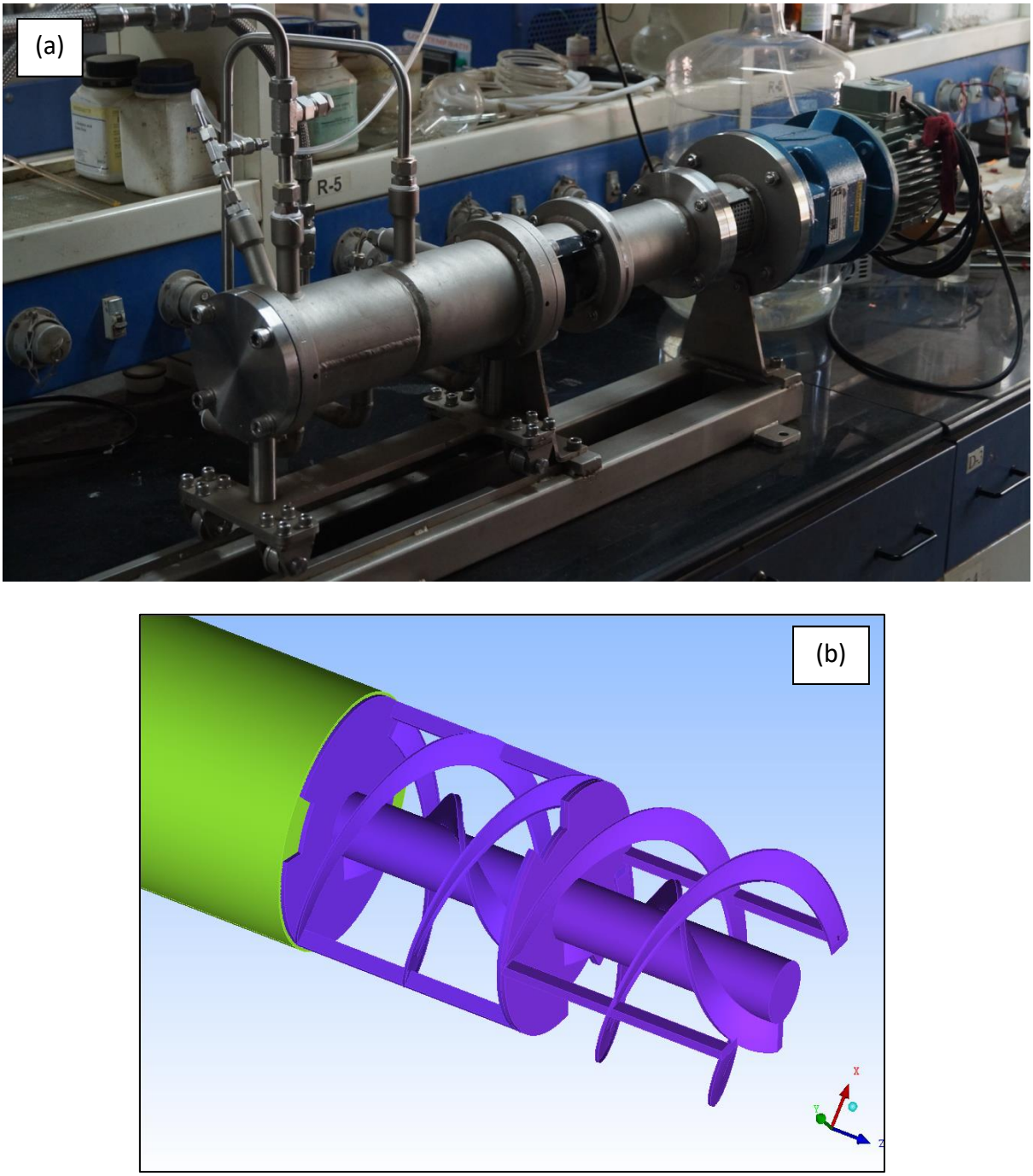

Figure 4.2. (a) The continuous crystalliser assembly provided by TechnoForce; (b) A representation of the novel impeller design used in the continuous crystalliser

Continuous crystallisation experiments were carried out under a fixed flow rate of 20 ml/min. Different methods of conductivity measurements, absorbance measurements and refractance measurements were evaluated for their effectiveness to measure the liquid phase concentration. It was determined that the refractance based measurements yielded the most accurate and repeatable results. Due to time constraints, liquid phase concentration measurements at the crystalliser outlet were done for only one set of experiments using a refractometer. The liquid sample for concentration measurements was collected after vacuum filtration of the outlet slurry.

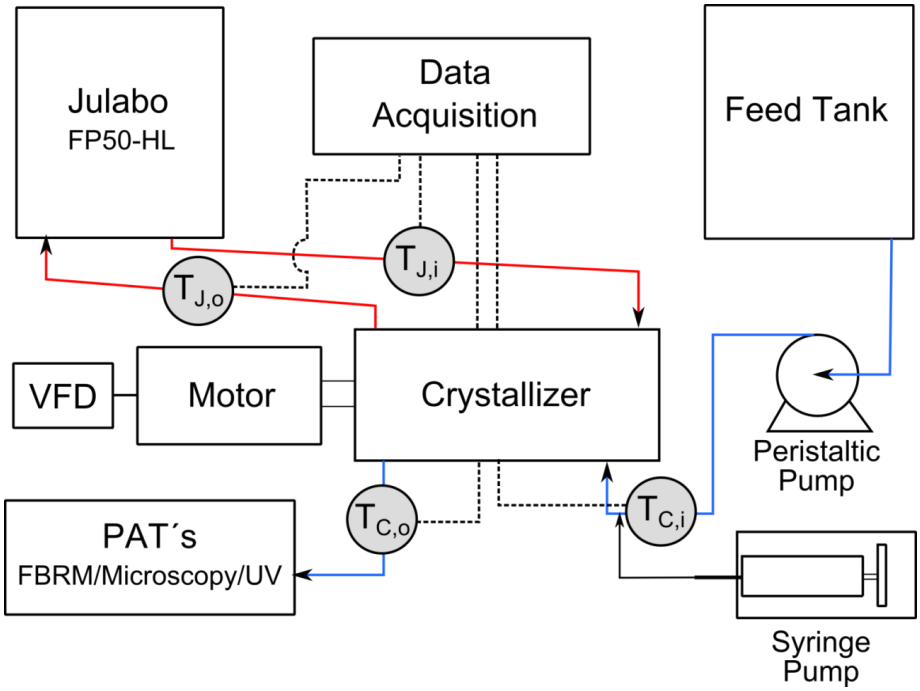

Figure 4.3. Schematic of the experimental setup

4.3. Mathematical Model

The tanks-in-series modelling framework is popular in chemical reaction engineering as a generic framework to model chemical reactors (Levenspiel, 1972). They provide fairly accurate results by mimicking the mixing behaviour of real reactors while still retaining an 'idealized' framework which is straightforward to implement. In the model, a reactor is assumed to be equivalent to a sequence of CSTR's connected in a series. By varying the number of CSTR's (n) one can essentially capture the mixing behaviour ranging from an ideal CSTR ($n = 1$) to an ideal PFR ($n > 10$). The number of tanks corresponding to a particular reactor

is an empirical parameter and can be determined by matching model predicted residence time distribution (RTD) with experimental RTD. The equations for the rate of change of concentrations etc. can then be solved for each of the CSTR's simultaneously to get accurate predictions of the reactor behaviour.

In the present study, we have proposed a generic modelling framework for continuous crystallization processes. The model proposed here builds upon the tanks-in-series modelling framework. In addition to solving the mass, species and energy balance equations, the population balance equation (PBE) is also solved for each tank. A general schematic which identifies the variables of interest for both continuous and batch crystallization processes is shown in Figure 4.4. The main distinction between the batch and continuous modes of operation is that for the continuous mode, the considered slurry volume is constant. For the batch mode, the considered slurry volume keeps on changing as the crystallization progresses and hence the equation for the total considered slurry volume must also be solved.

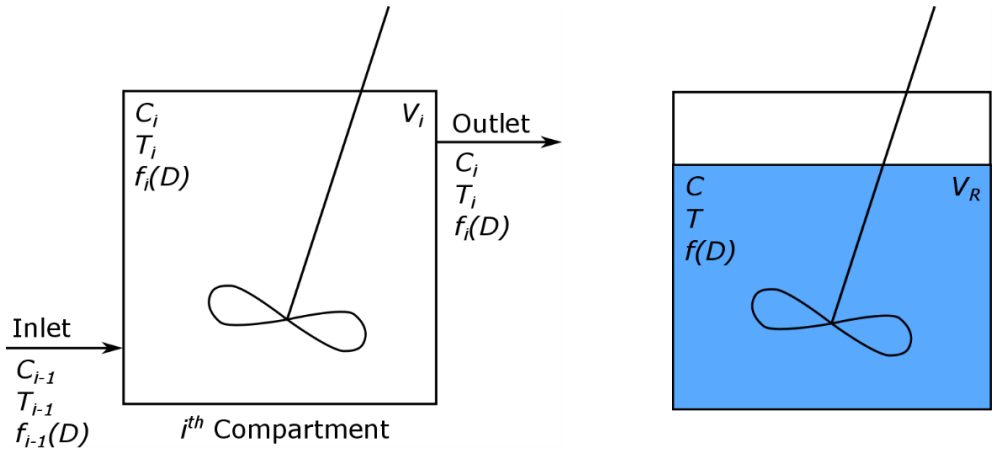

Figure 4.4. (a) Model schematic of continuous crystallization (b) Model schematic for batch crystallization

4.3.1. Model for Continuous Mode

In order to formulate the model, we will formulate the model equations for a single tank and then later generalize the model for multiple tanks. The general form of the population balance equation for continuous processes is:

$$\frac{\partial n(L)}{\partial t} + \frac{\partial n(L)G(L)}{\partial L} = \frac{v_0 n_0(L) - v n(L)}{V_R} \tag{4.1}$$

It should be noted that the outlet volumetric flow is not equal to the inlet flow rate. As discussed in the previous Chapter, there are multiple methods to solve a PBE. In the present study, it was sufficient to implement the solution of the PBE using the standard method of moments. Following the method by Randolph et. al. (1988) the PBE can be written in terms of moment equations as:

$$\frac{dM_i}{dt} = 0^i B_0 + iGM_{i-1} + \frac{v_0 M_{i,0} - vM_i}{V_R} \tag{4.2}$$

A detailed derivation is provided in the Appendix A3. If the crystallizer volume is not constant (as in the cases of batch reactors), then the equation can be rewritten as:

$$\frac{dV_R M_i}{dt} = 0^i B_0 V_R + iGM_{i-1} V_R + v_0 M_{i,0} - vM_i \tag{4.3}$$

The mass balances can be written separately for the solid and the liquid phase as:

$$\frac{dM_L}{dt} = v_0 \rho_{L,0}(1 - \epsilon_0) - v\rho_L(1 - \epsilon) - \dot{M}_C \tag{4.4}$$

$$\frac{dM_S}{dt} = v_0 \rho_S \epsilon_0 - v\rho_S \epsilon + \dot{M}_C \tag{4.5}$$

To find out the value of M_C, we multiply the equation for the third moment on both sides by $\sigma_V \rho_S V_R$ and some rearrangement (regardless of crystallizer volume being constant or not), we get the following equation:

$$\frac{dM_s}{dt} = 3GM_2 \sigma_V \rho_S V_R + \rho_S v_0 \epsilon_0 - \rho_S v \epsilon \tag{4.6}$$

It is useful to recognize that, $\sigma_V M_3 = \varepsilon$. The first term in the RHS is the mass transfer to the crystals and the second term is the inflow and outflow due to convection. Hence, when we compare the above equation to the equation for mass balance of solid phase, we can get the relation for the mass transfer to crystals as:

$$\dot{M}_C = 3GM_2 \sigma_V \rho_S V_R \tag{4.7}$$

The mass balance equation for the dissolved solids can be written as:

$$\frac{dM_L y_D}{dt} = v_0 \rho_{L,0}(1 - \epsilon_0) y_{D,0} - v\rho_L(1 - \epsilon) y_D - \dot{M}_C \tag{4.8}$$

The heat balance for the crystallizer should account for the convective heat in and out of the system. The heat balance can be written as:

$$\begin{aligned}\frac{d\left(M_L(1-y_D)C_{P,L}+M_L y_D C_{P,S}+M_S C_{P,S}\right)(T-T_{ref})}{dt} &= v_0\rho_{L,0}(1-\epsilon_0)y_{D,0}C_{P,S}\left(T_0-T_{ref}\right)\\ &+ v_0\rho_L(1-\epsilon_0)(1-y_{D,0})C_{P,L}\left(T_0-T_{ref}\right)\\ &+ v_0\rho_S\epsilon_0 C_{P,S}\left(T_0-T_{ref}\right)-v\rho_L(1-\epsilon)y_D C_{P,S}\left(T-T_{ref}\right)\\ &- v\rho_L(1-\epsilon)(1-y_D)C_{P,L}\left(T-T_{ref}\right)-v\rho_S\epsilon C_{P,S}\left(T-T_{ref}\right)\\ &+ \dot{M}_C(-\Delta H_C)+\langle UA\rangle_J\left(T_J-T\right)-\langle UA\rangle_E(T-T_E)\end{aligned} \quad (4.9)$$

The variable T_{ref} can be eliminated from the above equation. For a detailed derivation kindly refer to the Appendix A3. After the elimination of T_{ref} the heat balance equation can be written as:

$$\begin{aligned}\frac{d\left(M_L(1-y_D)C_{P,L}+M_L y_D C_{P,S}+M_S C_{P,S}\right)T}{dt} &= v_0\rho_{L,0}(1-\epsilon_0)y_{D,0}C_{P,S}T_0+v_0\rho_{L,0}(1-\epsilon_0)(1-y_{D,0})C_{P,L}T_0\\ &+ v_0\rho_S\epsilon_0 C_{P,S}T_0-v\rho_L(1-\epsilon)y_D C_{P,S}T\\ &- v\rho_L(1-\epsilon)(1-y_D)C_{P,L}T-v\rho_S\epsilon C_{P,S}T+\dot{M}_C(-\Delta H_C)\\ &+ \langle UA\rangle_J\left(T_J-T\right)-\langle UA\rangle_E(T-T_E)\end{aligned} \quad (4.10)$$

This can also be written as:

$$\begin{aligned}\frac{d\left(M_L C_{P,MIX}+M_S C_{P,S}\right)T}{dt} &= v_0\rho_{L,0}(1-\epsilon_0)C_{P,MIX,0}T_0-v\rho_L(1-\epsilon)C_{P,MIX}T\\ &+ v_0\rho_S\epsilon_0 C_{P,S}T_0-v\rho_S\epsilon C_{P,S}T+\dot{M}_C(-\Delta H_C)+\langle UA\rangle_J\left(T_J-T\right)\\ &- \langle UA\rangle_E(T-T_E)\end{aligned} \quad (4.11)$$

Where $C_{P,mix}=y_D C_{P,S}+(1-y_D)C_{P,L}$

The only thing that is unknown in the above equations is how to account for the unknown outlet velocity. An explicit formulation for the outlet velocity may be obtained by making either of two assumptions: (a) Constant liquid phase density (b) Linearly varying liquid phase density. Depending of the assumption, we obtain two formulation for the outlet velocity. A detailed derivation of the outlet velocity relations is given in the Appendix A3.

Constant density

$$v=v_0-\dot{M}_C\left\{\frac{\rho_S-\rho_L}{\rho_S\rho_L}\right\} \quad (4.12)$$

Linearly varying density

$$\rho_L = A + By_D$$

$$v = \left\{v_0 \frac{\rho_{L,0}}{\rho_L}(1-\epsilon_0) + v_0\epsilon_0\right\} - \frac{BM_L}{\rho_L^2}\frac{dy_D}{dt} - \left\{\frac{\dot{M}_C}{\rho_L} - \frac{\dot{M}_C}{\rho_S}\right\} \tag{4.13}$$

$$\frac{dy_D}{dt} = \frac{1}{M_L}\left\{v_0\rho_{L,0}(1-\epsilon_0)\left(y_{D,0} - y_D\right) - \dot{M}_C(1-y_D)\right\}]$$

It should be noted that for the constant density and linearly varying density assumptions, the outlet volumetric flow rate may be obtained explicitly and does not need to be solved simultaneously.

4.3.2. Model extension for Batch Mode

For the case of a batch reactor, instead of solving for the outlet velocity, the equation for the crystallizer volume needs to be solved. The equations for the rate of change in crystallizer volume depending upon the density assumptions are given below. A detailed description of the same is provided in the Appendix A3.

Constant density

$$\frac{dV_R}{dt} = -\frac{\dot{M}_C}{\rho_L} + \frac{\dot{M}_C}{\rho_S} \tag{4.14}$$

Linearly varying density

$$\frac{dV_R}{dt} = -\frac{\dot{M}_C}{\rho_L} - \frac{BM_L}{\rho_L^2}\frac{dy_D}{dt} + \frac{\dot{M}_C}{\rho_S} \tag{4.15}$$

$$\frac{dy_D}{dt} = \frac{-\dot{M}_C(1-y_D)}{M_L}$$

4.3.3. Equations for tanks-in-series

For multiple tanks in series the above equations can be written as:

$$\frac{dM_{i,k}}{dt} = 0^i B_{0,k} + iG_k M_{i-1,k} + \frac{v_{k-1}M_{i,k-1} - v_k M_{i,k}}{V_{R,k}} \tag{4.16}$$

And for non-constant volume as:

$$\frac{dV_{R,k}M_{i,k}}{dt} = 0^{i}B_{0,k}V_{R,k} + iG_kM_{i-1,k}V_{R,k} + v_{k-1}M_{i,k-1} - v_kM_{i,k} \tag{4.17}$$

$$\frac{dM_{L,k}}{dt} = v_{k-1}\rho_{L,k-1}(1-\epsilon_{k-1}) - v_k\rho_{L,k}(1-\epsilon_k) - \dot{M}_{C,k} \tag{4.18}$$

$$\frac{dM_{S,k}}{dt} = v_{k-1}\rho_S\epsilon_{k-1} - v_k\rho_S\epsilon_k + \dot{M}_{C,k} \tag{4.19}$$

$$\dot{M}_{C,k} = 3G_kM_{2,k}\sigma_V\rho_SV_{R,k} \tag{4.20}$$

$$\begin{aligned}\frac{dM_{L,k}y_{D,k}}{dt} &= v_{k-1}\rho_{L,k-1}(1-\epsilon_{k-1})y_{D,k-1} - v_k\rho_{L,k}(1-\epsilon_k)y_{D,k} \\ &\quad - \dot{M}_{C,k}\frac{dV_{R,k}M_{i,k}}{dt} \\ &= 0^{i}B_{0,k}V_{R,k} + iG_kM_{i-1,k}V_{R,k} + v_{k-1}M_{i,k-1} - v_kM_{i,k}\end{aligned} \tag{4.21}$$

$$\begin{aligned}&\frac{d\left(M_{L,k}C_{P,MIX,k} + M_{S,k}C_{P,S}\right)T_k}{dt} \\ &= v_{k-1}\rho_{L,k-1}(1-\epsilon_{k-1})C_{P,MIX,k-1}T_{k-1} \\ &- v_k\rho_{L,k}(1-\epsilon_k)C_{P,MIX,k}T_k + v_{k-1}\rho_S\epsilon_{k-1}C_{P,S}T_{k-1} \\ &- v_k\rho_S\epsilon_kC_{P,S}T_k + \dot{M}_{C,k}(-\Delta H_C) + \langle UA\rangle_{J,k}\left(T_J - T_k\right) \\ &- \langle UA\rangle_{E,k}(T_k - T_E)\end{aligned} \tag{4.22}$$

The relations for the tank outlet velocities can be written as:

Constant density

$$v_k = v_{k-1} - \dot{M}_{C,k}\left\{\frac{\rho_S - \rho_L}{\rho_S\rho_L}\right\} \tag{4.23}$$

Linearly varying density

$$v_k = \left\{v_{k-1}\frac{\rho_{L,k-1}}{\rho_{L,k}}(1-\epsilon_{k-1}) + v_{k-1}\epsilon_{k-1}\right\} - \frac{BM_{L,k}}{\rho_{L,k}^2}\frac{dy_{D,k}}{dt} - \left\{\frac{\dot{M}_{C,k}}{\rho_{L,k}} - \frac{\dot{M}_{C,k}}{\rho_S}\right\} \tag{4.24}$$

$$\frac{dy_{D,k}}{dt} = \frac{1}{M_{L,k}}\left\{v_{k-1}\rho_{L,k-1}(1-\epsilon_{k-1})\left(y_{D,k-1} - y_{D,k}\right) - \dot{M}_{C,k}\left(1 - y_{D,k}\right)\right\}$$

4.3.4. Non-Dimensional form of Equations

It is useful to identify the dimensionless numbers which characterize the system. Identifying these numbers provide a generalized platform to quickly assess the behaviour of systems by simply calculating the values to these numbers. In order to obtain the non-dimensional numbers that characterize the system, the model equations presented in the previous section must be non-dimensionalized. The final form of the non-dimensional equations for the tanks-

in-series model are given below. For a detailed derivation of the non-dimensional equations, kindly refer to the Appendix A3.

Moment equations for a constant crystallizer unit volume:

$$\frac{dM'_{i,k}}{dt'} = 0^i B'_{0,k} + iG'_k M'_{i-1,k} + \frac{v'_{k-1}M'_{i,k-1} - v'_k M'_{i,k}}{V'_{R,k}} \tag{4.25}$$

Moment equations for non-constant crystallizer unit volume:

$$\frac{dV'_{R,k}M'_{i,k}}{dt'} = 0^i B'_{0,k}V'_{R,k} + iG'_k M'_{i-1,k}V'_{R,k} + v'_{k-1}M'_{i,k-1} - v'_k M'_{i,k} \tag{4.26}$$

Equation for mass of liquid phase in crystallizer unit:

$$\frac{dM'_{L,k}}{dt'} = v'_{k-1}\rho'_{L,k-1}(1-\epsilon_{k-1}) - v'_k\rho'_{L,k}(1-\epsilon_k) - \dot{M}'_{C,k} \tag{4.27}$$

Equation for mass of solid phase in crystallizer unit:

$$\frac{dM'_{S,k}}{dt'} = v'_{k-1}\rho'_S\epsilon_{k-1} - v'_k\rho'_S\epsilon_k - \dot{M}'_{C,k} \tag{4.28}$$

$$\dot{M}'_{C,k} = 3\beta_1 G'_k M'_{2,k}\rho'_S V'_{R,k} \tag{4.29}$$

$$\beta_1 = \frac{\sigma_V L^3_{ref} M_{0,ref}}{V_R} \tag{4.30}$$

Equation for mass of dissolved solid:

$$\frac{dM'_{L,k}y_{D,k}}{dt'} = v'_{k-1}\rho'_{L,k-1}(1-\epsilon_{k-1})y_{D,k-1} - v'_k\rho'_{L,k}(1-\epsilon_k)y_{D,k} - \dot{M}'_{C,k} \tag{4.31}$$

Equation for heat balance of crystallizer unit:

$$\begin{aligned}\frac{d\left(M'_{L,k}C'_{P,MIX,k} + M'_{S,k}C'_{P,S}\right)T'_k}{dt'} &= v'_{k-1}\rho'_{L,k-1}(1-\epsilon_{k-1})C'_{P,MIX,k-1}T'_{k-1} \\ &- v'_k\rho'_{L,k}(1-\epsilon_k)C'_{P,MIX,k}T'_k + v'_{k-1}\rho'_S\epsilon_{k-1}C'_{P,S}T'_{k-1} \\ &- v'_k\rho'_S\epsilon_k C'_{P,S}T'_k + \beta_2\dot{M}'_{C,k} + \beta_{3,k}\left(T'_J - T'_k\right) - \beta_{4,k}(T'_k - T'_E)\end{aligned} \tag{4.32}$$

$$\beta_2 = \frac{(-\Delta H_C)}{C_{P,ref}T_{ref}} \tag{4.33}$$

$$\beta_{3,k} = \frac{\langle UA\rangle_{J,k}t_{ref}}{\rho_{ref}V_{ref}C_{P,ref}} \tag{4.34}$$

$$\beta_{4,k} = \frac{\langle UA \rangle_{E,k} t_{ref}}{\rho_{ref} V_{ref} C_{P,ref}} \tag{4.35}$$

The relations for the tank outlet velocities can be written as:

Constant density

$$v'_k = v'_{k-1} - \dot{M}'_{C,k} \left\{ \frac{\rho'_S - \rho'_L}{\rho'_S \rho'_L} \right\} \tag{4.36}$$

Linearly varying density

$$v'_k = \left\{ v'_{k-1} \frac{\rho'_{L,k-1}}{\rho'_{L,k}} (1 - \epsilon_{k-1}) + v'_{k-1} \epsilon_{k-1} \right\} - \frac{\beta_{D,2} M'_{L,k}}{\rho'^2_{L,k}} \frac{dy_{D,k}}{dt'} - \left\{ \frac{\dot{M}'_{C,k}}{\rho'_{L,k}} - \frac{\dot{M}'_{C,k}}{\rho'_S} \right\} \tag{4.37}$$

$$\frac{dy_{D,k}}{dt'} = \frac{1}{M'_{L,k}} \left\{ v'_{k-1} \rho'_{L,k-1} (1 - \epsilon_{k-1}) \left(y_{D,k-1} - y_{D,k} \right) - \dot{M}'_{C,k} \left(1 - y_{D,k} \right) \right\}$$

For the batch mode, the equation for volume can be written as:

Constant density

$$\frac{dV'_R}{dt'} = -\frac{\dot{M}'_C}{\rho'_L} + \frac{\dot{M}'_C}{\rho'_S} \tag{4.38}$$

Linearly varying density

$$\frac{dV'_R}{dt'} = -\frac{\dot{M}'_C}{\rho'_L} - \frac{\beta_{D,2} M'_L}{\rho'^2_L} \frac{dy_D}{dt} + \frac{\dot{M}'_C}{\rho'_S} \tag{4.39}$$

$$\frac{dy_D}{dt'} = \frac{-\dot{M}'_C (1 - y_D)}{M'_L}$$

4.3.5. Reference Variables

The values for the reference variables need to be defined in order to obtain the non-dimensional variables. It helps to make intelligent choices for the reference values as that would be helpful in making more generalized insights for the system. The first reference variable we encounter is L_{ref}. For L_{ref}, in the present study we will define as the target particle size for the crystallization. This would be a user defined value. The second variable we encounter is V_{ref}. It is convenient to define V_{ref} as directly the volume of the crystallizer unit for a continuous mode or the initial volume for the batch mode. The third variable is $M_{0,ref}$.

We will define $M_{0,ref}$ as the number of particles of target size which will be formed, if all solute mass inside the crystallizer (taking the inlet/initial conditions as the basis) is crystallized. The total solute mass taking inlet/initial conditions as the basis can be found out as:

$$M_{S,ref} = m_W C_0 V_{ref} \tag{4.40}$$

So, $M_{0,ref}$ can be written as:

$$M_{0,ref} = \frac{M_{S,ref}}{\sigma_V L_{ref}^3 \rho_S} = \frac{m_W C_0 V_{ref}}{\sigma_V L_{ref}^3 \rho_S} \tag{4.41}$$

The reference time for the continuous mode can be defined as the residence time and can directly be written as:

$$t_{ref} = \frac{V_R}{v_0} \tag{4.42}$$

For a batch mode of operation, the total batch time can be considered as the reference time.

ρ_{ref}, $C_{P,ref}$ are taken to be same as the pure solvent phase properties. T_{ref} is defined as the inlet temperature. The reference value for concentration can be specified as the total solute mass inside the crystallizer taking the inlet/initial condition as the basis.

$$C_{ref} = C_0 \tag{4.43}$$

The non-dimensional numbers that emerge from these equations are:

$$\beta_1 = \frac{\sigma_V L_{ref}^3 M_{0,ref}}{V_R}$$

$$\beta_2 = \frac{(-\Delta H_C)}{C_{P,ref} T_{ref}}$$

$$\beta_{3,k} = \frac{\langle UA \rangle_{J,k} t_{ref}}{\rho_{ref} V_{ref} C_{P,ref}}$$

$$\beta_{4,k} = \frac{\langle UA \rangle_{E,k} t_{ref}}{\rho_{ref} V_{ref} C_{P,ref}}$$

4.3.6. Constitutive Laws

4.3.6.1. Crystal growth

Surface integration controlled crystal growth is assumed similar to that in Chapter 2. The growth rate can then be written for each crystallizer unit by an Arrhenius type rate expression as follows:

$$G_k = k_{g,0} exp\left(-\frac{E_A}{RT_k}\right)(C_k - C_k^*(T_k))^g \tag{4.44}$$

This can also be written in a non-dimensional form as:

$$G_k' = \beta_{g,1} exp\left(-\frac{\beta_{g,2}}{T_k'}\right)(C_k' - C'^*(T_k'))^g \tag{4.45}$$

$$\beta_{g,1} = \frac{k_{g,0} t_{ref} C_{ref}^g}{L_{ref}} \tag{4.46}$$

$$\beta_{g,2} = \frac{E_A}{RT_{ref}} \tag{4.47}$$

4.3.6.2. Primary Nucleation

Similar to the primary nucleation rate assumed in the Chapter 3, the primary nucleation rate can be written by a simple power law relation such as:

$$B_{0,k,pri} = k_1(C_k - C_k^*(T_k))^{n_1} \tag{4.48}$$

In a non-dimensional form, the same relation can be written as:

$$B_{0,k,pri}' = \beta_{N,1}(C_k' - C_k'^*(T'))^{n_1} \tag{4.49}$$

$$\beta_{N,1} = \frac{V_{ref} t_{ref} k_1 C_{ref}^{n_1}}{M_{0,ref}} \tag{4.50}$$

4.3.6.3. Secondary Nucleation

$$B_{0,k,sec} = k_2 M_{2,k}(C_k - C_k^*(T_k))^{n_2} \tag{4.51}$$

In a non-dimensional form, the secondary nucleation rate can be written as:

$$B_{0,k,sec}' = \beta_{N,2} M_{2,k}'(C_k' - C_k'^*(T_k'))^{n_2} \tag{4.52}$$

$$\beta_{N,2} = k_2 L_{ref}^2 C_{ref}^{n_2} t_{ref} \tag{4.53}$$

The total nucleation rate can be written as the sum of the primary and the secondary nucleation rates. For a detailed derivation of the non-dimensional forms of the constitutive law equations, kindly refer to the Appendix A3.

4.3.7. Auxiliary Laws

4.3.7.1. Concentration

$$C(y_D) = \frac{y_D \rho_L(y_D)}{m_W} \tag{4.54}$$

$$C'(y_D) = \frac{\rho_{ref}}{C_{ref} m_W} y_D \rho_L'(y_D) = \beta_C y_D \rho_L'(y_D) \tag{4.55}$$

4.3.7.2. Solubility

Solubility as a function of temperature is typically represented in the form of kg-solute/kg-solvent. The solubility in the present text needs to be calculated in the form of kmol/m^3 to be used in the constitutive law relations.

$$x_{D,sol}(T) = \frac{kg_{solute}}{kg_{solvent}} = C_1 e^{C_2 T} \tag{4.56}$$

$$y_{D,sol} = \frac{kg_{solute}}{kg_{solute} + kg_{solvent}} = \frac{x_{D,sol}}{1 + x_{D,sol}}$$

$$C^*(T) = C\left(y_{D,sol}\right) = \frac{y_{D,sol} \rho_L(y_{D,sol})}{m_W}$$

$$x_{D,sol}(T') = C_1 e^{C_2 T_{ref} T'}$$

$$x_{D,sol}(T') = \beta_{S,1} e^{\beta_{S,2} T'} \tag{4.57}$$

$$\beta_{S,1} = C_1 \tag{4.58}$$

$$\beta_{S,2} = C_2 T_{ref} \tag{4.59}$$

$$y_{D,sol}(T') = \frac{kg_{solute}}{kg_{solute} + kg_{solvent}} = \frac{x_{D,sol}(T')}{1 + x_{D,sol}(T')}$$

$$C'^*(T') = C'\left(y_{D,sol}\right) = \beta_C y_{D,sol}(T') \rho_L'\left(y_{D,sol}(T')\right) \tag{4.60}$$

4.3.7.3. Density

In the present study, we assume the density to be represented by the mass weighted average.

$$\rho_L(y_D) = A + By_D \tag{4.61}$$

$$A = \rho_L; B = (\rho_S - \rho_L)$$

$$\rho_L'(y_D) = \frac{A}{\rho_{ref}} + \frac{B}{\rho_{ref}} y_D$$

$$\rho_L'(y_D) = \beta_{D,1} + \beta_{D,2} y_D \tag{4.62}$$

4.3.7.4. Specific Heat

In the present study, we assume the specific heat to be represented by the mass weighted average.

$$C_{P,MIX}(y_D) = C_{P,L} + (C_{P,S} - C_{P,L})y_D \tag{4.63}$$

$$C_{P,MIX}'(y_D) = \frac{C_{P,L}}{C_{P,ref}} + \frac{(C_{P,S} - C_{P,L})}{C_{P,ref}} y_D$$

$$C_{P,MIX}'(y_D) = \beta_{CP,1} + \beta_{CP,2} y_D \tag{4.64}$$

4.3.8. Onset of Crystallisation

4.3.8.1. Batch Processes

For the implementation of the model, it is important to address the question of onset of crystallization. The concept of MSZW and induction time have been extensively researched previously and deal with the specific issue of onset of crystallization. In a batch mode operating with a linear cooling profile, the MSZW is a good estimate of the point at which crystallization will start. However, this is an experimental parameter. For a batch kept in a constant super saturated state, the induction time gives a good estimate about when the crystallization will start. Kubota developed a model which connected the two seemingly disconnected system characteristics. For a detailed description about the Kubota model kindly refer to the Appendix A3. In the present case, instead of going to simulate for the induction time, we will only consider the case of cooling crystallization where the MSZW is relevant. The MSZW will be provided as an input parameter and it will be assumed that crystallization will start only after the MSZW period.

4.3.8.2. Continuous Processes

In batch crystallisation, according to the model proposed by Kubota (2008), nucleation initiates as soon as the solution reaches super-saturation. However, at this point the nucleation events are not observable and hence cannot be detected. For a particular level of super-saturation, a suitable amount of time (referred to as the induction time) needs to pass after the nucleation events become detectable that we say that nucleation has occurred. It is worth noting that the time is thus dependent on the type of detection equipment used. However, for a given level super saturation, the time measured using a particular type of detection equipment is repeatable. Now, consider a continuous crystalliser operating under a certain level of super saturation. The exact level of super saturation is irrelevant for the purposes of this argument. According to the model proposed by Kubota (2008), there will be a particular value for induction time which is associated with that level of super saturation. So, any parcel of liquid which spends time/resides in the crystalliser for more than the said induction time will have detectable nucleation events occurring within it. Also, according to the mixing behaviour for tanks-in-series, theoretically, it is always possible to find such a percentage of liquid which has resided for a period more than the induction time. As this statement does not depend upon the level of super-saturation, it may be inferred that the crystallisation initiates as soon as the crystalliser reaches super-saturation.

4.3.9. Model Implementation

The non-dimensional form of the tanks-in-series model which comprise of equations 4.25 to 4.35 were solved simultaneously using an ordinary differential equation (ODE) solver. For the batch mode, the equation for the changing process fluid volume was solve by considering a general case of density varying linearly with solute mass fraction (Equation 4.39). For the case of continuous mode, the equation for the outlet volumetric flowrate was calculated dynamically again by considering a case of linearly varying density (Equation 4.37). The special case of a constant density may be obtained by just setting the value of the linear component to zero. The code was written in MATLAB. A simple spreadsheet interface to provide inputs for the code was designed using Excel. The stiff-ODE solver 'ode23s' from the MATLAB suite of ODE solvers was used. Absolute and relative tolerances of $1x10^{-12}$ were used to solve the code. First, the verification of the code was performed independently for the different modules of heat transfer, tanks-in-series and crystallisation. For a detailed discussion with

regards to the verification of the solver kindly refer to the Appendix A3. The model was then used to model batch and continuous crystallisation processes.

4.4. Results and Discussion

4.4.1. Crystallisation of Batch Processes

As per the methodology described in the present Chapter, to model continuous crystallisation processes, it is necessary to first model batch crystallisation processes. Values for key crystallisation kinetic parameters may first be estimated accurately through batch crystallisation studies. These same parameters may then be used for simulations of continuous crystallisation. Accordingly, temperature cycling experiments were performed in a batch mode for different values for heating/cooling rates. The model described earlier in the present Chapter was implemented for the batch mode of operation. First, values for heat transfer parameters were estimated to allow for simulation by giving jacket temperature as the input. Then, key crystallisation kinetic parameter values were estimated by comparing model predictions against experiments simultaneously for the particle counts profiles and the Sauter mean diameter profiles. The model was then validated against the other sets of experiments. The model was then used to estimate the value for the heat of crystallisation.

4.4.1.1. Heat transfer parameters

Simulations were performed for the system of Sodium Nitrite-DI Water. The quantity of sodium nitrite and water corresponding to the first fill conditions used in the batch reactor experiment was considered for heat transfer simulations (195gm $NaNO_2$ and 200g of DI Water). For estimating the heat transfer parameters, the crystallization conditions were presently switched off. After crystallization, there will be some changes in the density and the specific heat capacity of the liquid phase. However, for the time being, we shall neglect these changes and estimate the heat transfer parameters regardless. Indeed a better way of doing the experiments to estimate heat transfer parameters would be to carry out the heat transfer simulation in non-crystallizing conditions. However, we do not expect the system to change the concentration drastically due to crystallisation as in case of some other systems (Ibuprofen). Hence, in the present case, the heat transfer parameters estimated through the present process will be fairly accurate.

The parameters used for the simulation of the $NaNO_2$-DI Water system are provided in the Appendix A3. To simulate for batch processes, the inlet velocity was considered to be 0 and the number of tanks were set to 1. The jacket temperature profile used for the experiment was provided as the input for the solver. The solver was expected to calculate the reactor temperature profile using the heat transfer model. The experimental run using a heating/cooling rate of 0.3K/min was considered. The parameter values for the universal heat transfer coefficient times area for both the heat transfer between the jacket and the solution (UA_J) and the environment and the solution (UA_E) were not known. The unknown parameter values were tweaked until an excellent agreement was obtained between the simulated temperature profile and the experimental temperature profile. A comparison between these profiles and the jacket temperature profile is shown in Figure 4.5(a). As can be seen from the Figure, the heat transfer model could capture the crystalliser behaviour well. The value for UA_J was found to be 1.4 J/K and the value for UA_E was found to be 3E-2 J/K.

The parameters estimated using the 0.3K/min cooling/heating rate experiment was used to simulate for the experiments using 0.5 K/min and 0.7 K/min cooling/heating rates. Comparisons between the model predictions and the experimental predictions for these experiments are shown in Figures 4.5(b) and 4.5(c). As can be seen that there is excellent agreement between the model predictions and the experiments. Thus, can assume that the heat transfer model has been validated successfully. It should be noted however that there is a slight bump in the jacket temperature profile (around 2000s to 3000s period in the 0.3 K/min experiment). This bump is present for all the experimental profiles. On comparing the jacket temperature profile with the counts profile, it was observed that the bump coincided with the onset of crystallization. This is evidence that the crystallization of NaNO2 is a exothermic process as the jacket dips below the current trajectory to maintain the crystalliser temperature trajectory to compensate for this heat release. We may however, comment that the exothermicity is not very high as other systems such as Ibuprofen. Quantitative estimation of key crystallisation kinetic parameters including the heat of crystallization will be covered in the following section.

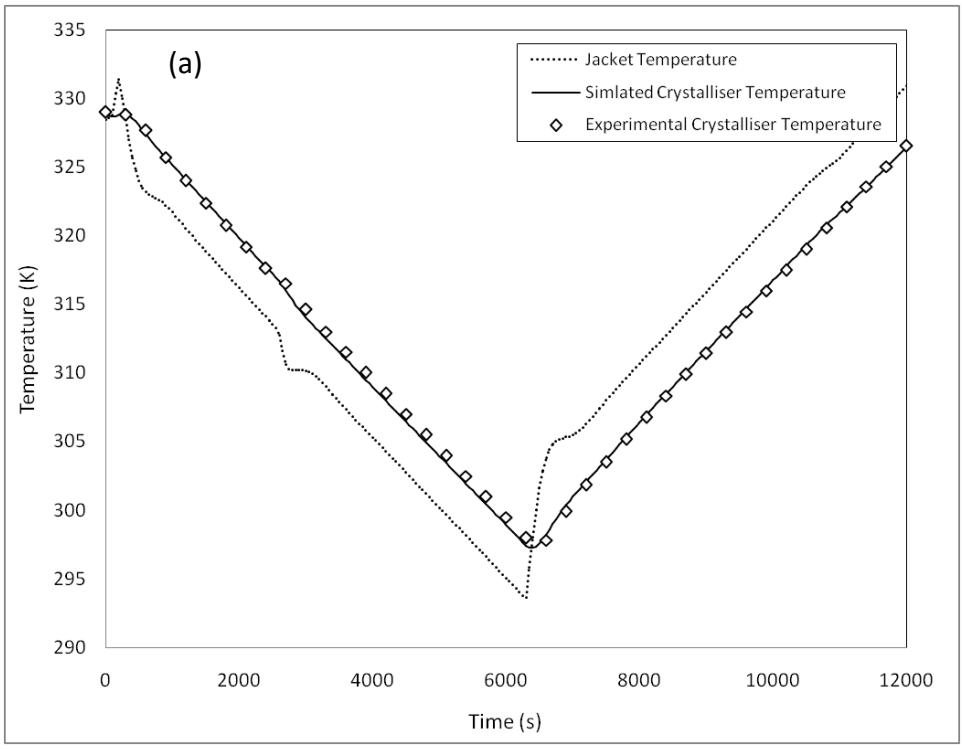
(a)
Jacket Temperature
Simlated Crystalliser Temperature
Experimental Crystalliser Temperature
Temperature (K)
335
330
325
320
315
310
305
300
295
290
0
2000
4000
6000
8000
10000
12000
Time (s)

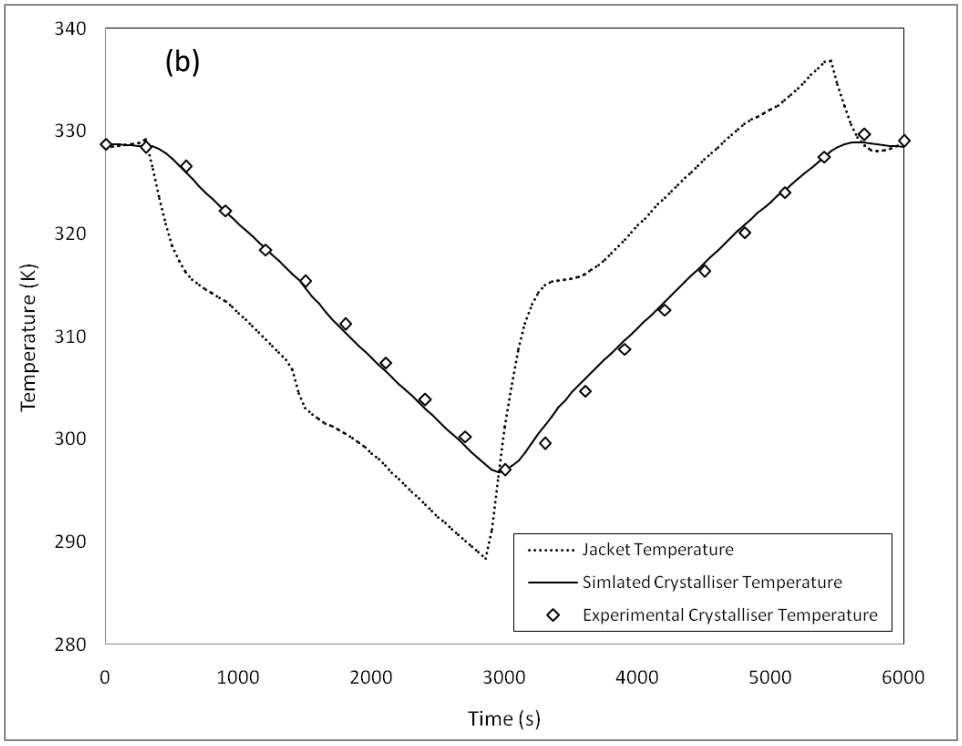
(b)
Jacket Temperature
Simlated Crystalliser Temperature
Experimental Crystalliser Temperature
Temperature (K)
340
330
320
310
300
290
280
0
1000
2000
3000
4000
5000
6000
Time (s)

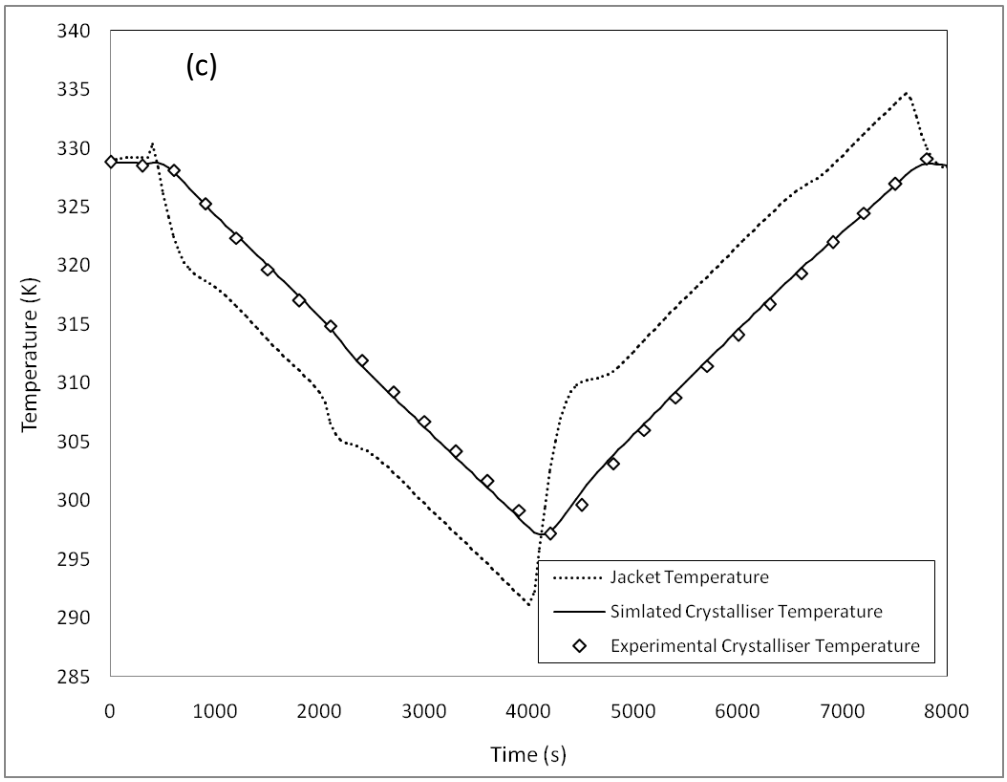

Figure 4.5. Comparison of experimental temperature profile with simulated temperature profile for (a) 0.3 K/min (b) 0.7K/min (c) 0.5K/min heating/cooling rate profile

4.4.1.2. Estimation of mean particle size

For the purposes of estimating reliable values for crystallisation kinetics, it is important to obtain estimates for the average particle size distribution during the crystallisation process. The model described in Chapter 2 was used to estimate the mean particle size for the present case. A validation for the Chord Length Distribution (CLD) to Particle Size Distribution (PSD) model for the case of Sodium Nitrite was not performed. In Chapter 2, the model was validated for a variety of shapes and particle systems. Hence, the authors believe that, the values obtained using the model would serve as a good starting point for estimating crystallisation kinetics. Kinetic parameter values may be re-estimated when more reliable values for the mean particle size become available.

The PSD can be estimated by comparing the experimental normalized CLD against the model predicted one. For this purpose, as described in Chapter 2, both the unweighted and the square-weighted forms of the CLD were used depending upon the system considered. In most cases (regular uni-modal systems), the PSD obtained using both forms of the CLD are nearly identical. However, in certain cases, such as where the shape of the original CLD is not entirely

uni-modal (due to a disproportionate recording of smaller particles), different PSD's are predicted using the two CLD forms. The CLD to PSD procedure was implemented for both the forms of the CLD and comparisons between the normalized experimental and model predicted CLD's are shown in Figure 4.6. The CLD for a particular instance after crystallisation had occurred in the 0.5 K/min cooling rate experiment was considered.

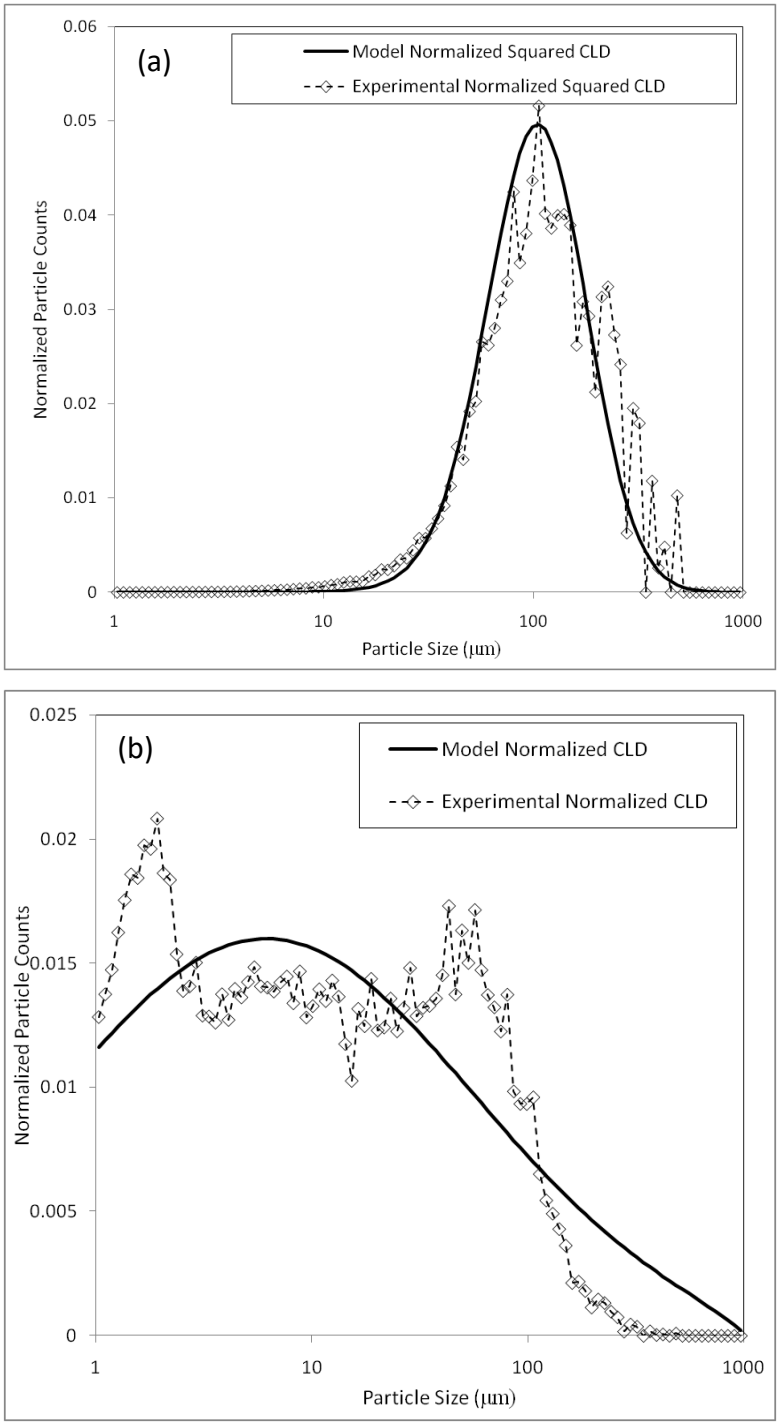

Figure 4.6: (a) Comparison of the measured squared normalized CLD to the model predicted squared normalized CLD; (b) Comparison of normalised experimental CLD to the normalised model predicted CLD

A limitation of the CLD to PSD model is that it can model only normal or lognormal shaped distributions. It can be seen from Figure 4.6(b), the experimental unweighted CLD was not properly captured using the model predicted one (R^2 = 0.93). This lead to a significant difference between even the mean chord lengths predicted by the model and the experiment. On the other hand, the model predicted normalized square-weighted CLD resembled the experimental one to a very high degree (R^2 = 0.97) as can be seen in Figure 4.6(a). Thus, the average particle sizes were obtained using the square-weighted form of the CLD which was seen give predictions consistent with experimental data.

4.4.1.3. Estimating crystallisation kinetic parameters

Simulations were carried out for the crystallisation leg of the batch experiments for the system of sodium nitrite-water. The present procedure differs from the procedure presented in Chapter 3 in the manner that additional parameters for growth rate kinetics and heat of crystallisation also were estimated along with the crystallisation kinetic parameters. Additionally, the meta-stable zone width (MSZW) needs to be supplied for simulations. The MSZW was determined experimentally for each of the experiments. First, the kinetic parameter values were estimated by simultaneously matching the simulated and experimental normalized 0th moment curves and the simulated and experimental Sauter mean diameter (d_{32}) curves for one set of experiments (0.7 K/min). The comparison were then done for the other sets of experiments (0.3 K/min and 0.5 K/min) using the parameter values estimated in the first step.

The methodology for estimating the parameter values used in the present chapter was similar to the one described in Chapter 3. The methodology involves iteratively changing the most sensitive unknown parameter values while keeping the least sensitive parameters constant. The parameter values were changed with subsequent iterations by comparing suitable model predicted and experimental objective functions. A list of parameter values obtained by the matching simulated data to experiments is shown in Table. A comparison between the experimental and simulated normalized 0^{th} moment for the 0.7 K/min heating/cooling rate is shown in Figure 4.7(a). A comparison for the experimental and simulated Sauter mean diameter values is shown in Figure 4.7(b). Parameter values estimated using 0.7K/min cooling/heating rate were then used to simulate for the 0.5K/min and 0.3K/min

cooling/heating rates. Comparison between the respective experimental and simulated profiles are given in Figures 4.8 and 4.9. It can be seen from the Figures that the model predictions agree with the experimental data obtained for the batch mode of operation.

Table 4.1. Crystallisation kinetics parameter values for the batch crystallisation of Sodium Nitrite-Water system

Symbol	Description	Value	Unit
$k_{g,0}$	Pre-exponential constant for growth rate	9.0E+01	$(m/s)(kmol/m^3)^{-g}$
E_A	Activation energy	4.0E+07	J/(kmol-K)
R	Universal gas constant	8.314E+03	J/kmol
g	Growth rate exponent	2	-
k_1	Constant for primary nucleation rate expression	1.5E+08	$\#/(m^3\text{-}s)(kmol/\ m^3)^{-n1}$
n_1	Exponent for primary nucleation rate expression	2	-
k_2	Constant for secondary nucleation rate expression	1.5E+10	$1/((\ m^2\text{-}s)(kmol/\ m^3)^{-n2})$
n_2	Exponent for secondary nucleation rate expression	4.5	-
$-\Delta H_C$	Heat of crystallization	1.5E+05	J/kg
MSZW	Meta Stable Zone Width	3.5	^0C

As was discussed in the previous Chapter, it is possible to have multiple solutions for the crystallisation parameter values if just the normalised 0th moment curves are considered for comparison. This may be achieved, starting from a set of already 'validated' parameters by increasing the constant for the growth kinetics while simultaneously reducing the constants for the nucleation kinetics and vice versa. However, the story changes if both the normalized 0th moment curve and the Sauter mean diameter curves are considered for comparison. For instance, if the value of the growth rate constant is increased and the values of the nucleation constants are reduced to match the normalized moment curves, this effectively serves in increasing the average Sauter mean diameter curve from the base case. And decreasing growth rate constant and increasing the nucleation rate constants effectively serves in decreasing the average Sauter mean diameter curve from the base case. Thus, we can say that for the present case, the solution is unique.

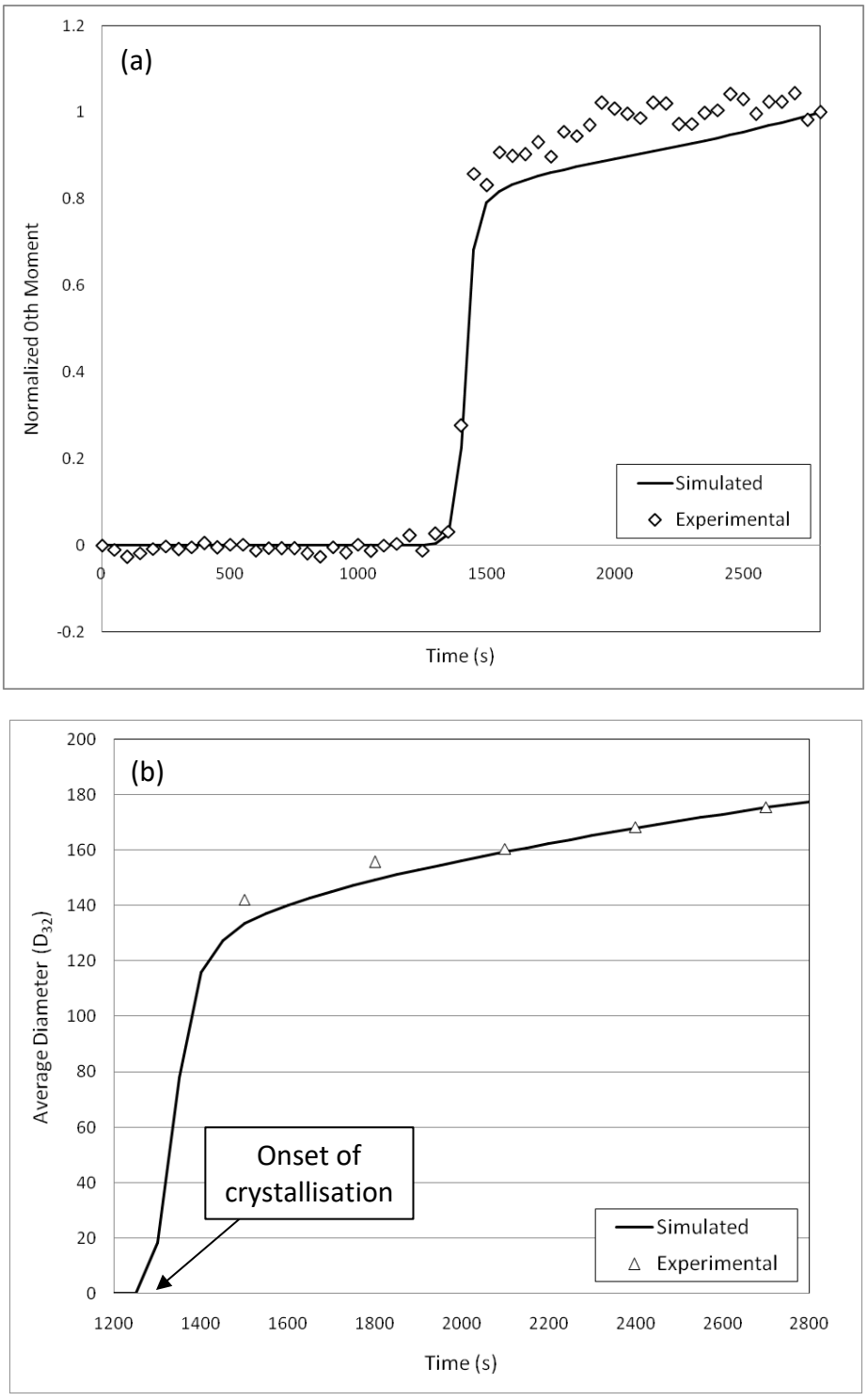

Figure 4.7. (a) Comparison of experimental and simulated 0th Moment for the 0.7 K/min batch experiment; (b) Comparison of experimental and simulated Sauter mean diameter (d_{32}) for the 0.7 K/min batch experiment

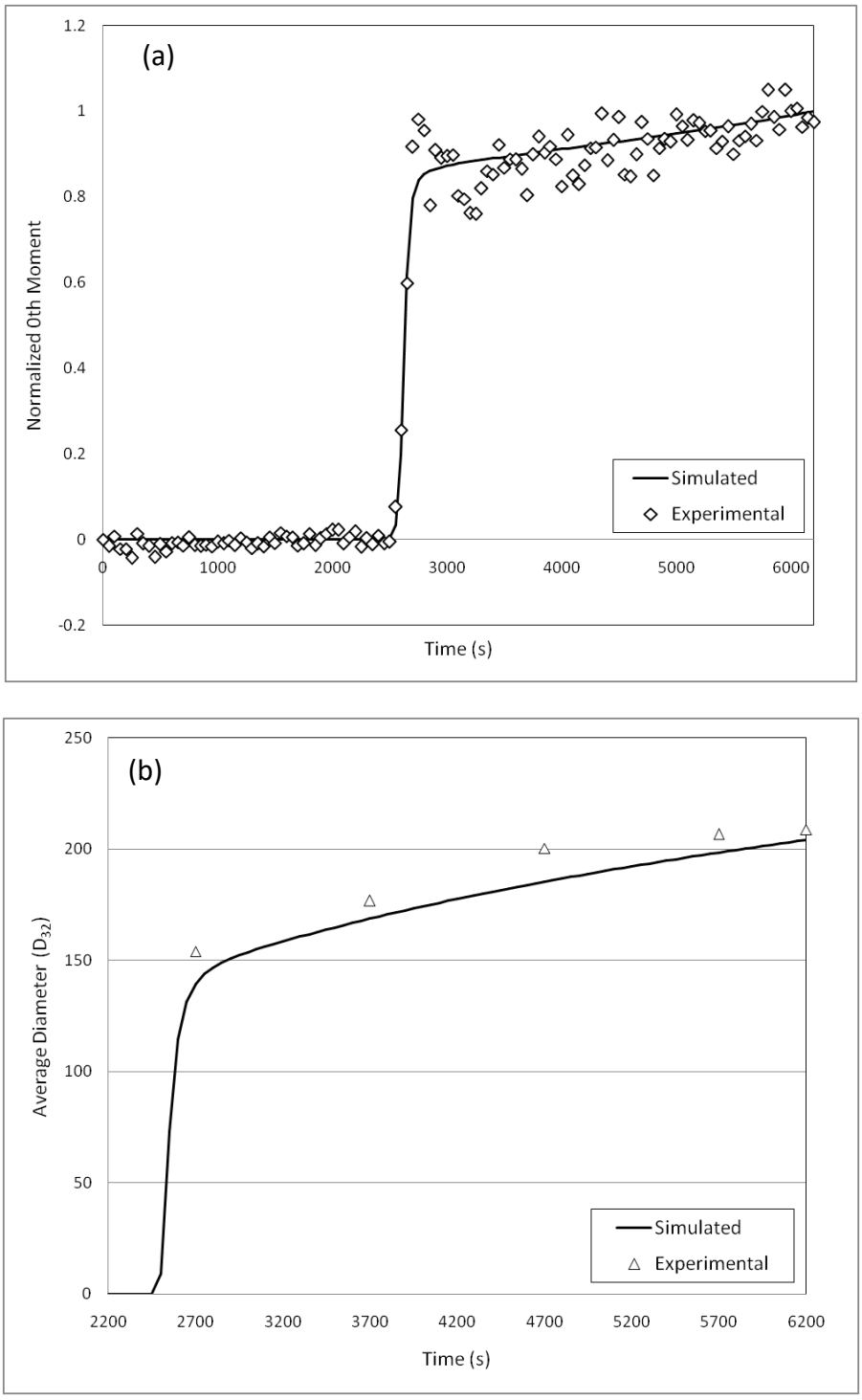

Figure 4.8. (a) Comparison of experimental and simulated 0th Moment for the 0.3 K/min batch experiment; (b) Comparison of experimental and simulated Sauter mean diameter (d_{32}) for the 0.7 K/min batch experiment

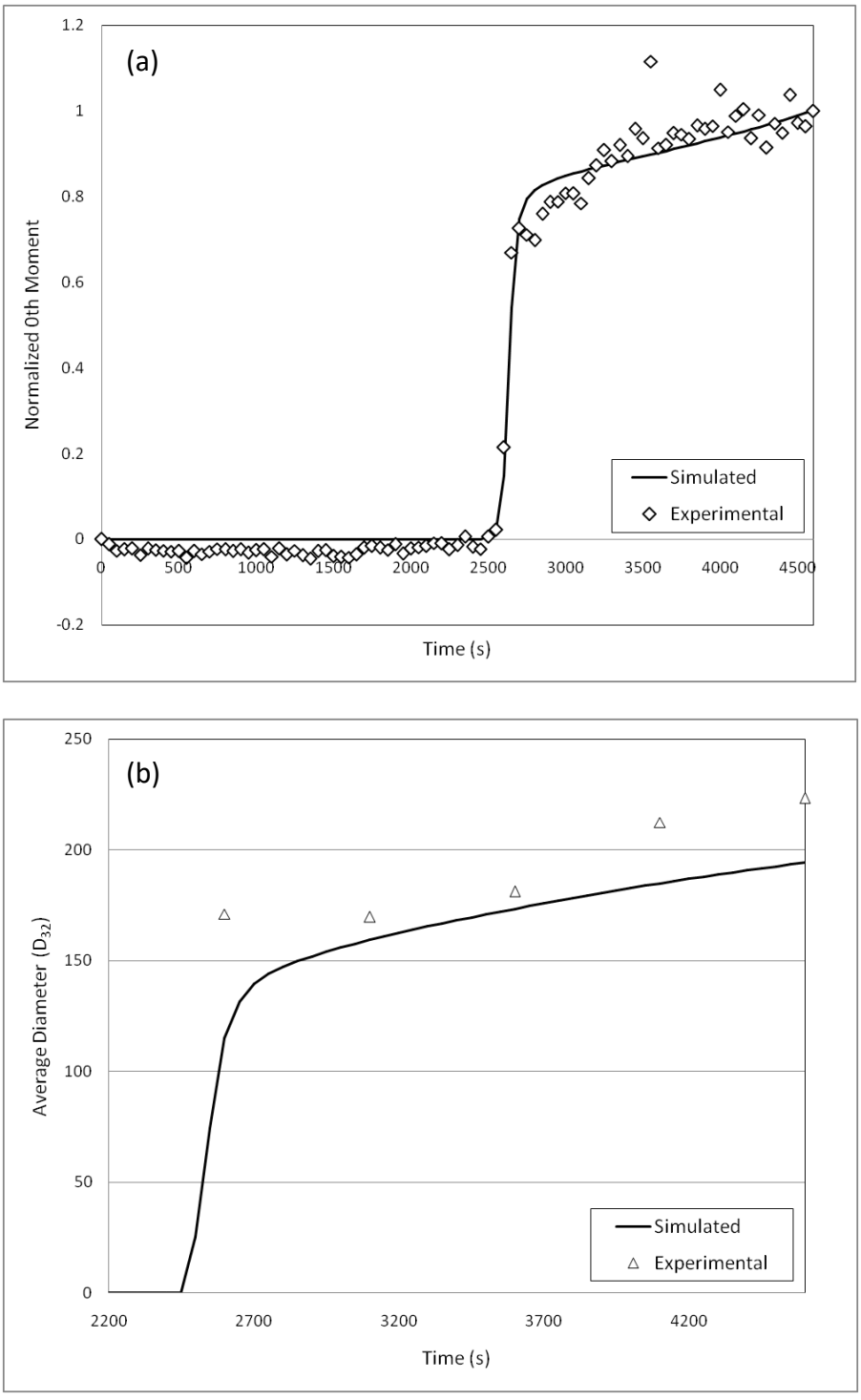

Figure 4.9. (a) Comparison of experimental and simulated 0th Moment for the 0.5 K/min batch experiment; (b) Comparison of experimental and simulated Sauter mean diameter (d_{32}) for the 0.7 K/min batch experiment

Multiple solutions may in fact be possible for the growth rate constant and the activation energy for the estimated nucleation kinetic parameters. The parameter for activation energy is chiefly responsible in characterising how the growth rate depends on the temperature. However, in the present case, the crystallisation occurs very fast and does not span a very

wide temperature range. Hence, the effect of temperature (significance of the activation energy parameter) on the growth rate parameters cannot be studied. Hence, for the present case from the preceding discussion we may say that the obtained total contribution of the growth rate term won't vary drastically even though the individual parameter values may vary.

4.4.1.4. Effect of Heat of Crystallisation

The crystallisation of sodium nitrite from water is exothermic. That is, on crystallisation, heat is liberated into the solution thereby increasing the solution temperature. As precise temperature control was maintained in the batch process by the virtue of the OptiMAX Peltier elements, the jacket temperature dipped to compensate for the heat gained. This dip (shown in Figure 4.10(a)) was observe to coincide with the onset of crystallisation. In contrast to the model described in Chapter 3, the heat balance equation was included in the present model. Hence, it was possible using the present model to capture the heat transfer exchanges occurring in the system. For simulation purposes, the jacket temperature profile was provided as an input to the crystalliser temperature profile was calculated by solving the model equations. The heat of crystallisation was estimated by making the simulated crystalliser temperature match the experimental crystalliser temperature.

A comparison between the simulated crystalliser temperature profiles obtained for different values of heat of crystallisation and the experimental temperature profile is given in Figure 4.10(a). The effect of the heat of crystallisation of the Sauter mean diameter is given in Figure 4.10(b). As can be seem from the figure, a lower heat of crystallisation results in a higher SMD. This is because, as crystallisation progresses and heat is released, lesser is the heat released, lesser is the super saturation decreased due to heat effects. A higher heat of crystallisation suppresses both growth and nucleation due to the reduction in the degree of super saturation. A comparison between the experimental and simulated (for different values of heat of crystallisation) normalized 0^{th} moment during crystallisation is shown in Figure 4.10(c)

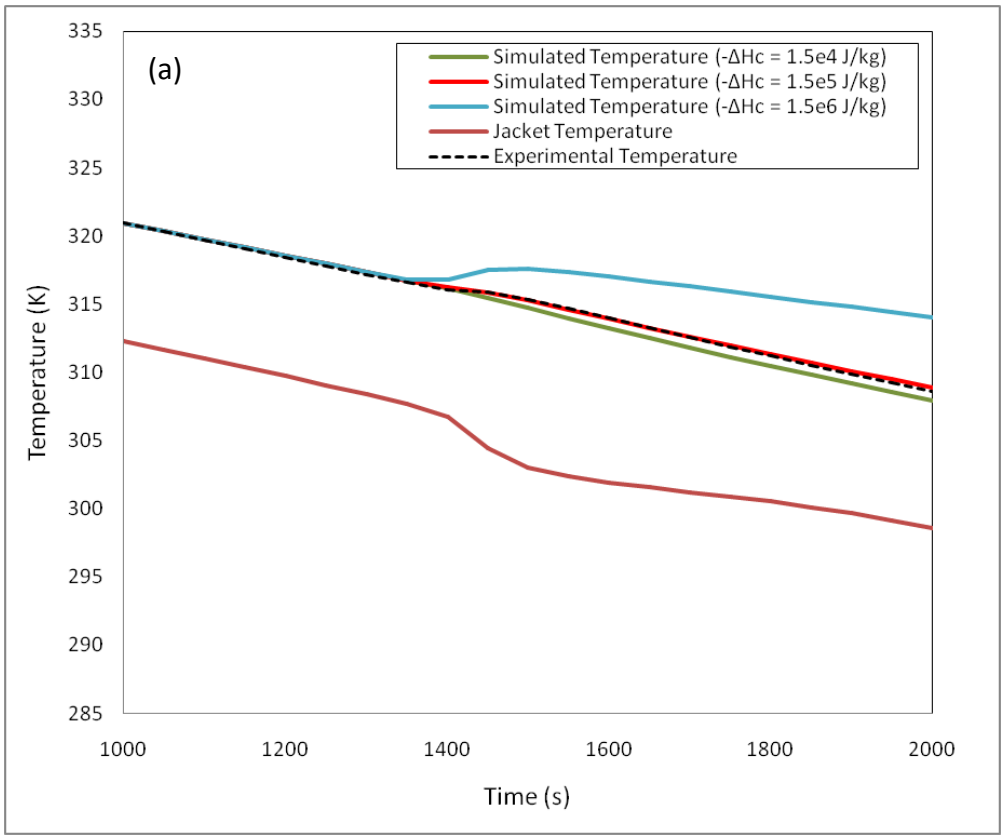
(a)
Simulated Temperature (-ΔHc = 1.5e4 J/kg)
Simulated Temperature (-ΔHc = 1.5e5 J/kg)
Simulated Temperature (-ΔHc = 1.5e6 J/kg)
Jacket Temperature
Experimental Temperature
Temperature (K)
335
330
325
320
315
310
305
300
295
290
285
1000
1200
1400
1600
1800
2000
Time (s)

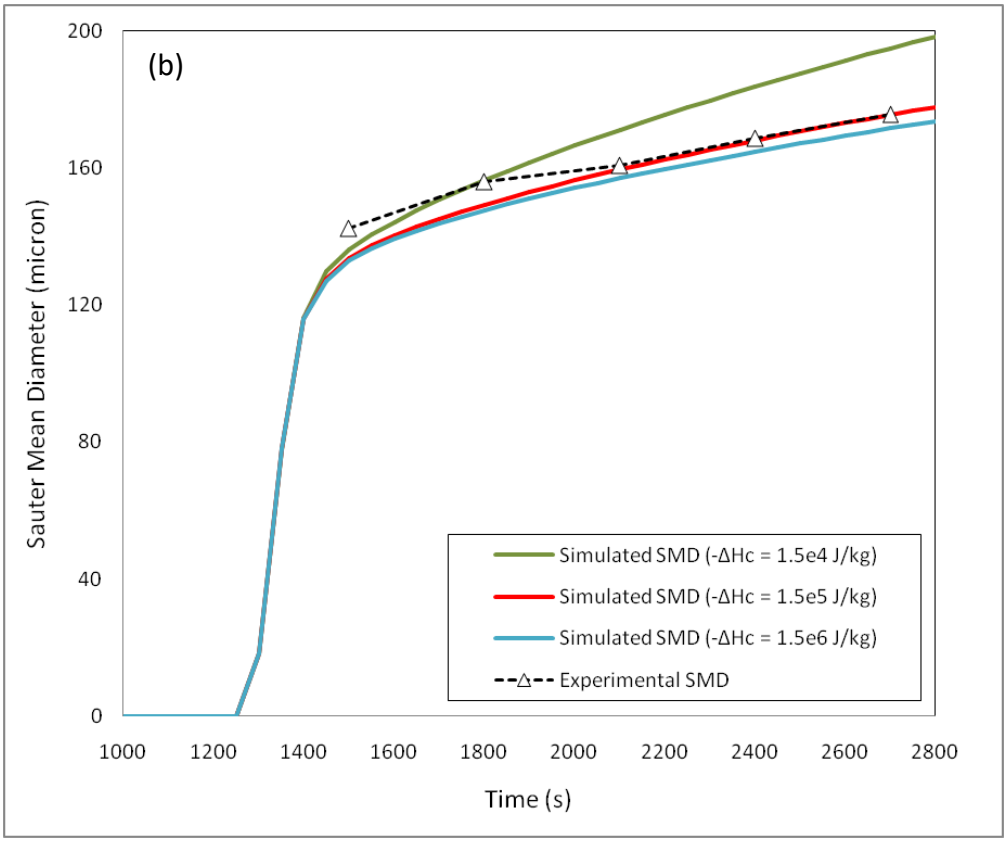
(b)
Simulated SMD (-ΔHc = 1.5e4 J/kg)
Simulated SMD (-ΔHc = 1.5e5 J/kg)
Simulated SMD (-ΔHc = 1.5e6 J/kg)
Experimental SMD
Sauter Mean Diameter (micron)
200
160
120
80
40
0
1000
1200
1400
1600
1800
2000
2200
2400
2600
2800
Time (s)

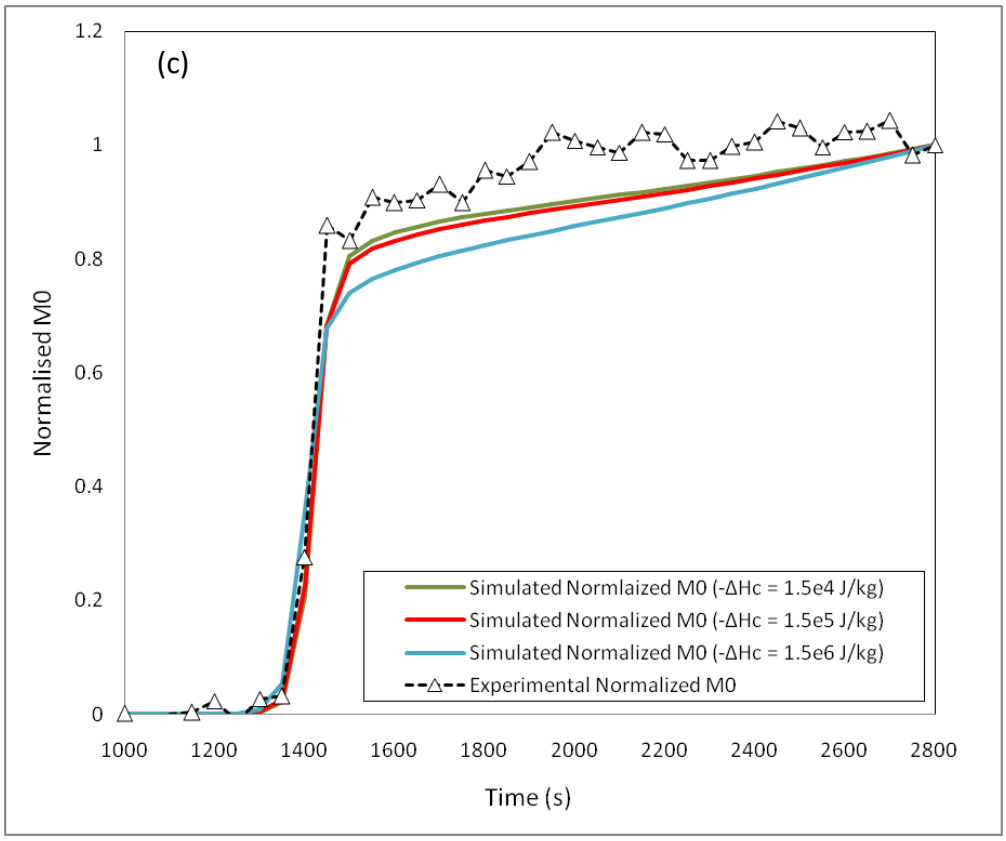

Figure 4.10. Comparison between experimental and simulated values for different values of heats of crystallisation for the 0.7K/min experiment of (a) Crystalliser temperature (b) Sauter Mean Diameter (d_{32}) (c) Normalised 0^{th} moment

4.4.2. Crystallisation of Continuous Processes

In the previous section, the model was validated for a batch system of sodium nitrite and water. The batch experiments were instrumental in estimating key crystallisation kinetic parameter values. In the present section, the case of a continuous crystalliser will be investigated. Sodium Nitrite-Water system - used in batch - was also considered for continuous crystallisation. Experiments were performed to understand the mixing and heat transfer characteristics of the continuous crystalliser assembly. Then continuous crystallisation experiments were performed under different ambient conditions. Side by side, the model described earlier in the Chapter, was implemented for the specific case of continuous crystallisation considered in the experiments. The mixing and heat transfer behaviour was characterised by comparing model predictions to experiments. The model was then used to simulate continuous crystallisation. The model was then used to understand the effect of different operating conditions on the crystallisation behaviour.

4.4.2.1. Characterising Mixing Behaviour

It is important from the point of view of crystalliser design and modelling to characterise the mixing behaviour of the crystalliser. The residence time distribution is one of the most popular methods to characterise the mixing behaviour of reactors. To determine the exit age distribution or more commonly known as the residence time distribution (RTD) of a crystalliser at a particular flow rate, a pulse of tracer is injected into the inlet in steady flowing conditions. The outlet concentration of the tracer is monitored with time. The profile of the tracer concentration with respect to time is known as the RTD. As discussed earlier in the present Chapter, the tanks in series is an efficient way for a generalised modelling framework. Amongst other things, the RTD curve helps to identify the number of perfectly mixing tanks that should be connected in series to obtain a mixing behaviour similar to the device considered.

RTD experiments were performed using the present continuous crystalliser assemble at different flow rates. Salt water solution was used as a tracer and DI water was used as the solvent phase. A pulse input of about 20 ml was pumped in using a syringe at the inlet. The outlet tracer concentration was measured using a conductivity probe. The RTD was obtained for different configurations for the inlet port (upper/lower) and the stirrer mode (forward /reverse). A comparison of the normalised RTD plotted versus the time (normalised by the average residence time) for different operating modes and residence times is shown in Figure 4.11(a). It can be concluded from the figure that there is not much change in the mixing characteristics of the crystalliser due to the different operating modes or residence times. Going by standard practises, the bottom inlet was chosen as the inlet port for the crystallisation experiments. The stirrer mode was chosen to be as a forward mode.

As discussed earlier, the RTD experiments enable us to characterise the mixing behaviour of crystallisers. Simulations were performed using the tanks in series model developed here for modelling continuous crystallisation processes. A pulse was simulated as setting the initial concentration of the first tank to a specific value. The initial concentration of the other tanks and the inlet was fixed to zero. The simulations were then performed for one, two and three tanks in series. The outlet concentration of the last tank was normalised to determine the RTD. A comparison between the experimentally obtained RTD for the chosen configuration and the RTD's obtained through simulations are shown in Figure 4.11(b). As can be seen from

the Figure, two tanks in series seem to capture the mixing characteristics of the continuous crystalliser well. Hence, in further simulations, the number of tanks in series for the continuous crystalliser was set to two.

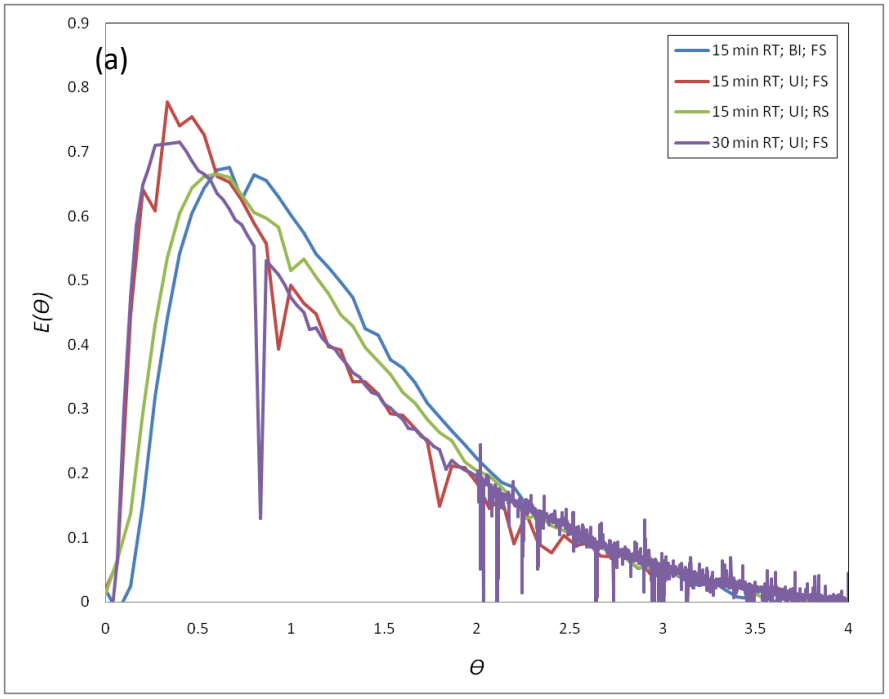

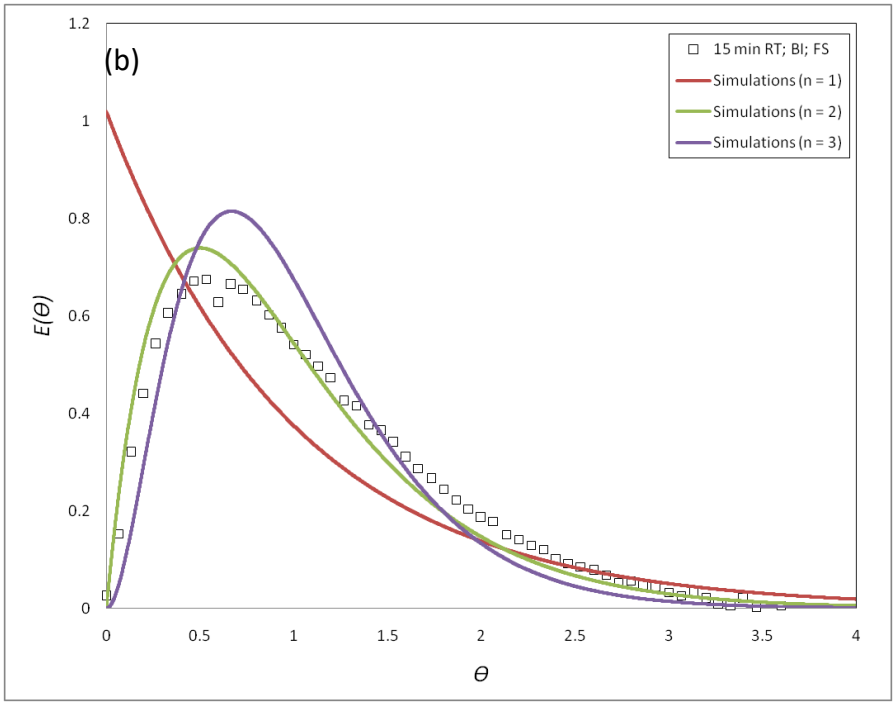

Figure 4.11. (a) Comparison of normalized exit age distribution curves plotted against time normalized by the residence time (RT) for different operating modes (BI - Bottom Inlet, UI - Upper Inlet)(FS - Forward Stirrer, RS - Reverse Stirrer) (b) Comparison of normalized exit age distribution curves plotted against time normalized by the residence time (RT) obtained experimentally and through simulations using multiple tanks

4.4.2.2. Characterising Heat Transfer

For completing simulations, heat transfer parameters need to be estimated as done for batch processes. However, there was a problem for the case of the continuous process considered. Heat transfer experiments were done under different ambient conditions. Experimentally, for a given jacket temperature, the steady state temperature at the crystalliser outlet attained the same value regardless of the ambient temperatures. Thus, we may conclude that the contribution towards the environmental losses was not significant. However, when the source term for the environmental losses was switched off in the model, it was not possible to simulate the crystalliser outlet temperature profile. This meant that the heat transfer model described in the present Chapter was not adequate.

The reason for this mismatch was that in the experiments, the heat was first transferred from the jacket to the crystalliser body. From the crystalliser body the temperature was transferred to the process fluid and the environment. However, while modelling, the thermal inertia of the crystalliser body was not considered and the heat transfer was said to occur directly between the process fluid and the jacket/environment. The thermal inertia of the crystalliser body was significant in comparison with that of the process fluid and arguably controlled most of the thermal behaviour. A more detailed discussion about characterising heat transfer in the continuous process is provided in the Appendix A3.

4.4.2.3. Simulations for continuous crystallisation

As discussed earlier, it was not possible to estimate the heat transfer characteristics using the present model. A consequence of this was that the heat of crystallisation could not be estimated and was set to zero. Simulations were carried out by manipulating the heat transfer parameters so as to impose the expeirmental crystalliser outlet temperature profile on the simulations. As done in previous cases, the experimental jacket temperature was taken as the input. A comparison between the same may be seen in Figure 4.12(a). Simulations were carried out by using the crystallisation parameter values obtained during the batch crystallisation. The experimental conditions of the *CC8* experiment were simulated. The outlet flowrate was 20ml/min. The inlet concentration of the solvent-solute mixture was taken to be equal to the initial experimental outlet concentraiton. Simulation profiles for the outlet normailzed 0^{th} moment, the outlet temperature and experimental profiles for the jacket

temperature and the outlet crystalliser temperature are shown in Figure 4.12(a). Simulation profiles for the mean and variances of the outlet PSD and the outlet super saturation ratio are shown in Figure 4.12(b).

There was a significant difference between the absolute steady state outlet concentration values between the experimental and simulated conditions. The reason for this mismatch was attributed to the fact that solubility measurements for the case of sodium nitrite-water system were done using visual methods whereas the concentration measurements were done by more accurate and precise refractometer based measurements. Solubility data for sodium nitrite-water system was not reported in litereature and hence could not be used for simulations. Ideally, the crystallisation kinetic parameters need to be re-estimated with more accurate solubility data. However, even with the mismatch, we may say that the overall methodolgy to model continuous crystallisation processes would remain the same.

A useful inference may still be made by considering the model predicted and experimental normalized outlet concentraiton profiles. To enable the comparison between the simulated and experimental profiles, they were normalised according to the following formula:

$$Y_{norm,i} = (Y_i - Y_{last})/(Y_{first} - Y_{last}) \tag{4.69}$$

A comparison between the normalized simulated and experimental outlet concentration profiles is shown in Figure 4.13. As can be seen from the Figure there is an excellent comparison between the normalised simulated and experimental outlet concentration profiles. Hence, it may be inferred that the assumption that the MSZW for the case of continuous crystallisation is zero is validated. Also, the model was successful in capturing the overall concentration profile.

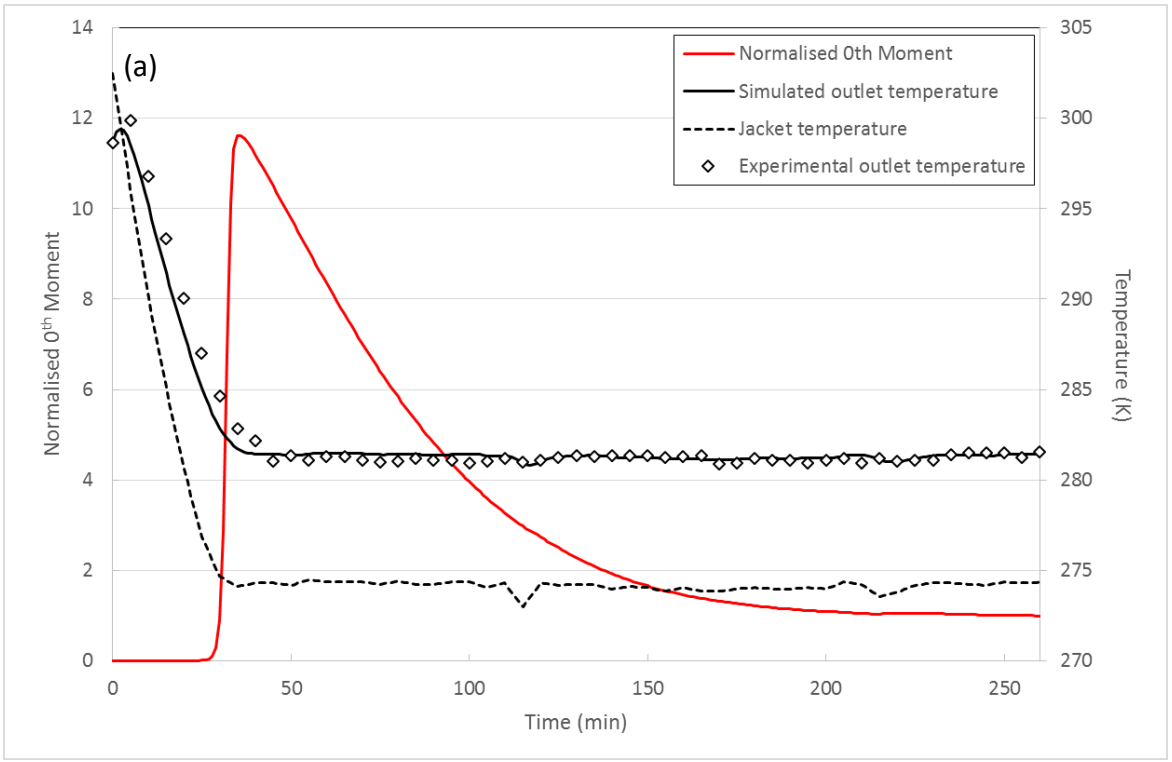

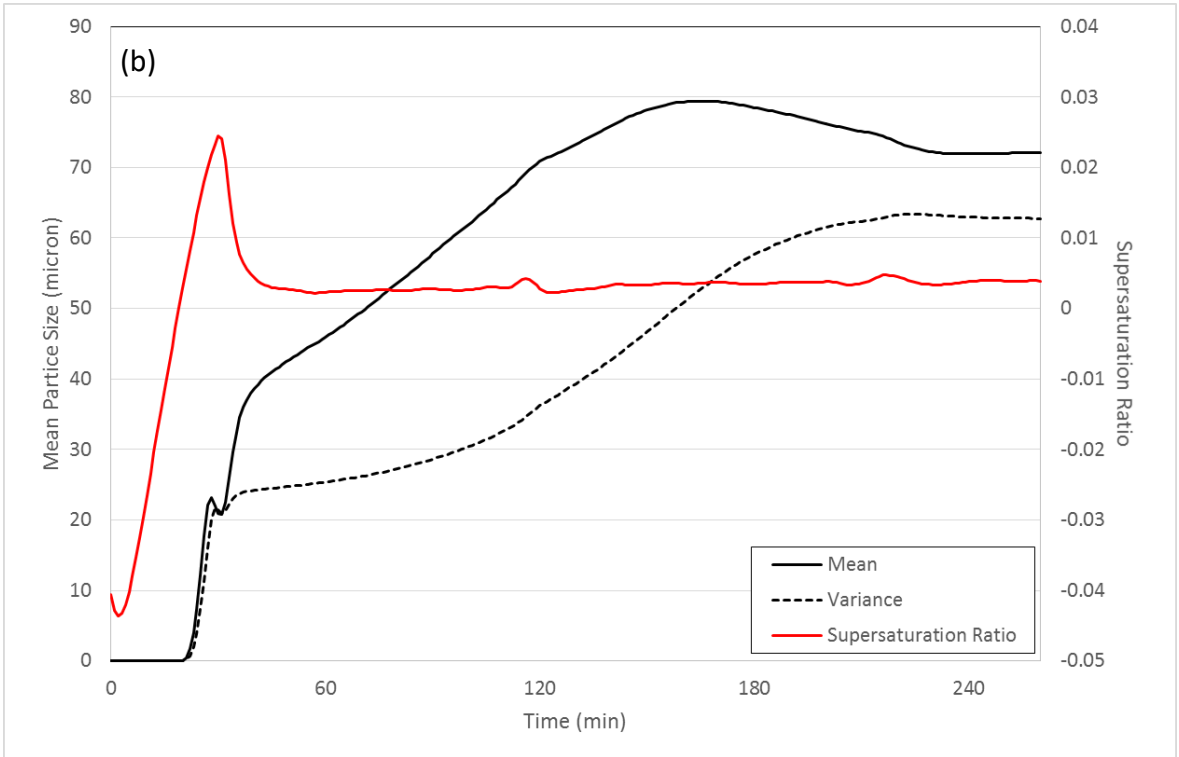

Figure 4.12. Simulation profiles for the CC8 experiment of (a) normalised 0th moment, the experimental and simulated outlet temperature and the experimental jacket temperature (b) mean and variance of the outlet particle size distribution and the outlet supersaturation ratio

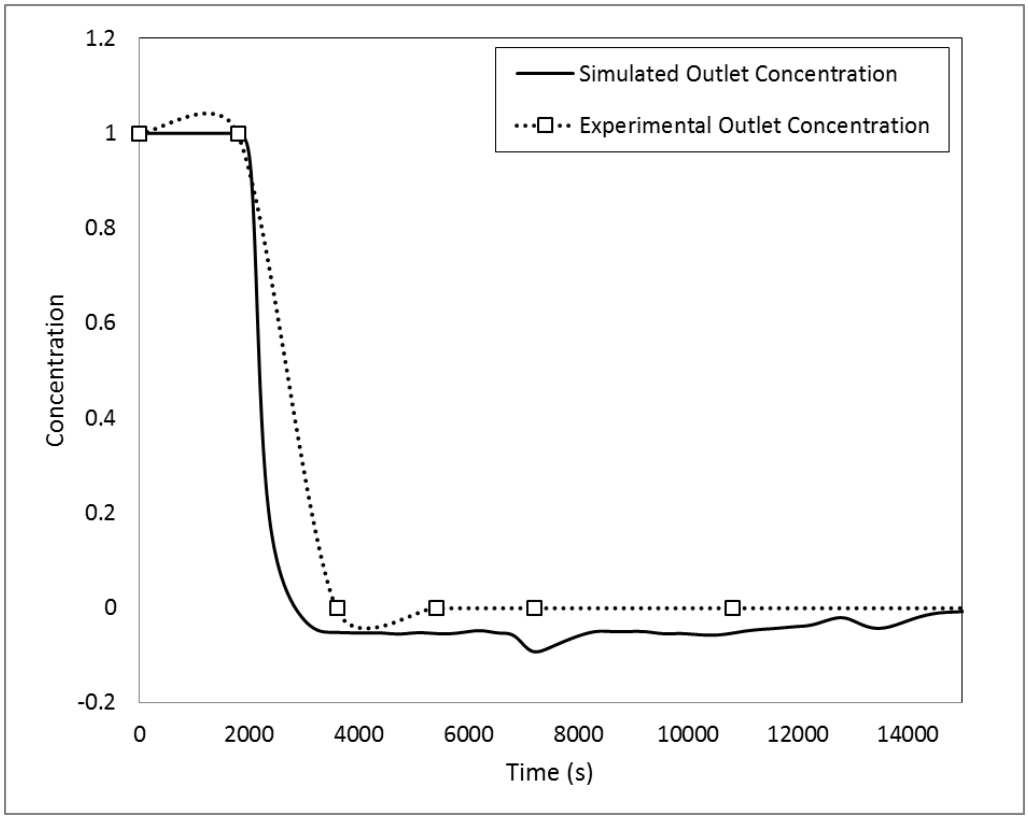

Figure 4.13. Comparison between the normalised experimental and simulated outlet concentration profiles for the *CC8* experiment

4.4.2.4. Influence of operating parameters

The developed model was used to understand the influence of key operating parameters on the product quality parameters. The product quality parameters of the mean and the variance of the PSD were considered. The mean of the PSD was defined using the moments as follows:

$$\mu = \frac{\int_0^\infty Ln(L)dL}{\int_0^\infty n(L)dL} = \frac{M_1}{M_0} \tag{4.70}$$

The variance of the PSD was defined using the moments as follows:

$$\sigma^2 = \frac{\int_0^\infty (L-\mu)^2 n(L)dL}{\int_0^\infty n(L)dL} = \frac{M_2}{M_0} - \mu^2 \tag{4.71}$$

Besides these, the yield of the crystallisation process and the time required to reach steady state were also investigated as key process performance parameters. The yield of the process can be defined as:

$$yield(\%) = 100\left(\frac{C_{in} - C_{out}}{C_{in} - C^*(T)}\right) \quad (4.72)$$

The time required to reach steady state is important from a process control point of view. A system which has a faster response to step changes can essentially be controlled more easily.

The influence of the crystalliser mixing behaviour (number of tanks) and key operating parameters of residence time and jacket temperature on the product quality and process performance parameters was investigated. Simulations were carried out considering a constant jacket temperature of 280^0K and a very high heat transfer coefficient such that the reactor operating temperature is maintained equal to the jacket temperature. The term for the environmental losses was not considered in the present hypothetical study. The inlet temperature of the liquid was considered to be equal to the jacket temperature. The inlet concentration of the sodium nitrite solution was 0.81 g-solute/g-solvent. For carrying out the base case simulations, a flow rate of 20 ml/min (residence time of 65 min) and a mixing behaviour equivalent of 2 tanks in series was considered.

As can be seen from the Figure 4.14(a), increasing the number of tanks-in-series leads to a substantial decrease in the time required to reach steady state. This can be observed for all the flow rates considered. Hence, we may conclude that crystallisers with more of a plug-flow like mixing behaviour respond faster to step changes and can be controlled easily. The time was normalised using residence time. From the Figure 4.14(b), it can be seen that the mean size of the outlet particle size distribution keeps on decreasing with decreasing residence time (increasing flow rates). The difference between the mean and the variance of the outlet particle size distribution, however, seems to remain unaffected by the residence time. A shift towards smaller particle sizes is also seen on increasing the number of tanks-in-series across all residence times. Hence, it may be concluded that to achieve smaller particle sizes, either the flow rates must be increased or the crystalliser should be designed to have a more 'plug-flow like' mixing behaviour.

On increasing the number of tanks-in-series, the difference between the mean and the variance of the outlet particle size distribution also increased. Thus, narrower particle size distributions are expected for crystallisers with a mixing behaviour approaching plug flow. With regards to yield (Figure 4.14(c)), it was observed that the yield decreases with decreasing residence time (increasing flow rates) regardless of the mixing behaviour. Also, crystallisers

with a mixing behaviour approaching plug flow were seen to give significantly higher yields for the same residence time than their CSTR counterparts.

From the results discussed above, it may be concluded that **crystallisers with mixing behaviours approaching plug flow offer higher yield, narrower outlet particle size distributions and better process control than their CSTR counterparts**. Plug-flow crystallisers were also seen to offer smaller particle sizes for the same residence time than their CSTR counterparts. The residence time distribution was also identified as a key variable to control the mean size of the outlet particle size distribution. Decreasing the residence time (increasing flow rate) was seen to provide smaller particle sizes, however, at the expense of a lower yield.

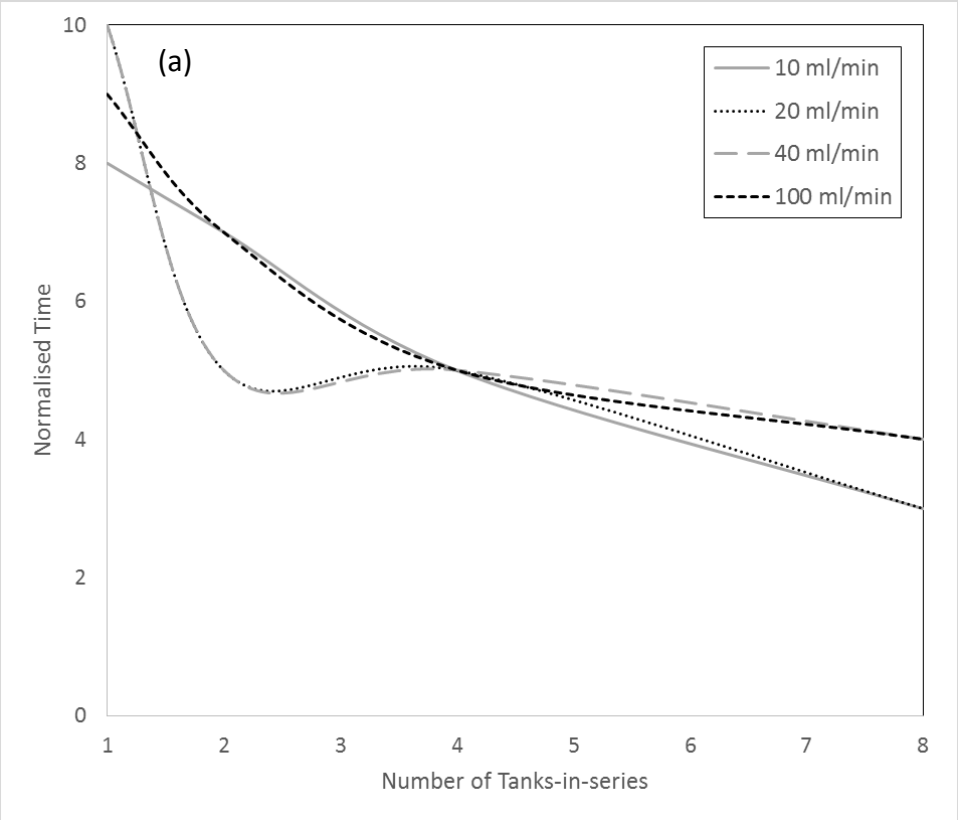

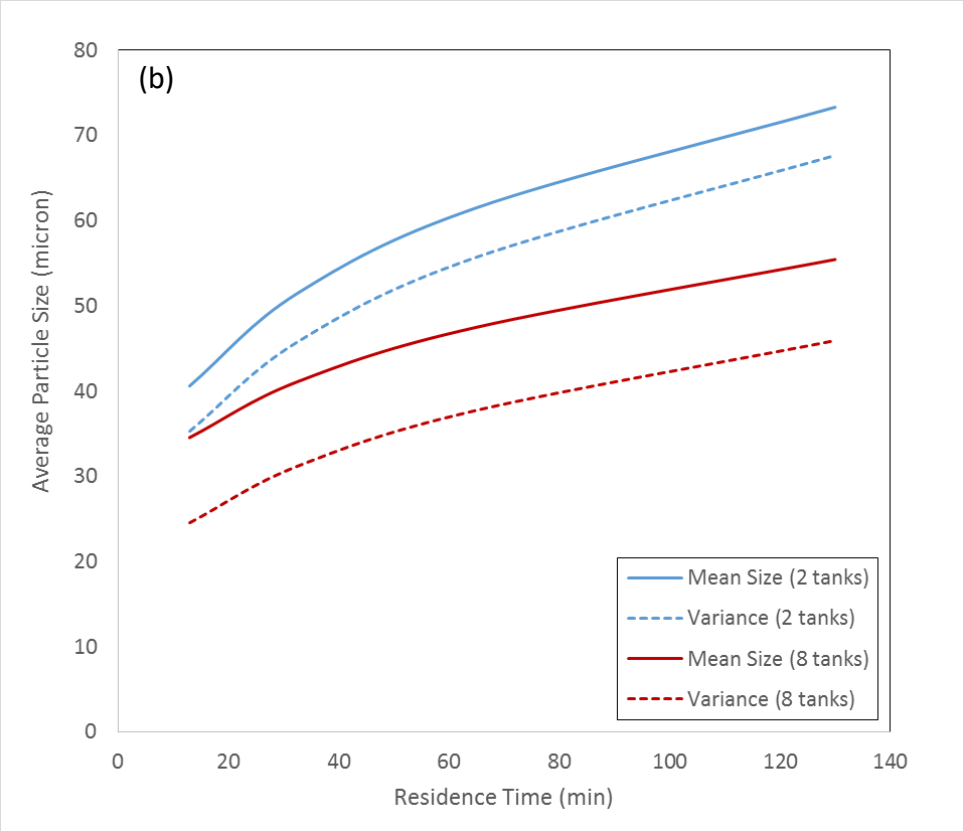

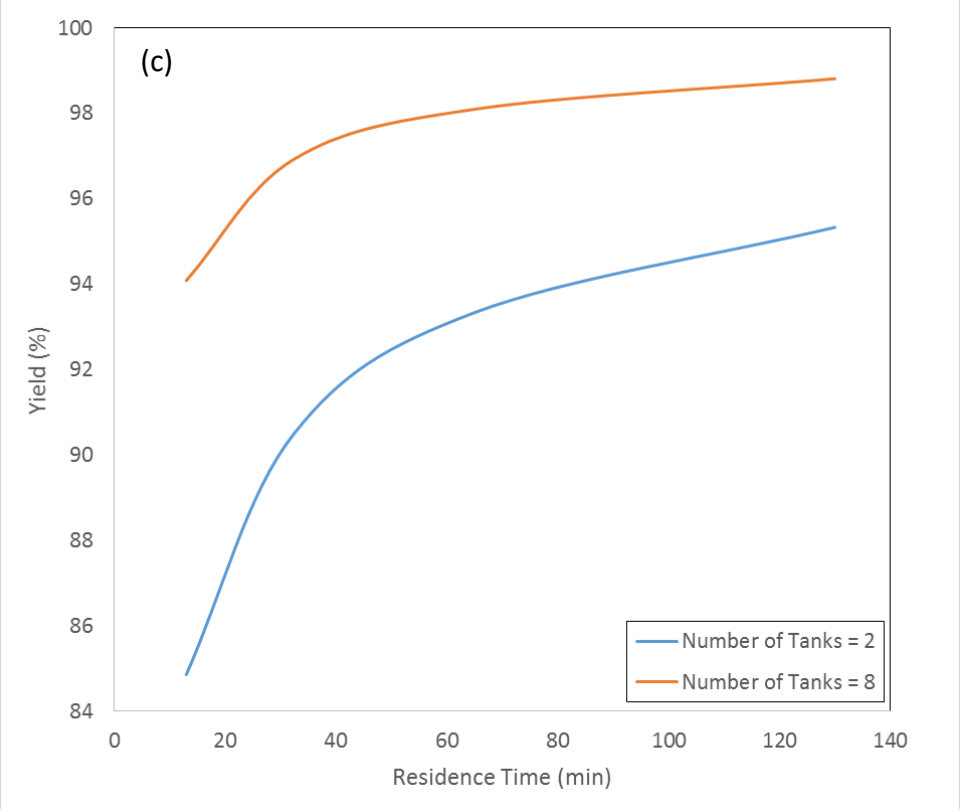

Figure 4.14. Comparison between the (a) normalised time to reach the steady state for different flow rates (b) mean and variance of the particle size distribution using 2 tanks and 8 tanks-in-series (c) yield versus residence time plots obtained using 2 and 8 tanks-in-series

4.5. Summary & Conclusions

In the present Chapter, a methodology to model continuous crystallisation processes was developed and implemented. According to the methodology, key crystallisation kinetic parameter values are first required to be estimated from experimental and modelling studies of batch processes. These parameter values can then be used while simulating continuous crystallisation processes. In line with this methodology, first, the experimental methods for the batch and continuous processes were discussed. The system considered was sodium nitrite in water. A comprehensive mathematical model based on a tanks-in-series framework was formulated. The model was formulated such that both continuous and batch processes could be simulated within the same framework. Appropriate reference variables were identified and used for formulating suitable dimensionless parameters to characterize crystallizer performance. The key issues relating to the onset of crystallisation for batch and continuous processes were addressed. For continuous crystallisation processes, it was argued that the onset of crystallisation occurs immediately after the solution reaches supersaturation.

As per the methodology described in this Chapter, first, key crystallisation kinetic parameter values and heat transfer parameter values need to be estimated from batch studies. Then, the methods based on the CLD to PSD model described in Chapter 2 were used to estimate the average Sauter mean diameter during crystallisation for sodium nitrite crystals. It was observed that the square weighted chord length distribution (CLD) provide more robust estimate of the PSD than the unweighted CLD. Hysteresis style experiments (described in Chapter 3) were performed. The kinetic parameter values were estimated by comparing model predictions to the experimental results for the normalised 0^{th} moment of particle counts and the average Sauter mean diameter simultaneously. The model was validated by comparing model predictions with experimental results for different sets of experiments. The validated model was then used to estimate the heat of crystallisation (-1.5×10^5 J/kg).

For continuous crystallisation, first the mixing behaviour was characterised. Classical pulse-tracer experiments were performed to find out the residence time distribution (RTD). By comparing the model predicted RTD to the experimental RTD, it was found that the continuous crystalliser used in this work resembled the mixing behaviour of two tanks-in-

series. While characterizing heat transfer behaviour, it was observed that the developed heat transfer model was inadequate considering the large thermal inertial of the particular setup used in this work. It was argued that for continuous crystallisations, the onset of crystallisation occurs as soon as the crystalliser reaches supersaturation (in other words there is effectively no meta stable zone width). Simulations revealed that the onset of crystallisation was captured accurately for continuous crystallisation. Though there were some gaps in the validation of mathematical model, the results presented here indicate satisfactory support for the developed model. Further work such as measuring the outlet particle size distributions and gathering reliable solubility data will provide further validation of the continuous crystalliser model which was outside the scope of this work.

The continuous crystalliser model was used to investigate the effect of key operating/design parameters (number of tanks, mean residence time) on key performance parameters (yield, mean and variance of the outlet PSD). It was concluded that crystallisers with a more 'plug-flow' like behaviour were better from a process control point of view, providing for faster response to step changes. Smaller particle sizes and narrower PSD were also obtained as the mixing behaviour became more 'plug-flow' like. Crystallisers with more 'plug-flow' mixing behaviour were seen to offer substantially high yield as compared to the CSTR configuration. It was observed that as the mean residence time decreased, both the yield and the mean particle size decreased. There was no effect of the mean residence time on the 'narrowness' (difference between the mean and variance) of the PSD. *In summary, crystallisers with increasing 'plug-flow' like mixing behaviour offer better control, higher yields and narrower PSD's*. The presented approach and modelling framework will be useful to design and optimize continuous crystallizers.

Acknowledgement

Authors are grateful towards Technoforce, Nashik for providing the continuous crystalliser setup which made this work possible.

Symbols & Notation

Symbol	Description	Unit
L	Particle size co-ordinate to describe the number distribution function	m
t	Time	s
$n(L,t)$	Number density distribution function	#/(m^3-m)
$G(L,t)$	Crystal growth rate	m/s
B_0	Nucleation rate	#/(m^3-s)
δ	Kronecker delta function	-
v	Volumetric flow rate	m^3/s
V_R	Volume of crystallizer	m^3
M_i	ith moment of the number density distribution function	m^i/m^3
M_L	Total liquid phase mass	kg
ρ_L	Liquid phase density	kg/m^3
ϵ	Solid phase hold-up	-
$\dot{M}_C$	Rate of mass transfer between solid and liquid phases	kg/s
M_S	Total solid phase mass	kg
ρ_S	Solid phase density	kg/m^3
σ_V	Particle volume shape factor	-
y_D	Mass fraction of dissolved solute in liquid phase	-
A, B	Constants for the linear liquid phase density function	kg/m^3
$C_{P,S}$	Specific heat capacity of the solid phase	J/(kg-K)
$C_{P,L}$	Specific heat capacity of the liquid phase	J/(kg-K)
T	Temperature	K
$(-\Delta H_C)$	Heat of crystallization	J/kg
$\langle UA \rangle$	Lumped heat transfer coefficient	J/(K-s)
$k_{g,0}$	Pre-exponential constant for growth rate	(m/s)(kmol/m^3)$^{-g}$
E_A	Activation energy	J/(kmol-K)
g	Growth rate exponent	-
R	Universal gas constant	J/kmol
C	Liquid phase solute concentration	kmol/m^3
$C^*(T)$	Solubility concentration as a function of temperature	kmol/m^3
k_1	Constant for primary nucleation rate	#/(m^3-s)(kmol/ m^3)$^{-n1}$
n_1	Exponent for primary nucleation rate	-
k_2	Constant for secondary nucleation rate	#/((m^2-s)(kmol/ m^3)$^{-n2}$)
n_2	Exponent for secondary nucleation rate	-
μ	Mean of particle size distribution	m
σ^2	Variance in particle size distribution	m^2

Subscripts

i	Moment index	S	Solid phase
k	Tank index	J	Jacket
o	Crystallizer inlet	E	Environment
L	Liquid phase	ref	Reference variable

References

Brown C., Adelakun J., Ni X., 2015. Characterization and modelling of anti-solvent crystallization of salicylic acid in a continuous oscillatory baffled crystallizer. Chemical Engineering and Processing: Process Intensification, 97, pp.180-186.

Jolliffe H., Gerogiorgis D., 2016. Process modelling and simulation for continuous pharmaceutical manufacturing of artemisinin. Chemical Engineering Research and Design, 112, pp.310-325.

Kubota N., 2008. A new interpretation of metastable zone widths measured for unseeded solutions. Journal of Crystal Growth, 310, 3, pp.629-634.

Nagy Z., Fevotte G., Kramer H., Simon L., 2013. Recent advances in the monitoring, modelling and control of crystallization systems. Chemical Engineering Research and Design, 91(10), pp.1903-1922

Octave Levenspiel, 1972. Chemical reaction engineering, Wiley, New York.

Pandit, A.V. and Ranade, V.V., 2015. Modeling Hysteresis during Crystallisation and Dissolution: Application to a Paracetamol–Ethanol System. Industrial & Engineering Chemistry Research, 54(42), pp.10364-10382.

Peña R., Nagy Z., 2015. Process Intensification through Continuous Spherical Crystallization Using a Two-Stage Mixed Suspension Mixed Product Removal (MSMPR) System. Crystal Growth & Design, 15 (9), pp.4225-4236.

Ramkrishna, D., 2000. Population Balances: Theory and Applications to Particulate Systems in Engineering. Academic Press: San Diego, 1st edition.

Randolph, A. D. and Larson, M. A., 1988. Theory of Particulate Processes: Analysis and Techniques of Continuous Crystallisation. San Diego, CA: Academic Press, Inc.

Su Q., Nagy Z., Rielly C., 2015. Pharmaceutical crystallisation processes from batch to continuous operation using MSMPR stages: Modelling, design, and control. Chemical Engineering and Processing: Process Intensification, 89, pp.41-53.

Vetter T., Burcham C., Doherty M., 2014. Regions of attainable particle sizes in continuous and batch crystallisation processes. Chemical Engineering Science, 106, pp.167-180.

5. Summary and Conclusions

The particle size distribution (PSD) is an important product quality attribute. The focused beam reflectance measurement (FBRM) probe allows for the online and in-situ detection of the chord length distribution (CLD). It is possible to derive the PSD from the FBRM probe measured CLD by applying suitable transformations. Majority of the existing models for the CLD to PSD problem follow a three-step approach: First a simple model is proposed to determine the CLD for a monodisperse particle population. Then, the CLD for a population of particles with a known PSD is determined by summing the individual contributions for each of the size classes. The individual contributions are calculated using the monodisperse particle population model. Finally, the inverse problem of deriving the PSD from a FBRM measured CLD becomes similar to a root finding problem wherein the guess PSD is changed iteratively until the model predicted CLD matches the measured CLD.

Previous work which addressed the CLD to PSD problem contributed towards developing more 'accurate' models for the PSD to CLD problem by considering effects of particle shape or orientation and/or developing better mathematical methods for solving the mathematically ill-posed CLD to PSD inversion problem. These models were often cumbersome to implement and for many cases, numerically stable solutions could not be guaranteed. Some of these models also required an additional parameter (to describe the particle shape) which could not be specified a-priori. In the present study, a simple model was proposed for the PSD to CLD problem by making suitable simplifying assumptions for the monodisperse particle population model. Further, the particle population was represented by standard two parameter (mean, variance) forms for size distribution (normal, lognormal). Due to both these simplifying assumptions, the multi-parameter CLD to PSD inversion problem as encountered in previous studies was reduced to a two parameter inversion problem. Thereby, it was possible to implement the model using simple spread sheeting tools. The model was then validated for systems of spherical particles, irregularly shaped particles and for other systems of practical relevance.

Modelling of crystallisation processes is important from a process design and control point of view. For the reliable prediction of crystalliser behaviour, it is important to have accurate

estimates for the values of key crystallisation kinetic parameters which describe phenomena like growth, nucleation and dissolution. However, the values for these parameters for even industrially important systems such as paracetamol-ethanol or ibuprofen-ethanol are not readily available in literature. Further, there is a lack of general consensus with regards to which rate laws (and consequently the choice of parameters) best describe crystallisation processes (nucleation, growth, dissolution) and how to go about estimating the parameter values for the same. Typically, these parameter values are highly system specific and need to be estimated through experimentation. Further, previous studies which estimate the kinetic parameter values, validate those values over a limited range of operating conditions and focus primarily of seeded crystallisation.

Motivated by the general lack of reliable crystallisation kinetic parameter values, Chapter 3 presents a protocol for their estimation. The specific case of unseeded cooling crystallisation of paracetamol in ethanol was considered. Experiments were performed wherein an undersaturated solution was cooled at specific cooling rates until after crystallisation and immediately reheated (using the same rate as applied for cooling) to the initial temperature. The particle counts were monitored during these crystallisation and subsequent dissolution cycles using the FBRM probe. Population balance equation (PBE) based models are widely used to model crystallisation processes. A standard method of moment's solution to the PBE coupled with the equation for mass of dissolved solids was implemented. Parametric sensitivity studies were performed to identify the most critical parameters. Parameter values for the case of paracetamol-ethanol were estimated by comparing model predictions to experiments for one cooling rate. The kinetic model was then validated by comparing model predictions to experiments for other cooling rates using the parameters estimated previously.

When the FBRM measured particle counts were plotted against the temperature, a hysteresis in particle counts was observed. Further it was observed that reducing the magnitude of the heating/cooling rate resulted in a twisting of the hysteresis loop. Capturing this effect of the twisting of the hysteresis loop through modelling was proposed for the rigorous validation of the crystallisation kinetic model. To enable to modelling of the dissolution stage, a full resolution of the PSD was needed. Hence, for the crystallisation stage, the PBE was solved using the high resolution finite volume method. For the dissolution stage, the PBE was solved using the moving pivot method. The kinetic parameter values for crystallisation estimated in

the previous step were used. The effect of the cooling/heat rates on the average diameter profiles was studied.

Crystallisation processes are typically carried out in a batch mode of operation. Recent studies have shown that operating crystallisers in a continuous mode potentially offer several benefits over the batch mode of operation. Some of these are better product consistency, more control over product quality and reduced operating cost and space. However, the implementation of continuous crystallisation can be cumbersome due to the complex process dynamics involved. Recent studies which investigated the potential benefits of continuous crystallisation were performed on a lab-scale. Issues related to scale up and design were not addressed (except for the continuously oscillating baffled crystalliser). Mathematical modelling can go a long way towards aiding in process design and control especially when complex process dynamics are involved. Validated mathematical models may also cleverly be used to reduce the uncertainties associated with scaling up.

In chapter 4, a generalised framework for modelling batch and continuous (fixed volume) crystallisation processes was presented. Key in capturing the performance of continuous crystallisers was capturing the mixing behaviour of the crystallisers. For capturing mixing behaviour, the tanks-in-series framework – a popular approach in chemical reaction engineering, was adopted in the presented model. The Population Balance Equation (PBE) was coupled with equations for solvent mass, dissolved solutes' mass and the energy balance equation corresponding to each tank and equations for all tanks were solved simultaneously. The outlet flowrate through each tank was calculated by considering the volume changes occurring due to crystallisation in a fixed volume crystalliser. A separate equation for the volume of the crystalliser was solved for the batch mode of operation. The PBE solution was implemented using the standard method of moments.

For model validation, the unseeded cooling crystallisation for a system of sodium nitrite in water was considered. A novel fixed volume continuous crystalliser assembly was considered in the present study. Hysteresis style batch experiments as described in chapter 3 were first performed to enable the estimation of kinetic parameters. Then, classical pulse tracer experiments were carried out to determine the mixing behaviour of the continuous crystalliser assembly. An assessment was made with regards to the best means to measure the outlet concentration in crystallisation operations. Heat transfer experiments were

performed to characterise the thermal behaviour of the crystalliser. Finally, continuous crystallisation experiments were performed under a fixed set of operating conditions. From a modelling point of view, the kinetic parameter values were estimated by the protocol described in Chapter 3 using batch experimental data. Simulations were performed for continuous crystallisation using the experimental operating conditions and using the batch kinetic model. The model was used to understand the effect of residence time and mixing behaviour (number of tanks) on the key performance parameters of mean, variance and yield. The following section summarises the major conclusions for each of the chapters.

The simple model developed for deriving the Particle Size Distribution (PSD) from the Chord Length Distribution (CLD) measured by the FBRM probe did not require the specification of an additional parameter and enabled the direct calculation of the PSD from known CLD measurements using simple spread sheeting tools. The model was shown to accurately predict PSDs of two systems of regularly shaped (spherical) particles both consisting of ceramic beads. The model was then extended for various systems of irregularly shaped particles: sand, plasma alumina and zinc dust. The model was seen to reasonably predict the PSD, wherein the mean of the PSD was accurately predicted and the variance was over predicted. The applicability of the model was then demonstrated for couple of industrially relevant systems: paracetamol crystals and p-aminophenol crystals. The model was seen to accurately predict the PSD for both these cases. The performance of the present model for all the presented systems was seen to be at par with the popular models which were more cumbersome to implement.

Chapter 3 described a general protocol to estimate key crystallisation kinetic parameters. Temperature cycling experiments were performed by varying the cooling/heating rates (0.3, 0.5 and 0.7 K/min) for the unseeded cooling crystallisation of a system of paracetamol-ethanol. A hysteresis was observed when the FBRM measured particle counts were plotted against the solution temperature (due to crystallisation and subsequent dissolution). Further it was observed that the cooling/heating rate had an effect of ‘twisting’ the hysteresis loop. It was argued that the ‘twisting’ effect of the hysteresis experiments could be used to develop a robust crystallisation kinetic model. A model was formulated by solving the PBE using the standard method of moments. Growth rate parameters were taken from literature. A detailed parametric sensitivity study was performed with regards to the nucleation rate parameters.

It was concluded that it is sufficient to estimate only the constants for the nucleation rate expressions for the purposes of a fairly accurate crystallisation kinetic model. The parameters of the exponents for the primary and secondary nucleation rate laws may be assigned fixed 'representative' values. Parameters estimated by comparing model predictions to experimental data for the 0.7 K/min experiment could be used to predict experimental data for the 0.3 K/min experiment. There was some mismatch with regards to the 0.5 K/min experiment.

To enable simulation of the hysteresis loop, the full resolution of the PSD needed to be solved. For this purpose, a combined solver using the high resolution finite volume (HRFV) method for the crystallisation step and the moving pivot method for the dissolution step was implemented. The solver was seen to reasonably capture the 'twisting' effect of the hysteresis loop. The model was also seen to be able to predict qualitatively, the counter-intuitive trend of increasing average particle size during dissolution. Further, the dissolution could be captured a-priori as no additional parameters were needed for specifying the dissolution rate. The shape of the dissolution curve depends on the PSD after crystallisation for obvious reasons. Hence, it can be argued that the hysteresis loop overall provided a 'stronger' validation for the crystallisation kinetic model.

Chapter 4 described a generalised framework for modelling batch and continuous crystallisation processes. For the purposes of model validation, the accuracy of the CLD to PSD model described in Chapter 2 to estimate the average Sauter mean diameter during crystallisation for sodium nitrite crystals was investigated. It was observed that the square weighted chord length distribution (CLD) gave 'lesser error prone' estimates of the PSD than the unweighted CLD. The crystallisation kinetic parameter values were estimated by comparing model predictions to the experimental results for the normalised 0^{th} moment of particle counts and the average Sauter mean diameter simultaneously. The model was validated by comparing model predictions with experimental results for different sets of experiments. The validated model was then used to estimate the heat of crystallisation (-1.5e5 J/kg).

For the novel continuous crystalliser considered, classical pulse-tracer experiments were performed to find out the residence time distribution (RTD). By comparing the model predicted RTD to the experimental RTD, it was found that the continuous crystalliser

resembled the mixing behaviour of two tanks-in-series. While characterizing heat transfer behaviour, it was observed that the developed heat transfer model was inadequate considering the particular setup. It was concluded that the thermal inertia of the continuous crystalliser needed to be considered for any meaningful heat transfer study. It was hypothesized for continuous crystallisation simulations that the onset of crystallisation occurs as soon as the crystalliser reaches supersaturation. Simulations revealed that the onset of crystallisation was captured accurately for continuous crystallisation.

The continuous crystalliser model was used to investigate the effect of key operating/design parameters (number of tanks, mean residence time) on key performance parameters (yield, mean and variance of the outlet PSD). It was concluded that crystallisers with a more 'plug-flow' like behaviour were better from a process control point of view, providing for faster response to step changes. Smaller particle sizes and narrower PSD were also obtained as the mixing behaviour became more 'plug-flow' like. Crystallisers with more 'plug-flow' mixing behaviour were seen to offer substantially high yield as compared to the CSTR configuration. It was observed that as the mean residence time decreased, both the yield and the mean particle size decreased. There was no effect of the mean residence time on the 'narrowness' (difference between the mean and variance) of the PSD. *In summary, crystallisers with increasing 'plug-flow' like mixing behaviour offered better control, higher yields and narrower PSD's*.

The following section outlines the further work that may be carried out to build upon the work presented in this thesis. In Chapter 2 a simple model was presented to estimate the PSD from the FBRM probe measured CLD. Further work would be to test the validity of the model for more systems of practical relevance. Separate single particle models may be developed for specific shapes such as needle shape, plate shape etc. while keeping the same framework as described in Chapter 2 for the CLD to PSD problem.

Further work for chapter 3 would be to investigate in more detail the different rate laws that govern the crystallisation kinetic processes. The effect of particle size on the growth rate, the effect of temperature and other factors on the secondary nucleation rate etc. need to be investigated in more detail. On an experimental side, the crystallisation processes must be characterised using more process analytical technologies (like the measurement of concentration, particle size, shape etc.). These experimental measurements when coupled

with modelling studies will provide more insights into the dynamics of crystallisation processes (evolving better rate laws, accurate estimation of kinetic parameters etc.). Further work may also be directed along estimating the crystallisation kinetic model parameters for different systems of practical relevance by following the protocol mentioned in the present study. Such a database would be helpful for rapid designing of crystallisation processes for those systems.

Chapter 4 presented a generalised framework to model batch and continuous crystallisation processes. A novel continuous crystalliser assembly was investigated experimentally. From an experimental point of view, further work would be to better characterise the continuous crystallisation experiments using process analytical technologies (particle size, concentration, yield etc.). The effects of scaling up of a continuous crystalliser assembly also need to be investigated. Crystallisation is highly system dependent and hence studying the same crystalliser assembly for various types of systems will also yield valuable insights into continuous crystalliser design. From a modelling perspective, inclusion of the thermal inertia of the crystalliser body in the heat transfer model and experimentally measuring the crystalliser body temperature are required to accurately characterize heat transfer behaviour. Further work along the fundamental crystallisation kinetic aspects may be coupled by similar studies as for Chapter 3.

Annexure A1

A1.1. Bertrand's Paradox

Consider an equilateral triangle inscribed in a circle. Suppose that a chord is chosen at random. What is the probability that the chosen chord is longer than the side of the triangle?

Bertrand proposed three different methods to determine this probability. All of these methods apparently seemed valid yet yielded significantly different results.

A1.1.1. Method 1

Suppose two points are chosen at random on the circumference of the circle. Now, the triangle is rotated along the circumference of the circle such that a vertex of the triangle coincides with one of the points chosen at random as shown in Figure A1. The triangle naturally divides the circle into three different arcs. If the other endpoint lies within the arcs of the circle corresponding to the red chords, then, the chord length will be less than the side of the triangle. The only way for the chord length to be longer than the side of the triangle is for the second end point to lie within the arc of the circle represented by the blue chord. Thus the probability that the chosen chord is longer than the side of the triangle is 1/3.

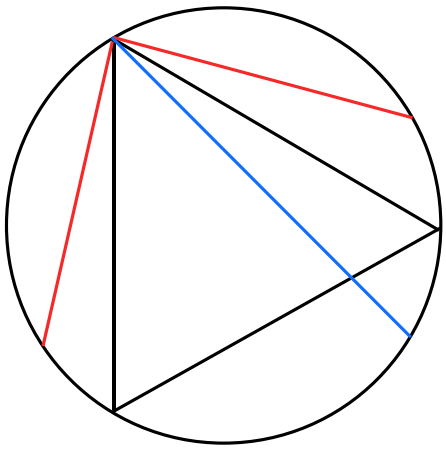

Figure A1.1. Method to determine the probability problem posed by Bertrand by Method 1

A1.1.2. Method 2

After a chord is chosen randomly, consider the radius of the circle which is perpendicular to these chords. This radius will pass through the midpoint of the chord in question. Now,

assume that the triangle is rotated such that a side of the triangle is perpendicular to the radius as shown in Figure A1.2. Now, a side of the triangle necessarily divides the radius into 2 equal divisions. Now, if the chord lies in the region of the radius indicated by the blue chord, then the size of the chord will be greater than the length of the triangle. If it falls in the region of the radius as indicated by the red chord, then the size of the chord will be smaller than the length of the triangle. Thus the probability that a chosen chord is longer than the length of the triangle is 1/2.

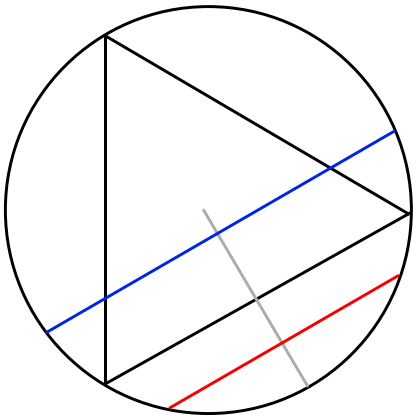

Figure A1.2. Method to determine the probability problem posed by Bertrand by Method 2

A1.1.3. Method 3

Consider a circle inscribed with the equilateral triangle as shown in Figure A1.3. The circle has half the radius of the original circle. Now, consider a randomly chosen chord. If the midpoint of the chord lies inside the circle, as indicated by the blue chord, then the length of the chord will be longer than the side of the triangle. If however, the midpoint lies outside the circle, the length will be lesser than the side of the triangle. The area of the smaller circle is one fourth the area of the larger circle. Hence, the probability that a chosen chord is longer than the length of the triangle is 1/4.

The classical solution of the paradox depends upon the method by which a chord is chosen at random. The three scenarios mentioned by Bertrand correspond to three different methods by which the random chord is chosen. In the absence of additional information with regards to how the random chord is chosen, there is no reason to prefer one over another.

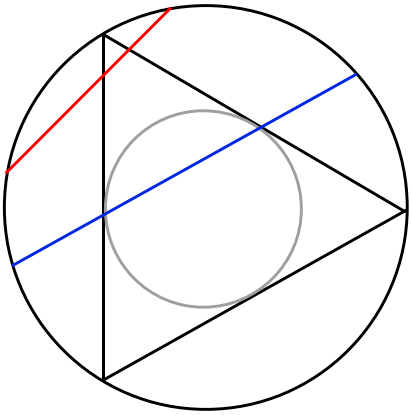

Figure A1.3. Method to determine the probability problem posed by Bertrand by Method 3

A1.1.4. Classical Solution

Annexure A2

A2.1. Discrete Equations for High Resolution Finite Volume Scheme (HRFV)

The equation for concentration, Equation 3.26, is discretized in first order with respect to time and the discretized version can be written as follows:

$$C^{m+1} = C^{m} - \left(\frac{\rho_p}{M_w}\right)\left(\frac{\pi}{6}\right)\sum_{i=1}^{N} X_i^3 \,(f_i^{m+1} - f_i^{m}) \qquad \text{A2.1}$$

The equation for temperature of the solution is written as Equation 3.15 and the discretized form of the temperature equation may be written as:

$$T^{m+1} = T^{m} + \frac{kR}{60} \qquad \text{A2.2}$$

The temperature is also discretized as first order with respect to time in line with the HRFV solution scheme. The Equations A2.1 and A2.2, along with the other discretized equations for the HRFV scheme, were solved simultaneously forward in time to obtain the solution of the population balance equation for the case of nucleation and growth.

A2.2. Discrete Equations for Moving Pivot Method

The moving pivot method presents an initial value problem. The equations for the boundary pivot location and the representative pivot location required for the solution of the population balance equation for dissolution are presented as Equations 3.26 and 3.27. The equations were discretized with first order with respect to time and the discrete forms of the equation may be written as:

$$V_i^{m+1} = V_i^{m} - 2kS \qquad \text{A2.3}$$

$$X_i^{m+1} = X_i^{m} - 2kS \qquad \text{A2.4}$$

The discrete equation for the concentration of the dissolved solids presented in Equation 3.30 may be written as:

$$C^{m+1} = C^{m} - \left(\frac{\rho_p}{M_w}\right)\left(\frac{\pi}{6}\right)\sum_{i=1}^{N} 3X_i^2 f_i \,(X_i^{m+1} - X_i^{m}) \qquad \text{A2.5}$$

The discrete equation for the temperature is the same as that for the HRFV scheme and is given as in Equation A2.2. These equations are solved simultaneously forward in time starting from the initial conditions to obtain the solution of the population balance equations.

A2.3. Mass Transfer Coefficient for Dissolution

The coefficient of mass transfer may be calculated as follows. The first parameter that we require is the diffusion coefficient which may be estimated from the Stokes-Einstein equation as:

$$D = \frac{kT}{2\pi\eta_l d_m} \qquad \text{A2.6}$$

The molecular diameter used in the Stokes-Einstein equation is estimated from the following relation:

$$d_m = \sqrt[3]{\frac{M_w}{\rho_p N_A}} \qquad \text{A2.7}$$

The mass transfer coefficient can then be predicted as a function of the particle size 'X' from the following relationship:

$$k_d = \frac{D}{X}\left(2 + 0.8\left(\frac{\epsilon X^4 \rho_l^3}{\eta_l^3}\right)^{0.2} Sc^{1/3}\right) \qquad \text{A2.8}$$

The Schmidt number is defined as:

$$Sc = \frac{\eta_l}{D\rho_l} \qquad \text{A2.9}$$

For stirred vessels, the mean specific power input can be estimated from:

$$\epsilon = Ne\,\frac{v_s^3 d_s^5}{V_r} \qquad \text{A2.10}$$

Typical values of Newton numbers for the stirred vessels with axial flow impellers ($Re<10^4$) are in the range of 0.3 to 0.7. Thus, an intermediate value of 0.5 is used as is also done by Worlitschek et. al. (2004)

For a detailed Symbols & Notations, kindly refer to the Symbols & Notations of Chapter 3 given on page 110.

Annexure A3

A3.1. Derivation of the moment equations

The population balance equation is:

$$\frac{\partial n(L)}{\partial t} + \frac{\partial n(L)G(L)}{\partial L} = \frac{v_0 n_0(L) - v n(L)}{V_R} \qquad \text{A3.1}$$

Multiplying L^i and integrating both sides with respect to *dL*, the RHS becomes:

$$\int_0^\infty L^i \, \frac{v_0 n_0(L) - v n(L)}{V_R} dL = \frac{v_0 M_{i,0} - v M_i}{V_R}$$

Multiplying L^i to the first term in the LHS we get the following:

The second terms in the LHS can be integrated by parts (assuming size independent growth rate) to give the following:

$$\int_0^\infty L^i \, \frac{\partial n(L)G(L)}{\partial L} dL = \; -0^i B_0 - iGM_{i-1}$$

B_0 is the flux of particles entering at $L = 0$ or also the nucleation rate.

Combining all the above equations, the moment transformation of the PBE becomes:

$$\frac{dM_i}{dt} = 0^i B_0 + iGM_{i-1} + \frac{v_0 M_{i,0} - v M_i}{V_R} \qquad \text{A3.2}$$

If the crystallizer volume is not constant (as in the cases of batch reactors), then the equation can be rewritten as:

$$\frac{dV_R M_i}{dt} = 0^i B_0 V_R + iGM_{i-1} V_R + v_0 M_{i,0} - v M_i \qquad \text{A3.3}$$

A3.2. Elimination of T_{ref} from the Heat Balance Equation

The heat balance can be written as:

$$\begin{aligned}\frac{d\left(M_L(1-y_D)C_{P,L}+M_L y_D C_{P,S}+M_S C_{P,S}\right)(T-T_{ref})}{dt} &= v_0\rho_{L,0}(1-\epsilon_0)y_{D,0}C_{P,S}\left(T_0-T_{ref}\right)\\ &+ v_0\rho_L(1-\epsilon_0)(1-y_{D,0})C_{P,L}\left(T_0-T_{ref}\right)\\ &+ v_0\rho_S\epsilon_0 C_{P,S}\left(T_0-T_{ref}\right)-v\rho_L(1-\epsilon)y_D C_{P,S}\left(T-T_{ref}\right)\\ &- v\rho_L(1-\epsilon)(1-y_D)C_{P,L}\left(T-T_{ref}\right)-v\rho_S\epsilon C_{P,S}\left(T-T_{ref}\right)\\ &+ \dot{M}_C\,(-\Delta H_C)+\langle UA\rangle_J\left(T_J-T\right)-\langle UA\rangle_E(T-T_E)\end{aligned} \quad \text{A3.4}$$

Multiplying mass balance of the dissolved solid's phase by C_pT_{ref}:

$$\begin{aligned}\frac{dM_L y_D C_{P,S}T_{ref}}{dt} &= v_0\rho_{L,0}(1-\epsilon_0)y_{D,0}C_{P,S}T_{ref}-v\rho_L(1-\epsilon)y_D C_{P,S}T_{ref}\\ &- \dot{M}_C C_{P,S}T_{ref}\end{aligned}$$

Multiplying mass balance of solvent phase by $C_{P,L}T_{ref}$ and adding the resulting equation into the above equation, we get the following relation independent of T_{ref}:

$$\begin{aligned}\frac{dM_L(1-y_D)C_{P,L}T_{ref}}{dt} &= v_0\rho_{L,0}(1-\epsilon_0)(1-y_{D,0})C_{P,L}T_{ref}\\ &- v\rho_L(1-\epsilon)(1-y_D)C_{P,L}T_{ref}\end{aligned}$$

Similarly for the solid phase we have:

$$\frac{dM_S C_{P,S}T_{ref}}{dt}=v_0\rho_S\epsilon_0 C_{P,S}T_{ref}-v\rho_S\epsilon C_{P,S}T_{ref}+\dot{M}_C C_{P,S}T_{ref}$$

Adding the above equations to the original energy balance equation, we are left with the following relation independent of T_{ref}:

$$\begin{aligned}\frac{d\left(M_L(1-y_D)C_{P,L}+M_L y_D C_{P,S}+M_S C_{P,S}\right)T}{dt} &= v_0\rho_{L,0}(1-\epsilon_0)y_{D,0}C_{P,S}T_0+v_0\rho_{L,0}(1-\epsilon_0)(1-y_{D,0})C_{P,L}T_0\\ &+ v_0\rho_S\epsilon_0 C_{P,S}T_0-v\rho_L(1-\epsilon)y_D C_{P,S}T\\ &- v\rho_L(1-\epsilon)(1-y_D)C_{P,L}T-v\rho_S\epsilon C_{P,S}T+\dot{M}_C\,(-\Delta H_C)\\ &+ \langle UA\rangle_J\left(T_J-T\right)-\langle UA\rangle_E(T-T_E)\end{aligned} \quad \text{A3.5}$$

A3.3. Outlet velocity relations

It should be noted that for a constant volume process the following relation holds true:

$$\frac{M_L}{\rho_L} + \frac{M_S}{\rho_S} = V_R \qquad \text{A3.6}$$

Differentiating w.r.t *t* we get:

$$\frac{1}{\rho_L}\frac{dM_L}{dt} - \frac{M_L}{\rho_L^2}\frac{d\rho_L}{dt} + \frac{1}{\rho_S}\frac{dM_S}{dt} = 0$$

$$\frac{M_L}{\rho_L^2}\frac{d\rho_L}{dt} = \frac{1}{\rho_L}\frac{dM_L}{dt} + \frac{1}{\rho_S}\frac{dM_S}{dt}$$

$$\frac{M_L}{\rho_L^2}\frac{d\rho_L}{dt} = \frac{1}{\rho_L}\{v_0\rho_{L,0}(1-\epsilon_0) - v\rho_L(1-\epsilon) - \dot{M}_C\} + \frac{1}{\rho_S}\{v_0\rho_S\epsilon_0 - v\rho_S\epsilon + \dot{M}_C\}$$

$$\frac{M_L}{\rho_L^2}\frac{d\rho_L}{dt} = \left\{v_0\frac{\rho_{L,0}}{\rho_L}(1-\epsilon_0) - v(1-\epsilon) - \frac{\dot{M}_C}{\rho_L}\right\} + \left\{v_0\epsilon_0 - v\epsilon + \frac{\dot{M}_C}{\rho_S}\right\}$$

$$\frac{M_L}{\rho_L^2}\frac{d\rho_L}{dt} = \left\{v_0\frac{\rho_{L,0}}{\rho_L}(1-\epsilon_0) + v_0\epsilon_0\right\} - v - \left\{\frac{\dot{M}_C}{\rho_L} - \frac{\dot{M}_C}{\rho_S}\right\}$$

$$v = \left\{v_0\frac{\rho_{L,0}}{\rho_L}(1-\epsilon_0) + v_0\epsilon_0\right\} - \frac{M_L}{\rho_L^2}\frac{d\rho_L}{dt} - \left\{\frac{\dot{M}_C}{\rho_L} - \frac{\dot{M}_C}{\rho_S}\right\} \qquad \text{(3.7}$$

Now there are two simplifying assumptions we can make to proceed from here.

Constant density

Assuming a constant density, the above equation for velocity directly reduces to:

$$v = v_0 - \dot{M}_C\left\{\frac{\rho_S - \rho_L}{\rho_S\rho_L}\right\} \qquad \text{A3.8}$$

Linearly varying density

$$\rho_L = A + By_D \qquad \text{A3.9}$$

$$v = \left\{v_0\frac{\rho_{L,0}}{\rho_L}(1-\epsilon_0) + v_0\epsilon_0\right\} - \frac{BM_L}{\rho_L^2}\frac{dy_D}{dt} - \left\{\frac{\dot{M}_C}{\rho_L} - \frac{\dot{M}_C}{\rho_S}\right\} \qquad \text{A3.10}$$

Differentiating the dissolved solute mass:

$$\frac{dM_L y_D}{dt} = y_D \frac{dM_L}{dt} + M_L \frac{dy_D}{dt}$$

$$M_L \frac{dy_D}{dt} = v_0 \rho_{L,0}(1-\epsilon_0) y_{D,0} - v\rho_L(1-\epsilon) y_D - \dot{M}_C - y_D\{v_0 \rho_{L,0}(1-\epsilon_0) - v\rho_L(1-\epsilon) - \dot{M}_C\}$$

$$\frac{dy_D}{dt} = \frac{1}{M_L}\{v_0 \rho_{L,0}(1-\epsilon_0)(y_{D,0} - y_D) - \dot{M}_C(1-y_D)\}$$

It should be noted that for the linearly varying density and constant density, the outlet volumetric flow rate may still be obtained explicitly and does not need to be solved simultaneously.

A3.4. Equation for Crystallizer Volume in Batch Mode

For the case of a batch reactor, instead of solving for the outlet velocity, we will have to solve for the crystallizer volume instead.

$$\frac{M_L}{\rho_L} + \frac{M_S}{\rho_S} = V_R \qquad \text{A3.11}$$

Differentiating w.r.t *t* we get:

$$\frac{dV_R}{dt} = \frac{1}{\rho_L}\frac{dM_L}{dt} - \frac{M_L}{\rho_L^2}\frac{d\rho_L}{dt} + \frac{1}{\rho_S}\frac{dM_S}{dt}$$

Setting $v_0 = v = 0$, we get:

$$\frac{dV_R}{dt} = -\frac{\dot{M}_C}{\rho_L} - \frac{M_L}{\rho_L^2}\frac{d\rho_L}{dt} + \frac{\dot{M}_C}{\rho_S} \qquad \text{A3.12}$$

Again as before, there are two simplifying assumptions we can make to proceed from here.

Constant density

$$\frac{dV_R}{dt} = -\frac{\dot{M}_C}{\rho_L} + \frac{\dot{M}_C}{\rho_S} \qquad \text{A3.13}$$

Linearly varying density

$$\frac{dV_R}{dt} = -\frac{\dot{M}_C}{\rho_L} - \frac{BM_L}{\rho_L^2}\frac{dy_D}{dt} + \frac{\dot{M}_C}{\rho_S} \qquad \text{A3.14}$$

Differentiating the dissolved solute mass:

$$\frac{dM_L y_D}{dt} = y_D \frac{dM_L}{dt} + M_L \frac{dy_D}{dt}$$

$$\frac{dy_D}{dt} = \frac{1}{M_L}\{v_0 \rho_{L,0}(1-\epsilon_0)(y_{D,0} - y_D) - \dot{M}_C(1-y_D)\}$$

Setting $v_0 = v = 0$, we get:

$$\frac{dy_D}{dt} = \frac{-\dot{M}_C(1-y_D)}{M_L}$$

A3.5. Derivation of Non-Dimensional Equations

Moment equations for constant crystallizer unit volume:

$$\frac{L_{ref}^i M_{0,ref}}{V_{ref} t_{ref}} \frac{dM'_{i,k}}{dt'} = 0^i \frac{L_{ref}^i M_{0,ref}}{V_{ref} t_{ref}} B'_{0,k} + i \frac{L_{ref}}{t_{ref}} G'_k \frac{L_{ref}^{i-1} M_{0,ref}}{V_{ref}} M'_{i-1,k} + \frac{L_{ref}^i M_{0,ref}}{V_{ref} t_{ref}} \frac{v'_{k-1} M'_{i,k-1} - v'_k M'_{i,k}}{V'_{R,k}}$$

$$\frac{dM'_{i,k}}{dt'} = 0^i B'_{0,k} + i G'_k M'_{i-1,k} + \frac{v'_{k-1} M'_{i,k-1} - v'_k M'_{i,k}}{V'_{R,k}} \quad \text{A3.15}$$

Moment equations for non-constant crystallizer unit volume:

$$\frac{L_{ref}^i M_{0,ref}}{t_{ref}} \frac{dV'_{R,k} M'_{i,k}}{dt'} = 0^i \frac{L_{ref}^i M_{0,ref}}{t_{ref}} B'_{0,k} V'_{R,k} + i \frac{L_{ref}}{t_{ref}} G'_k \frac{L_{ref}^{i-1} M_{0,ref}}{V_{ref}} M'_{i-1,k} V_{ref} V'_{R,k} + \frac{L_{ref}^i M_{0,ref}}{t_{ref}} \left(v'_{k-1} M'_{i,k-1} - v'_k M'_{i,k}\right)$$

$$\frac{dV'_{R,k} M'_{i,k}}{dt'} = 0^i B'_{0,k} V'_{R,k} + i G'_k M'_{i-1,k} V'_{R,k} + v'_{k-1} M'_{i,k-1} - v'_k M'_{i,k} \quad \text{A3.16}$$

Equation for mass of liquid phase in crystallizer unit:

$$\frac{\rho_{ref} V_{ref}}{t_{ref}} \frac{dM'_{L,k}}{dt'} = \frac{\rho_{ref} V_{ref}}{t_{ref}} v'_{k-1} \rho'_{L,k-1}(1-\epsilon_{k-1}) - \frac{\rho_{ref} V_{ref}}{t_{ref}} v'_k \rho'_{L,k}(1-\epsilon_k) - \frac{\rho_{ref} V_{ref}}{t_{ref}} \dot{M}'_{C,k}$$

$$\frac{dM'_{L,k}}{dt'} = v'_{k-1}\rho'_{L,k-1}(1-\epsilon_{k-1}) - v'_k\rho'_{L,k}(1-\epsilon_k) - \dot{M}'_{C,k}\frac{\rho_{ref}V_{ref}}{t_{ref}}\frac{dM'_{L,k}}{dt'}$$

$$= \frac{\rho_{ref}V_{ref}}{t_{ref}}v'_{k-1}\rho'_{L,k-1}(1-\epsilon_{k-1}) - \frac{\rho_{ref}V_{ref}}{t_{ref}}v'_k\rho'_{L,k}(1-\epsilon_k) \quad \text{A3.17}$$

$$- \frac{\rho_{ref}V_{ref}}{t_{ref}}\dot{M}'_{C,k}$$

Equation for mass of solid phase in crystallizer unit:

$$\frac{\rho_{ref}V_{ref}}{t_{ref}}\frac{dM'_{S,k}}{dt'} = \frac{\rho_{ref}V_{ref}}{t_{ref}}v'_{k-1}\rho'_S\epsilon_{k-1} - \frac{\rho_{ref}V_{ref}}{t_{ref}}v'_k\rho'_S\epsilon_k + \frac{\rho_{ref}V_{ref}}{t_{ref}}\dot{M}'_{C,k}$$

$$\frac{dM'_{S,k}}{dt'} = v'_{k-1}\rho'_S\epsilon_{k-1} - v'_k\rho'_S\epsilon_k - \dot{M}'_{C,k} \quad \text{A3.18}$$

$$\frac{\rho_{ref}V_{ref}}{t_{ref}}\dot{M}'_{C,k} = 3\sigma_V\frac{L_{ref}}{t_{ref}}G'_k\frac{L^2_{ref}M_{0,ref}}{V_{ref}}M'_{2,k}\rho_{ref}V_{ref}\rho'_SV'_{R,k}$$

$$\dot{M}'_{C,k} = 3\sigma_V\frac{L^3_{ref}M_{0,ref}}{V_{ref}}G'_kM'_{2,k}\rho'_SV'_{R,k} = 3\beta_1G'_kM'_{2,k}\rho'_SV'_{R,k} \quad \text{A3.19}$$

Equation for mass of dissolved solid:

$$\frac{\rho_{ref}V_{ref}}{t_{ref}}\frac{dM'_{L,k}y_{D,k}}{dt'}$$

$$= \frac{\rho_{ref}V_{ref}}{t_{ref}}v'_{k-1}\rho'_{L,k-1}(1-\epsilon_{k-1})y_{D,k-1} - \frac{\rho_{ref}V_{ref}}{t_{ref}}v'_k\rho'_{L,k}(1$$

$$- \epsilon_k)y_{D,k} - \frac{\rho_{ref}V_{ref}}{t_{ref}}\dot{M}'_{C,k}$$

$$\frac{dM'_{L,k}y_{D,k}}{dt'} = v'_{k-1}\rho'_{L,k-1}(1-\epsilon_{k-1})y_{D,k-1} - v'_k\rho'_{L,k}(1-\epsilon_k)y_{D,k} - \dot{M}'_{C,k} \quad \text{A3.20}$$

Equation for heat balance of crystallizer unit:

$$\frac{\rho_{ref}V_{ref}C_{P,ref}T_{ref}}{t_{ref}}\frac{d\left(M'_{L,k}C'_{P,MIX,k}+M'_{S,k}C'_{P,S}\right)T'_k}{dt'}$$
$$=\frac{\rho_{ref}V_{ref}C_{P,ref}T_{ref}}{t_{ref}}v'_{k-1}\rho'_{L,k-1}(1-\epsilon_{k-1})C'_{P,MIX,k-1}T'_{k-1}$$
$$-\frac{\rho_{ref}V_{ref}C_{P,ref}T_{ref}}{t_{ref}}v'_k\rho'_{L,k}(1-\epsilon_k)C'_{P,MIX,k}T'_k$$
$$+\frac{\rho_{ref}V_{ref}C_{P,ref}T_{ref}}{t_{ref}}v'_{k-1}\rho'_S\epsilon_{k-1}C'_{P,S}T'_{k-1}$$
$$-\frac{\rho_{ref}V_{ref}C_{P,ref}T_{ref}}{t_{ref}}v'_k\rho'_S\epsilon_kC'_{P,S}T'_k$$
$$+\frac{\rho_{ref}V_{ref}C_{P,ref}T_{ref}}{t_{ref}}\dot{M}'_{C,k}\frac{(-\Delta H_C)}{C_{P,ref}T_{ref}}$$
$$+\frac{\rho_{ref}V_{ref}C_{P,ref}T_{ref}}{t_{ref}}\frac{\langle UA\rangle_{J,k}t_{ref}}{\rho_{ref}V_{ref}C_{P,ref}}\left(T'_J-T'_k\right)$$
$$-\frac{\rho_{ref}V_{ref}C_{P,ref}T_{ref}}{t_{ref}}\frac{\langle UA\rangle_{E,k}t_{ref}}{\rho_{ref}V_{ref}C_{P,ref}}(T'_k-T'_E)$$

$$\frac{d\left(M'_{L,k}C'_{P,MIX,k}+M'_{S,k}C'_{P,S}\right)T'_k}{dt'}$$
$$=v'_{k-1}\rho'_{L,k-1}(1-\epsilon_{k-1})C'_{P,MIX,k-1}T'_{k-1}$$
$$-v'_k\rho'_{L,k}(1-\epsilon_k)C'_{P,MIX,k}T'_k+v'_{k-1}\rho'_S\epsilon_{k-1}C'_{P,S}T'_{k-1}$$
$$-v'_k\rho'_S\epsilon_kC'_{P,S}T'_k+\beta_2\dot{M}'_{C,k}+\beta_{3,k}\left(T'_J-T'_k\right)-\beta_{4,k}(T'_k-T'_E) \quad \text{A3.21}$$

The equations for the outlet velocity can be written as:

Constant density

$$\frac{V_{ref}}{t_{ref}}v'_k=\frac{V_{ref}}{t_{ref}}v'_{k-1}-\frac{\rho_{ref}V_{ref}}{t_{ref}}\dot{M}'_{C,k}\frac{1}{\rho_{ref}}\left\{\frac{\rho'_S-\rho'_L}{\rho'_S\rho'_L}\right\}$$

$$v'_k=v'_{k-1}-\dot{M}'_{C,k}\left\{\frac{\rho'_S-\rho'_L}{\rho'_S\rho'_L}\right\} \quad \text{A3.22}$$

Linearly varying density

$$\frac{V_{ref}}{t_{ref}}v'_k=\left\{\frac{V_{ref}}{t_{ref}}v'_{k-1}\frac{\rho'_{L,k-1}}{\rho'_{L,k}}(1-\epsilon_{k-1})+\frac{V_{ref}}{t_{ref}}v'_{k-1}\epsilon_{k-1}\right\}$$
$$-\frac{V_{ref}}{t_{ref}}\frac{\beta_{D,2}M'_{L,k}}{\rho'^2_{L,k}}\frac{dy_{D,k}}{dt'}-\frac{V_{ref}}{t_{ref}}\left\{\frac{\dot{M}'_{C,k}}{\rho'_{L,k}}-\frac{\dot{M}'_{C,k}}{\rho'_S}\right\}$$

$$\frac{1}{t_{ref}}\frac{dy_{D,k}}{dt'} = \frac{1}{t_{ref}}\frac{1}{M'_{L,k}}\left\{v'_{k-1}\rho'_{L,k-1}(1-\epsilon_{k-1})\left(y_{D,k-1}-y_{D,k}\right) - \dot{M}'_{C,k}\left(1-y_{D,k}\right)\right\}$$

$$v'_k = \left\{v'_{k-1}\frac{\rho'_{L,k-1}}{\rho'_{L,k}}(1-\epsilon_{k-1}) + v'_{k-1}\epsilon_{k-1}\right\} - \frac{\beta_{D,2}M'_{L,k}}{\rho'^2_{L,k}}\frac{dy_{D,k}}{dt'} - \left\{\frac{\dot{M}'_{C,k}}{\rho'_{L,k}} - \frac{\dot{M}'_{C,k}}{\rho'_S}\right\} \quad \text{A3.23}$$

$$\frac{dy_{D,k}}{dt'} = \frac{1}{M'_{L,k}}\left\{v'_{k-1}\rho'_{L,k-1}(1-\epsilon_{k-1})\left(y_{D,k-1}-y_{D,k}\right) - \dot{M}'_{C,k}\left(1-y_{D,k}\right)\right\} \quad \text{A3.24}$$

Equation for solution volume for batch mode:

Constant density

$$\frac{V_{ref}}{t_{ref}}\frac{dV'_R}{dt'} = -\frac{V_{ref}}{t_{ref}}\frac{\dot{M}'_C}{\rho'_L} + \frac{V_{ref}}{t_{ref}}\frac{\dot{M}'_C}{\rho'_S}$$

$$\frac{dV'_R}{dt'} = -\frac{\dot{M}'_C}{\rho'_L} + \frac{\dot{M}'_C}{\rho'_S} \quad \text{A3.25}$$

Linearly varying density

$$\frac{V_{ref}}{t_{ref}}\frac{dV'_R}{dt'} = -\frac{V_{ref}}{t_{ref}}\frac{\dot{M}'_C}{\rho'_L} - \frac{V_{ref}}{t_{ref}}\frac{B'M'_L}{\rho'^2_L}\frac{dy_D}{dt} + \frac{V_{ref}}{t_{ref}}\frac{\dot{M}'_C}{\rho'_S}$$

$$\frac{1}{t_{ref}}\frac{dy_D}{dt'} = \frac{1}{t_{ref}}\frac{-\dot{M}'_C(1-y_D)}{M'_L}$$

$$\frac{dV'_R}{dt'} = -\frac{\dot{M}'_C}{\rho'_L} - \frac{\beta_{D,2}M'_L}{\rho'^2_L}\frac{dy_D}{dt} + \frac{\dot{M}'_C}{\rho'_S} \quad \text{A3.26}$$

$$\frac{dy_D}{dt'} = \frac{-\dot{M}'_C(1-y_D)}{M'_L} \quad \text{A3.27}$$

A3.6. Derivation of Non-Dimensional Constitutive Laws

Crystal Growth

$$G_k = k_{g,0}exp\left(-\frac{E_A}{RT_k}\right)(C_k - C^*_k(T_k))^g \quad \text{A3.28}$$

$$C_k = \frac{M_{L,k}y_{D,k}}{(1-\epsilon_k)V_{R,k}m_W}$$

$$\frac{L_{ref}}{t_{ref}} G'_k = k_{g,0} exp\left(-\frac{E_A}{RT_{ref}T'_k}\right) C^g_{ref} (C'_k - C'^*(T'_k))^g$$

$$G'_k = exp\left(-\frac{E_A}{RT_{ref}T'_k}\right) (C'_k - C'^*(T'_k))^g$$

$$G'_k = \beta_{g,1} exp\left(-\frac{\beta_{g,2}}{T'_k}\right) (C'_k - C'^*(T'_k))^g \quad \text{A3.29}$$

$$\beta_{g,1} = \frac{k_{g,0} t_{ref} C^g_{ref}}{L_{ref}}$$

$$\beta_{g,2} = \frac{E_A}{RT_{ref}}$$

Primary Nucleation

$$B_{0,k,pri} = k_1 (C_k - C^*_k(T_k))^{n_1} \quad \text{A3.30}$$

$$\frac{M_{0,ref}}{V_{ref} t_{ref}} B'_{0,k,pri} = k_1 C^{n_1}_{ref} (C'_k - C'^*_k(T'))^{n_1}$$

$$B'_{0,k,pri} = \beta_{N,1} (C'_k - C'^*_k(T'))^{n_1} \quad \text{A3.31}$$

$$\beta_{N,1} = \frac{V_{ref} t_{ref} k_1 C^{n_1}_{ref}}{M_{0,ref}}$$

Secondary Nucleation

$$B_{0,k,sec} = k_2 M_{2,k} (C_k - C^*_k(T_k))^{n_2} \quad \text{A3.32}$$

$$\frac{M_{0,ref}}{V_{ref} t_{ref}} B'_{0,k,sec} = k_2 \frac{L^2_{ref} M_{0,ref}}{V_{ref}} M'_{2,k} C^{n_2}_{ref} (C'_k - C'^*_k(T'_k))^{n_2}$$

$$B'_{0,k,sec} = \beta_{N,2} M'_{2,k} (C'_k - C'^*_k(T'_k))^{n_2} \quad \text{A3.33}$$

$$\beta_{N,2} = k_2 L^2_{ref} C^{n_2}_{ref} t_{ref}$$

A3.7. Derivation of Non-Dimensional Auxiliary Laws

Solubility

$$x_{D,sol}(T) = \frac{kg_{solute}}{kg_{solvent}} = C_1 e^{C_2 T} \quad \text{A3.34}$$

$$y_{D,sol} = \frac{kg_{solute}}{kg_{solute} + kg_{solvent}} = \frac{x_{D,sol}}{1 + x_{D,sol}}$$

$$C^*(T) = C\left(y_{D,sol}\right) = \frac{y_{D,sol}\rho_L(y_{D,sol})}{m_W}$$

$$x_{D,sol}(T') = C_1 e^{C_2 T_{ref} T'}$$

$$\beta_{S,1} = C_1$$

$$\beta_{S,2} = C_2 T_{ref}$$

$$x_{D,sol}(T') = \beta_{S,1} e^{\beta_{S,2} T'}$$

$$y_{D,sol}(T') = \frac{kg_{solute}}{kg_{solute} + kg_{solvent}} = \frac{x_{D,sol}(T')}{1 + x_{D,sol}(T')}$$

$$C'^*(T') = C'\left(y_{D,sol}\right) = \beta_C y_{D,sol}(T')\rho'_L\left(y_{D,sol}(T')\right) \quad \text{A3.35}$$

Concentration

$$C(y_D) = \frac{y_D \rho_L(y_D)}{m_W} \quad \text{A3.36}$$

$$C_{ref} C'(y_D) = \frac{y_D \rho_{ref} \rho'_L(y_D)}{m_W}$$

$$C'(y_D) = \frac{\rho_{ref}}{C_{ref} m_W} y_D \rho'_L(y_D) = \beta_C y_D \rho'_L(y_D) \quad \text{A3.37}$$

Density

$$\rho_L(y_D) = A + B y_D \quad \text{A3.38}$$

Considering mass weighted average,

$$A = \rho_L; B = (\rho_S - \rho_L)$$

$$\rho'_L(y_D) = \frac{A}{\rho_{ref}} + \frac{B}{\rho_{ref}} y_D$$

$$\rho'_L(y_D) = \beta_{D,1} + \beta_{D,2} y_D \quad \text{A3.39}$$

Specific Heat

$$C_{P,MIX}(y_D) = X + Y y_D \quad \text{A3.40}$$

Considering mass weighted average,

$$X = C_{P,L}; Y = (C_{P,S} - C_{P,L})$$

$$C'_{P,MIX}(y_D) = \frac{X}{C_{P,ref}} + \frac{Y}{C_{P,ref}} y_D$$

$$C'_{P,MIX}(y_D) = \beta_{CP,1} + \beta_{CP,2} y_D \quad \text{A3.41}$$

A3.8. Model Verification for Batch Processes

A3.8.1. Heat Transfer Model

Both the jacket-side heat transfer and the environmental side heat transfer are identical in their implementation. Hence, model verification was only done considering the jacket-side heat transfer. Analytical solution was derived for the heat transfer problem for a batch reactor by solving the Equation A3.21 using suitable assumptions. The analytical solution for the cooling of a batch reactor using a constant jacket temperature in a non-dimensional form can be written as follows:

$$T'_2 = T'_J + (T'_1 - T'_J) exp\left(-\frac{\beta_3 t'}{M'_L C'_{P,L}}\right) \quad \text{A3.42}$$

A comparison of the analytical solution and the simulated results for different values of β_3 is given in the Figure A3.1. The model predicted results can be seen to match the analytical results. Thus, the model can be said to be verified for the capturing heat transfer.

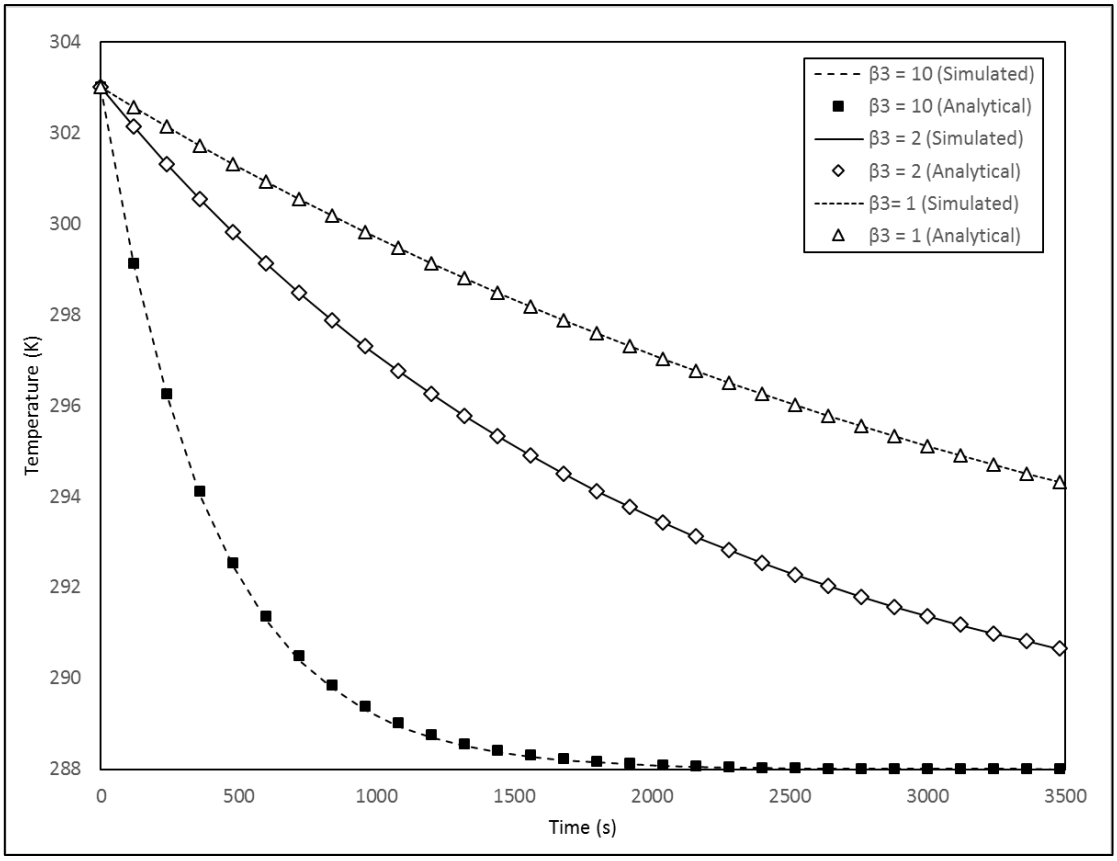

Figure A3.1. Comparison between simulated and analytical solutions for a jacket maintained at 288K and the crystalliser with initial temperature 303K

A3.8.2. Verification of Tanks-in-series Model

For the verification of the tanks-in-series model, a comparison was made between the model predicted solution and the solution obtained by directly solving the tanks-in-series ODE's. In a non-dimensional form, the ODE's for tanks-in-series model can be written as:

$$\frac{dC_1'}{dt'} = n(1 - C_1') \qquad \text{A3.43}$$

$$\frac{dC_i'}{dt'} = n(C_{i-1}' - C_i') \; for \; i > 1 \qquad \text{A3.44}$$

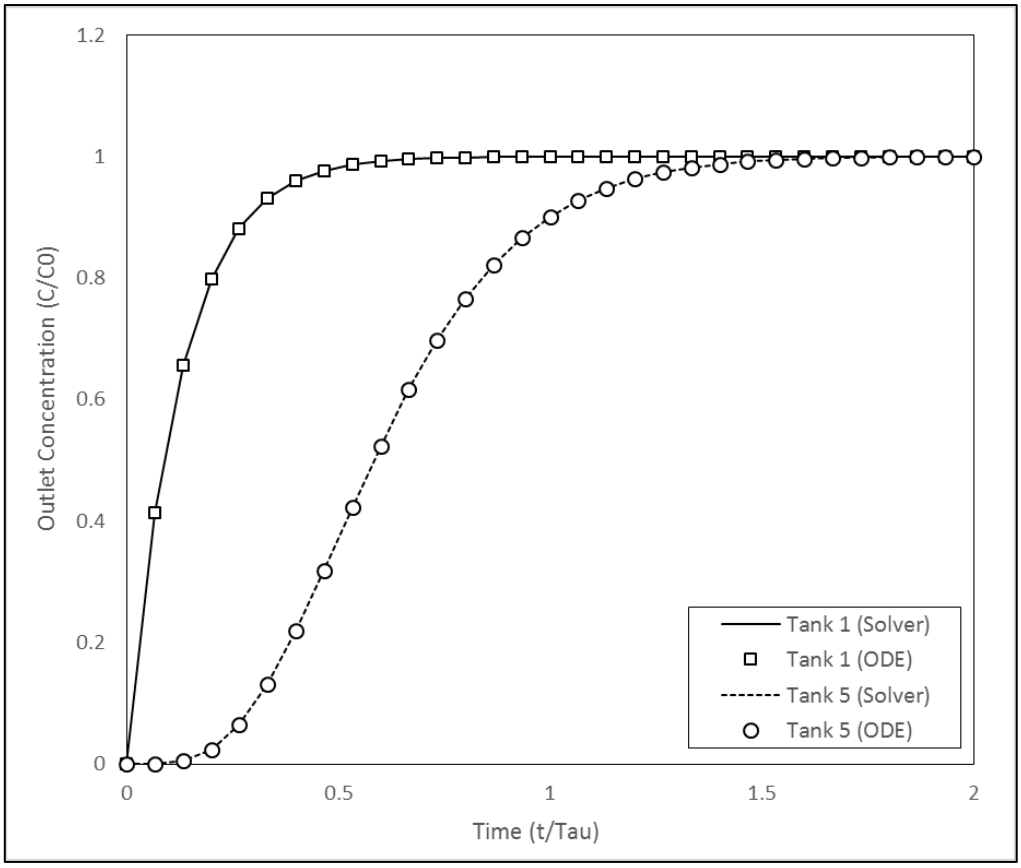

Figure A3.2. Comparison between simulated and ODE results for tanks-in-series model for a step response tracer experiment (solved for 8 tanks)

It should be noted that *n* is the number of tanks and it appears in the equations because the reference time used for non-dimensionalization was taken as the total residence time rather than the residence time for a tank. The inlet concentration was used for the non-dimensionalization of concentration. Both the model equations and the above equations were solved for 8 tanks in series for a standard step response type of tracer experiment. A comparison between the model predicted and the tanks-in series ODE predicted concentration profiles for the 1^{st} and the 5^{th} tanks is shown in the Figure A3.2. As can be seen, there is excellent agreement between the two. Hence, the model was verified for the tanks in series model.

A3.8.3. Crystallization model

For the verification of the crystallization part of the solver, the simulation results were compared to the simulation results obtained using a previous solver. Simulations were performed for a model system of Paracetamol-Ethanol having a concentration of 1.37 kmol/m^3 corresponding to a solubility temperature of ~326K. The solution was assumed to be

completely clear. The solution temperature was assumed to be held constant at 285 K to simulate induction time. The period after the nucleation events had started was simulated. For the new solver, simulations were performed using both constant and variable liquid density assumptions. The crystallization kinetic parameter values estimated in Chapter 3 were used for the simulations.

A comparison between the simulated concentration profiles using the previous solver and the new solver (using constant and varying liquid density assumptions) is shown in Figure A3.3. A comparison between the simulated 0^{th} moment profiles using the previous solver and the new solver (using constant and varying liquid density assumptions) is shown in Figure A3.4. A comparison between the simulated Sauter mean diameter profiles using the previous solver and the new solver (using constant and varying liquid density assumptions) is shown in Figure A3.5. Let us first consider the case of comparison between the previous solver and the new solver implemented using a constant density assumption. As can be seen from Figure A3.3, there is an excellent agreement between the concentration profiles, although the agreement is not exact. As seen from Figures A3.4 and A3.5, there is good agreement between the 0^{th} moment and Sauter mean diameter profiles although there is some discrepancy towards the end. The discrepancy arises due to the fact that in the previous solver does not consider the volume change in the liquid phase due to the precipitation of solids. As the volume of the liquid phase will decrease when this happens, the 0^{th} moment (which is the number density of particles), will increase correspondingly.

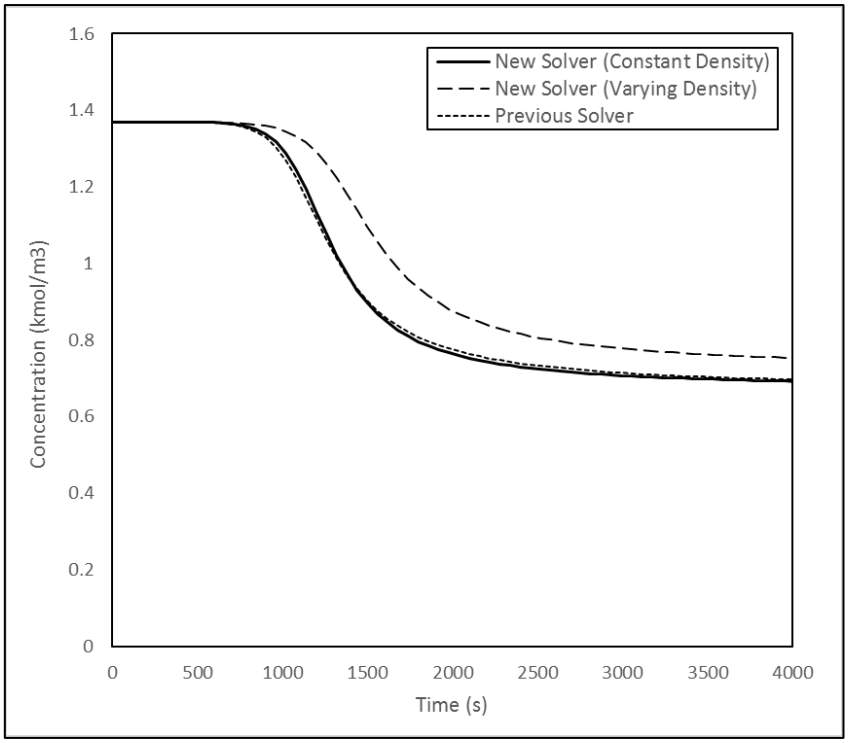

Figure A3.3. Comparison between the concentration profiles predicted using the previous solver and the new solver (using constant and variable liquid density assumptions)

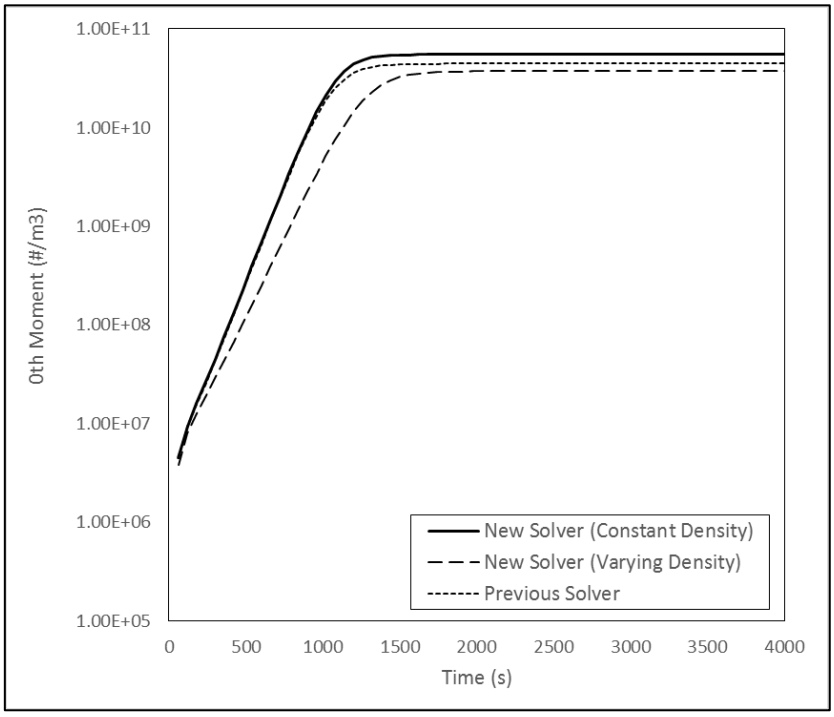

Figure A3.4. Comparison between the 0th moment profiles predicted using the previous solver and the new solver (using constant and variable liquid density assumptions)

As can be seen from the Figures A3.3-A3.5, there is a difference between the concentration, 0^{th} moment and Sauter mean diameter profiles predicted using the varying density assumptions as opposed to using the constant density assumption. However, the difference

is not drastic as is indicated by the relatively close values for the Sauter mean diameters (~ 200 micron) for both cases. Hence values estimated for the crystallisation kinetic parameters estimated using the previous solver and the new solver will not differ by order(s) of magnitude.

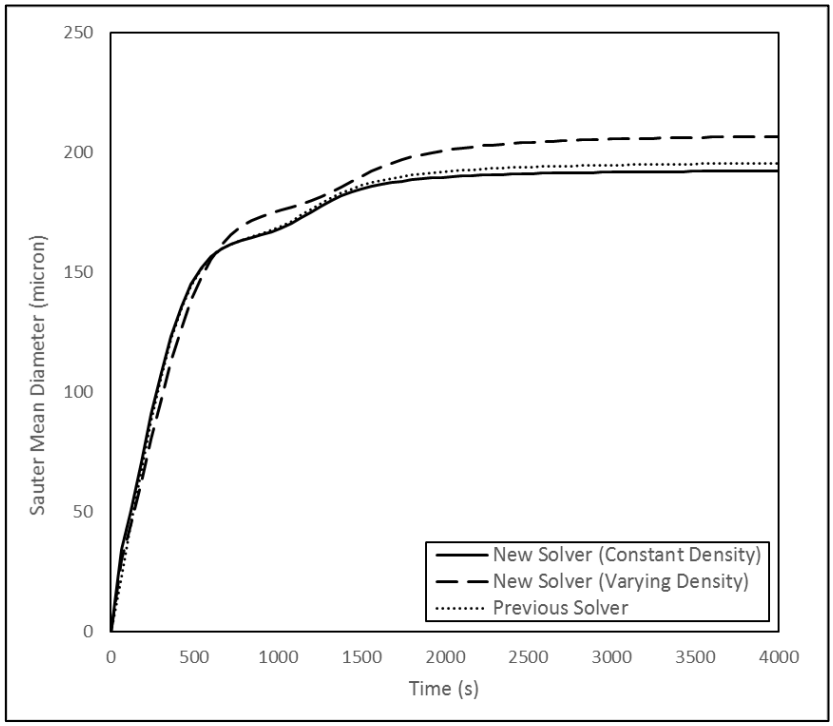

Figure A3.5. Comparison between the Sauter Mean Diameter profiles predicted using the previous solver and the new solver (using constant and variable liquid density assumptions)

Hence, from the above section, we can conclude that the model has been verified for different modules of heat transfer, crystallization and tanks-in-series. The next section deals with the validation studies of the model.

A3.9. Characterising Heat Transfer for Continuous Crystallisation

As done for the batch process, it is necessary to estimate the parameter values required for the heat transfer model. Two model parameters are required to characterise the heat transfer model as described earlier. The first to describe the heat transfer between the jacket and the fluid and the second the heat transfer between the fluid and the environment. As discussed in the batch process, both these parameters are important to accurately capture the heat transfer behaviour of a crystalliser. Going along the same lines as the batch reactor, heat transfer experiments were performed in the continuous crystalliser. Experiments were performed wherein the steady state outlet temperature was measured as a function of the

jacket set-point temperature for different mean residence time values. The experiments were performed for 2 values of jacket set-point temperatures (1^0C and 8^0C). A plot showing the LMTD values calculated for different values of mean residence time at the two jacket set-point temperatures is shown in Figure A3.6.

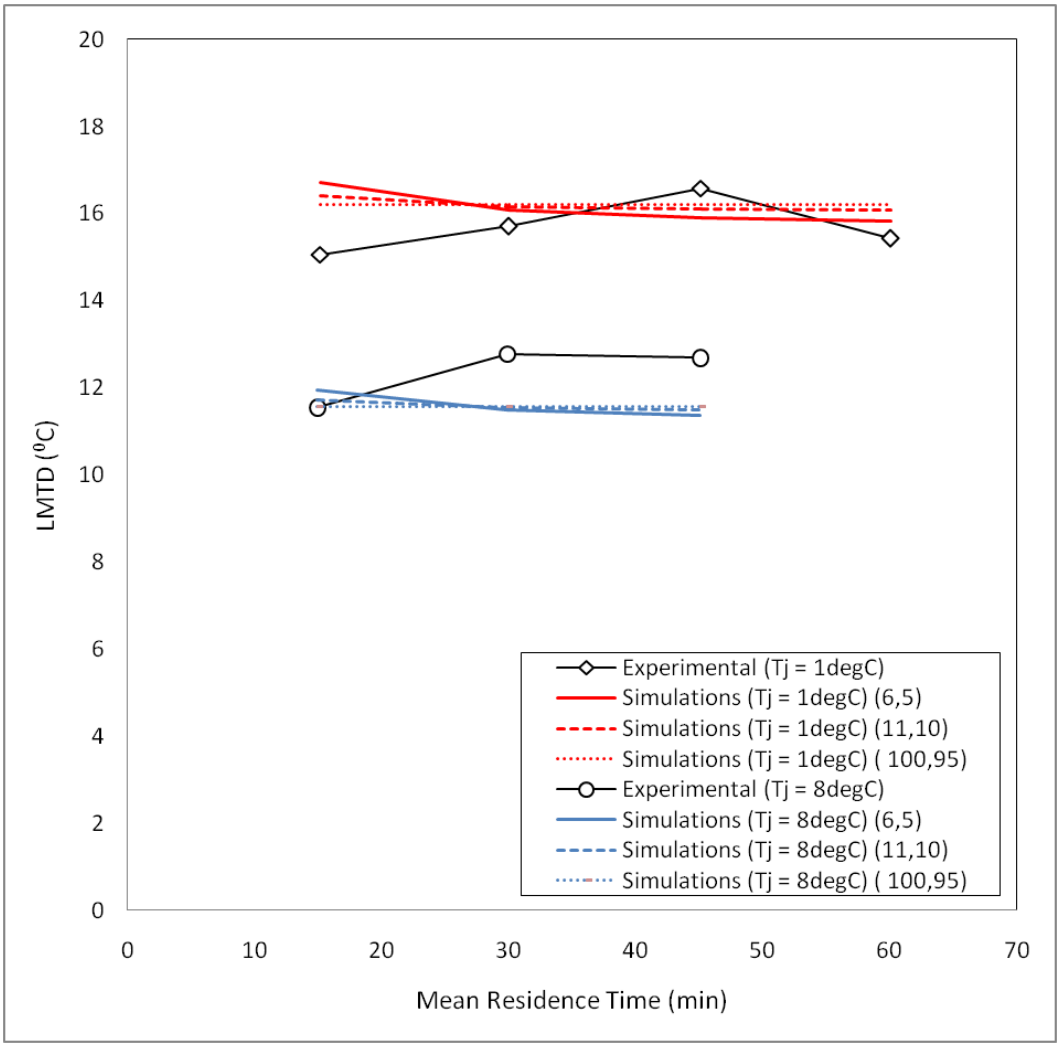

Figure A3.6. Comparison of LMTD values for different mean residence times for jacket set-point temperatures of 1^0C and 8^0C

To estimate the parameter values for the heat transfer parameters, the simulation results for the LMTD versus the mean residence time curves for the two set-point jacket temperatures were performed. It was observed that there were multiple pairs of parameter values which could capture the heat transfer behaviour as shown in Figure A3.6. As the parameter values increase, the LMTD values do not depend on the mean residence time. This implies that the time scales for heat transfer are significantly faster than the residence time. It can be seen from the Figure A3.6 that all three sets of parameter values seem to capture the heat transfer behaviour reasonably. Furthermore, the same set of parameter values can be used to

simulate for both the jacket set-point temperatures. As can be seen from the parameter values, a higher rate of jacket-side heat transfer is compensated by a higher rate of heat loss to the environment to obtain the same behaviour. Further, it should be noted that the pair (5.5, 5) is the minimum value for which the desired heat transfer behaviour was observed.

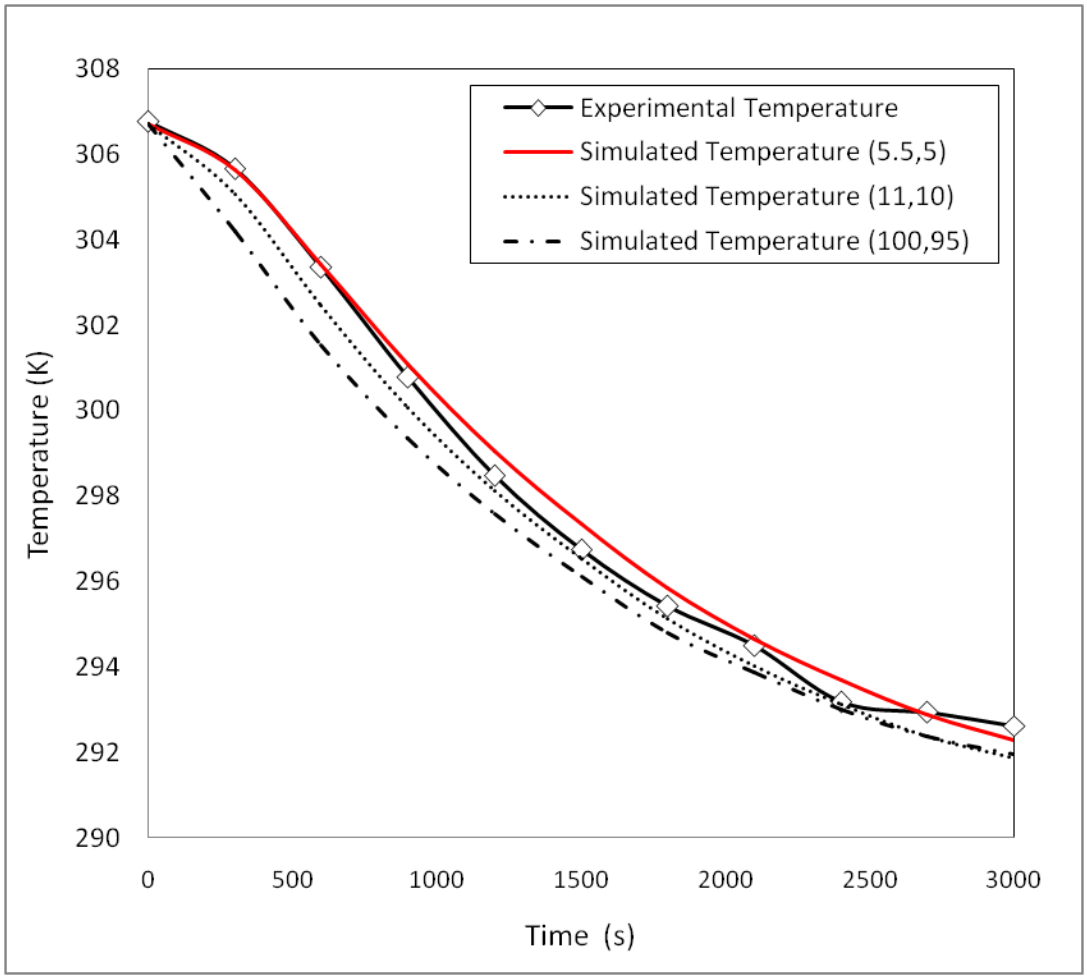

Figure A3.7. Comparison of the experimental and simulated initial temperature response to changing jacket temperature for 3 pair of parameter values

Even though the heat transfer behaviour is captured correctly, while considering the exothermic/endothermic processes, the order of magnitude of the heat transfer rates (from the jacket/to the environment) with respect to the heat of crystallisation becomes important. Thus, it becomes important to eliminate the unrealistic pairs of parameter values in hopes of accurately capturing the crystalliser behaviour. Rigorous temperature cycling experiments performed under different conditions are ideal for narrowing down the 'realistic' set of parameter values. However, in the present text, as such experiments were not performed, we will instead study the initial temperature response of the outlet of the crystalliser to the change in jacket temperature. For performing the simulations, as done for the batch process,

the jacket temperature profile was supplied as input. A comparison between the simulated and experimental initial temperature response for a changing jacket temperature is shown in Figure A3.7. As can be seen from the Figure A3.7, the parameter values of (5.5, 5) is closest in predicting the crystalliser temperature response. Hence, in the present study, the parameter values (5.5, 5) shall be used for the heat transfer model. A comparison between the experimental and simulated crystalliser temperature and the experimental jacket temperatures using the values (5.5, 5) is shown in Figure A3.8.

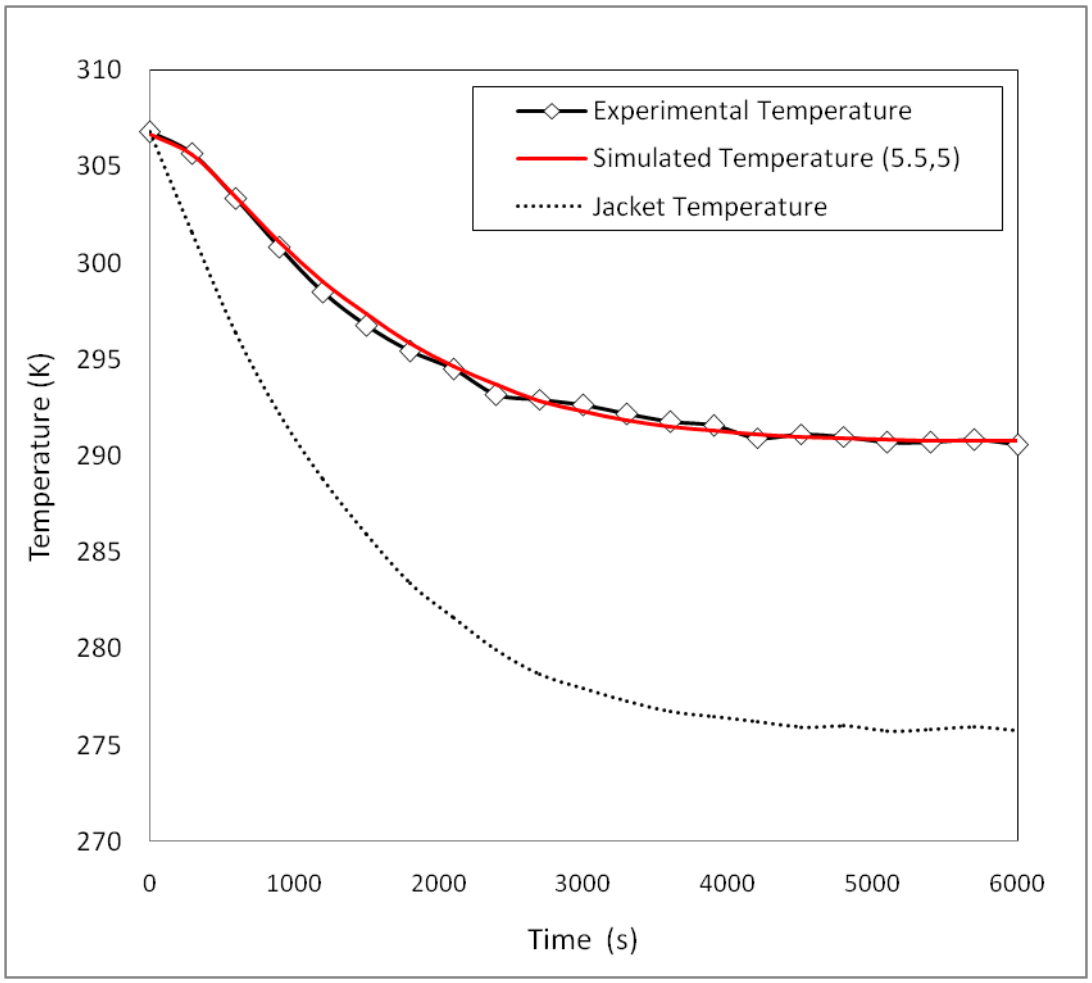

Figure A3.8. Comparison between the simulated and experimental crystalliser temperature and the experimental jacket temperature

The aforementioned values estimated for the heat transfer parameters were estimated for water. Before directly using these values for understanding the heat transfer behaviour of a solution of water saturated with sodium nitrite, the effect of sodium nitrite concentration on the heat transfer behaviour must be investigated. For this, the simulated temperature response of pure water was compared to the simulated temperature response of a solution of sodium nitrite in water. The same jacket temperature profile was used to simulate for both

cases and such a comparison is shown in Figure A3.9. It was observed through simulations that there is no observable effect of the sodium nitrite concentration on the heat transfer behaviour of the solution. Thus, we may directly use the parameter values estimated earlier to simulate for the continuous crystallisation experiments.

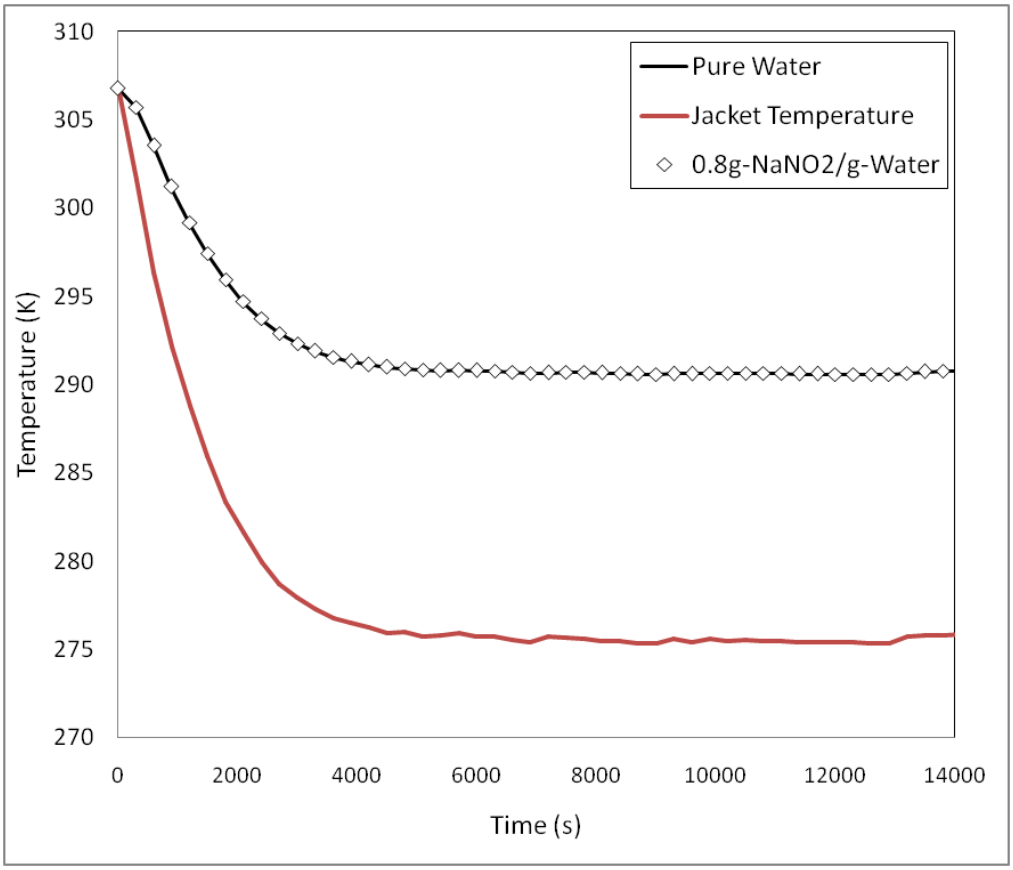

Figure A3.9. Effect of solute concentration on the heat transfer characteristics

Before moving on to simulating the heat transfer behaviour for a continuous crystallisation operation, it would be helpful to analyse the experimental data for the same. Nine continuous crystallisation experiments were performed using similar conditions. The only difference in those experiments was that they were performed under different ambient conditions. Figure A3.10 shows the comparison between the crystalliser outlet and jacket outlet temperatures under ambient temperatures of 30^0C and 34^0C. It can be seen from Figure A3.10 that experimentally, there is no observable difference between the two in the steady state temperature even though the initial temperatures were different. However, as seen in Figure A3.10 simulations using the parameter values estimated in the previous section reveal a difference between the predicted temperature profiles under different ambient conditions. Hence the parameter values estimated previously seemed to be inaccurate. The parameter

values were estimated under a constant ambient condition and hence could not capture the effect (or the lack thereof) of the ambient temperature on the heat transfer behaviour.

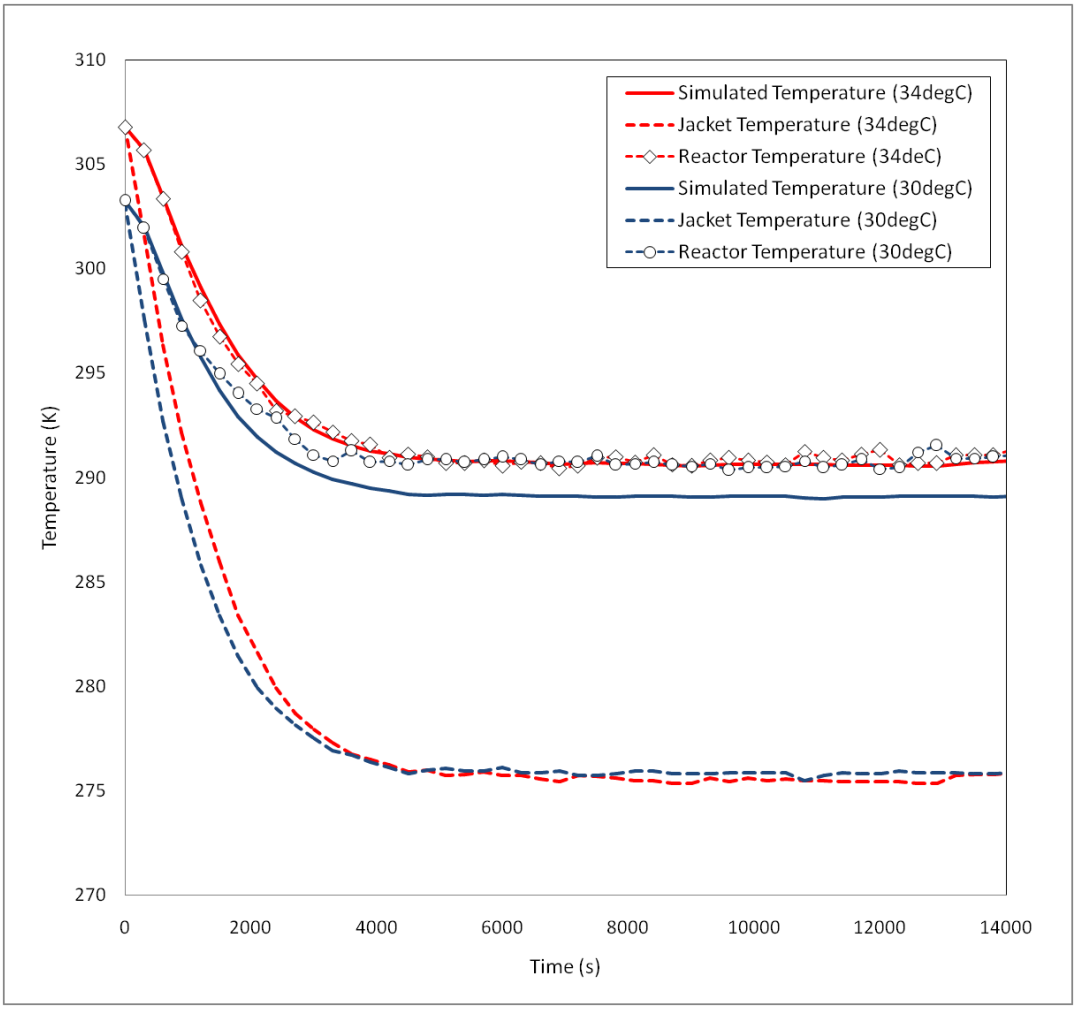

Figure A3.10. Comparison between the crystalliser outlet and jacket outlet temperature profiles for ambient temperature conditions of 30^0C and 34^0C

Although the discrepancy observed in Figure A3.10 does not seem significant, it was seen to affect the crystallisation behaviour significantly. Hence, the parameter values need to be re-estimated to account for the lack of impact of environmental conditions on the thermal behaviour of the crystalliser. The interpretation of the experimental results suggest that the thermal behaviour of the continuous crystalliser may be obtained even considering insulated conditions. In order to simulate for such a case, the lumped parameter for environmental side heat transfer was set to zero. The value for the lumped parameter for the jacket to solution heat transfer ($\boldsymbol{UA_J}$) was adjusted by matching the experimental and simulated steady state crystalliser outlet temperatures. However, as can be seen from the Figure A3.11, there is a significant mismatch between the simulated and experimental crystalliser outlet temperature

profiles considering 'insulated' conditions. Thus, it may be concluded that the present model cannot reasonably capture the thermal behaviour of the present continuous crystalliser. The reason for the mismatch can be attributed to the fact that the thermal inertia of the continuous crystalliser itself was not considered in the model. The actual mode of heat transfer was from the jacket fluid to the crystalliser walls and then from the crystalliser walls to the solution. Since the continuous crystalliser was made entirely of metal, the thermal inertia of the continuous crystalliser would be significant (many times that of the process fluid).

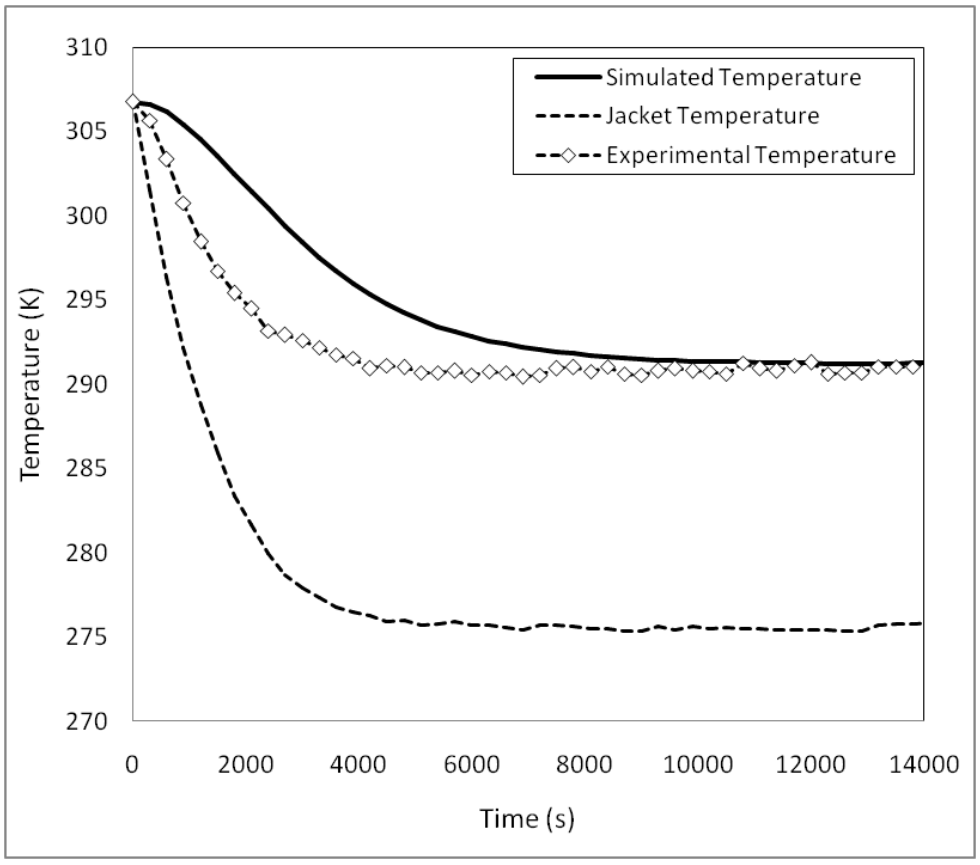

Figure A3.11: Comparison between the simulated crystalliser outlet temperature (under insulated conditions), experimental crystalliser outlet temperature and jacket outlet temperature

Further work to improve the heat transfer model would be to write a separate heat balance equation for the crystalliser body and couple it with the process fluid heat balance equation. Experimental measurements of the crystalliser body temperature profiles would also be required to calibrate the improved heat transfer model. Such a study was not carried out in the present text. To get around this issue, for the present case, the heat transfer parameter values from the experimental data were re-estimated for different ambient conditions. These

parameter values were then used for the corresponding continuous crystallisation simulations. Although this hindered the predictive capability of the heat transfer behaviour of the continuous crystalliser, it provided a workable solution to study crystallisation in the continuous crystalliser behaviour.

Before carrying out an exercise in re-estimating heat transfer parameter values for different experimental data, it was important to interpret the experimental data at different ambient conditions. Certain unusual thermal behaviour was observed from the experimental data. Comparisons between the experimental crystalliser outlet temperature profiles and the jacket outlet temperature profiles for ambient temperatures of 25^0C and 30^0C are shown in Figure A3.12. After 10000s, a steady state thermal behaviour similar to that obtained for ambient temperatures of 30^0C and 34^0C was observed for the case of 25^0C ambient temperature (*CC5*). However, before 10000s, the crystalliser outlet temperature had stabilised to a much lower value (~285K) before the sudden jump to 'normal operation' was observed. This suggests that it might be possible that before 10000s, a highly endothermic polymorphic form of sodium nitrite might have been produced which reverted back to the 'standard' form after 10000s of operation. The alternate hypothesis that the 'standard' form is exothermic might also be true. The exothermicity of sodium nitrite crystallisation has already been established in batch crystallisation experiments. However, it was also seen through preliminary simulations that the exothermicity for the present case was insignificant so as to cause any temperature fluctuations. The polymorph hypothesis is both supported and contradicted when another experiment (*CC8*) under 25^0C ambient conditions was considered. The *CC8* experiment does not contain the abrupt temperature change as observed in the previous experiment. However, it is stabilised at a much lower value of temperature than the *CC5* experiment. This may be explained by the hypothesis that in both experiments, a mixture of the 'standard' and the highly endothermic polymorphs are obtained. A lower value of temperature in the *CC8* experiment can then be attributed to a higher percentage of endothermic polymorph as compared to the *CC5* experiment.

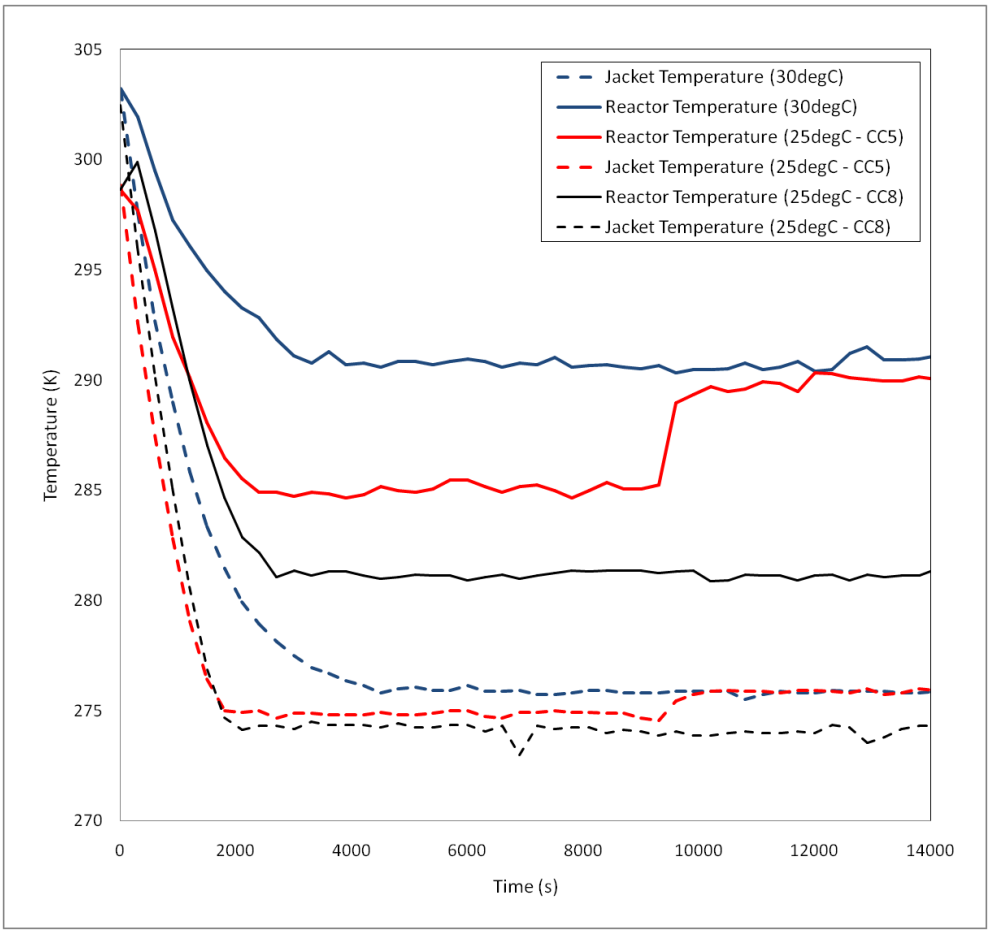

Figure A3.12. Comparison between the crystalliser outlet temperatures and the jacket outlet temperatures at ambient temperatures of 30^0C and 25^0C

In the next section, an attempt is made to quantify the endothermicity of the hypothesized sodium nitrite polymorph. However, in order to carry out the continuous crystallisation simulations, as discussed earlier, the heat transfer parameter values must be re-estimated for the ambient temperatures of 25^0C, 30^0C and 34^0C. The parameter values are listed in Table. As can be seen from the table, for the same value of $\boldsymbol{UA_J}$, the value for $\boldsymbol{UA_{ENV}}$ keeps increasing with decreasing ambient temperature. As discussed earlier, it is not possible to derive any meaningful logic in the trend of parameters as the thermal inertia of the crystalliser body was not accounted for. The present values are only for the sake of estimating the order of magnitude of the heat losses/transfers and to simulate the temperature profile of the continuous crystalliser given the jacket temperature profile and the ambient temperature. More meaningful parameter values and logical inferences may be obtained if the moment of inertia of the crystalliser body is accounted for in the model. A comparison between the simulated and experimental crystalliser outlet temperatures for different ambient temperatures is given in Figure A3.13.

Table A3.1: Re-estimated parameter values for different ambient temperatures

Ambient Temperature	UA_J	UA_{ENV}
^{0}C	Joule/K	Joule/K
25	5.5	8.5
30	5.5	6.5
34	5.5	5

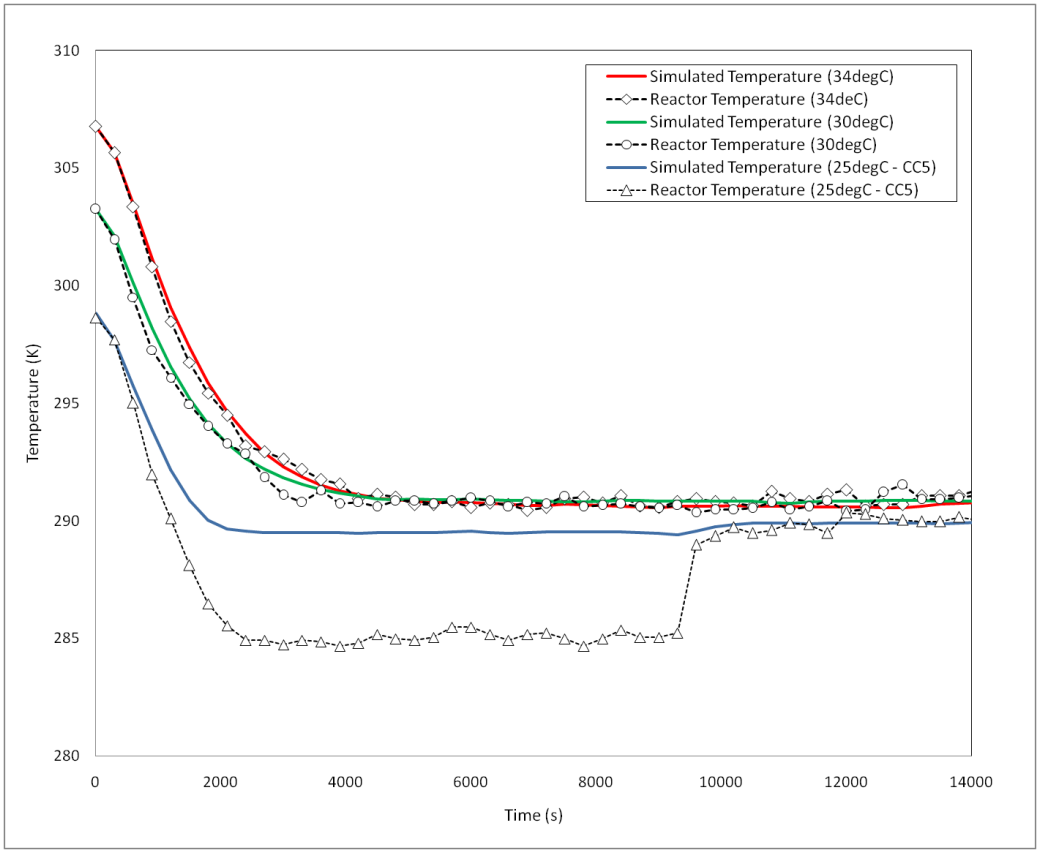

Figure A3.13: Comparison between the simulated and experimental crystalliser outlet temperature profiles for different ambient temperatures

The cooling mechanism employed in the continuous crystalliser was first the transfer of heat from the jacket cooling fluid to the metal crystalliser body which in turn transferred heat to the solution. The thermal inertia of the continuous crystalliser was significantly more than the thermal inertia of the process fluid itself (many times higher). Thus, in order to model the heat transfer behaviour of processes adequately, the heat balance equation for the crystalliser body must be coupled with the existing set of model equations. Additional experimental measurements of the temperature profile of the crystalliser metal body along-with those of solution and jacket fluid temperature profiles would be required to completely

capture the heat transfer effects. Additional data such as the total thermal inertia of the continuous crystalliser would also be required.

For a detailed Symbols & Notations, kindly refer to the Symbols & Notations of Chapter 4 given on page 156.